Investigation and Modelling of Fetal Sheep Maturation

A thesis submitted
for the degree of
Doctor of Philosophy
in Physics
by

Yanyang Xu

June 2010
The University of Waikato

Abstract

In this thesis, I study the maturational changes of the fetal sheep ECoG (electrocorticogram) in its third-trimester of gestation (95-140 days of gestation), investigate three continuum models for electrical behaviour of the cortex, and tune the parameters in one of these models to generate the discontinuous EEG waves in the immature cortex. Visual inspection of the ECoG time-series shows that the third-trimester of fetal sheep is comprised of two stages: *early third-trimester* characterised by bursting activity separated by silent intervals, and *late third-trimester* with well-defined SWS (slow wave sleep) and REM (rapid eye movement) sleep states. For the late third-trimester, the results of power, correlation time, and SVD (singular value decomposition) entropy analysis demonstrate that the sleep state change is a cortical phase transition—with SWS-to-REM transition being a first-order transition, and REM-to-SWS second-order. Further analyses by correlation time, SVD entropy, and spectral edge frequency display that the differentiation of the two distinct SWS and REM sleep states occurs at about 125 dGA (day gestational age). Spectral analysis divides the third-trimester into four stages in terms of the frequency and amplitude variations of the major resonances. Spindle-like resonances only occur in the first stage. A power surge is observed immediately prior to the emergence of the two sleep states. Most significant changes of the spectrum occur during the fourth stage for both SWS (in amplitude) and REM (in frequency) sleep states.

For the modelling of the immature cortex, different theoretical descriptions of cortical behaviour are investigated, including the `ccf` (cortical column field) model of J. J. Wright, and the Waikato cortical model. For the `ccf` model at centimetric scale, the time-series, fluctuation power, power law relation, gamma oscillation, phase relation between excitatory and inhibitory elements, power spectral density, and spatial Fourier spectrum are quantified from numerical simulations. From these simulations, I determined that the physiologically sophisticated `ccf` model is too large and unwieldy for easy tuning to match the electrical response of the immature cortex. The Waikato *near-far fast-soma* model is constructed by incorporating the back-propagation effect of the action potential into the Waikato fast-soma model, state equations are listed and stability prediction are performed by varying the gap junction diffusion strength, subcortical drive, and the rate constants of the near- and far-dendritic tree. In the end, I selected the classic and simpler Waikato *slow-soma* mean-field model to use for my immature cortex simulations.

Model parameters are customised based on the physiology of the immature cortex, including GABA (an inhibitory neurotransmitter in adult) excitatory effect, number of synaptic connections, and rate constants of the IPSPs (inhibitory postsynaptic potential). After hyperpolarising the neuron resting voltage sufficiently to cause the immature inhibitory neuron to act as an excitatory agent, I alter the rate constant of the IPSP, and study the stability of the immature cortex. The bursting activity and quiet states of the discontinuous EEG are simulated and the gap junction diffusion effect in the immature cortex is also examined. For a rate constant of $18.6\ \mathrm{s}^{-1}$, slow oscillations in the quiet states are generated, and for rate constant of $25\ \mathrm{s}^{-1}$, a possible cortical network oscillation emerges. As far as I know, this is the first time that the GABA excitatory effect has been integrated into a mean-field cortical model and the discontinuous EEG wave successfully simulated in a qualitative way.

Dedication

To my parents

To my grandparents

For their endless love and for loving me for who I am.

Acknowledgements

I owe a great debt of gratitude to many people for helping me accomplish this thesis. First and foremost, I would like to express my deep thanks to my supervisors. I heartfully thank my chief supervisor, Associate Professor Alistair Steyn-Ross, for his graceful guidance at every step of my study at the University of Waikato. I am especially thankful for his patience, encouragement, discussion, and inspiration at every difficult moment. The theoretical guidance by Professor Moira Steyn-Ross was critical for the modelling work in this thesis. Deep thanks for that. I would like to especially thank Dr Marcus Wilson for his help at the beginning of my study for making my transfer into the new environment quick and smooth. And also thanks for his influence on many places of my research. For Professor Jamie Sleigh, thanks for the advice on the physiological aspects of the research project.

A large part of this thesis is based on the work of Professor James Wright at the University of Auckland. Thanks to Professor Wright and Nicholas Hawthorn for providing the raw fetal sheep data and the source code of the `ccf` model.

This thesis could not have been finished without the technical support from the department. I wish to express my gratitude to David Nicholls, Ian Honey, Lawrence D'Oliveiro, Bruce Rhodes, and David Bugden. They were always there ready to help when I met problems. Also thanks Dr Michael Cree for help on LaTeX, computer, and network matters, to librarian Cheryl Ward for the paper searches, and to secretary Heidi Eschmann and Mary Dalbeth for routine matters.

I also wish to thank fellow graduate students, and the new friends I have met in New Zealand. I am grateful for the pleasurable moments we shared which has made my adventure on the research journey not so dull.

In the end, I dedicate this thesis to my parents and grandparents, thanks for always standing behind me, understanding me, believing in me, and unconditionally loving me.

Contents

Acronyms and Abbreviations

ADC	analogue-to-digital converter
AMPA	α-amino-3-hydroxy-5-methyl-4 isoxazole propionic acid (a neurotransmitter associated with the fast-decaying "early" current in the excitatory postsynapse; cf. NMDA)
AP	action potential
ccf	cortical column field (cortical model developed by J. J. Wright)
dGA	day gestational age
DN	digital number (uncalibrated digital output from ADC)
ECoG	electrocorticogram (brain activity recorded via electrodes attached directly to the cerebral cortex; cf. EEG)
EEG	electroencephalogram (brain activity recorded via scalp electrodes; cf. ECoG)
EOG	electrooculogram (recording of eye movements and eye position provided by the difference in electrical potential between two electrodes placed on the skin on either side of the eye)
EMG	electromyogram (a record of the intrinsic electric activity in a skeletal muscle)
ENOs	early network oscillations
EPSP	excitatory postsynaptic potential
FFT	fast Fourier transform
GA	gestational age
GABA	γ-aminobutyric acid (an inhibitory neurotransmitter)
GDPs	giant depolarising potentials
HVA	high-voltage activity (similar to slow-wave sleep)
IPSP	inhibitory postsynaptic potential
LVA	low-voltage activity (similar to REM sleep)
MEG	magnetoencephalogram (brain activity recorded via magnetic-field probes)
NMDA	N-methyl-D-aspartate (a neurotransmitter associated with the slowly-decaying "late" current in the excitatory postsynapse; cf. AMPA)
NREM	non-rapid eye movement
NSF	nonspecific flux (part of `ccf` model)
PSD	power spectral density
PSP	postsynaptic potential
REM	rapid eye movement
SEF	spectral edge frequency
SVD	singular value decomposition
SWS	slow wave sleep
TCF	transcortical flux (part of `ccf` model)

List of Figures

List of Tables

Chapter 1

Introduction and Literature Review

In this chapter, I first discuss the motivation for the fetal sheep maturation study and elaborate the importance of constructing mathematical models to facilitate the understanding of the development of the immature brain activity. Following the motivation and significance, I give a brief explanation and justification for studying fetal sheep as an aid to understanding human fetal development, then I summarise the work of a representative subset of the literature relevant to investigations of brain development and maturation in fetal sheep. The last part of this chapter is a brief overview of developments in approaches to cortical modelling.

1.1 Motivation

Sleep is a universal phenomenon existing in all mammals, whose daily sleep time ranges from 4 to 9 hours. As is well known, adult mammalian sleep study results show adult sleep alternates between desynchronised, low-amplitude REM (rapid eye movement) sleep state and synchronised, high-amplitude NREM/SWS (non-rapid eye movement/slow wave sleep) sleep state. At the present time, sleep is poorly understood. Almost all studies on sleep are performed exclusively on adults. Studying the fetal and neonatal sleep and sleep ontogenesis is critical for understanding the sleep function across the lifespan, sudden-infant-death syndrome (SIDS) and infancy origin of childhood and adult sleep disorders.

The development and maturation of the human brain is a complex and long-lasting process. Fetal, neonatal, and infant sleep differs remarkably from the adult sleep and is hard to categorise because of reduced or lack of some sleep components. The most significant difference between fetus/infants and adults is the absence of well-differentiated and sleep-related neocortical EEG activity during a certain period of time. The emergence of differentiated sleep states—quiet sleep (QS or NREM) and active sleep (AS or REM), is one of the most significant and fundamental events during early brain maturation. Substantial differences also exist in the development of organised sleep patterns across different mammalian species due to their different brain maturation rates.

It is ethically impossible to directly record the brain activity of human fetus in the womb to obtain knowledge of brain development. Similar to a human being with gestation lasting about 280 days, sheep is also a precocious mammal that is born in a relatively mature state (gestation length is approximately 150 days). The differentiated and electroencephalography (EEG) determined sleep states appear before birth for both human and sheep fetus. In addition, the sheep fetus has similar weight and size to the human fetus. Therefore, fetal sheep is a good auxilliary model to facilitate the understanding of the brain development in the human being.

By studying fetal sheep, we may gain a better understanding of the origin and the purpose of the sleep in humans. It also provides a tool to study how the brain develops and to identify the critical periods in brain development and possible origin of certain diseases appearing in later life.

During the developing process of the sleep states in the fetus brain, gap junctions, dendritic arborisation, synaptogenesis, myelinisation, neurotransmitter and neuromodulators development evolve rapidly in the immature brain. The developmental processes signify how signalling at the molecular level influences both individual cell types as well as interconnected neural networks which help to build complex brain functions. Based on the research studies of the fetus/infants brain, a mathematical brain model is developed to describe the immature brain activity using the mean-field method. With the aid of the physiologically-based cortical modelling, we hope to expand the understanding of the developing dynamics of the fetal brain, especially the ontogenesis of sleep cycles.

1.2 Thesis Structure and Original Work

Chapter 1 motivates the present study, presents a literature survey of prior studies of fetal sheep maturation, and summarises developments in cortical modelling.

Chapter 2 describes the signal processing methods used for the fetal sheep ECoG time-series analysis, including average power, correlation time, SVD entropy, and spectral edge frequency. Some techniques used to improve the analysis results are also introduced, such as signal averaging, overlapping, and smoothing.

Chapter 3 introduces the fetal sheep surgical procedures, ECoG recordings, and subsequent data storage. ECoG recordings are categorised into early- or late-term third-trimester in terms of emergence of differentiated SWS and REM sleep states. For the late-term third-trimester sheep fetus, the results of average power, correlation time, and SVD entropy demonstrates sleep state transitions between SWS and REM are cortical phase transitions.

In **Chapter 4**, I investigate the maturational changes of fetal sheep sleep during the third-trimester of gestation by correlation time, SVD entropy, and spectral edge frequency analyses. All analysis results show the differentiation of SWS and REM sleep states occurs at about day 125 of gestation. Power spectrum analyses are performed to explore the frequency and amplitude variations of the major resonances over the third-trimester of the gestational age. Based on the developmental changes of the frequency and amplitude of the major resonances, the third-trimester of the sheep fetus can be divided into four stages.

As a first step towards modelling fetal sheep maturation phenomena, I examine the viability of the cortical column field (`ccf`) model due to its completeness and sophistication. **Chapter 5** introduces the structure of the `ccf` model and its state equations. Extensive explorations are conducted on the centimetric scale, including firing rates and membrane potentials, power and power law, gamma oscillation, phase relation between the excitatory and inhibitory elements, power spectral density, and spatial Fourier spectrum. I conclude that the `ccf` model is too unwieldy to be used in the fetal sheep simulation, and resort to the more simplified and compact Waikato mean-field model.

Action potential back-propagation into the dendritic tree effects the succeeding action potential generation by altering the synaptic weight on the near and far dendritic tree and for the first time is incorporated here into the Waikato mean-field model. In **Chapter 6**, the modified near-far Waikato cortical model is presented and the corresponding steady states are computed. First-order state equations are then derived and stability of the cortical system is predicted by varying the subcortical drive, inhibitory diffusion strength, and rate constants of the near and far dendritic tree. The original slow- and fast-soma Waikato cortical models are also introduced in this chapter. The stability analysis shows that the near-far dendritic tree model and the original cortical model are not too dissimilalr. Therefore, I decide to use the well-studied Waikato slow-soma model as a starting point for the subsequent fetal sheep simulation.

In **Chapter 7**, I discuss the model parameter customisation for the fetal sheep maturation simulation, including GABA excitatory effects, inhibitory PSP, gap junction, axonal conduction speed, and synaptic connectivity. Since most model parameters are drawn from rat pups, the brain maturation is compared between different mammal species, such as sheep, rats, and human beings. Applying these modified model parameters to Waikato slow-soma model, theoretical stability predictions are undertaken by eigenvalue analysis, and numerical simulations are performed to compute plausible time series of the ECoG of fetal sheep.

Chapter 8 outlines possible future work which can be carried out to extend current research in fetal sheep ECoG analysis and fetal sheep maturation modelling. **Appendix A** illustrates all 324 available ECoG time-series recorded from 15 sheep fetuses obtained from the University of Auckland. **Appendix B** displays ECoG time-series with SWS-to-REM or REM-to-SWS sleep state transitions and the corresponding analysis results by average power, correlation time, and SVD entropy methods. **Appendix C** shows the major source code elements used for the ECoG signal analysis and cortical simulation.

Original Work

My original contributions to the work include:

- All the ECoG analyses for the fetal sheep maturation study presented in Chapters 3 and 4;
- All the simulation work for the `ccf` model (Chapter 5);
- Derivation of differential equations for the near-far dendritic tree model and the steady states and stability predictions (Chapter 6). (The idea of incorporating the near-far dendritic tree into Waikato model is from Prof M. Steyn-Ross.);
- Customisation of the modelling parameters for the fetal sheep simulation, and all the simulation results of Chapter 7.

The thesis work was presented at two conferences:

"Do fetal sheep show brain-state phase transitions during sleep?", New Zealand Institute of Physics (NZIP), Dunedin, 2007

"Investigation of sleep cycle maturation and brain-state phase transitions in fetal sheep", Australasian Winter Conference on Brain Research (AWCBR), Queenstown, 2007

1.3 Advantage of Studying Sheep

Barcroft and Barron [10] pointed out there are several advantages in using sheep to study sleep development in the fetus. First, sheep have a long gestation period, about 150 days. When the fetus is born, the lamb brain has reached a rather mature status in utero. Therefore, sheep offer good opportunities for studying developmental stages. Importantly, from neurophysiological and metabolic points of view, there is no relationship between fetal ECoG pattern and the states of vigilance of the ewe [89].

Second, it is possible to implant various electrodes (ECoG, EMG, and EOG) on the fetal sheep and record the activity of the fetal sheep for a very long time continuously with the fetus *in utero* in the absence of anaesthesia. Similar to fetal sheep, the human fetus develops distinguishable REM and NREM sleep states and fully organised fetal sleep states in utero. However, it is ethically impossible to perform EEG recordings on human fetus *in utero* to detect the onset of REM and NREM differentiation, and EEG recordings on very premature infants are not considered as reliable because the measurments are not done in the *in utero* environment. As for the human fetus, the cyclic REM and NREM ECoG activity in fetal sheep can be detected using the same signal processing methods. Therefore, the fetal sheep is a highly suitable animal species for studying human fetus brain activity and sleep cycle development.

For fetal sheep electrocortical measurement, usually the electrodes are mounted bilaterally over the *parietal cortex* (positioned above the occipital lobe and behind the frontal lobe; it integrates sensory information from different modalities, particularly determining spatial sense and navigation). This is because the amplitude contrast of the electrocorticogram (ECoG) between the high-voltage activity (HVA) and the low-voltage activity (LVA) is greatest when ECoG is recorded bilaterally from parietal electrodes. Clewlow et al [22] tested five different electrode positions: parietal, frontal, occipital, fronto-parietal, and occipito-parietal (see Fig. 1.1). In Fig. 1.1, the upper three waveforms are measured bilaterally and the lower two waveforms are measured *ipsilaterally* (on the same side as another structure). The recording results show that biparietal electrodes give the best well-defined HVA and LVA states. Bifrontal electrodes measurements give smaller ECoG amplitude contrast between HVA and LVA. Bi-occipital electrodes measurements displayed large spikes and showed even less amplitude contrast. The recording results from ipsilateral fronto-parietal and occipito-parietal electrodes gave worst amplitude contrast and it is hard to differentiate the HVA and LVA. Clewlow et al's experiment also showed that the distance between the electrode pair affected the ECoG amplitude contrast. The further the electrodes are apart, the larger the amplitude contrast between HVA and LVA.

1.4 Brain Maturation of Fetal Sheep

Before the Bernhard group's 1959 paper [14], the existence of obvious fetal activity during late pregnancy was well documented, particularly in ungulates (hoofed mammals), species which are rather mature at birth from the neurophysiological and behavioural point of view. But few studies were conducted to investigate the development of cortical electrical activity in the prenatal fetal sheep. In the following, I will summarise the main research results regarding brain development and maturation of fetal sheep starting from Bernhard's 1959 work.

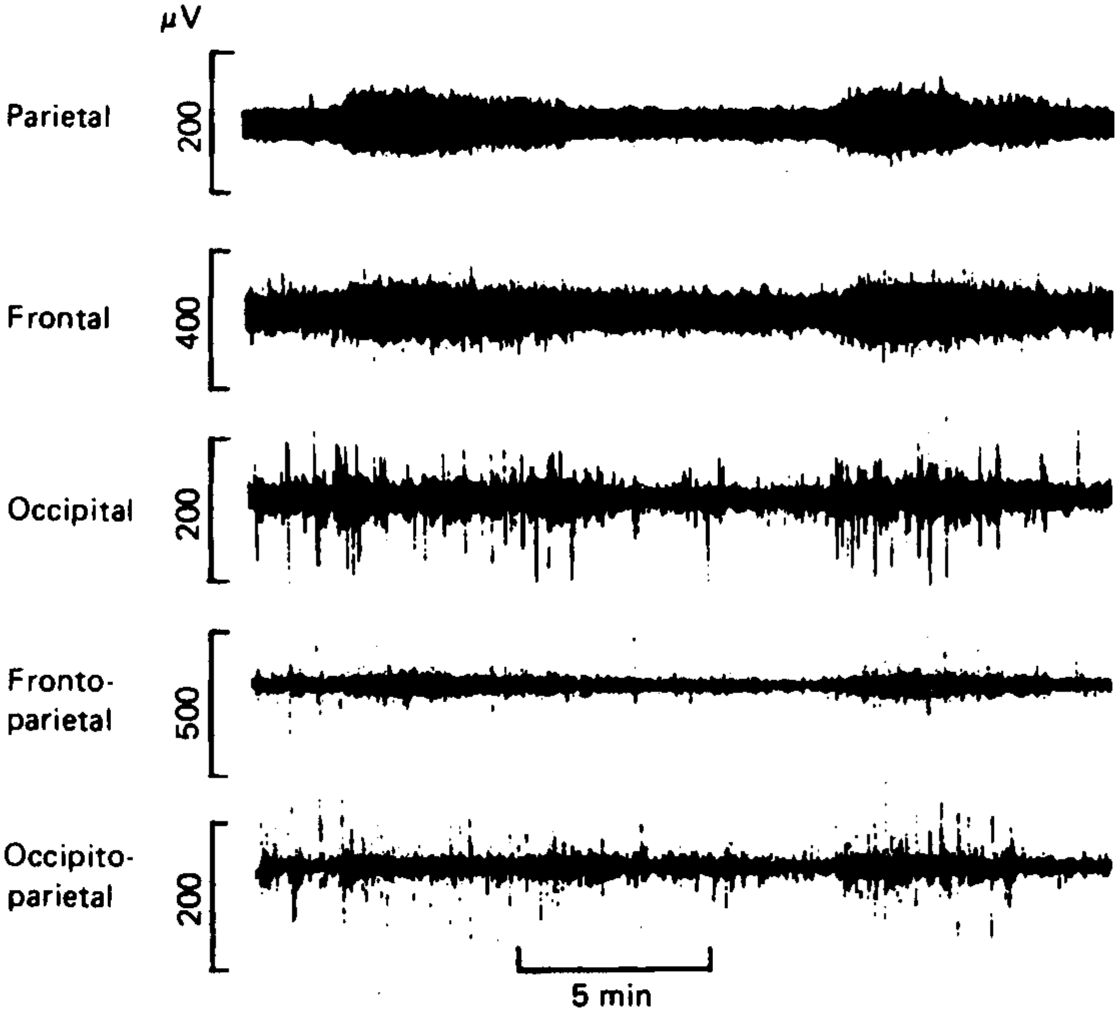

Figure 1.1: Fetal sheep electrocortical activity recorded simultaneously from various brain sites. From top to bottom, the five electrocortical waveforms are recorded from bilateral parietal electrode pair, bilateral frontal electrode pair, bilateral occipital electrode pair, ipsilateral frontal and parietal electrode pair, and ipsilateral occipital and parietal electrode pair simultaneously. Optimum contrast between HVA and LVA states is achieved with bilateral parietal electrodes [22].

Bernhard and colleagues in 1959 [14] recorded the electrocortical activity directly from the cerebral cortex at 65 to 151 days gestational age (GA). They observed two types of spontaneous cortical activity: PN (prenatal) I activity and PN II activity. PN I activity is spindle-shaped bursts of regular waves at a frequency of 13 to 14 Hz against a background of electrical silence. PN II activity is periods of irregular activity which contains waves of longer and varying duration. In the very immature fetus (78 days or less), only PN I activity appears. Around day 80 GA, PN II activity adds to the PN I activity and both types of activity are present. During the last part of the gestation, PN II activity dominates.

Meyerson [74] studied the interhemispheric functional relationship with electrophysiological methods using fetus of age 60 days GA to full term (145 days). He reviewed the electrocortical activity of the intact preparation in fetal sheep. Bernhard et al (1959) [14] had observed that at gestational age of 65 days, spontaneous cortical activity was first observed in the fetal sheep EEG. After improving his recording method, Bernhard et al [15,16] found spontaneous cortical activity was present at an earlier age, 60 days GA. This age corresponds to a fetus weight of 50 grams. For fetus at 60–65 days GA, the electrocortical activity is less well defined. At this age, cortical activity is discontinuous, and comprised mainly of slow waves, each lasting about 0.5 second, and separated by periods of electrical silence lasting 5 to 20 seconds. The slow waves are often clustered forming short periods of polymorphic (different forms or types) activities. Rhythmic activity is rare during this earliest EEG-development phase. Short bursts of 6–8 Hz diphasic waves occasionally may be spotted and generally superimposed on the slow wave activity. An example of the electrocortical recordings in a 60-day sheep fetus are replotted in Fig. 1.2. In Fig. 1.2, the electrodes setting of the upper recording channel is bipolar configuration between the two hemispheres. For the lower two recording channels, the electrodes pairs are monopolar configuration with measuring electrodes coupled to a common reference electrode on the neck of the fetus. In Fig. 1.2, the three left waveforms show the presence of the slow waves and each waveform on the right side illustrates the presence of an epoch of polymorphic activity.

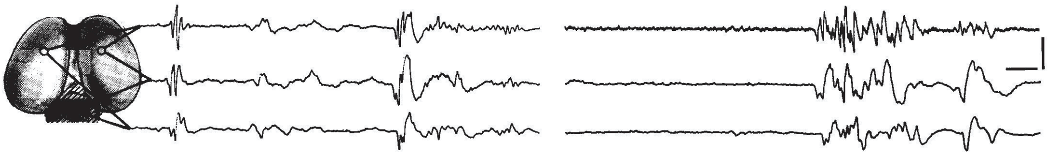

Figure 1.2: Electrocortical activity in a 60-day fetus [74]. Upper recording is transversal, bipolar recording. Lower two recordings are bilateral, monopolar recordings. Calibration: 25 μV; 1 sec.

When the fetus age is between 65 and 70 days, PN I cortical patterns (waxing and waning, regional spindle-like bursts with frequency of 8–14 Hz) are observed over the parietal region. Figure 1.3 gives examples of electrocortical activity in a 70-day sheep fetus recorded with monopolar electrodes from bilateral regions. Figure 1.3 (a) shows two types of rhythmic activity constitute the bursts, one at 6–8 Hz (left part) and another at 14–16 Hz (right part). The 6–8 Hz waves are monophasic positive with an arcade-shaped form, while the waves of the 14–16 Hz are diphasic. The two types of rhythmic activity usually appear in succession. Between these rhythmic activities there is complete electrical silence. During this period, sometimes the 6–8 Hz and 14–16 Hz burst activity are accompanied by slow components. The activity has a discontinuous polymorphic pattern. An example of this case is given in Fig. 1.3 (b).

During the period of 75 to 80 days GA, the 6–8 Hz arcade-shaped activity eventually disappears completely. Finally the high amplitude bursts of 14–16 Hz activity dominates over the parietal area. Usually these are spindle-shaped and the frequency of the waves remains constant. Figure 1.4 displays a recording result from a 80-day fetus using bilateral monopolar electrodes.

At 85–95 days GA, the rhythmic spindle activity can only be seen over the posterior regions of *g. suprasylvius* (above the fissure of Sylvius) [16]. All other regions have continuous cortical activity without dominating periodic components. Figure 1.5 (a) and (b) reproduce the recording results from a posterior region of *g. suprasylvius* and from *g. frontalis superior* (motor) in a 85-day fetus respectively. The measurement result in Fig. 1.5 (b) shows the cortical wave is highly periodic and similar to that found in younger fetuses with 14–16 Hz frequency component dominating. Compared with Fig. 1.5 (a), the result in Fig. 1.5 (b) recorded from *g. frontalis superior* reveals a more polymorphic appearance. The arrow in Fig. 1.5 (b) points out remnants of PN I activity, which can occasionally be seen at this age.

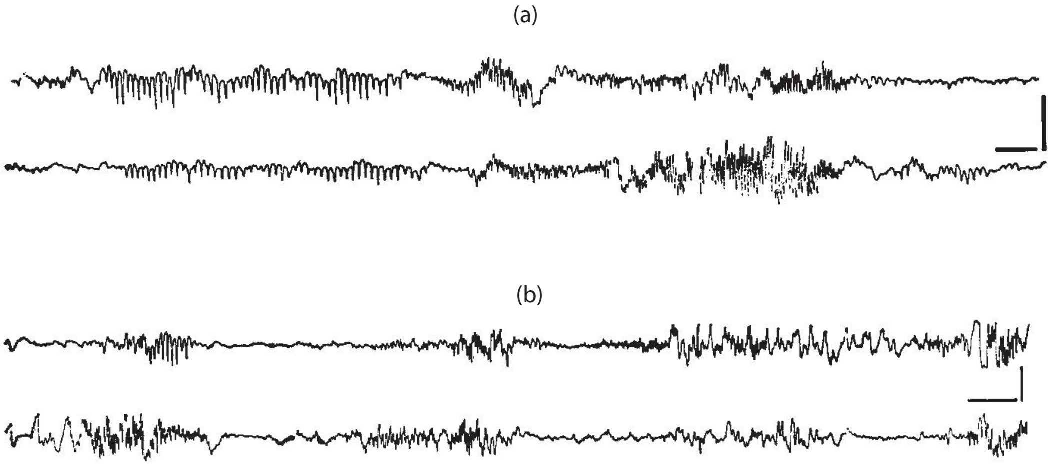

Figure 1.3: Electrocortical activity in a 70-day fetus [74]. (a) 6–8 Hz and 14–16 Hz burst activity. (b) Slow components exist with 6–8 Hz and 14–16 Hz burst activity. In both of (a) and (b), the two waves are bilateral, monopolar recordings from the parietal area. Calibration: 50 μV; 2 sec.

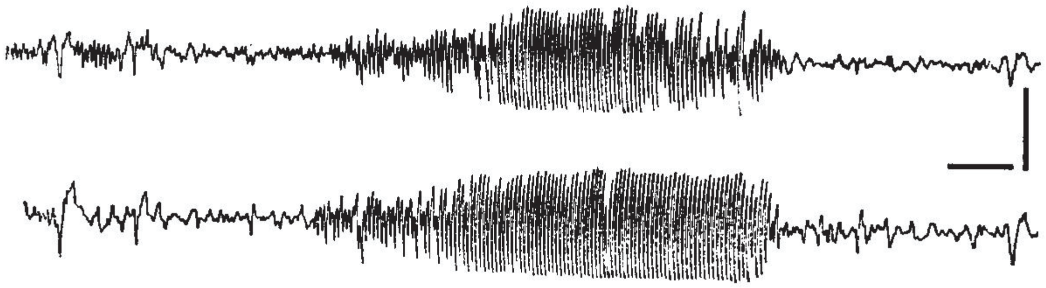

Figure 1.4: Electrocortical activity in a 80-day fetus [74]. The two waves are bilateral, monopolar recordings from the parietal area. Calibration: 50 μV; 1 sec.

From the age of around 100 days, the cortical activity is continuous all over the brain and PN I activity is very rare. The anterior part of the brain, *i.e. g. frontalis superior* and *g. frontalis medialis* (sensor) sometimes shows epochs of rhythmic 8–10 Hz. Figure 1.6 shows an example electrocortical activity recorded in a 98-day fetus.

Towards the end of the gestation period (145 days GA), the fetal sheep EEG is indistinguishable from that of the lamb when studied under acute experimental conditions. Sometimes, sudden high-amplitude bursts can be observed which resemble the intermittent activity pattern in the immature fetus. Frequently, in all regions, sustained high frequency, 30–40 Hz, activity of low amplitude dominates during times of fetal arousal.

Dawes group [28] studied sleep and wakefulness in fetuses exteriorized into a warm saline bath with intact umbilical cords. Observations were made on 22 fetal sheep at 40–55 days GA with body weight 4.9–42.5 g, and 21 fetal sheep at 70–98 days GA with body weight 163–1065 g. They observed three different types of behavioural state: awake, quiet sleep (NREM) and paradoxical sleep (REM). During wakefulness, the lamb fetus appears awake, moves its limbs, raises its head, and opens its eyes. During quiet sleep, the fetus only shows slow and gentle extensions of the limbs. For paradoxical sleep, movements of the eyeballs and intermittent twitching of the ears, lips and limbs were observed.

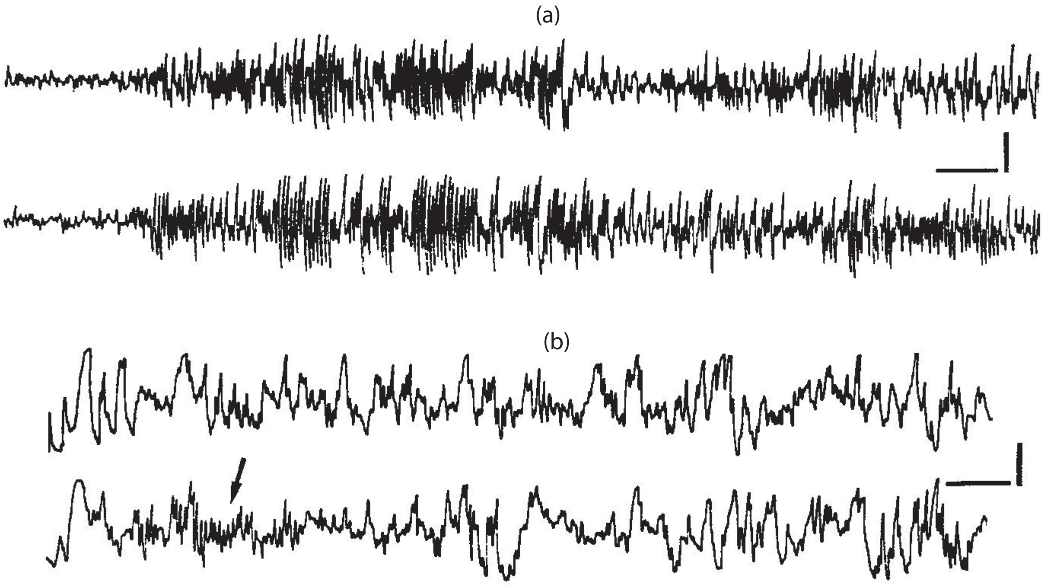

Figure 1.5: Electrocortical activity in a 85-day fetus [74]. The two waves are bilateral, monopolar recordings from the posterior of (a) *g. suprasylvius* and (b) *g. frontalis superior*. Calibration: 25 μV; 1 sec.

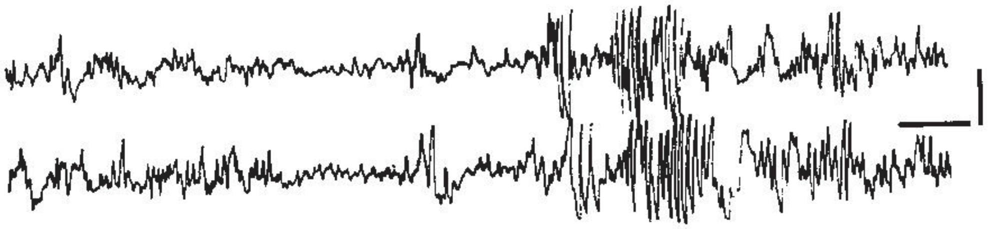

Figure 1.6: Electrocortical activity in a 98-day fetus [74]. The two waves are bilateral, monopolar recordings from *g. frontalis superior*. Calibration: 50 μV; 1 sec.

They reported a slow-wave and rapid-wave electroencephalogram in term sheep. They also demonstrated fetal respiratory excursions associated with REM sleep in the fetal sheep.

Dawes GS et al [30] measured the electrocortical and electromyographic activity on 10 fetal lambs *in utero* from 106–136 days GA. They found that before 112 days GA, ECoG did not display alternating periods of high and low voltage activity, and breathing movements were present for most of the time. Between 112 and 120 days GA, the high- and low-voltage ECoG activities gradually developed. Tonic and phasic intercostals (muscles between the ribs; they contract during inspiration) activity appeared during high- and low-voltage electrocortical activity respectively. After 120 days GA, breathing activity only exists in the low voltage ECoG activity.

Dawes et al [29] studied the breathing activity for 16 fetal sheep aged 118–123 days GA. Before differentiation into low- and high-voltage activity at about 115 days GA, Dawes et al found that breathing movement in the fetus is basically continuous. As the fetus matures, the breathing movements become more episodic, with longer intervening periods of apnea (transient cessation of respiration). For the near-term fetus, breathing normally occurs during periods of low-voltage electrocortical activity.

Ruckebusch [88] recorded regular low-voltage fast activity (LVF) and high-voltage slow activity (HVS). He regarded HVS as slow-wave or NREM sleep, because of the arousal effects and somatic movements induced by the stimuli; and LVF as paradoxical or REM sleep due to the presence of eye movement. Alert wakefulness (AW) was identified for LVF without eye movement.

Ruckebusch et al [89] recorded electrocortigram (ECoG), electrooculogram (EOG), heart rate, and gross body movements for many days before and after birth for 19 Mediterranean Lacaune ewes weighing 45–50 kg with full term at 150 days. The age of the studied fetus was at 0.6 term (about 90 days gestational age) and 0.8 term (about 120 days GA). The 0.6 term age was judged by fetus size and the appearance of a little hair around the eyes. The 0.8 term was judged by fetus size and a complete covering of wool. In this paper, Ruckebusch et al demonstrated that the sleep patterns of the fetal and neonatal sheep involved quantitative changes in the ratio of wakefulness and sleep. Wakefulness includes alert sleep state and drowsy state; sleep comprises the characteristic slow wave and paradoxical phases. Ruckebusch's results showed that fetal sheep spend 40% recording time in REM sleep for an average duration of 15.9 minutes, and 54% in NREM sleep with average duration 21.5 minutes. AW occupies the remaining 6%.

Ruckebusch et al [90] investigated fetal ECoG, eye and body movement, and heart rate during the last three weeks gestation because of initiation of obvious HVS and LVF differentiation. The ten Lacaune fetal sheep used in this research were 125 days GA weighing 45–50 kg (term 150 days). ECoG recordings showed alternating NREM and REM sleep occupied 90% of the recording time during the 3 weeks prior to birth. HVS had a frequency range 3–5 Hz and amplitude 100–200 μV; for LVF, the frequency range was 17–25 Hz with amplitude 20–50 μV. Occasionally, the amplitude of LVF increased to 50–100 μV. Each NREM to REM cycle lasted 30–40 minutes with a ratio of NREM/REM of 1/1 from 4 months gestation until 6–8 hours before delivery. After birth, the total sleep time reduced to 40% of the recording time. One week after birth, the ratio of NREM/REM increased to 5/1. In the new born, the NREM and REM sleep cycles continued, while the period was reduced by half. Wakefulness occupied about 10% of time in prenatal fetus and 60% of time in neonatal lamb for each 24-hour period.

Jost et al [57] carried out intrauterine electroencephalography on Dorset sheep of 135–145 days of gestation. The recording period was 32 minutes. Both high-voltage slow waves (HVS) and low-voltage high frequency activity (LVF) was observed in their *in utero* fetus EEG recordings. The power spectra showed the predominant frequency for the HVS activity was at 3–5 Hz. LVF activity usually lasted for 4 to 20 minutes and had a maximum frequency of 20–25 Hz. The HVS pattern was similar to that of adult non-REM sleep with slow or no eye movement. The LVF activity was identified as REM sleep rather than the awake state, because of a marked increase in oculomuscular activity and loss of auditory evoked response. But in their experiment, they did not measure the electromyelogram in the fetus. They found the fetus appears to spend about 30% of its time in REM sleep 72 hours before delivery.

Mann et al [70] also observed two dominant patterns in fetal EEG. The gestational age of the fetus ranged from 127 to 144 days with term 145 to 150 days. The first pattern consisted HVS, with frequency and amplitude depending on fetal age. From 127–135 days GA, the dominant frequency was 6 to 14 Hz with EEG amplitude of 50 to 100 μV. After 135 gestational days, low frequencies of 1 to 3 Hz added to the earlier higher frequency and the EEG amplitude approached 200 μV. The second pattern consisted of desynchronized LVF with frequency from 15 to 23 Hz and amplitude 15 to 40 μV. The second pattern persisted throughout the studied range of gestational ages. By analyzing continuous 24-hour EEG records, an approximately equal distribution of HVS and LVF was obtained. The length of LVF lasted from 10 to 20 minutes at most.

Ioffe et al [53] studied different behavioural states for fetal sheep to establish reliable criteria for recognizing wakefulness (AW) and different sleep states in fetal and newborn lamb. Ioffe and colleagues recorded ECoG, EOG, neck EMG, masseter (a large muscle that raises the lower jaw and is used in chewing) EMG, and fetal breathing (FB) activity on fetal sheep of 125–140 days gestation and in newborn lambs up to 11 days postnatal age. Standard adult criteria for ECoG, eye movements and postural muscle tone were used to define the awake state (AW), non-rapid eye movement sleep (NREM) and rapid eye movement sleep (REM). They found that criteria based on ECoG, nuchal muscle tone, and eye movements can readily identify the AW and sleep state. The masseter EMG was not so helpful for the state identification because of the inconsistency in any state. The statistical results showed fetuses spent 53% of their time in NREM sleep state, 41.4% time in REM sleep state, and 5.6% time in AW state. Spontaneous intrauterine breathing activity occurred only during the REM sleep, but 35% of REM sleep was not associated with any FB activity. Gasp (isolated deep inspiration) were not related to any specific sleep state or awake state, and only occurred occasionally. Ioffe et al chose fetuses older than 125 days gestation because of the larger size at older age, which is required for instrumenting the fetus. Other findings include tonic activity in neck muscles of fetal lambs during NREM sleep and AW, and the occurrence of low-voltage activity (LVF) ECoG coupled with tonic activity of the nuchal muscles indicating wakefulness, since muscle tone is always suppressed during REM sleep.

Clewlow et al [22] recorded electrocortical and electro-ocular activity, breathing movements and nuchal muscle activity continuously over 40-minute periods in the unanaesthetized lamb *in utero* from 95 to 135 days gestational age. They examined the sequential changes and relationship between fetal electrocortical and electro-ocular activity, nuchal muscle and breathing movements. They also recorded the activity of the intercostal muscles to study the prenatal breathing movements. Postnatally, it was known that the intercostal muscles are inactive during the rapid-eye-movement phase of sleep. For the electrocortical activity, during the gestational age 95–135 days, the amplitude of the recorded electrocortical activity increased, as the fetus became mature. Before 110 days, no evidence of episodic changes in electrocortical activity was observed. Between 110 and 115 days of gestation, short periods of higher-voltage activity (HVS) appeared from time to time. They thought the HVS was superimposed on the existing lower-voltage activity (LVF). As the fetuses became mature, the mean ECoG amplitude increased for both HVS and LVF.

Clewlow et al also displayed the power spectral analysis results for a 79-minute biparietal ECoG measurement from a 127-day sheep fetus. It showed that during the high-voltage activity, power increases at lower frequencies (3–10 Hz). They summarized from their ECoG power spectral analysis that the major difference between the HVS and LVF activity was in the power in the 3–10 Hz lower frequencies.

They also observed that after fetal death the recorded electrocortical activity did not fall to zero: bursts up to 4 μV_{rms} were still present. This voltage amplitude is much smaller than the normally recorded ECoG signal from the biparietal electrodes, even smaller than the ECoG signal of a 95-day fetus.

Three different patterns of electrocortical activity (ECoG), electro-ocular activity (EOG) breathing movements, and nuchal muscle activity (EMG) were observed between 95 and 135 days. From 95–106 days, there was no HVS. Electro-ocular activity, nuchal muscle activity and breathing movements were continuous without obvious pattern or relationship. The diaphragm and intercostal EMG were active almost all the time.

From 107–114 days, brief episodes of HVS appeared when breathing movements were absent. During this period, the breathing movements were episodic and appeared when rapid eye movement was present and the nuchal muscle activity increased. In the absence of the breathing, sustained tonic intercostals EMG activity was observed. In the presence of the breathing movements, phasic intercostals activity was observed.

From 120–135 days GA, the ECoG was clearly differentiated into episodes of HVS and LVF. Rapid electro-ocular and phasic diaphragm activity occurred exclusively during the LVF period. Phasic intercostals activity was present in 10–80% of breaths during breathing episodes. During the HVS electrocortical activity, strong sustained contractions of the intercostals muscles were observed with increased tracheal pressure. Sustained contractions of the nuchal muscles were also observed during the HVS activity. During the LVF activity, these sustained contractions were less active.

Szeto and Hinman [108] studied the prenatal development of the sleep–wake pattern throughout the third trimester using chronic intrauterine ECoG, neck and diaphragm EMG, and EOG monitoring techniques. They used 21 fetal lambs of 112–114 days GA (term $\approx$ 145 days). Sixty-five polygraphic recordings were obtained from the 21 fetal lambs. Behavioural states were determined by visual analysis of the polygraphic recordings using the scoring criteria for adult sleep [81] and neonate sleep [7]. Their results showed that the transition from disorganized to organized behavioural state occurs at about 115–120 days of gestation. During this period, high-voltage slow-frequency (HVS) patterns and low-voltage fast-frequency (LVF) patterns emerged. LVF ECoG patterns, scored as REM sleep, are concurrent with the rapid eye movement (REM) and burst activity of diaphragmatic EMG (breathing movements) and absence of nuchal EMG, and the fetal heart rate was generally more irregular. HVS ECoG pattern, scored as quiet sleep (QS) in the fetus, was associated with the occasional nuchal EMG and absence of REM, and rapid breathing movements. In this study, the earliest date able to identify the organized QS–REM cycling was at 114 days GA and it only happened in one fetal lamb. By 120 days of gestation, all six studied fetal lambs exhibited a well-defined QS–REM cycle. The emergence of this organized cycle was very fast, occuring over 2 or 3 days at about 115–120 days of gestation. They also identified a third state: LVF ECoG coincident with burst of diaphragmatic EMG, increased nuchal EMG, absence of REM, and an increase of heart rate and blood pressure. They defined this third state as arousal, HVS state as quiet sleep (QS), and LVF state as REM sleep

(REMS) after comparing with the adult sleep criteria. At the beginning, more than 50% of recording time was spent in REMS with only 11% of recording time spent in arousal. Szeto summarised the distribution of the three states over the recording time. I have replicated her distribution here in Table 1.1, and plotted the distribution in Fig. 1.7, so that the percentage change of the distribution of the three sleep stages according to increased gestational age can be easily identified. Direct transition from arousal to REMS was observed frequently without passage through the QS stage.

Table 1.1: Distribution of arousal, quiet sleep (QS), and REM sleep (REMS) in the fetal lamb at different gestational ages (expressed as a percentage of total recording time). See Fig. 1.7 for a graphical display of these data. (Szeto and Hinman 1985 [108])

Gestational age (days)	Number of recordings	Behavioural state		
		Arousal	QS	REMS
≤ 120	9	11.2 ± 1.7	35.1 ± 2.5	52.7 ± 2.4
121–130	25	11.8 ± 1.6	38.4 ± 1.6	49.9 ± 1.7
131–140	22	15.1 ± 1.9	38.2 ± 1.8	46.1 ± 2.0
> 140	9	18.3 ± 2.9	43.8 ± 2.5	37.7 ± 2.8

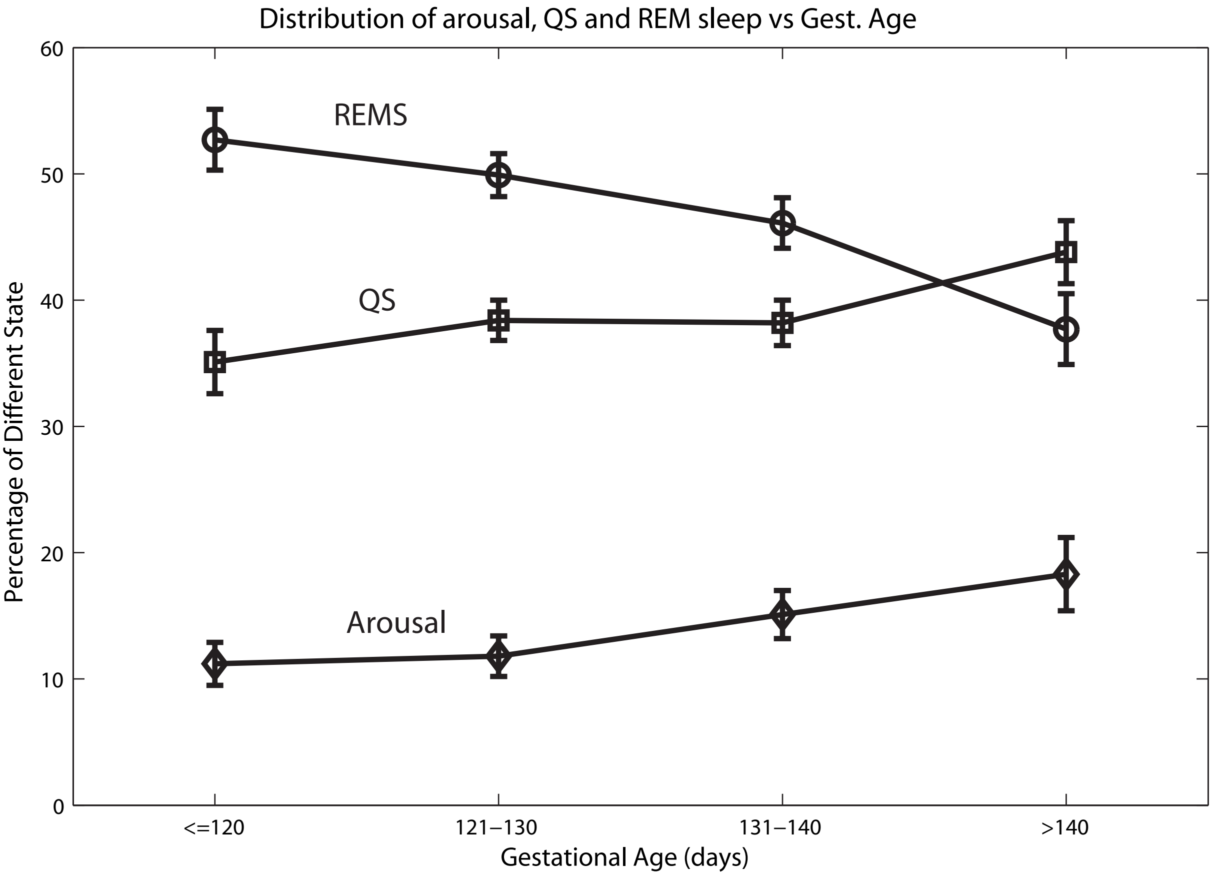

Figure 1.7: The distribution of sleep stages: arousal, quiet sleep (QS), and REM sleep in fetal lamb from Table 1.1 [108]. The circle (o) is for the REM sleep, the square (□) for the QS sleep, and the diamond (◊) for the arousal state.

Szeto et al [109] studied the fetal lamb electrocortical activity using spectral analysis. Nine fetal lambs of 114–139 days GA were used, and 26 electrocorticogram recordings were obtained. In that paper, Szeto investigated the quantitative changes of waveform characteristics from the emergence of organized sleep cycles (115 to 120 days gestation) until full term. Fundamental HVS and LVF activities were identified visually for fetuses of more than 120 days GA. The fetuses were classified into three groups according to gestational age: ≤ 120 days (group 1), 120–129 days (group 2), and 130–139 days (group 3). For the ECoG recordings, the corresponding power spectra were computed and the relative power density, defined as the percentage of total area under the curve, was graphed. Sezto summarised the power spectral analysis results in a table. I reproduce her results in Table 1.2 and Fig. 1.8; these show the distribution of the relative power density in different wave bands. In Fig. 1.8, the three columns of darker bars give the relative power density of HVS states, and the three columns of lighter bars shows the relative power density of LVF states.

Szeto and colleagues found that for the HVS activity, significant power density ($> 75\%$) was at the low-frequency delta-band (0.3–3 Hz) for all three age groups. Compared with HVS activity, the LVF activity has more theta-band (4–7 Hz) power and less delta-band power. Furthermore, the maturational changes mainly happened in the LVF activity. During this period, power density *decreased* in the delta (0.3–3 Hz) band and increased in the beta (15–30 Hz) band. In contrast, no significant changes were observed in the power spectrum of HVS activity with increased gestational age.

Table 1.2: Power spectral analysis for fetal sheep. Numbers in this table indicate relative power density from Szeto [108].

Days gestation	No. of animals	No. of recordings	Frequency interval (Hz)						
			0.3-3 (Delta)	4-7 (Theta)	8-11 (Alpha)	12-14 (Sigma)	15-19 (Beta1)	20-24 (Beta2)	25-30 (Beta3)
High-voltage slow activity									
< 120	3	7	80	12	4	1	0	0	0
120–129	5	9	78	12	3	1	0	0	0
130–139	5	10	75	18	5	1	0	0	0
Low-voltage fast activity									
< 120	3	7	65	17	8	4	2	1	0
120–129	4	8	50	21	12	6	4	2	1
130–139	5	10	37	23	11	7	8	5	4

Furthermore, Szeto [107] reinvestigated the maturation of the electrocortical activity using spectral edge frequency (SEF). Forty-two electrocortical recordings were obtained from 23 fetal lambs of 116–140 days of gestation. Fast Fourier transform was then performed and the 90% SEF was calculated. The SEF analysis results were consistent with the power spectral analysis [109]. Furthermore, she found the spectral-edge frequency is very effective in differentiating between HVS and LVF activity, and in identifying the starting date of the HVS and LVF cycling. The cyclic pattern could be detected as early as 116 days GA using the SEF method. But only later, at 122–125 days of gestation, could two stable states be clearly defined. Visual analysis revealed

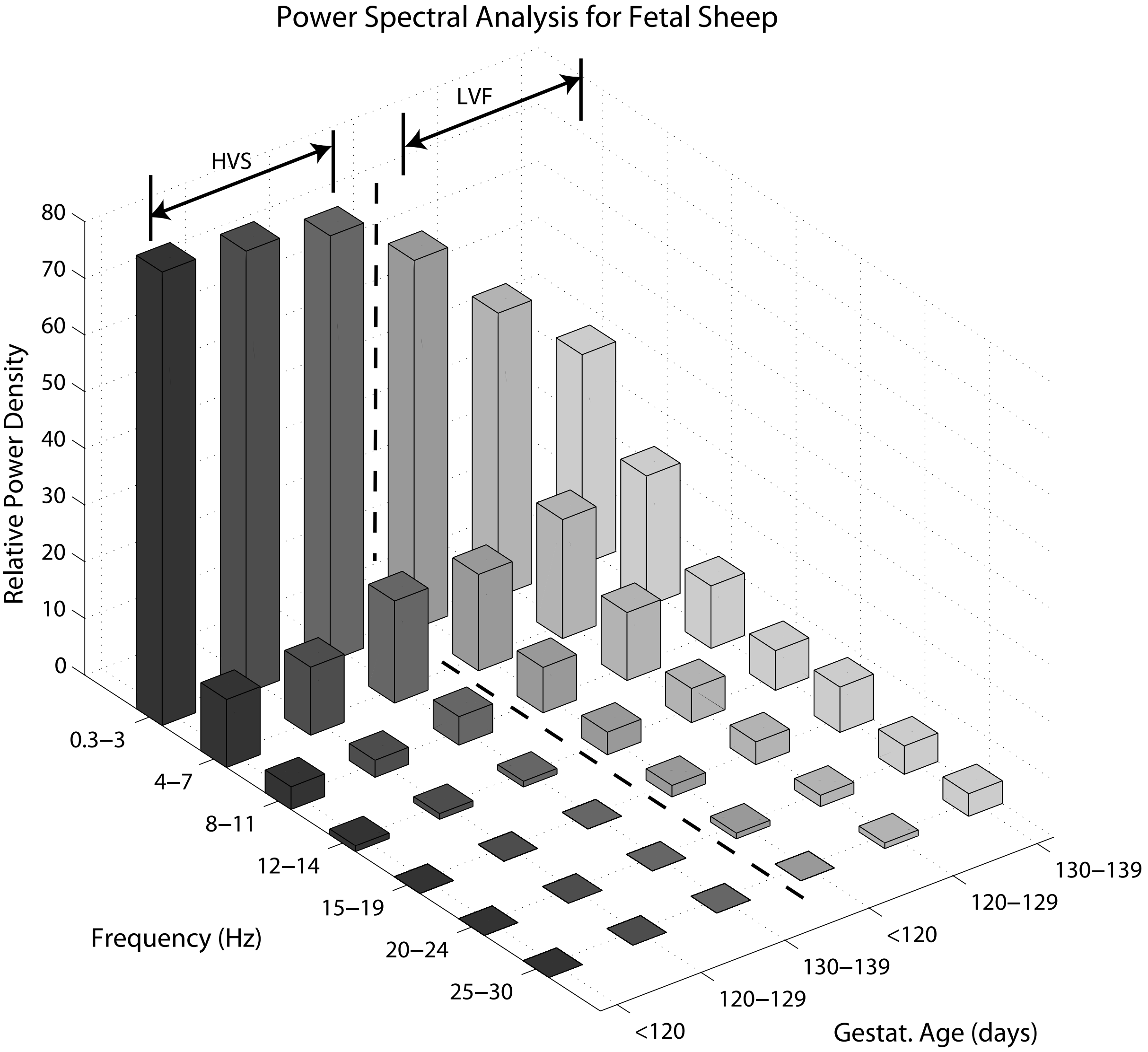

Figure 1.8: The distribution of relative spectral power within HVS (dark bars) and LVF (light bars) in fetal lamb from Table 1.2.

the differentiation started as early as 115 days. But the SEF analysis showed that these early patterns were not as homogenous as thought before.

Following the SEF analysis for the fetal sheep ECoG by Szeto [107], several other analysis methods were tried so that more accurate results could be achieved. McNerney et al and Szeto [107] attempted to automate the classification of ECoG activity into four states, so that the sleep staging could be decided without referring to the EMG (muscle tone) and EOG (eye activities) records.

Akay et al [2, 3] studied the maturational changes in the electrocortical activity using the wavelet transform (WT) method. Twenty-four fetal lambs of 110–144 days gestational age (term 145 days) were used for this study. They compared the short-term Fourier transform (STFT) and WT method, and found better time–frequency resolution was achieved by WT method.

Schmit and Schwab et al [91,92,95] investigated the developmental changes of ECoG activity in fetal sheep using nonlinear analysis. They developed a nonlinear algorithm which computes mean prediction error (MPE) of the ECoG time-series in phase space. Point prediction error

(PPE) has a better resolution in predicting the differentiation of the REM and NREM sleep at an early age. For example, at 115 days of gestation, SEF analysis cannot detect the REM and NREM cycling, while PPE can show distinct difference between REM and NREM sleep states.

Schwab et al [94] further adopted a time-variant nonlinear approach which combined time-continuous nonlinear stability analysis with a parametric bispectral method, to quantify the changes in the premature fetal ECoG. The authors claimed that this approach provides a very sensitive method for detection of unstable cycling between cortical activation and deactivation in the fetal ECoG as early as 106 days gestational age. They conclude that the early activation-deactivation cycles of cortical activity are distinct from the organised REM and NREM states that emerge closer to maturation.

Shinozuka et al [98] studied the electrocortical activity during the last seven gestational days in fetal sheep. They recorded the ECoG and myometrial (the smooth muscle forming the wall of the uterus) EMG continuously in late gestation sheep to analyze the 24-hour ECoG patterns, the relationship between ECoG and EMG, and the 24-hour ECoG patterns at the spontaneous onset of labour. A 24-hour rhythm was observed in ECoG cycling in the late gestation fetal sheep. But during the day before the spontaneous start of labour, the rhythm disappeared 4–5 hour before the onset of the labour, then reappeared.

Summary of Key Findings

In this section, I have summarised the major research results on fetal sheep electrocortical activity carried out since 1959. Early research concentrated on the exploration of the time series of the electrocortical activity of fetal sheep and its relationship with different behavioural states. Criteria for classifying different sleep states were established based on these behavioural states. The distribution of the quiet sleep, REM sleep, and arousal was also explored during the period of gestation. Power spectrum analysis was limited to the late-term fetal sheep EEG, which is after the sleep cycle starts. Recently, researchers have started applying nonlinear methods. Electrocortical activity during the last seven gestational days have been studied and interesting electrocortical activity found during the last 4–5 hours before commencement of labour.

For my thesis, I will be investigating the phase transition phenomena during fetal sheep sleep, applying power spectrum analysis to the fetal sheep to find the maturational changes of the frequency contents before and after the sleep cycles are established.

1.5 Approaches to Cortical Modelling

The brain is an open complex nonlinear dynamical system. We assume that the functional behaviour of the brain can be extracted from the dynamics of the macroscopic quantities measured by the electroencephalography (EEG). Widely used in clinical practice, the EEG provides information of the activity of the nervous system. In order to understand the operation of the brain, numerous mathematical models have been developed for the modelling of the dynamical phenomena observed on different spatial scales in the brain. These models can be divided into two classes according to the elementary units used in the EEG simulation. The first class is the neural network model which describes the interconnections between individual neurons [6,49,68,69,121]. The second class is the continuum or mean-field model which considers average properties of neural populations [37–39, 63, 82, 86, 113, 119, 120, 125, 128].

1.5.1 Neural Network Model

It is well known that the neuron is the elemental unit of the nervous system consisting of three basic components: the soma, the dendrites, and the axon. The dendrites receive inputs from presynaptic neurons, and the axon transmits the output to postsynaptic neurons. The output is generated from the initial segment of the soma. Each neuron has 1000 to 10,000 synapses or connections with other neurons, forming an extremely extensive and complicated synpato-dendritic coupling neuronal network linking the billions of neurons in the human brain. Furthermore, neural activity is believed to be the source of the EEG, therefore, the neuron is frequently used as the starting point to simulate the neural system. Over the past century, the dynamics of the individual neuron has been widely studied and used by modellers to build artificial neural networks. The Hodgkin-Huxley equations can be used as a model to describe the generation of the action potential by a set of nonlinear ordinary differential equations [50]. The cable theory, a second-order partial differential equation in space and first-order in time, characterises the conduction of the potentials along the passive neuronal fibers, including axons and dendrites [51, 80].

Neural network models at the larger mesoscale and macroscopic scales, have been constructed to study various brain phenomena, such as synchronous rhythms, slow oscillation activity during sleep etc. The large-scale Lumber model [68, 69] had ∼65,000 spiking neurons with ∼5 million connections to investigate the structural basis for the generation of fast synchronous rhythms (20–60 Hz) in the thalamocortical system. Both excitatory and inhibitory individual neurons were modelled as standard single-compartment integrate-and-fire units. For a 1-ms simulation of the constructed neural network, about 10 s CPU time and 180 Mbytes of memory was required for a Sun Sparc 20 workstation with 256 Mbytes memory.

On a similar scale as the Lumber model, Hill and Tononi [49] ran their simulation on a dual-processor 2.0 GHz Power Macintosh G5 machine with 3.5 GBytes RAM to model the sleep and wakefulness in the thalamocortical system. For the full model, every 3-s simulation requires more than 5-h computation with roughly 1.7 GB RAM with a time step of 0.25 ms. A fourth-order Runge-Kutta algorithm was used to solve the differential equations.

Though the network model is straightforward and can show the detail of the connections and interactions between the neurons, to build a large-scale neural network able to simulate the macroscopic EEG time series based on the individual neurons is an impractically grand challenge that is limited by the dramatic increase in the numerical complexity as the scale and detail of simulation is increased.

1.5.2 Mean-Field Model

The continuum or mean-field model treats the cortex as a continuous sheet of neural tissue, instead of a set of individual neurons, and emphasises the properties of neuronal populations.

Hence, this kind of model is suitable for simulating the macroscopic EEG from a cortical electrode, which measures the activity of hundreds of thousands of neurons. Many continuum models have been developed since the 1950s with the first important study by Beurle in 1956 [17]. Beurle's model exclusively comprised excitatory neurons and he used this model to investigate the propagation of the waves of activity.

Wilson and Cowan Model

As an extension of Beurle model, Wilson and Cowan [119, 120] incorporated inhibitory neurons. They assumed all neural processes are the results of the interactions of excitatory and inhibitory neurons and, therefore, modelled the cortical or thalamic nervous tissue as a two-dimensional sheet with excitatory and inhibitory neurons homogeneously and isotropically distributed within the sheet. The lateral connectivity between the neurons is recurrent and all four types of interconnections are permitted: excitatory-excitatory, excitatory-inhibitory, inhibitory-excitatory, and inhibitory-inhibitory. The probability of various types of interconnections is a function of distance between the two neurons. The postsynaptic potential was defined by an exponential decaying function with a time constant of several milliseconds. The action potential was assumed to propagate without decay along the axons with a finite velocity. A sigmoidal function was used to represent the relationship between the firing rate and the membrane potential with a threshold for action potential generation. An absolute refractory period was also defined following the firing during which the neuron is not able to fire again immediately.

Based on these assumptions, coupled nonlinear integro-differential equations were derived and numerical solution was then used to investigate three different types of tissue: sensory neo-cortex, archi- or prefrontal cortex, and thalamus. This was realised by adjusting the corresponding connectivity parameters, which are anatomical in nature. The three anatomies support active transient responses, long-lasting oscillatory responses, and the generation of spatially inhomogeneous stable steady states of neuronal activity respectively. EEG phenomena were not investigated in their simulation. In the study, they also explained the justification of the mean-field approximation for their model.

Lopes de Silva Model

Lopes de Silva et al [25, 26] developed a lumped model including two populations of neurons, pyramidal neurons and local interneurons, interconnected only through negative feedback: excitatory-inhibitory and inhibitory-excitatory interconnections. Both excitatory and inhibitory postsynaptic potentials (EPSPs and IPSPs) were characterised by a linear transfer system. A sigmoid function was used to characterise the conversion of the average membrane potential to the pulse density of the action potential generated by the neuron. Interconnectivity constants represented the total numbers of synaptic contacts between the pyramidal neuron and the interneuron.

Compared with the Wilson and Cowan model, the Lopes de Silva model made several improvements, including more realistic dendritic transfer function, anatomically and physiologically-based model parameters, and system linearisation. However, unlike Wilson and Cowan, Lopes de Silva model did not have positive feedback: excitatory-excitatory and inhibitory-inhibitory interconnections. Using this lumped model, Lopes de Silva et al tested the hypothesis that alpha-rhythms were generated by neuron populations with frequency selective properties when submitted to random noise inputs. Interestingly, they also briefly explored the alpha rhythmic component variation when increasing the interconnections and synaptic contacts. They thought this variation approximated the development of the EEG as a function of age.

van Rotterdam Model

In the same group, van Rotterdam [113] extended the earlier lumped model developed by Lopes de Silva et al into a spatially distributed model by arranging the two populations of neurons into an infinite one-dimensional neuronal chain interconnected by recurrent collaterals and inhibitory fibres. Using this spatially distributed model, they were able to investigate the alpha activity as a function of both time and space. The spatial spreading of the alpha rhythmic activity was studied by assuming that the propagation of the alpha activity depended on the spatial properties of the cortical neuronal networks. By driving the neuronal chain with a spatial and temporal white noise, the dispersive waves with alpha frequency propagated in the neuronal chain. The phase velocity of the wave was estimated and it was found to be dependent on the interconnections of pyramidal neurons and interneurons. Because of its mathematical rigor, the van Rotterdam model has become a classic in the cortical model field.

Nunez Model

Nunez [75–77] developed a global EEG model. He assumed that the surface macroscopic EEG is due to the postsynaptic potentials in vertically oriented neurons in the cortex, so divided the cortex into neocortical columns consisting of large numbers of neurons described in terms of average properties of the "neural masses". In this model, the synaptic action at one location was caused by the action potentials fired from other locations and at earlier times. The synaptic action generation is also determined by the number density of corticocortical fibres connecting the two locations, the separation distance, and the action potential propagation velocities. A linearised sigmoidal relationship between action potential and firing rate was assumed.

Compared with the Lopes de Silva model, Nunez extended the mathematical neural model in several ways. First, the long-range corticortical fibres are included in the model with a significant delay in the action potential propagation along the axon; delays in the short-range intracortical fibres are ignored. He also assumed the long-range corticortical fibres are exclusively excitatory and the short-range intracortical fibres are both excitatory and inhibitory. The inclusion of long-range corticortical fibres and the axonal conduction delay is very important for simulating the large mammalian brain, such as human brain. Second, periodic boundary conditions are imposed in order to approximate the cortical surface as an oblate spheroid, and therefore, allow for possible emergence of global resonances and standing waves (i.e., alpha rhythm as a global standing wave). Third, Nunez considers some practical technical problems in his model: cortical folding, spatial and temporal biological filtering, volume conduction, and scaling of the electrode size etc.

Nunez incorporated local theory (lumped model of Lopes de Silva) into his global theory. In this combined local/global theory, for the cortical interconnections, Nunez assumed the inhibitory feedback and excitatory intracortical interactions arise from the local theory, while the excitatory corticocortical interactions arise from the global theory. He found that both global and combined local/global theory can generate certain EEG rhythms observable in human brain. The weakness of the Nunez model is the uncertainty of the range of the key model parameters for the mammalian brain; the strength of the Nunez model is widely differing classes of solutions to his fundamental equations, with varied variations of key structural parameters.

Freeman Model

Since 1964, Freeman and colleagues have developed a model to investigate the perceptual processing in the olfactory bulb [36–39]. Using a "bottom-up" method, Freeman constructed different structures of neuronal aggregates: KO, KI, KII, and KIII sets based on the basic building block/unit, "neural masses", and in which, the most common structure is the KII configuration with interactive excitatory and inhibitory neuronal aggregates. Based on the knowledge obtained from the olfactory system, and the assumption that neocortex shares the same properties as the paleocortex, he predicted the properties of the neocortex. After considering dendritic and synaptic delays (but ignoring axonal delays) in the interactive excitatory and inhibitory KII configuration, an oscillation with fundamental frequency of 40-Hz is generated by the cyclic process of excitation, recurrent inhibition, de-excitation, and disinhibition in the neuronal loop. A coherence between EEG and the local cell firing is experimentally observed around this 40-Hz frequency. Also, a quarter-cycle phase-lag between the excitatory and inhibitory neuronal populations is developed in the loops.

The conversions between pulses (action potentials) and waves (dendritic currents) are defined in Freeman model. A piece of most important work completed by Freeman is that he theoretically derived a precise form for the nonlinear asymmetric sigmoid function for the wave-to-pulse conversion and determined the maximum pulse density of the neuron population as the asymptotic limit of the sigmoid curve, which holds for both excitatory and inhibitory neuronal populations. Freeman model also predicted the emergence of chaotic dynamics in the KII sets with the properties of near "$1/f$" spectrum of the EEG and the Poisson distribution of cell-firing rates.

Jirsa and Haken Model

Based on the models of Wilson-Cowan and Nunez, Jirsa and Haken [55, 56] developed a field theory to describe the dynamics of EEG and MEG (magnetoencephalogram), which is generated by dendritic potentials and currents from synaptic activity. Their model emphasises the conversion operations between pulses and waves: pulse-to-wave conversion at the synapses and the wave-to-pulse conversion at the somas. Borrowing the mathematical descriptions for the action potential density (wave) in the Wilson-Cowan model and the synaptic activities (pulse) in the Nunez model, Jirsa and Haken formulated two pairs of integral equations for the excitatory and inhibitory wave and pulse amplitudes, in which the wave amplitudes correspond to the quantities measured by EEG and MEG and both wave and pulse amplitudes are functions of location and time.

In Jirsa and Haken model, pulse-to-wave conversion is assumed as linear, and wave-to-pulse conversion as nonlinearly sigmoidal. They only considered one type of synapse for each neuron: excitatory neurons only have excitatory synapses and inhibitory neurons only have inhibitory synapses. Significant delay only exists in the corticocortical fibers and no delays are considered for the dendritic and intracortical fibers. They derived a nonlinear partial differential equation of the excitatory field variable (wave amplitude) by reducing the pairs of integral equations of synaptic activity to a one-variable field equation. One-dimensional periodic boundaries were applied to the field equation to connect the brain spatio-temporal dynamics to the motor behaviour. One disadvantage of Jirsa and Haken model is that their model ignored the delays between the conversions of pulses and waves: presynaptic pulse converting to dendritic potentials and then converting back to the pulse. Another disadvantage is its lack of the effects of lateral inhibition (no inhibitory short-range delay considered), which is thought to be important for the response properties of the cortical cells [5].

Wright Model

The Wright model [124, 125, 128] treats the cortex as a 2-dimensional cortical sheet and divides the sheet into a number of elements. Each element consists of lumped excitatory and inhibitory neural populations that are characterised by their mean firing rates, mean membrane potentials, mean densities, and mean densities of interconnections. Both axonal and dendritic delays are included and various boundaries are allowed in Wright's model. The strength of Wright's model is that its parameters are mostly physiologically-based, therefore, it is possible to make predictions that are comparable to the real measurements. A weakness of this model is that the model is only applicable to a very small system, or a very coarse resolution in a large system, because the interconnections between different elements are modelled by a spatial-temporal dependent Green-function which is large scale and time-consuming due to integral over time and space. In Chapter 5 I test the applicability of Wright equations to my fetal sheep simulation, but find the Wright model to be rather unwieldy and slow.

Robinson and Rennie Model

The Robinson and Rennie continnum model [82, 86, 87] is a reformulation of the Wright model that retains most of its features, such as nonlinearities, axonal and dendritic delays, and a 2-dimensional cortex. Like Wright, they incorporate both excitatory and inhibitory neuron populations, and all parameters are spatially-averaged values over a neuronal volume. The main difference between the two models is that Robinson describes the axonal propagation by a damped wave equation, instead of the Green function. This modification greatly improves spatial resolution and simulation speed, and permits analytic study of wave properties and stability. It was used to simulate both alpha and gamma rhythms.

Liley Model

The Liley model [63] assumes the cortex is homogeneous and the mean soma membrane potential of the excitatory neurons is linearly related to the local field potential and EEG. Each neural mass consists of two types of neuronal populations— excitatory and inhibitory. Both long-range (cortico-cortical) and short-range (intra-cortical) connections are considered in this model and long-range connections are exclusively excitatory. The refractory periods and the intra-cortical axonal conduction delays are ignored. Sigmoid function of the mean soma membrane potential is used to define the firing rate of the action potential. Therefore, each neuron mass can be modelled as a single RC compartment with efferent synaptic fluxes injecting into it. Like Wright model, Green function is used for the axonal propagation approximation. A pair of coupled non-linear partial differential equations can then be derived to describe the mean soma membrane potential after the Green function is determined. This model has successfully simulated the alpha rhythmic activity in the human brain.

Steyn-Ross Model

The Waikato Steyn-Ross model [100–102] is a simplified mean-field cortical model developed from earlier models by Wright [124, 125, 128], Liley [63], Robinson [86, 87] and Rennie [82]. Like the Wright model, it divides the cortex into macrocolumns, that describe the mean properties of neuronal populations. Both local (excitatory and inhibitory) and long- (excitatory only) range connections are modelled as a damped wave equation following Robinson and Rennie model. Dendritic response is modelled by a biexponential function, and the relationship between firing rate and membrane potential by a sigmoidal function. One difference between the Steyn-Ross model and the Wright model is that the Wright model sums up the excitatory and inhibitory pulse inputs at the synapses, while the Steyn-Ross model sums up the excitatory and inhibitory postsynaptic potentials at the soma. Though the consequent field equations and mathematical treatments are different, the results are comparable.

By setting a set of first-order partial differential equations to zero, the steady states of the cortical system can be obtained and stability analyses can then be carried out by calculating the eigenvalues of the Jacobian matrix of the set of differential equations. The mean firing rates and mean membrane potentials can then be achieved by numerical computation based on the set of partial differential equations. The advantage of the Steyn-Ross model is its fast computation speed when applied to the whole-cortex scale simulation and with reasonably good resolution. The Steyn-Ross model has been successfully utilised in the predictions on anaesthesia phase transition [100–102], sleep cycle [99], K-complex [122], and Turing pattern formation [104]. After comparing with the Wright model, I chose the Steyn-Ross model for my fetal sheep simulation.

Chapter 2

EEG Signal Analysis Techniques

The small and measurable electroencephalogram (EEG) electrical signal was discovered over a century ago. In 1875, Richard Caton, a Liverpool physician, measured the electrical activity of the exposed cerebral cortex of rabbits and monkeys [19]. In 1929, Hans Berger first measured human EEG from a scalp recording [106], and in 1932, Berger and Dietsch applied Fourier analysis to EEG [31]. This was the first time in the history of EEG that computational techniques were applied to EEG analysis. In 1935, Loomis and his colleagues Harvey and Hobart were the first to systematically investigate human sleep EEG patterns and the stages of sleep [66, 67].

Although Berger and Dietsch had utilised Fourier analysis to assess EEG, historically, biomedical signals have often been evaluated visually. Nowadays, with advances in statistical and random signal processing techniques, biomedical signals can be processed using many different approaches depending on the objective of the signal analysis. Typically, a given technique extracts information in a certain domain, i.e., time domain, frequency domain, space domain, etc, emphasising one aspect of the information contained in the signal. For example, analysis in the Fourier frequency domain allows extraction of frequency information from the signal more readily than does a time-domain analysis.

For my fetal sheep EEG analysis, I utilised time domain, frequency domain, and nonlinear analysis techniques. For time-domain analysis, EEG average power and correlation time were computed. Spectral-edge frequency analysis was conducted in the frequency domain. Finally, for the nonlinear analysis, the singular value decomposition (SVD) entropy analysis was applied to explore the nonlinear property of the fetal sheep EEG.

Because EEG signal is a noisy, time-varying biomedical signal, I will discuss the important basic concept of *stationarity*. Various methods utilised in the fetal sheep EEG analysis to improve the clarity of the results, such as signal averaging, windowing, and smoothing, are also discussed in this chapter.

2.1 Stationarity

Signals can be classified into two main categories: *deterministic* and *random*. Deterministic signals can be described by explicit mathematical relationships. EEG recordings display irregular patterns, so belong to the class of random or statistical signals which cannot be described by explicit mathematical relations, but are described by statistical terms such as probabilities and statistical averages, i.e., means, variances, covariances, correlations, and spectra, etc.

Random signals can be further classified as being *stationary* or *nonstationary.* For a stationary signal, the statistical properties are not a function of time. This means that the mean, variance and autocorrelation structure do not change over time. In reality, biomedical signals including EEG cannot be exactly stationary. For example, the EEG recorded during sleep cycles is nonstationary. The total power, power in different frequency bands, and fluctuation correlation functions in EEG all change during sleep cycles. But stationarity is a necessary assumption for the computation of well-defined statistical parameters. Therefore, for the classic EEG analysis technique, such as correlation analysis, frequency analysis, the working assumption is that EEG signal *is* stationary (Wiener [116], Jenkins [54], McEwen and Anderson [73], Lopes da Silva [24]). Usually the nonstationary EEG signal is divided into epochs or segments, and each epoch can be regarded as stationary if the epoch is short enough that the parameters of interest do not vary too much during each epoch. In EEG signal analysis, the length of each epoch is generally of the order of a few seconds. The stationarity assumption is implicit in our EEG analysis of power, correlation time, SVD entropy, and spectral-edge frequency across different sleep states.

2.2 Power Analysis

The average power of the fetal sheep ECoG signal was calculated for each 3-second epoch by adding all the instantaneous signal powers, and then dividing by the length of the epoch $T = N\Delta t$ or equivalently, by the number of the sample points N in each epoch. The instantaneous ECoG power at time t is defined as $P(t) = V(t)^2$. In discrete form, this becomes $0P[n] = V_n^2$ giving the instantaneous signal power at time-step n.

The average power is then defined as:

$$P_{\text{ave}} = \frac{1}{T}\int_0^T V(t)^2\,dt \tag{2.1}$$

The corresponding equation for the discrete format of the average power is:

$$P_{\text{ave}}[n] = \frac{1}{N\Delta t}\sum_{n=1}^{N} V_n^2\Delta t = \frac{1}{N}\sum_{n=1}^{N} V_n^2, \tag{2.2}$$

where N is 750 samples for each 3-s epoch. The sampling rate for the fetal-sheep data is $f_{\text{s}} = \frac{1}{\Delta t} = 250\,\text{s}^{-1}$.

2.3 Correlation Function and Correlation Time

Correlation functions belong to the EEG time-domain class of analysis methods. Correlation analysis quantifies the degree of similarity of EEG waveforms. Autocorrelation measures the similarity between successive time samples from a single EEG time series, while cross-correlation characterizes the similarity between time samples from two different EEG time series, usually obtained from two EEG channels. The correlation function is defined as the lagged product of two timeseries. Its defining equation is very similar to the convolution equation, except the shift is in the opposite direction. In correlation analysis, it is assumed that the EEG time series are stationary.

The continuous forms of the cross-correlation and autocorrelation functions are expressed as,

$$C_{xy}(\tau) = \frac{1}{T}\int_0^T x(t)\, y(t+\tau)\, dt \tag{2.3}$$

$$C_{xx}(\tau) = \frac{1}{T}\int_0^T x(t)\, x(t+\tau)\, dt \tag{2.4}$$

For numerical computation, the discrete form of the correlation function is required:

$$C_{xy}[k] = \frac{1}{N}\sum_{n=1}^{N} x[n]\, y[n+k] \tag{2.5}$$

$$C_{xx}[k] = \frac{1}{N}\sum_{n=1}^{N} x[n]\, x[n+k] \tag{2.6}$$

where $x[n]$ and $y[n]$ are the two EEG time series at time step n, k is the time shift or lag of $y[n]$ with respect to $x[n]$, and N is the number of time points of each EEG epoch. For correlation calculations, the mean is first removed from each EEG time series. The cross-correlation function is computed as the sum of the cross-products of the voltages of the zero-mean EEG time series over one epoch at each of a number of successive and equal time lags.

The *cross-correlation coefficient* across lags is the normalized cross-correlation function, which is cross-correlation function divided by the square root of the product of the power of each EEG signal. The formula for the correlation coefficient function is,

$$\rho_{xy}(\tau) = \frac{C_{xy}(\tau)}{\sqrt{C_{xx}(0)C_{yy}(0)}} \tag{2.7}$$

The correlation coefficient lies between $+1$ and -1.

The maximum value of the cross-correlation function indicates the degree of similarity between two EEG signals: the larger the maximum, the more similar the two EEG waveforms are. The lag time corresponding to this maximum value indicates the time delay of the common component in the two EEG signals. Hence, this lag time can be used to evaluate the phase difference between the two signals. For a negative cross-correlation coefficient, the phase difference of the periodic components in the two EEG signals is 90° to 270° out of phase.

For the autocorrelation function, the comparison is with the EEG signal itself. Assume the zero-mean EEG time series is $V[n]$ at time step n. The autocorrelation function of the discretely sampled EEG time series can be expressed by the equation,

$$C[k] = \frac{1}{N}\sum_{n=1}^{N} V[n]\, V[n+k] \tag{2.8}$$

For our 3-second epoch and 250 s^{-1} sampling rate, the number of sample points for each epoch is $N = 750$ samples.

Because the autocorrelation function describes the similarity of an EEG waveform with itself at different time lags, at zero lag the autocorrelation compares two identical EEG waveforms. Therefore, the autocorrelation function will be maximal at zero lag. The normalised autocorrelation function is defined as the autocorrelation function divided by the correlation at zero lag. The autocorrelation function is symmetric about zero lag, so it has even symmetry:

$$C_{xx}(-t) \;=\; C_{xx}(t) \tag{2.9}$$

The cross-correlation function satisfies the relation

$$C_{xy}(-t) \;=\; C_{yx}(t) \tag{2.10}$$

so is neither odd nor even.

The correlation time $\tau = k\Delta t$ is defined as the lag time when $C[k]$ has decayed to $1/e$ of its zero-lag maximum $C[0]$.

The autocorrelation function provides information about the bandwidth of the EEG waveform. For an EEG signal with broader bandwidth, the autocorrelation function is sharper. A sharper autocorrelation function corresponds to a smaller first zero-crossing lag time, and therefore to faster and less correlated EEG waveforms. For example, we find that the autocorrelation function of the REM sleep has a sharper autocorrelation function than that of the SWS sleep. This is in agreement with the fact that REM sleep is characterised by faster and less synchronized EEG waves than is SWS sleep.

2.4 Power Spectral Density (PSD)

Correlation and spectral density functions provide basically the same information, although correlation methods quantify the EEG signal in the time domain and power spectral density in the frequency domain. The autospectrum (or autospectral density function or power spectrum) can be obtained by computing the Fourier transform of the autocorrelation function. Similarly, the cross-spectrum, also called the cross-spectral density function, can be obtained from the Fourier transform of the cross-correlation function.

There are several equivalent ways to define the spectral density function. In my EEG analysis, the spectral density function is computed by taking the Fourier transform to the calculated correlation function, giving a two-sided spectral density function. In continuous notation, the cross-spectral density function S_{xy} between signals $x(t)$ and $y(t)$ is defined in Eq. (2.11), and its corresponding discrete form in equation (2.12).

$$S_{xy}(f) \;=\; \int_0^T C_{xy}(\tau)\, e^{-j2\pi f\tau}\, d\tau \tag{2.11}$$

$$S_{xy}[k\Delta f] \;=\; \Delta t \sum_{n=1}^{N} C_{xy}[n]\, e^{-j2\pi nk/N} \tag{2.12}$$

where $C_{xy}(\tau)$ and $C_{xy}[n]$ are the continuous and discrete forms of the cross-correlation function defined in the last section. Similarly, the continuous and discrete form of the autospectral density function are defined,

$$S_{xx}(f) = \int_0^T C_{xx}(\tau)\, e^{-2\pi f \tau}\, d\tau \tag{2.13}$$

$$S_{xx}[k\Delta f] = \Delta t \sum_{n=1}^{N} C_{xx}[n]\, e^{-j2\pi nk/N} \tag{2.14}$$

where $C_{xx}(\tau)$ and $C_{xx}[n]$ are the continuous and discrete forms of the autocorrelation function. For stationary correlation functions, the autospectral density function is a real-valued nonnegative even function of f. That is

$$S_{xx}(-f) = S_{xx}(f) \tag{2.15}$$

The cross-spectral density function is a complex-valued function of f:

$$S_{xy}(-f) = S_{yx}(f) \tag{2.16}$$

For the purpose of spectral analysis, I assume that the EEG signal is stationary over the duration of the 3-s epoch.

2.5 Singular Value Decomposition (SVD)

In matrix computation [45], it is well known that any $m \times n$ rectangular matrix X, with $m \geq n$, can be expressed as the product of three matrices,

$$X_{m\times n} = V_{m\times m} S_{m\times n} U^T_{n\times n} \tag{2.17}$$

in which U^T is the transpose of the matrix U, S is an $n \times n$ diagonal matrix, and V is a real $m \times n$ orthogonal square matrix. The columns of V are called left singular vectors of X,

$$\left(V^T V\right)_{i,j} = \delta_{i,j} \tag{2.18}$$

Matrix U is a real $n \times n$ orthogonal square matrix. The rows of U^T (or, equivalently, the columns of U) contain the elements of the right singular vectors of X,

$$\left(U^T U\right)_{i,j} = \left(U U^T\right)_{i,j} = \delta_{i,j} \tag{2.19}$$

The diagonal elements of S are real positive numbers, and are called the *singular values* of matrix. The set of the singular values is called the *singular spectrum.* The diagonal contains the singular values in descending order,

$$S = \begin{bmatrix} \sigma_1 & 0 & 0 & \cdots & 0 \\ 0 & \sigma_2 & 0 & \cdots & 0 \\ 0 & 0 & \sigma_3 & \cdots & 0 \\ \vdots & \vdots & \vdots & \ddots & \vdots \\ 0 & 0 & 0 & \cdots & \sigma_n \end{bmatrix} \tag{2.20}$$

in which

$$\sigma_1 \geq \sigma_2 \geq \sigma_3 \geq \ldots \geq \sigma_n \geq 0$$

The singular values are unique for a given matrix X. The matrix singular-value decompositions were computed using the `Matlab` function `svd`().

2.6 SVD Entropy

Entropy is a statistical measure of the number of degrees of freedom available to a system. The entropy of a signal is a measure of the degree of disorder or randomness in the signal. Roberts et al [85] proposed *SVD entropy* as a measure of EEG signal complexity utilising both singular-value decomposition (SVD) and the Shannon definition of entropy. The singular values can be obtained by performing SVD on an n-dimensional *embedding matrix* (defined below). The entropy of the singular spectrum is calculated by converting the singular spectrum into a probability distribution,

$$p_i = \frac{\sigma_i}{\sum\limits_{k=1}^{n} \sigma_k} \tag{2.21}$$

Then the SVD entropy is given by the Shannon formula:

$$H_{\mathrm{SVD}} = -\sum_{i=1}^{n} p_i \ln p_i \tag{2.22}$$

in which n is the number of the singular values. Since we use natural logarithm (base of the logarithm is e) in the Shannon entropy definition, the standard unit for the entropy is nat. If the base of the logarithm is two, H_{SVD} has unit bit, and if the base is 10, the unit is dit (digit). One nat is about 1.44 bits ($\frac{1}{\ln 2}$). An increasing SVD entropy indicates increasing complexity in the temporal structure of the underlying timeseries.

An *embedding matrix* for the one-dimensional EEG signal must first be constructed in order to use the SVD algorithm. Let time-series $v(k)$, $k = 1, 2, \ldots, N$, be the originally measured EEG signal at equal sampling intervals T_s. To embed the original EEG signal, delay vectors x_ℓ are constructed:

$$x(\ell) = [v(\ell), v(\ell + \Delta), v(\ell + 2\Delta), \ldots, v(\ell + (D_e - 1)\Delta)] \tag{2.23}$$

where Δ is a dimensionless index giving time delay; D_e is the embedding dimension. The delay Δ gives the "stride" between selected samples, thus $\Delta = 1$ means every sample is selected, $\Delta = 2$ selects every second sample, etc. The time delay Δ can be chosen almost arbitrarily for a noiseless and infinite data set, which is assumed in Taken's theorem [110]. But for real noisy and finite data sets, if Δ is too large, the different coordinates will become uncorrelated. This is called *irrelevance*. If Δ is too small, all points will accumulate along the bisectrix line (bisector, line that bisects an angle) in the embedding space, and there will be no difference between different components or delay vectors. This is called the *redundancy* [60].

The embedding dimension, D_e, according to Taken's theorem [110] for a noiseless and infinite data set, must satisfy: $D_e \leq 2M+1$, which sets the lower bound for D_e given an M-dimensional manifold in the phase space. M is the true dimension and not known *a priori*, so this theorem has little practical significance. In practice, the embedding dimension D_e is chosen large enough to produce redundancy in the embedding results. The redundancy can be investigated using singular value decomposition.

After the delay vectors are built, the embedding space is then constructed by:

$$X = [x(1), x(2), \ldots, x(p)]^T \tag{2.24}$$

where $p = 1 + (N - (D_e - 1)\Delta - 1)/\Delta$. For example, for time delay $\Delta = 4$, embedding dimension $D_e = 5$, and data length $N = 97$, the embedding trajectory matrix X becomes

$$X = \begin{bmatrix} x(1) \\ x(2) \\ \vdots \\ x(21) \end{bmatrix} = \begin{bmatrix} v(1) & v(5) & v(9) & v(13) & v(17) \\ v(5) & v(9) & v(13) & v(17) & v(21) \\ & & \vdots & & \\ v(81) & v(85) & v(89) & v(93) & v(97) \end{bmatrix} \tag{2.25}$$

The one-dimensional scalar time series $v(k)$ is now mapped into D_e dimensional phase space.

For our fetal sheep EEG analysis, we use correlation time (time for autocorrelation function to decrease to $1/e$ of its maximum zero lag value where e is base of the natural logarithms) to select the Δ delay (stride) value for the time delay evaluation [1] [4]. Other widely utilised methods of deciding time delay Δ comprise of first zero-crossing of autocorrelation function [34] and first minimum of mutual information function [35]. Compared with the time of first-zero crossing, the correlation-time method is found to be more robust [4]. Although mutual information method also considers nonlinear correlations, no absolutely "best" algorithm exists for Δ delay determination.

The correlation-time computation results are shown in Fig. 2.1. From the figure, we can see the correlation time is about 14.9 ms for SWS-to-REM sleep state transition and about 15.9 ms for REM-to-SWS sleep state transition. This approximately corresponds to a stride of $\Delta = 4$ samples. So the delay of $\Delta = 4$ was chosen for our embedding matrix construction. The SWS (slow wave sleep) and REM (rapid eye movement) sleep are defined in Section 3.2.

The embedding parameters for our fetal sheep ECoG entropy evaluation are also examined for developing SWS and REM sleep state. The influence of *time delay* on the SVD entropy is shown in Fig. 2.2. The SVD entropy of both REM and SWS has lower values for smaller time

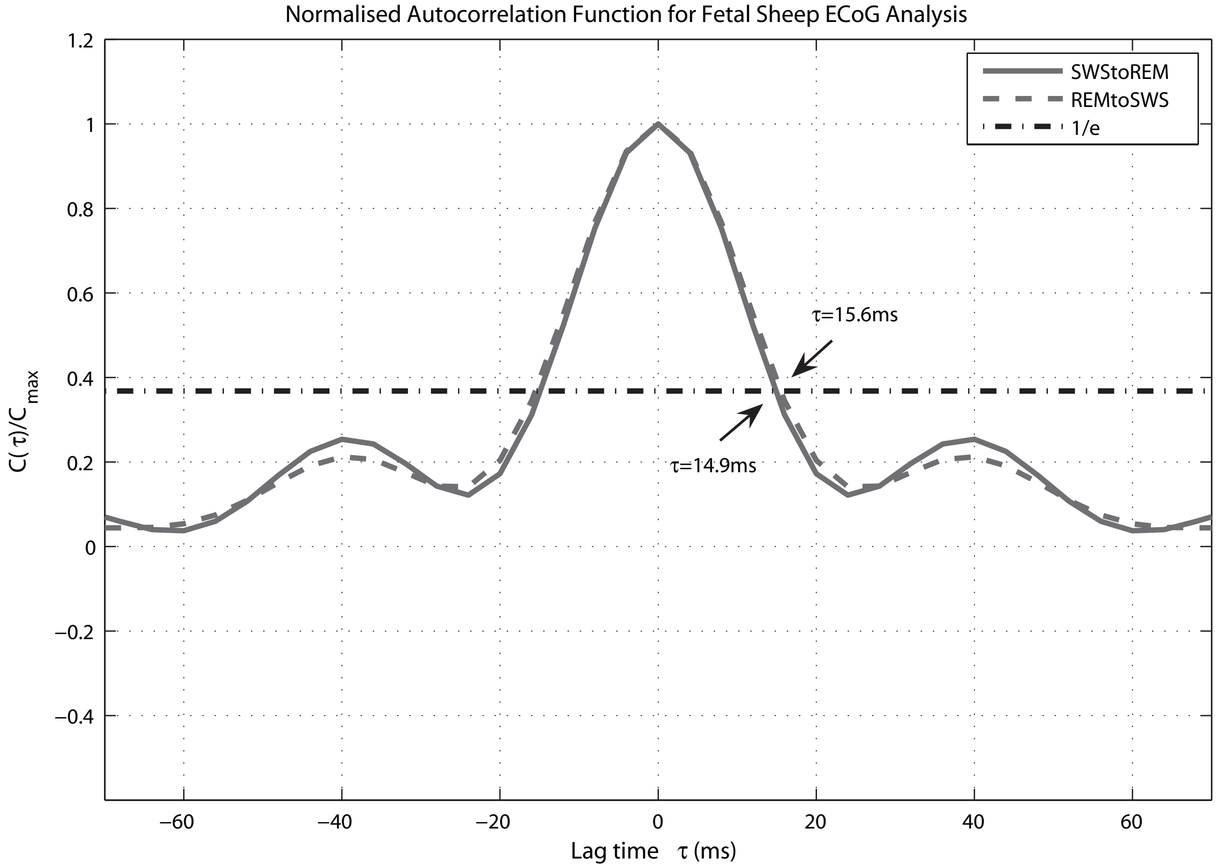

Figure 2.1: Autocorrelation function of fetal sheep ECoG for SWS-to-REM sleep state transition and REM-to-SWS sleep state transition. The correlation time for SWS-to-REM is about 14.9 ms, and for REM-to-SWS about 15.9 ms.

delays. The SVD entropy of SWS sleep state analysis did not show saturation. By saturation, I mean with increased time delay, the SVD entropy increases initially, but its rate of change diminishes at larger delays. For the REM sleep state analysis, saturation occurs when time delay equals 16 ms, which is 4 in terms of number of samples. This result is consistent with the correlation time analysis. So an embedding delay of 16 ms (i.e. Δ=4) was chosen for all our fetal sheep ECoG analysis.

The *epoch length* optimisation result is displayed in Fig. 2.3. For epoch length 1, 3, 5, 10 sec, the corresponding SVD entropy did not show any obvious change. Hence, SVD entropy is insensitive to epoch length in our case. Stationarity of ECoG analysis requires shorter ECoG data length. For time-series with sleep state transitions, the SWS-to-REM transition lasts about 30 seconds, and the REM-to-SWS transition about 200 seconds. These sleep state transitions are analysed and described in Chapter 3. A tradeoff between the stationarity requirement and optimised embedding parameters was made. I chose 3 sec as the epoch length in our ECoG analysis.

The *embedding dimension* analysis result is given in Fig. 2.4. The embedding dimension D_e does not show any saturation regions. Broomhead and King [20] proposed an alternative method to decide the upper bound of the sufficient embedding dimension. They suggested the sufficient embedding dimension is the number of linearly independent vectors, which is also the rank of the embedding trajectory matrix X. The number of linearly independent vectors can

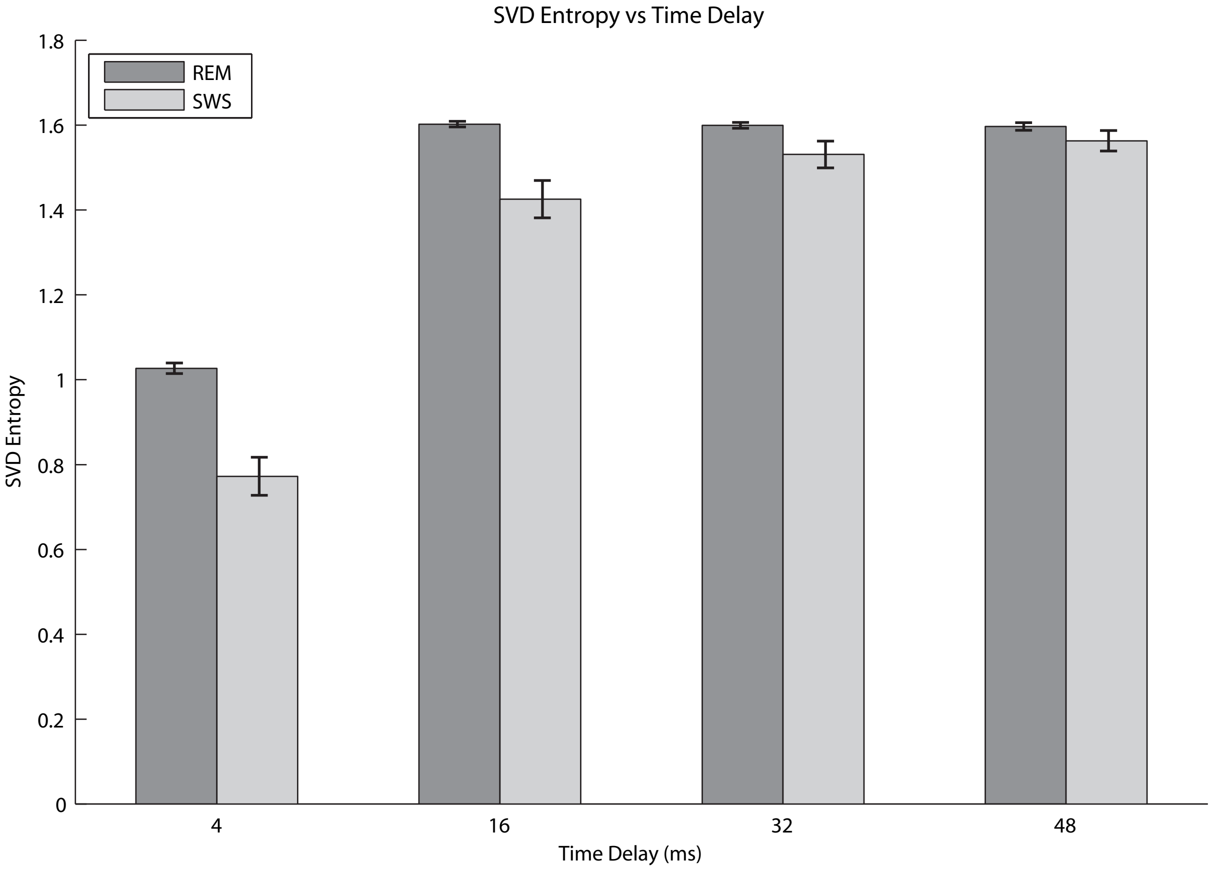

Figure 2.2: Influence of time delay on SVD entropy estimation for fetal sheep ECoG during REM and SWS sleep state at late gestational age. An embedding delay of 16 ms corresponds to stride $\Delta = 4$.

be conveniently obtained from the singular value decomposition performed on the embedding trajectory matrix X. By convention, singular values are given in decreasing order. For a redundant noiseless system, some singular values are zero. The rank of matrix X, $\text{rank}(X) = k$, if $\sigma_k > 0$ and $\sigma_{k+1} = 0$. For a system with noise, some singular values are not identically zero and will fall onto the noise floor composed of the smallest singular values [20]. In this case, the rank of matrix X is indicated by an abrupt decrease between adjacent diagonal elements of S. In practical measurement, EEG time series are noisy and have finite precision. The singular values have the form:

$$\sigma_1 \geq \ldots \geq \sigma_k \gg \sigma_{k+1} \geq \ldots \geq \sigma_n > 0 \tag{2.26}$$

Values σ_i, $i = k+1, \ldots, n$ are close to zero and in the so-called noise floor. Based on the relationship between singular values and rank of X, k should be the sufficient embedding dimension and sets the upper bound of the embedding dimension. When a sufficient embedding dimension has been reached, the number of singular values greater than the noise level should remain constant.

Fig. 2.5 shows the normalised singular values against normalised index. For convenient observation, we take the logarithm of normalised singular values in this graph. The normalised index is defined as i/D_e, in which i is the ith singular value computed from different embedding dimension D_e. For all cases, the singular values show dramatic decrease at certain singular

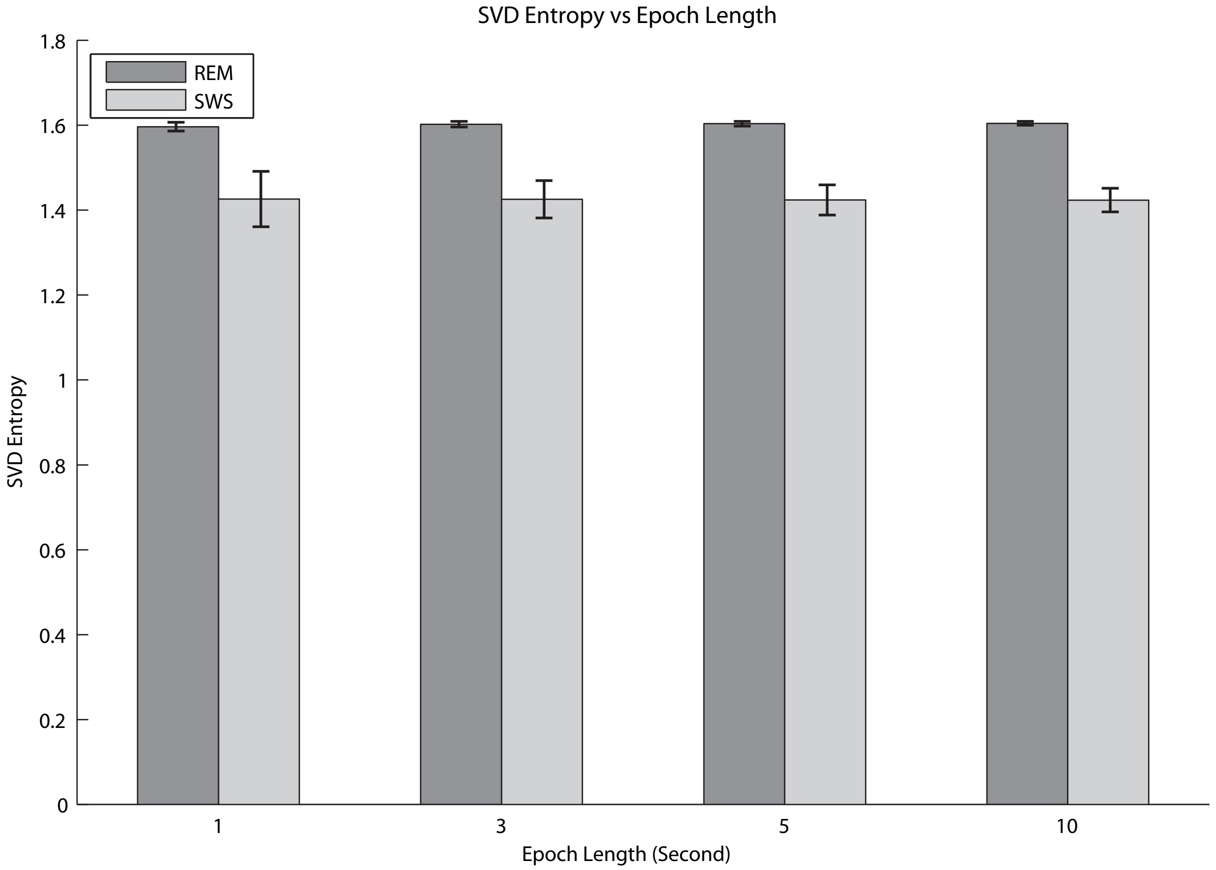

Figure 2.3: Influence of epoch length on SVD entropy estimation for fetal sheep ECoG during REM and SWS at late gestational age. SVD performance appears to be insensitive to epoch length.

values. For $D_e = 5, 6$, the singular values start to reach the flat noise floor, so I chose $D_e = 5$ as the embedding dimension for my ECoG analysis.

Singular values for SWS-to-REM and REM-to-SWS sleep state transitions computed using $D_e = 5$, $\Delta = 4$, are given in Figs. 2.6 and 2.7 respectively. Both figures show the five singular values for SWS and REM sleep states. For SWS sleep state, the first two singular values are much larger than the remaining three. This is consistent with what we saw in Fig. 2.5.

2.7 Spectral Edge Frequency

I define the *spectral edge frequency* to be the frequency below which 90% of the total EEG power in the power spectrum is located. The power spectral analysis was performed for each 3-second epoch using the fast Fourier transform (FFT) algorithm in `Matlab`. Then the power spectrum was averaged over all epochs for the 503-second ECoG signal. The sampling rate of the ECoG signal is 250 Hz. The resolution of the FFT is 0.33 Hz. Frequencies higher than 32 Hz were discarded because of negligible power in the power spectrum. The spectral edge frequency was

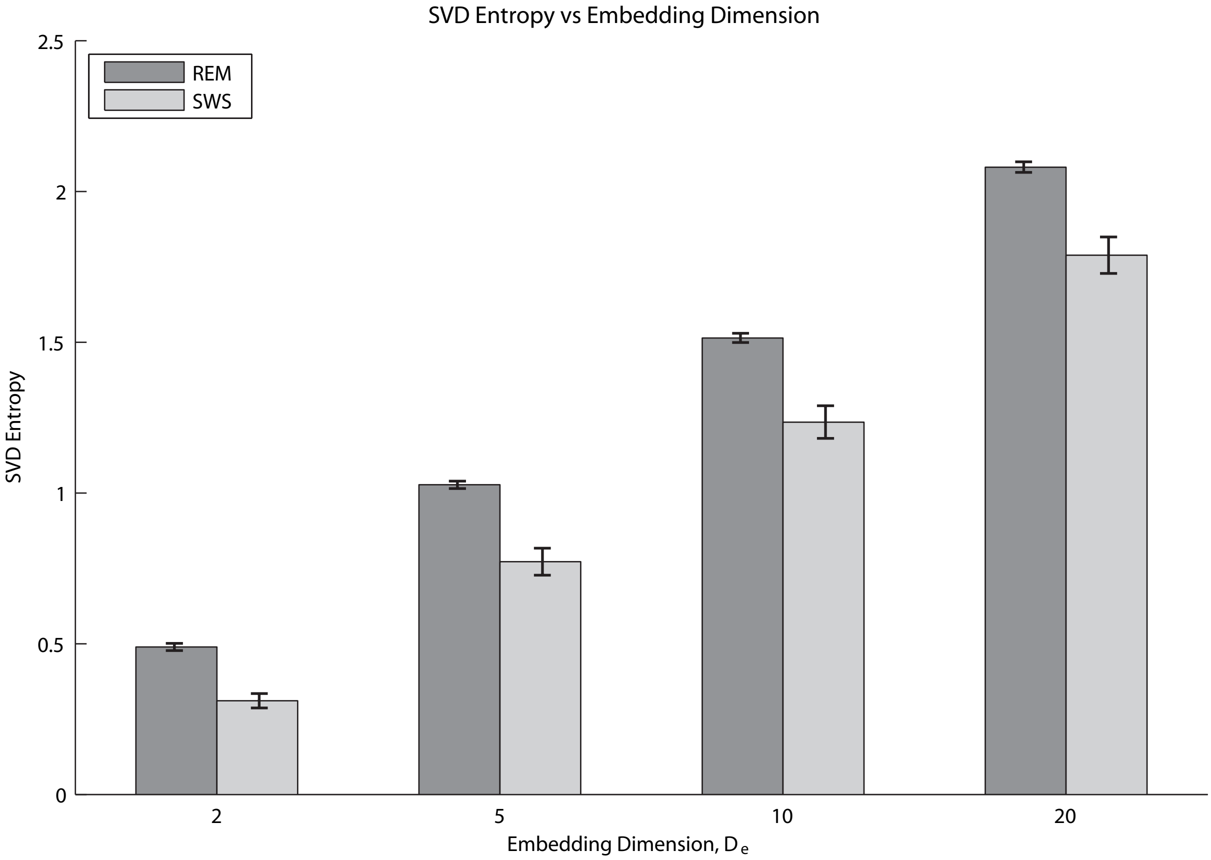

Figure 2.4: Influence of embedding dimension on SVD entropy estimation for fetal sheep ECoG during REM and SWS sleep state at late gestational age. There is no indication of saturation in these experiments, so the method of Broomhead and King [20] is used instead — see Fig. 2.5.

determined as the upper-bound frequency f_{edge} such that,

$$\frac{\int_{0\,\text{Hz}}^{f_{\text{edge}}} S(f)\,df}{\int_{0\,\text{Hz}}^{32\,\text{Hz}} S(f)\,df} = 0.9 \tag{2.27}$$

2.8 Epoch, Overlap, Averaging, and Windowing

Despite the fact that EEG is known to be nonstationary, the methods I adopted for the fetal sheep analysis assume stationarity. The nonstationarity of the real EEG signal will be considered as “noise”, with various smoothing and averaging techniques being used to reduce the so-called “noise”.

In our EEG analysis, power spectral density is computed by applying FFT to the EEG directly. For spectral analysis, averaging is essential to improve the statistical properties of the analysis results. Averaging is achieved by dividing the EEG signals into short equal-length epochs which partially overlap. The discrete Fourier transform was then applied to each successive epoch, and the final spectrum is taken as the average of the spectra obtained from all epochs. A shorter epoch length produces more epochs for averaging and achieves more reliable spectral estimation, but at the cost of decreased frequency resolution. When overlapping is used

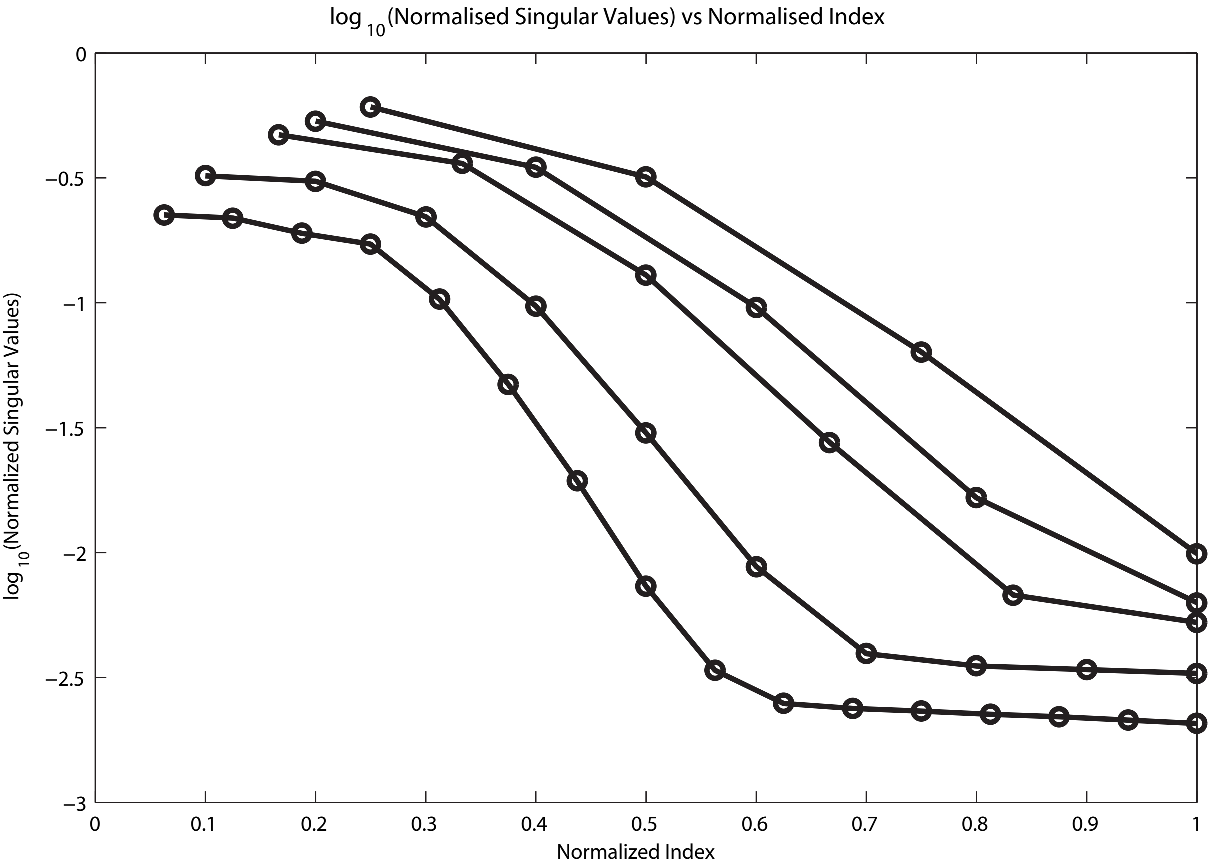

Figure 2.5: Normalised singular spectra plotted against the normalised index, i/D_e. The normalised singular values are indicated by circle markers. From top to bottom, the embedding dimensions D_e used here are 4, 5, 6, 10, 16. The timeseries used for the singular spectra analysis is in REM sleep state.

for the epochs, more epochs can be averaged for a given EEG recording session. For the noisy EEG signal, usually 50% overlap should be used in order to improve the reliability of the spectral estimate. If computation time allows, higher overlapping ratios will give better averaging results.

Data windowing is also used for sidelobe control. The Hamming window was used for my spectral-edge frequency analysis.

In the analysis, the ECoG was divided into epochs of 3 s with 25% overlap, the mean was removed from each epoch, and the FFT computed with frequency resolution of 0.33 Hz as given by the epoch length of 3 s.

2.9 Whittaker Smoothing

Smoothing is commonly used to remove noise and improve analysis results. A Whittaker smoother [33,115] was applied to my average power, correlation time, and SVD entropy analyses. Compared with other smoothers, Whittaker has several advantages: First, the signal peaks do not shift and no delay will be generated after the smoothing (i.e., it is phase preserving). Second, it can handle both short and large stretches of missing data. Third, it can be programmed in a couple of lines of Matlab. Fourth, by adjusting only one parameter, the smoothness can be controlled continuously.

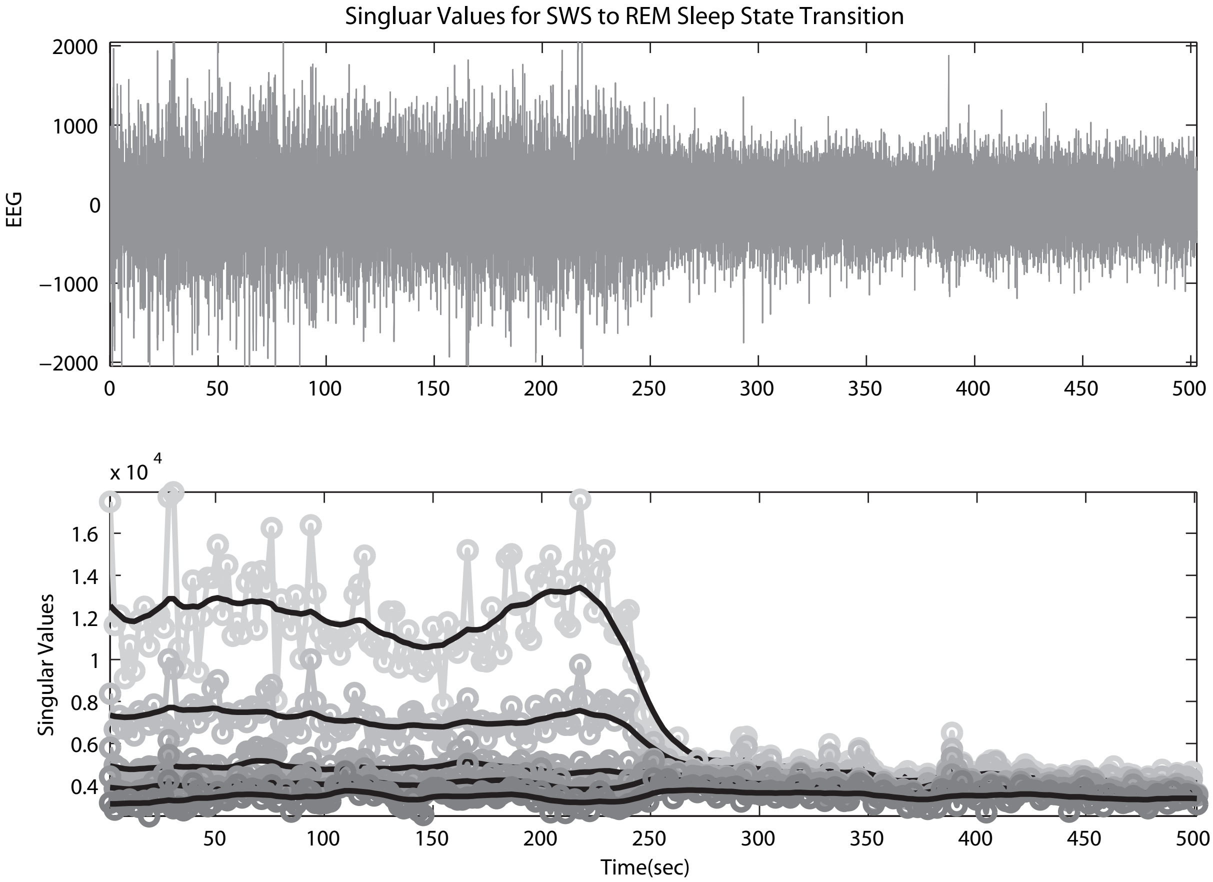

Figure 2.6: Singular values for SWS to REM state transition (fetus 172, gestational age: 144 days). Top: Time series; bottom: Singular values. Embedding parameters: $\Delta = 4$, $D_e = 5$.

Given a noisy time-series $x = \{x_1, x_2, ..., x_n\}$ sampled at equal intervals, a smoothed time series $y = \{y_1, y_2, ..., y_n\}$ can be obtained through the well-known Whittaker smoother. A measure of the construction quality of the smooth series y are the fit of the input and output time series x and y, and the smoothness of the output time-series y. This measure can be expressed as

$$S = \sum_{i=1}^{n} (x_i - y_i)^2 + \lambda \sum_{i=k+1}^{n-k} \left(\Delta^k y_i\right)^2 \tag{2.28}$$

where n is the number of data points in the time series x_i, λ is a smoothness parameter (discussed below), and Δ^k is the k-th order difference operator. For example, the first, second and third order differences are given as

$$\Delta y_i = y_i - y_{i-1} \tag{2.29a}$$

$$\Delta^2 y_i = \Delta\left(\Delta y_i\right) = y_i - 2y_{i-1} + y_{i-2} \tag{2.29b}$$

$$\Delta^3 y_i = \Delta\left(\Delta^2 y_i\right) = y_i - 3y_{i-1} + 3y_{i-2} - y_{i-3} \tag{2.29c}$$

The first term in Eq. (2.28) measures the fidelity or fitness of y to x, and the second term measures the roughness or smoothness of y. The parameter λ is a real positive number which controls the tradeoff between smoothness of y and fidelity to the data. The order k is an integer

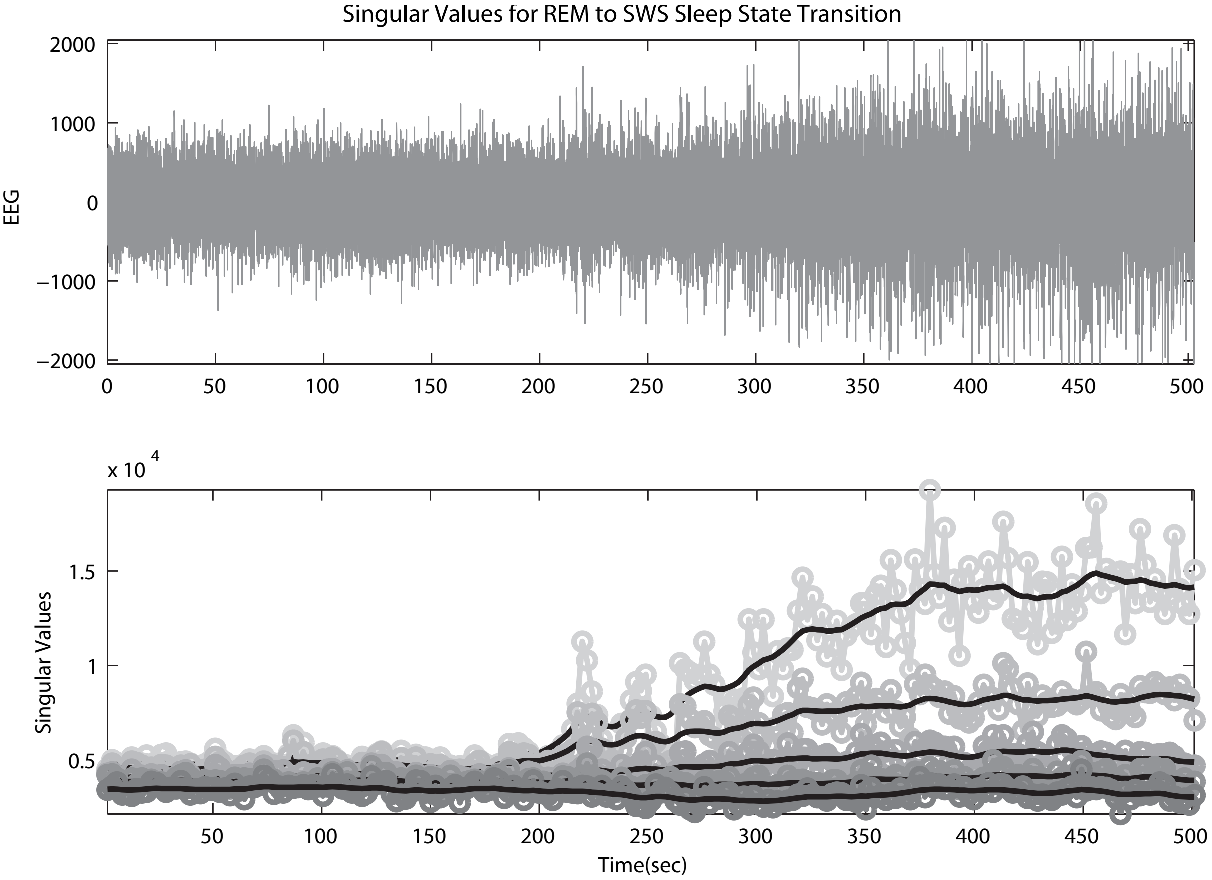

Figure 2.7: Singular values for REM to SWS state transition (fetus 172, gestational age: 144 days). Top: Time series; bottom: Singular values. Settings as for Fig. 2.6.

which sets the flexibility of the smoothed signal y. For a given k, the larger λ is, the smoother y is, corresponding to a degraded fitness to the data. If $\lambda = 0$, y converges to x. If λ is very large and $\to \infty$, y converges to a polynomial of degree $k-1$. In this case, for $k = 1$, y approaches a constant, which corresponds to a horizontal line. For $k = 2$, y approaches a tilted straight line with nonzero slope and for $k = 3$, y approaches a parabola. Large λ and small k give a more ragged fitting curve. On the contrary, large k and small λ will cause overfitting.

For optimum results, we want to balance the two conflicting goals: smoothness and fitness to the data, which means to minimise S in Eq. (2.28). This minimisation problem can be achieved by calculus of variations: set partial derivative $\partial S/\partial y$ equal to zero and solve for y. In order to implement the algorithm in `Matlab` efficiently, we rewrite Eq. (2.28) in its matrix form:

$$S \;=\; |x-y|^2 + \lambda\,|Dy|^2 \tag{2.30}$$

where D is a matrix such that $Dy = \Delta y$. D is a $(n-k) \times n$ differencing matrix, which means D has $n-k$ rows and n columns. For example, when $n = 6$ and $k = 2$,

$$D \;=\; \begin{bmatrix} 1 & -2 & 1 & 0 & 0 & 0 \\ 0 & 1 & -2 & 1 & 0 & 0 \\ 0 & 0 & 1 & -2 & 1 & 0 \\ 0 & 0 & 0 & 1 & -2 & 1 \end{bmatrix} \tag{2.31}$$

Using matrix calculus to compute the first derivative of S respect to y

$$\partial S/\partial y \;=\; -2\,(x-y) + 2\lambda D^T D y \tag{2.32}$$

where D^T is the transpose of D. Setting Eq. (2.32) equal to zero, we get

$$\left(I + \lambda D^T D\right) y \;=\; x \tag{2.33}$$

$$y \;=\; \left(I + \lambda D^T D\right)^{-1} x \tag{2.34}$$

where I is the identity matrix of order n.

After writing the solution in matrix form, its implementation in `Matlab` is very straightforward. The `Matlab` code for y can be written as

```
y = (I + lambda * D’ * D) \ x;
```

For a more general case, when the noisy time series x has some missing data points, Eq. (2.28) can be rewritten as

$$S \;=\; \sum_{i=1}^{n} w_i\,(x_i - y_i)^2 + \lambda \sum_{i=k+1}^{n-k} \left(\Delta^k y_i\right)^2 \tag{2.35}$$

where n again is the number of data points in the time series x_i and w_i are the weights. Normally $w_i = 1$; when x_i is missing, $w_i = 0$. The solution for y now becomes

$$y \;=\; \left(W + \lambda D^T D\right)^{-1} W x \tag{2.36}$$

in which W is a diagonal matrix with w on its diagonal. For the more general case, the `Matlab` implementation for y can be written as

```
y = (W + lambda * D’ * D) \ (W * x);
```

In order to solve y, smoothing parameters λ and d must be determined first. A less objective method to optimise the smoothing parameters is to inspect until visually pleasing results are achieved. Two of the most frequently used objective methods for estimating the smoothing parameters are cross-validation (CV) [114] and generalised cross-validation (GCV) [23].

The basic idea of cross-validation is to leave the data points out one at a time and smooth the remaining points by the remaining data and get a “prediction” $\hat{x}_{-1}$ for the left-out data point x_i. The cross-validation standard error is then defined as

$$\text{CVE} \;=\; \sqrt{n^{-1} \sum_i \left(x_i - \hat{x}_{-1}\right)} \tag{2.37}$$

The following relationship holds in the regression literature [47]:

$$x_i - \hat{x}_{-1} \;=\; \frac{x_i - \hat{x}_i}{1 - H_{ii}} \tag{2.38}$$

where H is the so-called *hat matrix*, H_{ii} is the diagonal element of H. For the case without missing data points, the hat matrix is given in Eq. (2.39), while the hat matrix in Eq. (2.40) is for the case with missing data points.

$$H = \left(I + \lambda D^T D\right)^{-1} I \tag{2.39}$$

$$H = \left(W + \lambda D^T D\right)^{-1} W \tag{2.40}$$

The cross-validation error (CVE) can then be computed using the results from Eqs. (2.34) and (2.36).

$$\text{CVE} = \frac{x_i - y_i}{1 - H_{ii}} \tag{2.41}$$

The cross-validation calculation can be easily implemented in `Matlab` by the above equations. In Fig. (2.8), I show an example of cross-validation optimisation and the smoothed curve for fetal sheep EEG correlation time by using automatically optimised λ from the CVE calculation. In this example, the step size for $\log_{10}(\lambda)$ is 0.2. Usually a sophisticated search algorithm to find minimum CVE is not needed in real applications.

The generalised cross-validation (GCV) can be calculated by

$$\text{GCV} = \sqrt{n^{-1} \sum_i \left(\frac{x_i - \hat{x}_{-1}}{1 - \text{Tr}(H)/n} \right)^2} \tag{2.42}$$

where $\text{Tr}(H)$ is the trace of matrix H. $\text{Tr}(H)/n$ is the average of the diagonal elements of H. Comparing with CV, GCV is thought to perform better for unequally spaced data [23]. Since our fetal sheep EEG data are equally spaced, I use CVE to optimise the smoothing parameter.

Gillies [42] also detailed the implementation of the Whittaker function in his MSc thesis using `Matlab`. Higher-order differences of $\Delta^k y_i$ can improve the results, but with more complicated computations. In a real application, it is not ideal to solely depend on the cross-validation method to blindly choose the smoothing parameters. I combined the cross-validation method and visual inspection to make a final decision about the optimal value for λ. After experimenting, I selected $\lambda = 20$ for smoothing.

2.10 Summary

In this chapter, the basic concept of *stationarity* was explained with respect to EEG analysis. The methods utilised in the analysis of the fetal sheep EEG in this thesis were then described; these include average power, correlation time, SVD entropy, and spectral edge frequency. For SVD entropy analysis, the first important step is construction of the embedding matrix. The process of determining the embedding parameters was then detailed. Techniques, such as signal averaging, windowing, and smoothing, were presented.

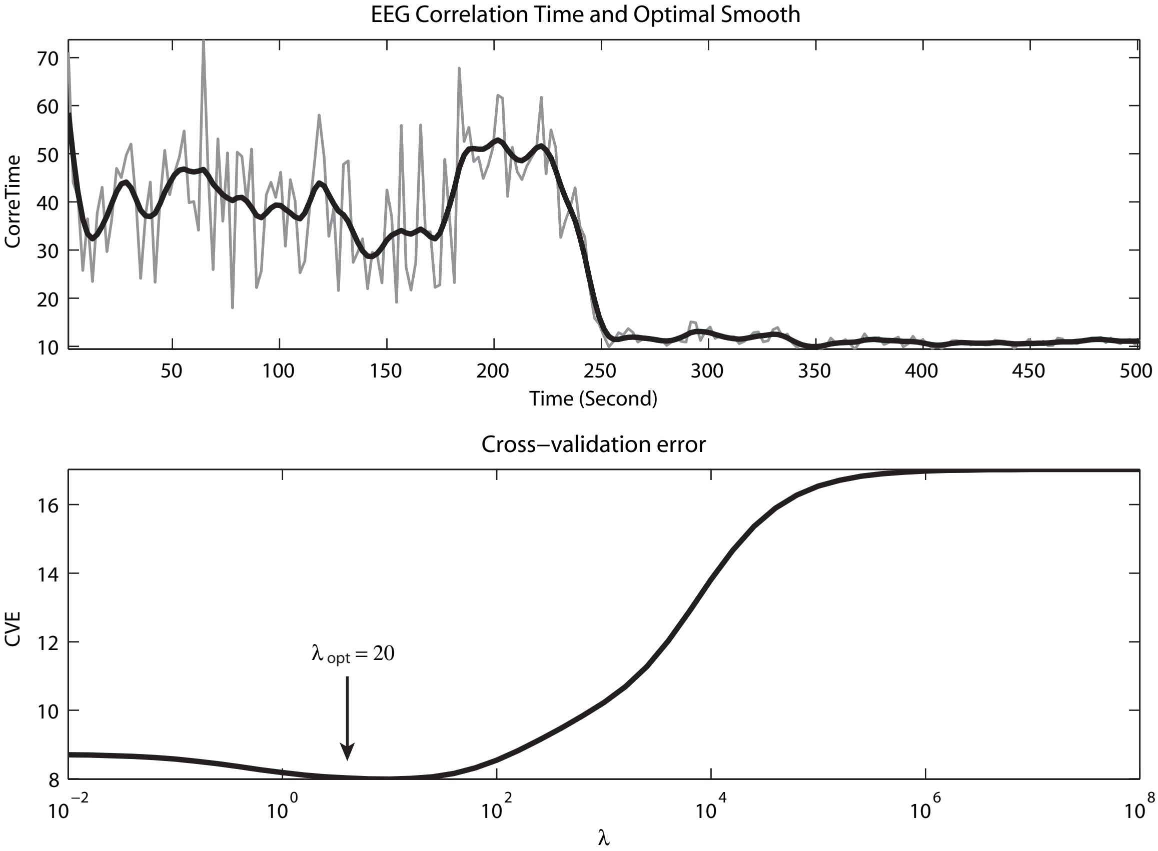

Figure 2.8: Optimisation of smoothing parameter λ for fetal sheep EEG correlation time using cross-validation. Upper panel: EEG correlation time and optimally smooth curve. Lower panel: cross-validation error plotted as a function of λ. The CVE minimum at $\lambda_{\text{opt}} = 20$ identifies the optimal value for λ.

Chapter 3

Analysis of Fetal Sheep Recordings

The fetal sheep is a good subject for brain maturation studies because of its long gestation period and its ease of instrumentation. In this chapter I describe the ECoG measurements and recorded data files of the fetal sheep obtained from the University of Auckland. After inspecting the ECoG times series, I partitioned the recordings into early third-trimester and late third-trimester (i.e., near full term) stages. The early third-trimester ECoG is characterised by intermittent high-voltage bursts separated by “silent” low-voltage intervals. For late-term fetal sheep, two well-differentiated sleep states, SWS and REM, emerge. I identified those ECoG time series having well-defined sleep state transitions, and for these calculated average power, correlation time, and SVD entropy. My results support the idea that the cortical change of state between SWS and REM can be regarded as a cortical phase transition.

3.1 Auckland Experiment

3.1.1 Surgical Instrumentation

The fetal sheep data were collected by the Department of Pediatrics at the school of Medicine at the University of Auckland in 1988 and 1989, and written up in Alex Sergejew’s PhD thesis (1997) [97]. All experimental procedures were approved by the University of Auckland Animal Ethics Committee. Fifteen Romney-Suffolk ewes carrying a fetus of known gestational age were used. Sterile techniques were used to anaesthetise the sheep (2% halothane), as detailed by Gluckman and Parsons 1983 [43], Gluckman and Parsons 1984 [44], and Williams et al 1990 [117, 118]. In the fetus, catheters were implanted into one of the auxilliary arteries to monitor blood gases to assess fetal well-being. To record the fetal electrocorticogram (ECoG) signal, teflon-insulated stainless-steel screw electrodes were implanted in the fetal skull over the parietal cortex. The electrodes were placed into the skull through drilled parasagittal burr holes on the skull, and secured with dental cement. Twelve sheep were instrumented with *bilateral* electrodes, and three sheep with *unilateral* electrodes (see Fig. 3.1 and Table 3.1). For the bilateral configuration, biparietal electrodes were positioned 15 mm and 5 mm ahead of bregma and 10 mm lateral to the midline (i.e., 20 mm apart). The unilateral electrodes pairs were placed 10 mm lateral to midline (i.e., 20 mm apart), with the positive (+) electrode placed 15 mm anterior to bregma and negative (−) electrode placed 1.5 mm anterior to bregma.

To assist in the classification of behavioural states, screw electrodes were also implanted into the supraspinal nuchal (neck) muscle, diaphragm (chest), and left eye socket respectively to record the nuchal and diaphragmatic electromyogram (EMG), and electrooculogram (EOG). This gave a total of five recording channels:

- two ECoG (electrocorticogram) to moniter brain activity;
- two EMG (electromyogram) to detect muscle tone;
- one EOG (electrooculogram) to detect eye movements.

The bilateral and unilateral electrode pairs were connected to the inputs of a two-channel differential amplifier. For bilateral electrodes, the anterior electrode pair was connected to channel-1 of the amplifier, and the posterior pair was connected to the channel-2. For unilateral electrodes, the left electrode pair was connected to channel-1, and the right electrode pair to channel-2. The differential amplifier was mounted on a head stage fixed to the fetus skull.

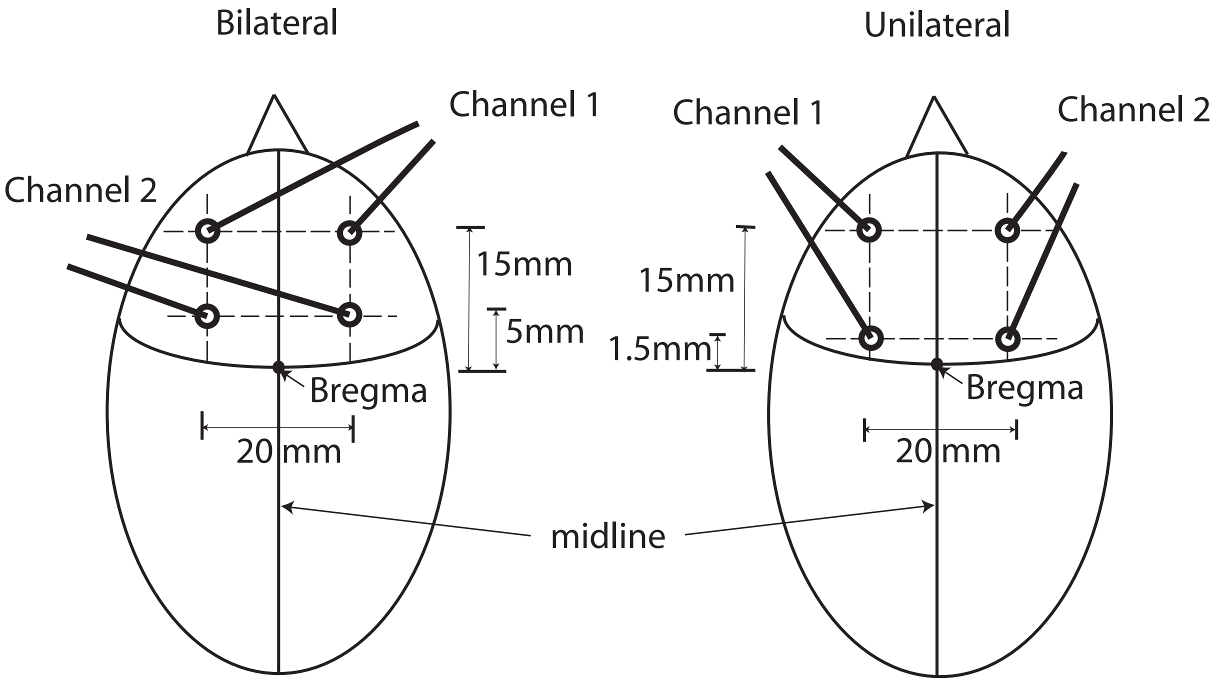

Figure 3.1: Bilateral and unilateral electrode settings used for recording fetal sheep ECoG. Distances between the electrodes and skull landmarks are as indicated in the figure. (Note that the diagrams are not drawn to scale.)

The fetus was returned to the uterus, and the uterus and abdomen closed. The leads from the output of the amplifier were exteriorized through an incision in the maternal flank. After the surgery, the ewe was kept in a metabolic cage. The cage temperature was set at 20°C and the cage humidity at 50%. The ewe was feed with hay, sheep nuts and alfafa, and water. The ewe received a course of antibiotics (80 mg gentamycin and 1 g cephalothin) intramuscularly daily for the first five post-operative days.

Immediately after surgery, spontaneous electrocortical activity was observed in all fetuses. Forty-eight hours after surgery, electrocortical activity returned to patterns normal for fetal age. Recordings began two to four days after surgery once the ewe had recovered. The plan was to record fetal ECoG from 95 days gestational age to full term (147 days ± 7 days) at regular two- to three-day intervals to assess maturation changes arising from development of neuronal myelination. The beginning recording date, 95 days GA, is at the premyelination stage. Because of the post-operation infection and electrode failures, only sheep ID 053 sustained chronic recording from 109 to 137 days GA. While recordings for sheep 172 ran from 130 to 144 days GA, this period was after the myelination stage. All other sheep measurements were not continuous and were only recorded when the opportunity arose. Thus, for different fetal sheep, recordings were made at different gestational ages. The nature of the various electrode failures were determined after fetus death or live delivery.

3.1.2 Data Acquisition

Fetal ECoG, diaphragmatic and nuchal EMG, and EOG signals of the unanaesthetised fetus were recorded between 95 and 144 days of gestation. ECoG, EMG and EOG signals were filtered, amplified and digitized using a 12-channel `A/D` board in an 8 MHz `IBM PC-AT` compatible computer. The filtering was implemented with an eighth-order Butterworth low-pass filter and a high-pass filter, giving a pass-band of 0.16 to 60 Hz. Filtered ECoG and EMG signals were sampled at 250 Hz (i.e. at 4 ms intervals) and stored continuously on magnetic media. Recordings were monitored on an analog chart recorder. More details about the acquisition system are given by Williams and Gluckman [117, 118].

For all five channels (two ECoG channels, two EMG channels, and one EOG channel), each recording session lasted either 502.78 or 394.396 s. Each day, several recording sessions were performed. For some sheep, up to ten sessions were recorded; most sessions were completed in the morning or early afternoon.

A Berkeley `Pascal` program was written by Nicolas Hawthorn to translate the data from the Department of Pediatrics file format (`.DAT` files) to a local format (`.ACQ` file). In March 2005 (approximately 15 years after the fetus experiments were performed), at the request of Prof James Wright, N. Hawthorn reassembled the `.ACQ` files onto a `CD-ROM` that was dispatched to A. Steyn-Ross at Waikato University.

3.1.3 Data Files

The `CDROM` contains 332 recording sessions from fifteen sheep. Eight of the 332 recording sessions were recorded from a dead sheep fetus, so they are not suitable for our fetal sheep ECoG study. Therefore, a total 324 ECoG recordings are available for our data analysis. Each 503-s (or 394-s) recording session was saved in one P*`.ACQ` file; each file contained the measurement data from all five channels. The file name gives information about the sheep identification, sheep gestational age and the recording-session number.

Take **P6172140** as an example, **P** is common for all files. The first “**6**” means the sixth file or session recorded on a given day for a particular sheep; “**172**” is the sheep ID; and “**140**” is the gestational age of the sheep at the date of measurement.

3.1.4 Subjects

Of the fifteen fetal sheep, four (031, 65, 279, 298)[1] were recorded completely within the early third trimester, corresponding to a GA of less than 115 days. Fetal sheep 172, 196, and 215 were recorded completely within the late third-trimester (129 days GA or older). Table 3.1

---

[1] Some of sheep files were labelled with a leading zero (e.g., 031), and some without (e.g., 65).

summarises the available recorded sessions of the 15 fetal sheep. The table lists the sheep ID (third column) and the gestational age (fourth column). If the year when the surgery and the experiment were conducted is known, it is also listed (second column). The fifth column gives the number of the recording sessions at a particular gestational age for each sheep, and the last column is its total number of recording sessions. There are a total of 324 recording sessions for the fifteen sheep, with gestational ages ranging from 95 to 144 days, corresponding to the 324 (live fetus) P*`.ACQ` files we received from the University of Auckland.

Table 3.1: Summary of the 324 recording sessions for the 15 fetal sheep. Three sheep IDs with † indicate *unilateral* electrode montage; the remaining 12 sheep have a *bilateral* electrode montage.

#	Year	ID	GA	Session	Tot. Sess.
1	?	65	95	0–2	
			98	0–2	
			100	0–2	
			105	0–2	
			107	0–2	
			111	0–2	18
2	?	031	103	1–9	9
3	?	279	104	1–9	9
4	?	298	105	1–9	
			112	1–9	18
5	?	267	106	1–9	
			111	1–9	
			118	1–9	
			125	1–9	36
6	1988	053	109	1–4	
			110	1–5	
			113	0–9	
			115	0–9	
			117	0–9	
			120	1–9	
			122	0–9	
			126	0–9	
			129	0–9	
			133	1–8	
			135	1–8	
			137	1–8	102
7	?	55	112	0–2	
			113	0–2	
			115	0–2	
			119	0–2	
			121	0–2	
			126	0–2	18
8	1989	188	116	1–3	
			118	1–3	
			121	1–5	
			124	1	12
9	?	178	122	1–4	
			123	1–6	
			124	1–2	12
10	1989	161†	123	1	
			124	2–4	4
11	1989	164†	124	1–3	3
12	1989	181	124	1–2	
			125	1–5	7
13	1989	196	129	1–3	3
14	1989	172†	130	1–3	
			131	1–2	
			132	1–4	
			134	1–8	
			136	1–8	
			138	1–8	
			140	0–9	
			142	0–9	
			144	0–9	63
15	?	215	131	0–9	10

Some other information about the sheep and the surgery were also passed to us by the University of Auckland. For example, for sheep 164, the surgery was performed on 29 June 1989. The sheep fetus was male and weighed 4.22 kg when sacrificed at 129 days of gestation. For this sheep, only one electrode pair was functional, the other electrode pair had failed. I chose to analyse the ECoG recordings for the functional channel, and manually excluded the files recorded from the malfunctioning channel.

3.2 Signal Classification for Late-Term ECoG

Early third-trimester sheep ECoG is rather bursty and intermittent (e.g., Fig. 3.3), while the more mature fetus displays sustained ECoG patterns that are either high-amplitude, low frequency, or reduced-amplitude fluctuations at higher frequencies. In our present study, the **high-voltage slow** (HVS) and **low-voltage fast** (LVF) states were classified according to the criteria described in Clewlow et al [22] and Ruckebusch [89]. Table 3.2 summarises these criteria.

Table 3.2: Criteria for classification of fetal states: high-voltage slow (HVS) or low-voltage fast (LVF) for mid to late third-trimester fetal sheep according to the criteria described in Clewlow [22] and Ruckebusch [89].

		Sleep State	
		High-Voltage Slow (HVS)	**Low-Voltage Fast (LVF)**
ECoG	Amplitude	Higher voltage amplitude	Lower voltage amplitude
	Power spectrum	Higher power at lower frequencies (3–10 Hz)	Lower power at lower frequencies (3–10 Hz)
Nuchal EMG		Sustained activity (contractions)	Less active or absent
Diaphragm EMG		Absent or sporadic	Sustained phasic
EOG		Absent or sporadic	Rapid, sustained eye movements

The high-voltage slow state is generally characterised by sustained nuchal EMG, but lack of diaphragmatic EMG and electroocular activity. HVS appears to be similar to slow-wave sleep EEG in humans.

The low-voltage fast state is characterised by sustained phasic diaphragmatic EMG and decreased nuchal EMG. The most distinct characteristic for the LVF state is the sustained rapid-eye movement. LVF probably corresponds to REM sleep in humans. According to Clewlow et al [22], there is diminished power at lower frequencies (3–10 Hz) for the LVF state compared with the HVS state.

In my fetal sheep studies, I assume that the HVS (high-voltage slow) state is equivalent to SWS (slow wave sleep), and that the LVF (low-voltage fast) state is equivalent to REM (rapid eye movement) sleep. Thus the SWS (or HVS) state is characterised by a high-voltage, slow-frequency ECoG pattern, absence of sustained, rapid-eye movements (EOG), and occasional nuchal muscle tone (EMG). Conversely, the REM sleep (or LVF) state is distinguished by a low-voltage, high-frequency ECoG, occurrence of rapid eye activity (EOG), and general absence of nuchal muscle tone (EMG).

Each recording session contains five channels of information: two ECoG channels, one nuchal EMG channel, one diaphragm EMG channel, and one EOG channel. A typical 5-channel recording session is displayed in Fig. 3.2. In this figure, the five subplots correspond to the five recording channels. This record shows a transition from SWS to REM sleep at time ∼150 second.

The EOG and EMG channels are only used for sleep-state classification purposes; the data in these channels were not analysed further. Prior to ECoG analysis, I inspected each ECoG trace visually for the presence of artifact. The recorded ECoG signals can be corrupted by different

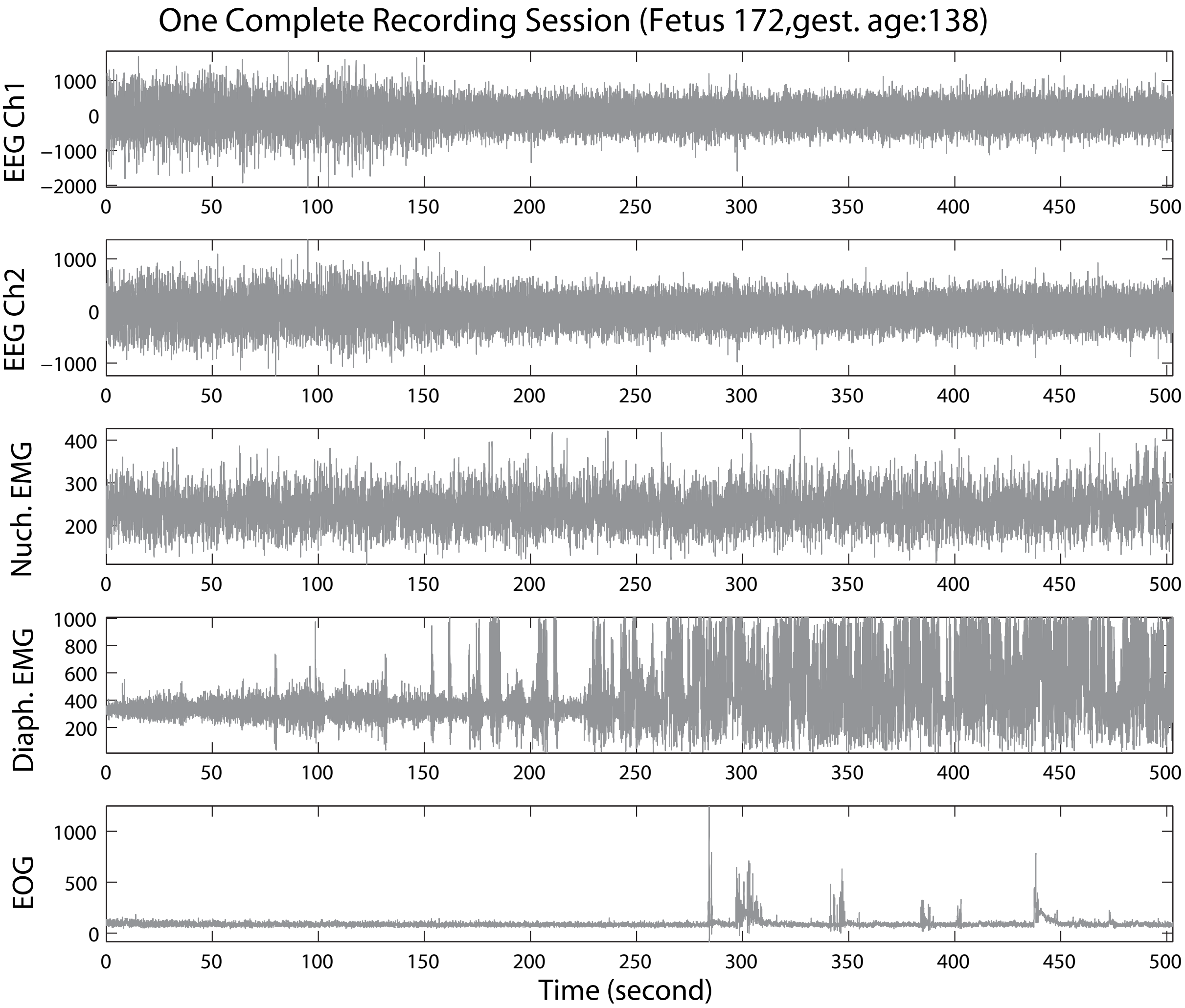

Figure 3.2: One complete 5-channel recording session. From top to bottom, the recordings are ECoG Channel 1, ECoG Channel 2, Nuchal EMG, Diaphragm EMG and EOG. The vertical scale is raw DN (digital numbers) output from the 12-bit A/D converter. The REM sleep state is characterised by sustained diaphragm EMG and EOG, while the SWS state by reduced or absent diaphragm EMG and EOG.

types of noise and interference, sometimes originating from another physiological process of the fetal body; for example, artifacts may arise when ocular activity interferes with the desired ECoG signal. Signal corruption can also occur when electrodes are poorly attached to the surface, or when an external source such as the sinusoidal 50-Hz powerline interferes with the signal.

3.3 Time Series in the Fetal Sheep Sleep

Spontaneous ECoG, EOG, and EMG activity can be seen in all of the recording sessions starting from as early as 95 gestational days, which is the youngest fetal data we received from Auckland University. For these early-term fetal sheep, the activities appear to occur randomly and do not seem to be associated with each other according to the criteria we defined in Sect. 3.2. No distinct sleep states (differentiated high-voltage slow activity versus low-voltage fast activity) defined by the ECoG, EOG and nuchal and diaphragm EMG can be discerned at this early stage.

Other researchers [108,109] report that organized HVS and LVF states can be observed after 110 to 115 days of gestation. However, for our data, the earliest age at which two distinct patterns began to emerge was 125 days GA (e.g. day 125 in sheep 267; day 131 in sheep 215; day 132 in sheep 172). This is significantly later than the 110 days. The reported average length of an HVS-LVF sleep cycle is about 20 minutes, with REM sleep (about 11 minutes) lasting longer than the SWS (about 8 minutes), and arousal lasting only about 2 to 4 minutes. For the Auckland data, the standard length for the fetal recording sessions is only about 8 minutes. Up to ten 8-min sessions were recorded per day, and sometimes as few as two or three sessions. Therefore, in our recordings, it is impossible to find a *complete* sleep cycle. The chance of capturing a REM-to-SWS or SWS-to-REM sleep transition is also not so high. In the vast majority of the Auckland recordings, no transition was detected; instead only 8 minutes of HVS (SWS) or LVF (REM) state was captured. This limitation compromises my analysis for the sleep cycle maturation study. Some investigations on the fetal sheep sleep maturation cannot be fulfilled, i.e., how the length of each sleep cycle evolves with increased gestational age and how the length of the SWS or REM sleep state within each sleep cycle varies with increased gestational age. Another limitation is that because no single complete sleep cycle is continuously recorded, exploring the property of the entire SWS or REM sleep state in each sleep cycle is impossible. The assumption that the property of the entire SWS or REM sleep state in each sleep cycle is the same is made in this thesis. Therefore, the analysis results for the SWS and REM sleep states in this thesis are just the properties of several 8-min EEG snapshots recorded within the same or different sleep cycles at certain gestational age.

Of the 324 usable recording sessions, only 14 SWS-to-REM transitions were detected (12 transitions from sheep 172 plus two from sheep 215). The earliest age at which the SWS-to-REM transition was detected, is at day 131 for sheep 215. A total of eight REM-to-SWS transitions were found in our recordings; these were for three sheep (172, 215, and 267). Table 3.3 summarises the transition occurrence statistics for late-term fetal sheep.

Table 3.3: Statistics for SWS-to-REM and REM-to-SWS transitions. There are 14 SWS→REM transitions and 8 REM→SWS transitions. The earliest sleep state transition is at 125 dGA (sheep 267). The majority of sleep state transitions occur in sheep 172. The dagger (†) indicates a unilateral (same side) electrode montage was used for sheep 172 (see Table 3.1). Sheep 215 and 267 had bilateral montage.

dGA		**125**	**131**	**132**	**134**	**136**	**138**	**140**	**142**	**144**
SWS-to-REM	No. of Transitions	–	2	1	1	1	2	1	3	3
	Sheep ID	–	215	172†	172†	172†	172†	172†	172†	172†
REM-to-SWS	No. of Transitions	1	2	–	–	–	–	2	2	1
	Sheep ID	267	215	–	–	–	–	172†	172†	172†

The early third-trimester fetal sheep display bursting ECoG patterns followed by periods of lower voltage activity. In contrast, late-term fetal sheep, like the adult sheep, have a well-defined slow-wave to REM sleep cycle. Figures 3.3 and 3.4 show representative time-series of the ECoG recordings obtained from the early third-trimester (gestational age: 95 days) and late-term (gestational age: 144 days) fetal sheep. Figure 3.3 (a) displays the 394-second early third-trimester fetal sheep ECoG signal; Figure 3.4 (a) illustrates the 503-second late-term fetal sheep ECoG signal. The graphs show the ECoG voltage time-series in raw digital numbers (DN) as recorded from the 12-bit A/D converter.

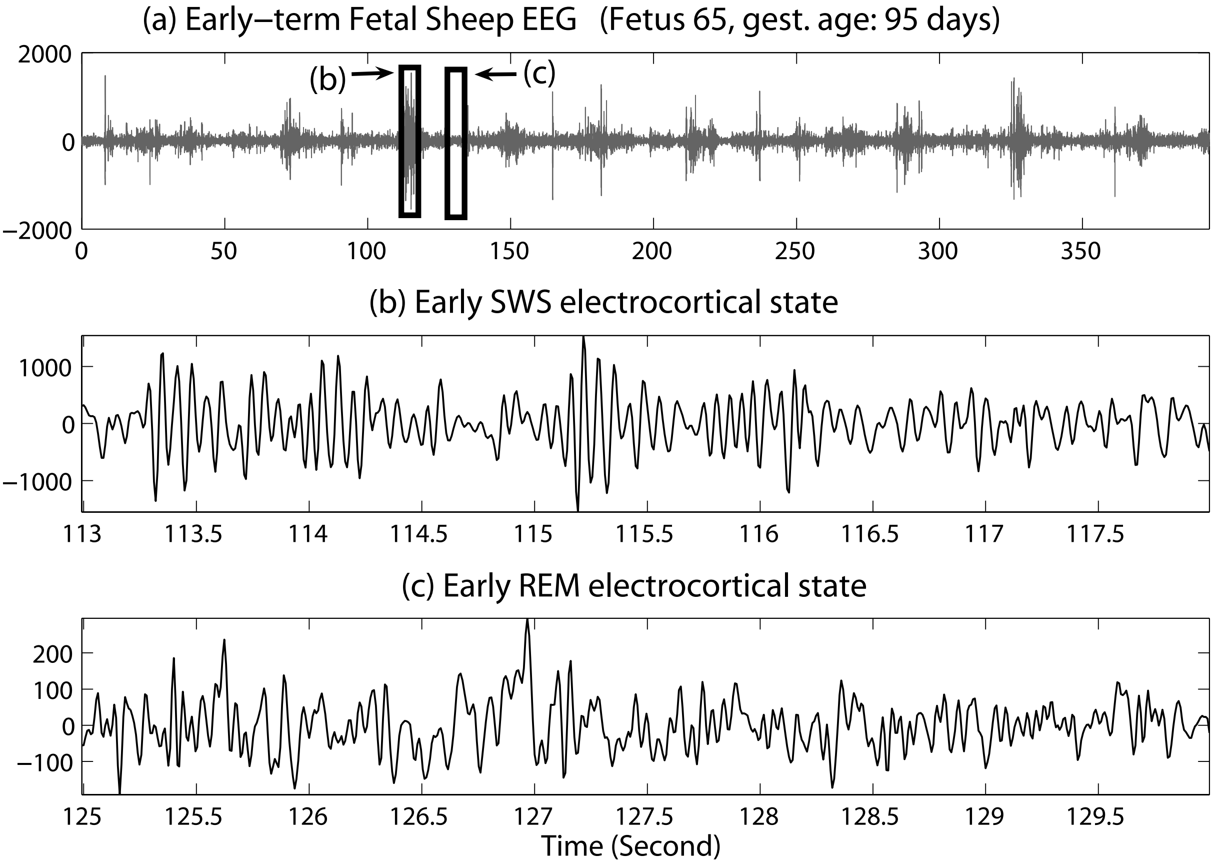

Figure 3.3: (a) Early third-trimester fetal sheep 394-s ECoG signal (sheep 65, gestational age: 95 days). (b) Five-second time series of high-voltage activity (burst). (c) Five-second time series of low-voltage activity. Vertical scales show ECoG voltage as a raw DN (digital number) as recorded from the A/D converter. Gestational age of 95 days is the youngest fetal sheep obtained from Auckland University. ECoG signal shows high-voltage bursts interrupted by low-voltage quieter intervals. This is very similar to the *tracé alternant* EEG signal seen in premature human infants. Spindle-like oscillations appears frequently during the high-voltage activity, panel (a), but are absent during the low-voltage activity, panel (c).

For the early third-trimester signal of Fig. 3.3, periods of high-voltage activity (burst) are separated by longer durations of low-voltage activity ("suppression"). Panels 3.3 (b) and (c) show five-second extracts of high-voltage and low-voltage activity respectively. The amplitude of the high-voltage activity in (b) is about 1000 DN (digital number) (the voltage unit for the A/D converter is unknown), roughly five times higher than for the low-voltage REM-like activity of (c).

For the late-term fetal sheep ECoG shown in Fig. 3.4 (a), a well-defined transition from high-voltage slow to low-voltage fast activity has been captured. The overall amplitude of the time-series is increased compared with the early third-trimester fetal sheep of Fig. 3.3, and two distinct ECoG patterns are now readily identified. Five-second samples of high-voltage (SWS) and low-voltage (REM) activity are shown in panels (b) and (c) respectively. The amplitude of the high-voltage activity state of the late-term fetal sheep is about 1000 DN, similar to that of

(a) Late–term fetal sheep EEG (Fetus 172, gest. age: 144 days)

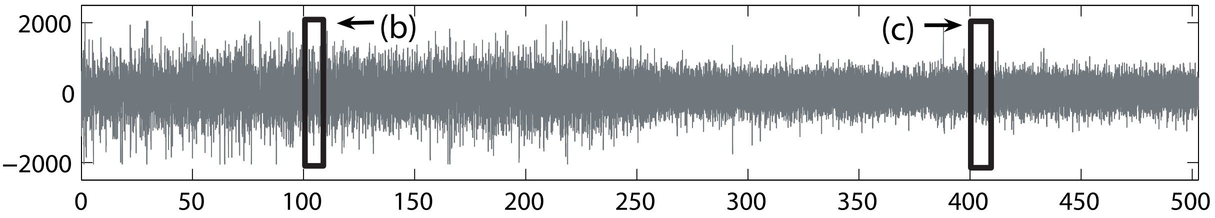

(b) SWS electrocortical state

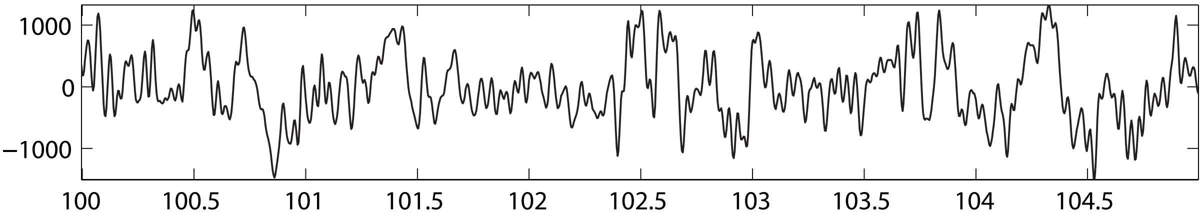

(c) REM electrocortical state

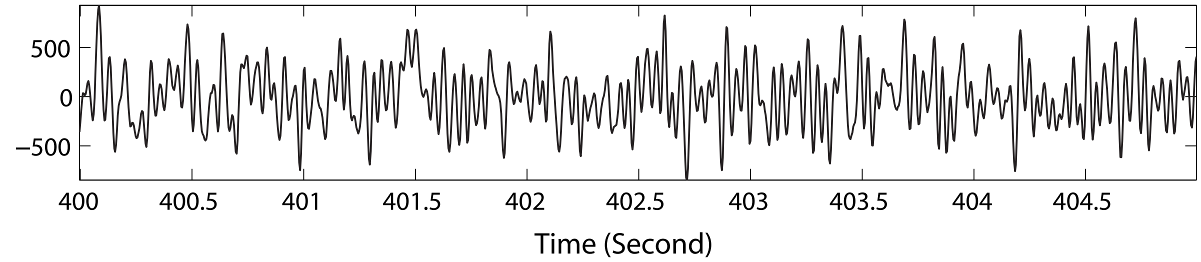

Figure 3.4: (a) Late-term fetal sheep 503-s ECoG signal (sheep 172, gestational age: 144 days). (b) High-voltage slow activity state (SWS) (c) Low-voltage fast activity state (REM). Vertical scale is raw DN (digital number). Gestational age of 144 days is the oldest fetus recorded (Full term for this fetal sheep is at day 147). SWS is characterised with high voltage and slow frequency as shown in panel (b). REM shows significantly lower voltage amplitude and faster oscillation frequency in panel (c). During the SWS state, a fast, low amplitude signal is superimposed onto the large amplitude slow oscillation.

the high-voltage activity state of the early-term fetal sheep. The amplitude of the low-voltage activity state of the late-term fetal sheep is about 500 DN. Hence, for the late-term fetal sheep, the amplitude of its high-voltage activity is about twice as large as its low-voltage activity. Furthermore, comparing Figs. 3.4 (b) and (c), it is obvious that the high-voltage activity state has a considerably slower frequency than the low-voltage state, consistent with our definition of SWS as a high-amplitude slow activity and the definition of REM as low-voltage fast activity.

For the late-term fetal sheep ECoG signal, I estimated the correlation time for ECoG voltage fluctuations by its normalised autocorrelation function. Figure 3.5 (a) gives the normalised autocorrelation plot for both of the high-voltage slow state and low-voltage fast state. The correlation time is defined as the lag time at which the autocorrelation falls to $1/e$ of its zero-lag value. From Fig. 3.5 (a), we can see the high-voltage activity state has larger correlation time (51.7±1.0 ms) than the low-voltage activity state (10.7±0.1 ms). Longer correlation times corresponds to slower oscillations, and vice versa. Therefore, high-voltage activity is dominated by slower fluctuations. This is consistent with a visual inspection of the HVS time-series.

In Fig. 3.5 (b), the autocorrelation without normalisation for the high-voltage activity and low-voltage activity signals is plotted. It is evident that the fluctuation power for the high-voltage activity state is about three times higher than fluctuation power for the low-voltage activity state.

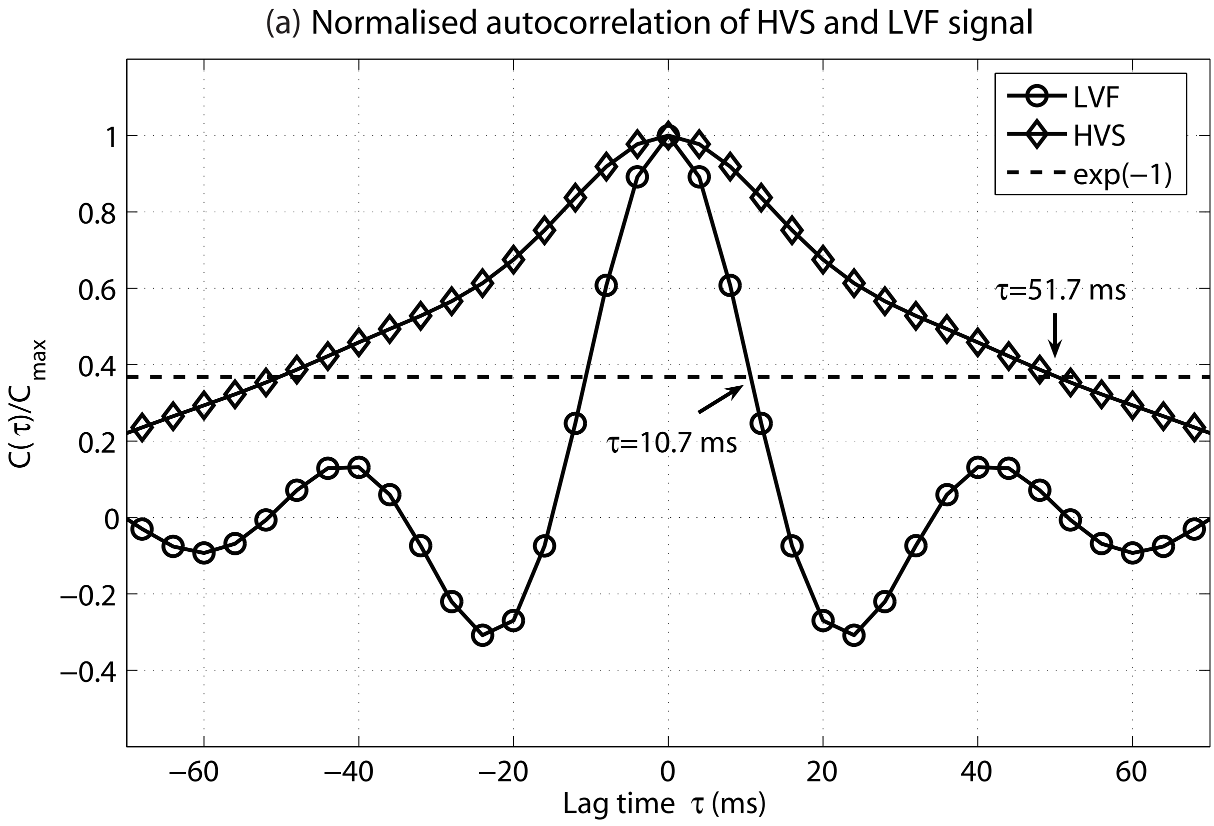

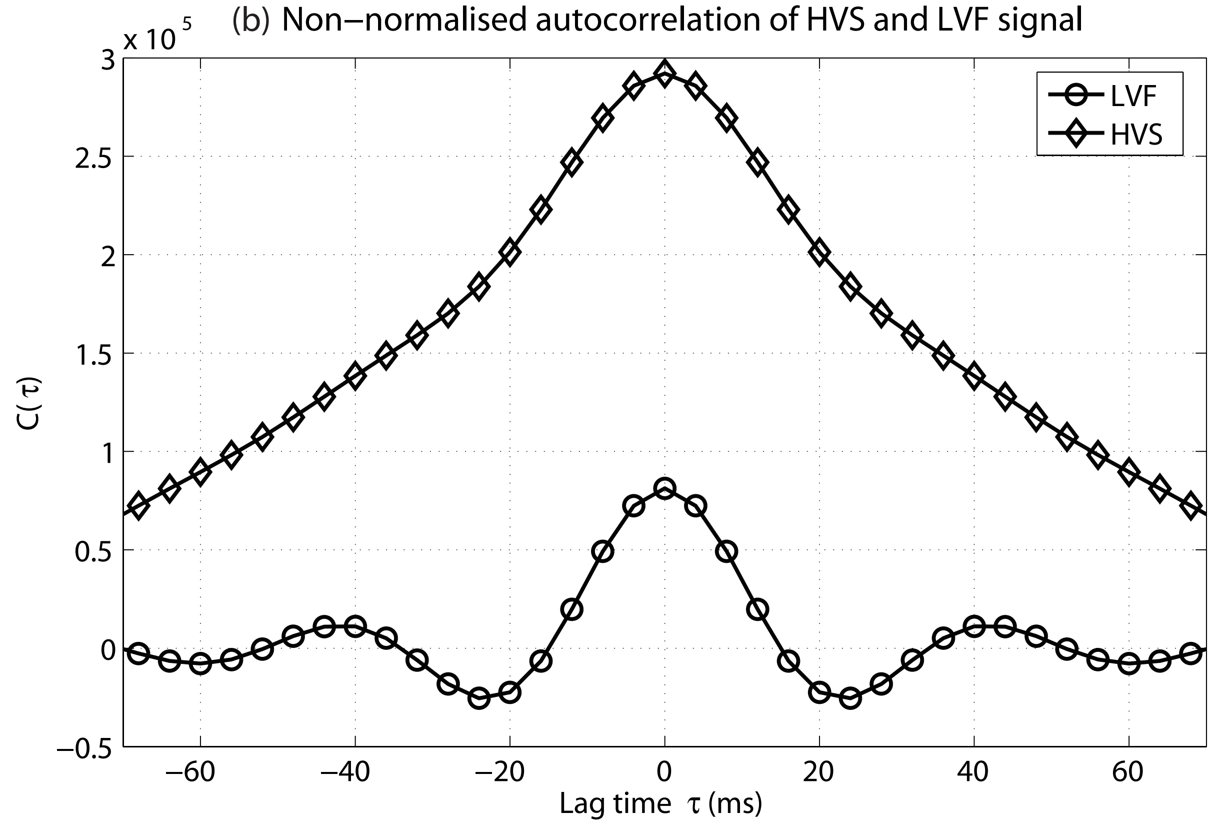

Figure 3.5: (a) Normalised autocorrelation of high-voltage slow (HVS) and low-voltage fast (LVF) signals for late-term fetal sheep. (b) Unnormalised autocorrelation of HVS and LVF signals. Correlation time is computed using conventional $1/e$ method from the normalised autocorrelation function and displayed in panel (a) for both HVS and LVF signals. The position of $1/e$ is shown as a dashed horizontal line in panel (a). For both panels, the HVS signal is recorded at 144 gestational day, and LVF signal at 142 gestational day from fetal sheep 172.

3.4 SWS and REM Sleep State Transitions

In order to investigate the sleep transitions in late-term fetal sheep, I identified (by visual inspection) those time-series containing a transition between high-voltage and low-voltage states, and for these, I computed the ECoG average power, correlation time, and SVD entropy. For all analyses, I used 3-second epochs with 25% overlap. The sampling rate was 250 s^{-1}.

Figure 3.6 displays a time-series with REM-to-SWS state transition recorded from sheep 172 with gestational age of 144 days. Figure 3.7 shows a SWS-to-REM transition for the same sheep on the same day, but from different recording session.

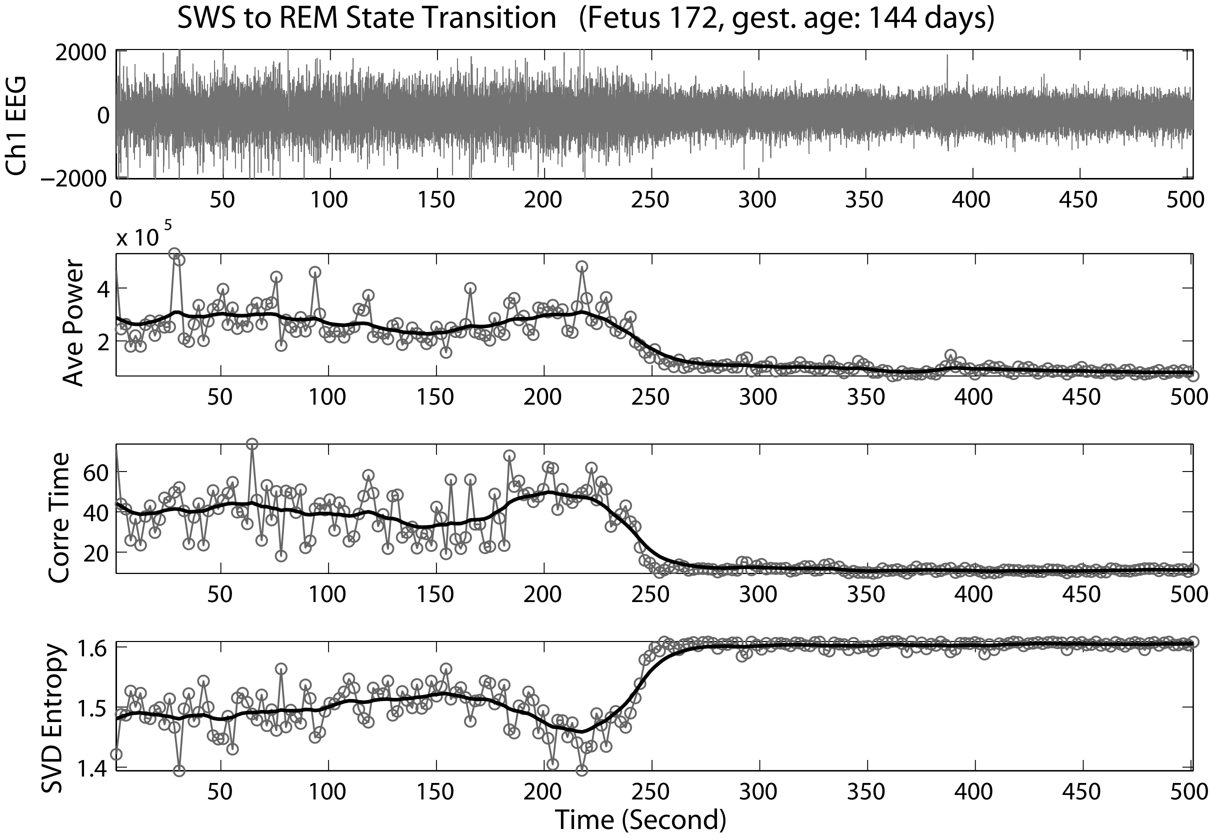

Figure 3.6: SWS-to-REM sleep state transition (fetus 172, gestational age: 144 days). (a) Time series (b) Average Power (c) Correlation time (d) SVD Entropy. It takes ∼30 second for the fetus to transit from SWS to REM sleep state. A power surge just before the SWS-to-REM sleep state transition is seen in this fetus. Correlation time in panel (b) has unit of ms. Black curves in panels (b), (c), and (d) show the smoothed results with Whittaker filter applied to the raw analysis data.

Comparing Figs 3.6 and 3.7, we can see that the SWS state has higher average power, longer correlation time and smaller SVD entropy than the fast (REM) sleep state. For the SWS-to-REM transition in Fig. 3.6, the average power decreased from about 3×10^5 to 1×10^5 DN^2, the correlation time decreased from 40 to 10 ms, and the SVD entropy increased from 1.5 to 1.6. In Fig. 3.7, when the sleep state changes from REM to SWS, the average power increases from about 1×10^5 to 4×10^5. Correspondingly, the correlation time increased from about 10 to 40 ms, and SVD entropy decreased from about 1.6 to 1.45. These analysis results support the idea that SWS is a higher-amplitude, synchronized or more organized, slower-frequency electrocortical activity state, and that REM sleep is a lower-amplitude, desynchronized or less organized, higher-frequency electrocortical activity state.

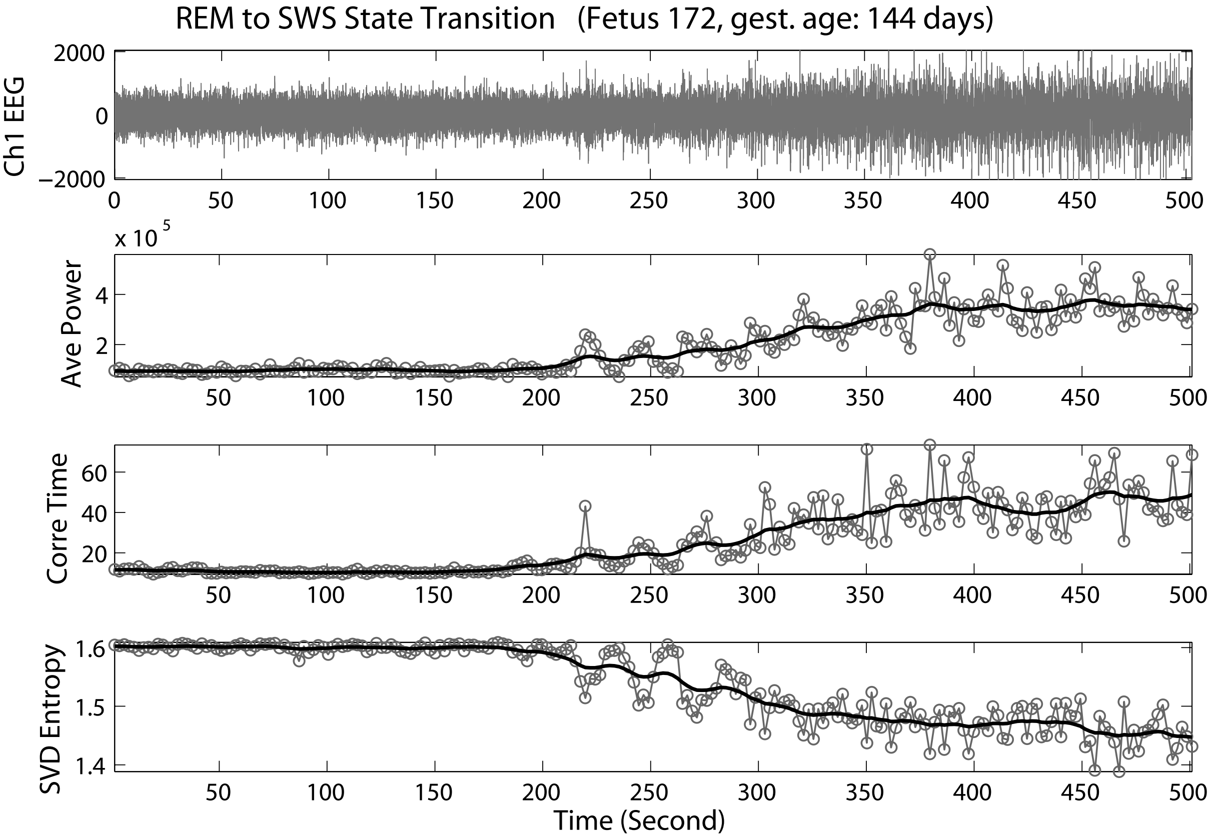

Figure 3.7: REM-to-SWS sleep state transition recorded from the same sheep analysed in Fig. 3.6 (fetus 172, gestational age: 144 days). (a) Time series (b) Average Power (c) Correlation time (d) SVD Entropy. The transition from REM to SWS is slow and gradual, taking ∼200-s to complete. This is much slower and less abrupt than the SWS→REM state change of Fig. 3.6. Correlation time in panel (b) has units of ms.

Furthermore, comparing Figs 3.6 and 3.7, we note that the ∼30-s transition from SWS to REM is *much more abrupt* than the ∼200-s reverse transition from REM to SWS. This asymmetric transition between sleep states is also observed in mature human sleep EEG [42]. These pronounced changes in EEG statistics are consistent with the hypothesis that REM and SWS are two distinct brain states separated by a phase transition. These observations suggested that the "up" transition from SWS to REM can be modeled as a first-order (discontinuous) phase change in cortical state, while the "down" transition from REM to SWS is a second-order (continuous) phase change [99].

From the 324 recording sessions, I identified 14 SWS-to-REM transitions, and 8 REM-to-SWS transitions, see Table 3.3. The analysis results of time-aligned SWS-to-REM transitions are plotted in Fig. 3.8, in which panel (a) displays the analysis results from channel-1 ECoG recordings and panel (b) from channel-2 ECoG recording. Similarly, Fig. 3.9 (a) and (b) shows the aligned time-series of REM-to-SWS transitions recorded from channel-1 and channel-2 and their corresponding analysis results. The time alignment was realised by shifting the transition point of each ECoG time series to $t = 250$ seconds, which is roughly the centre of the 503-second recording. The transition point was identified by first computing the correlation time of the time series with sleep state transition. The calculated correlation time was then smoothed with a low-pass Whittaker filter. The starting point and ending point of the transition was then determined by visual inspection of the smoothed correlation-time graph, and the instant of transition taken as the midpoint. Average power, correlation time, and SVD entropy were computed for each shifted ECoG time-series. Grand averages were then taken over the 14 SWS-to-REM transitions, and over the 8 REM-to-SWS transitions. Data from channel-1 and 2 were treated separately. In Figs 3.8 and 3.9, the grand averaged results of power, correlation time, and SVD entropy are plotted as thicker black lines; each grey line gives analysis result computed from individual shifted time-series.

Comparing panel (a) and panel (b) in Fig. 3.8 or Fig. 3.9, the results from channel-1 illustrate a larger contrast between the two sleep states and therefore give better demonstration of sleep state transition between SWS and REM. Examining Figs 3.8 and 3.9, we find that the SWS-to-REM transition is very abrupt, while the REM-to-SWS transition is considerably slower and more gradual. Thus the grand-averaged results confirm the single-trial analyses presented in Figs 3.6 and 3.7, and support the idea that the SWS→REM state change can be modelled as a first-order or jump transition, while the REM→SWS state change is a second-order, continuous phase transition.

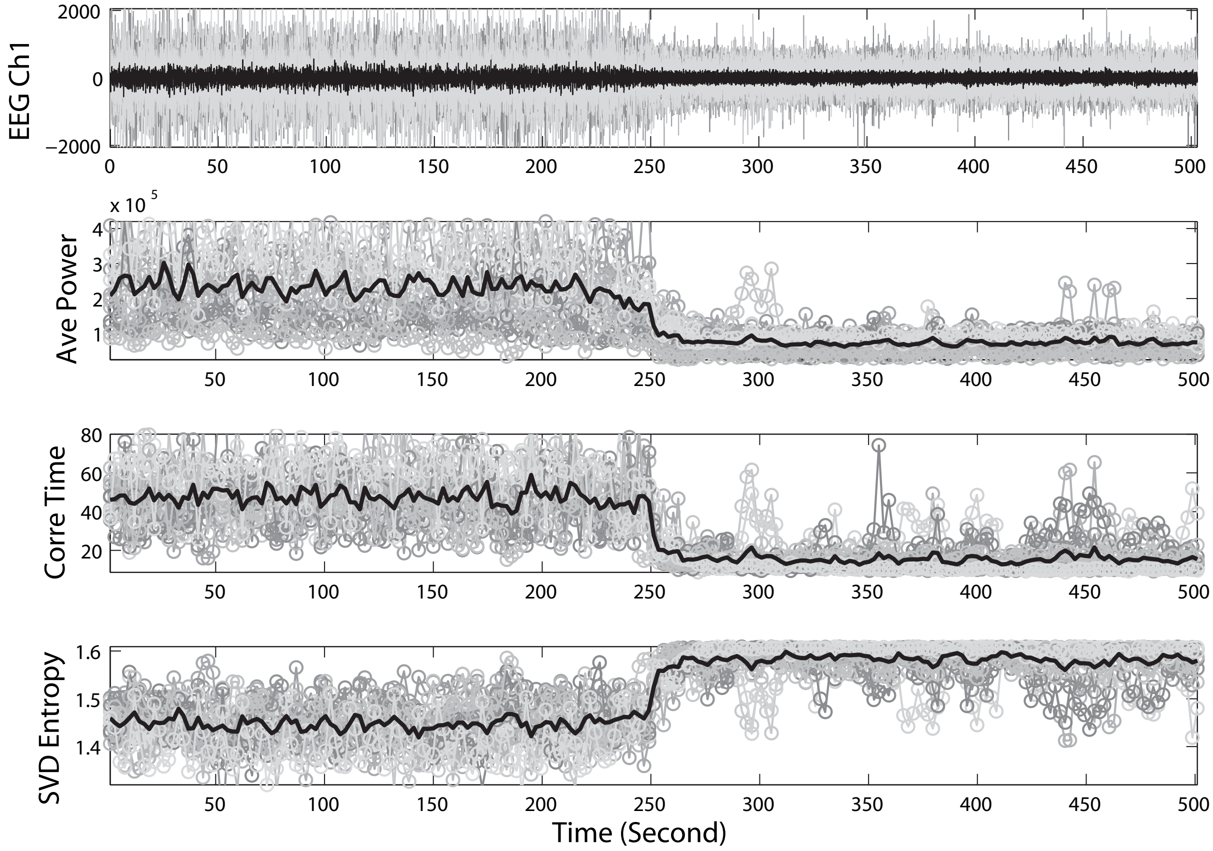
(a) Time–aligned SWS to REM Transitions for Ch1 (14 transitions)

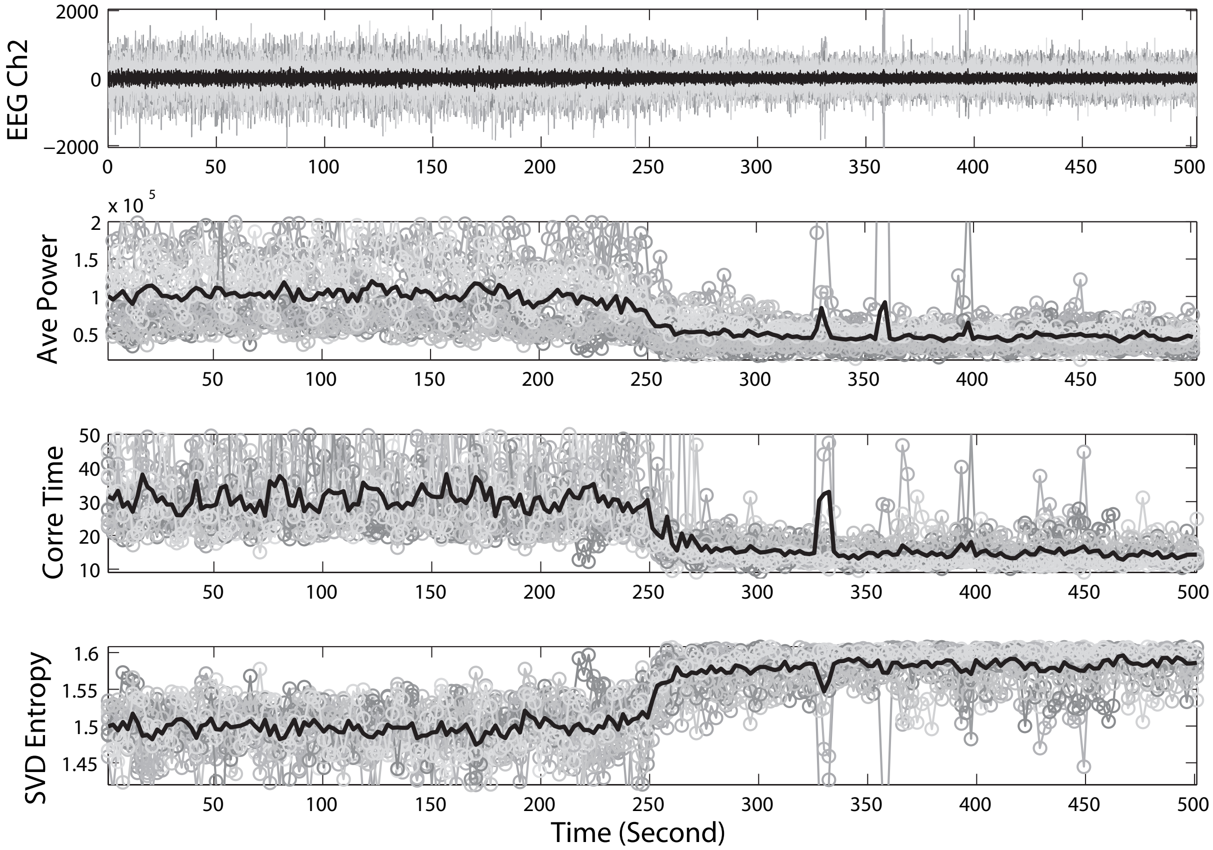
(b) Time–aligned SWS to REM Transitions for Ch2 (14 transitions)

Figure 3.8: Time-aligned SWS-to-REM transition analysis results for channel 1 (a) and channel 2 (b). For both (a) and (b), from top to bottom, the four subplots display the recorded 503-second ECoG signal, average power correlation time, and SVD entropy. The unit for the correlation time is ms.

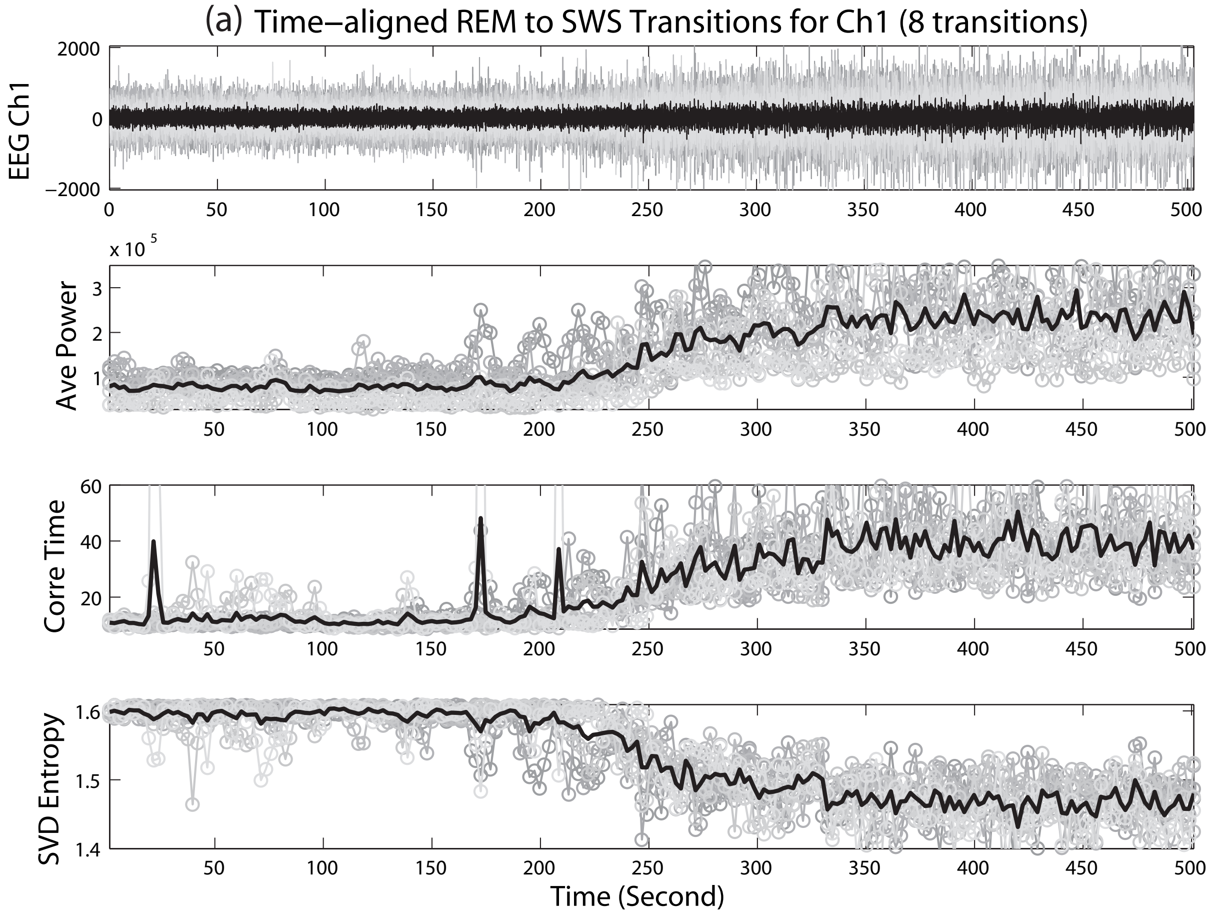
(a) Time–aligned REM to SWS Transitions for Ch1 (8 transitions)

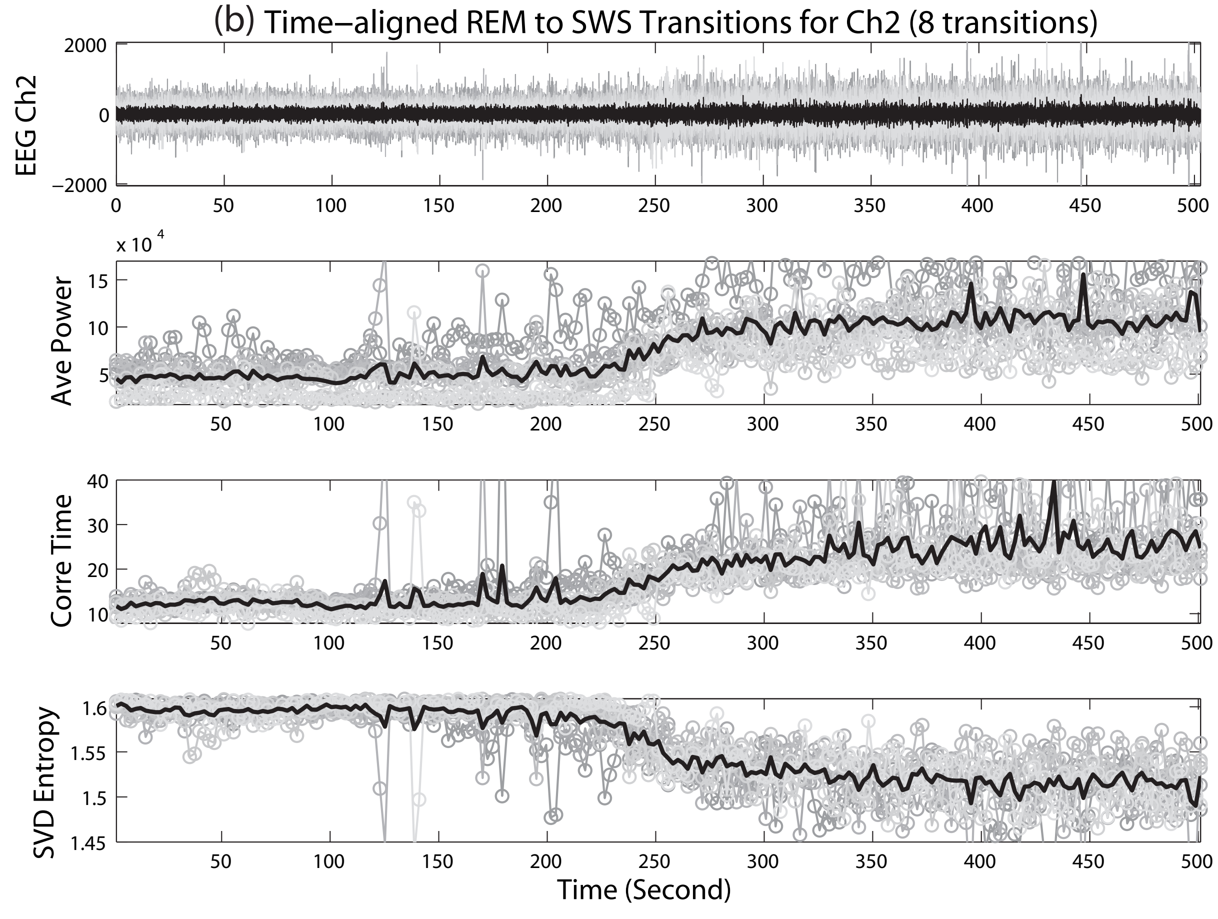
(b) Time–aligned REM to SWS Transitions for Ch2 (8 transitions)

Figure 3.9: Average power, correlation time, and SVD entropy analysis for time-aligned REM-to-SWS transition for channel 1 (a) and channel 2 (b). Top subplots in (a) and (b) gives the shifted raw ECoG time series.

Chapter 4

Maturational Changes in Fetal Sheep EEG

In this chapter, I investigate the emergence of the sleep cycle for the third-trimester fetal sheep by applying correlation time, SVD entropy, power spectrum, and spectral edge frequency (SEF) analyses. I utilize spectral analysis to classify fetal sheep development in the third trimester into four stages according to the frequency and amplitude changes in the power spectrum of the ECoG signal.

4.1 Sleep Cycle Maturation

4.1.1 Data Preparation

A total of 324 ECoG recordings were obtained from fifteen fetal sheep ranging from 95 to 144 days of gestational age (full-term is approximately 147 days). A longitudinal study was necessary to evaluate the development of the fetal sheep electrocortical activity. Ideally, the longitudinal measurement would be performed continuously on the same fetal sheep from early-term, prior to emergence of an organised sleep cycle, to late-term when ECoG is closely similar to new-born sheep. But for our fetal sheep study, several reasons made a continuous longitudinal study on a single fetal sheep impossible, such as fetus death before delivery because of infection (despite sterile steel technique used in the experiment), and measurement artifacts due to electrode failure. Because of these limitations, an approximated longitudinal study for the fetal sheep was realised by organising all 324 raw ECoG recordings from different fetal sheep according to gestational age. With the fifteen fetal sheep, a total of 37 gestational ages are available for our fetal ECoG maturational changes study. The 37 different gestational ages are day 95, 98, 100, 103–107, 109–113, 115–126, 129–133, 135–138, 140, 142, and 144. The largest gap is three days, which happened before day 103 and after day 126. For the sleep-cycle emergence period from gestational age 110 day to 125 day, only ECoG recordings from day 114 are missing. So the resolution in my sleep cycle maturation study will be roughly one day. For each gestational age, all available recording sessions, sometimes from several sheep, are grouped and analysed together. The detailed information, such as the number of recording sessions and the sheep IDs each recording session was recorded from on each gestational day, is listed in Table 3.1.

Correlation time, SVD entropy and 90% spectral-edge frequency (SEF) were computed for all artifact-free ECoG recording sessions in order to examine the maturational changes in the ECoG. All computations used 3-second epochs with 25% epoch overlap. Figures 4.1, 4.2, and 4.3

respectively illustrate the correlation time, SVD entropy, and SEF as a function of gestational age from day 95 to day 144. In all three figures, the analysis results from both channel-1 (black markers) and channel-2 (grey markers) are given.

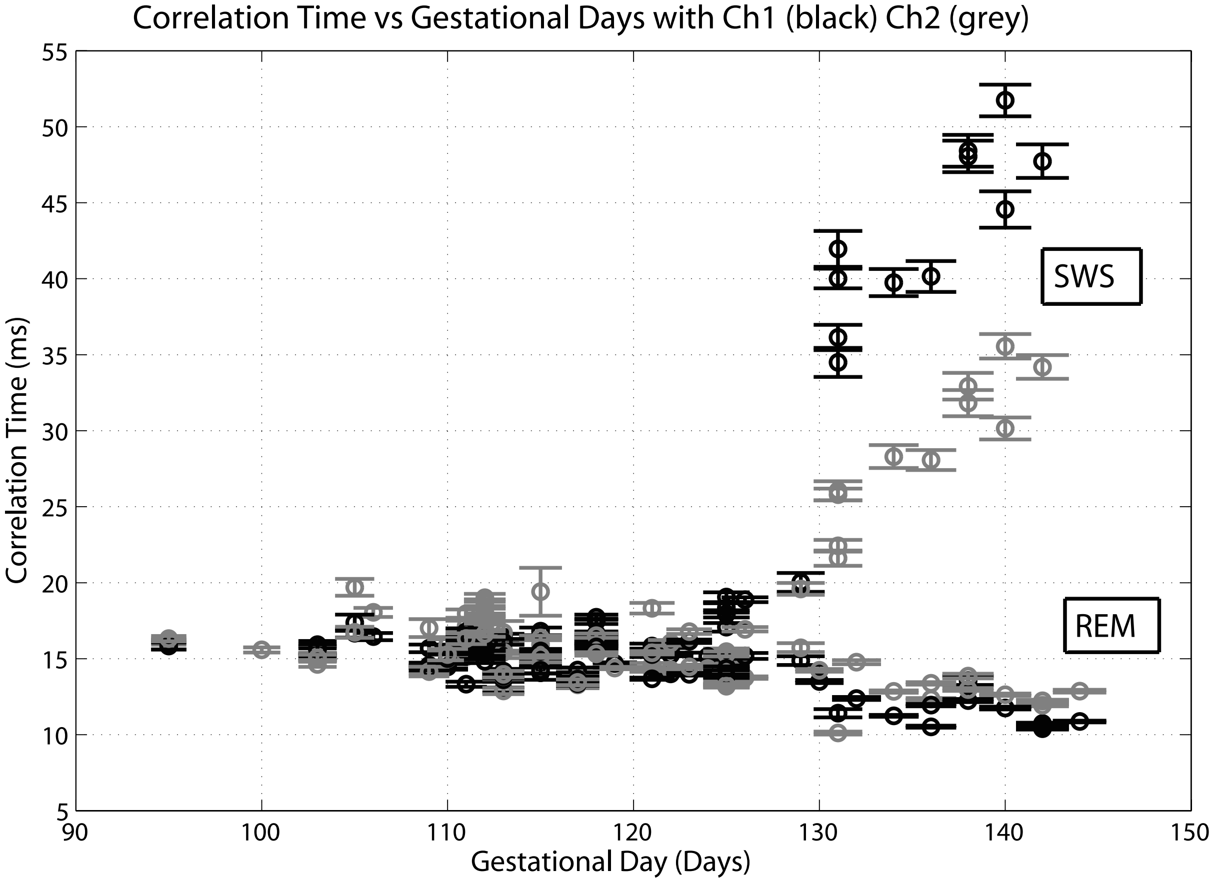

Figure 4.1: Developmental changes of the correlation time of the ECoG as a function of gestational age (from 95 to 144 days of gestation). The black and grey markers display the correlation time computed from ECoG time-series of channel-1 and channel-2 respectively. The uncertainty of the correlation time at each gestational day is indicated by the error bars calculated by the standard deviation of correlation time. The emergence of the two differentiated sleep state happens at about day 125. SWS sleep has larger correlation time, and REM sleep has smaller correlation time. After sleep cycle emergence until term, SWS exhibits a significant increase in correlation time while REM sleep state shows a small decrease.

4.1.2 Correlation Time

The correlation-time results in Fig. 4.1 show the onset of sleep cycling between SWS and REM states starts at approximately day 125. Prior to day 125, no differentiated brain states are observed. During this early gestational age, the correlation time remains approximately constant at about 15 ms for both channel-1 and channel-2 ECoG. After day 125, two brain states, identified as SWS and REM states, begin to emerge from the earlier single undifferentiated state. In Fig. 4.1, SWS is the sleep state with longer correlation times (top branch), and REM is the state with shorter correlation times (bottom branch). This identification is based on the fact that SWS is a more synchronised sleep state with slower frequency, while REM is a more desynchronised sleep state with higher oscillation frequency. Advancing gestational age leads to a progressive separation of the SWS and REM sleep states. The correlation time of SWS sleep state increases from 15 to 50 ms in channel-1 (and from 15 to 35 ms in channel-2) over the final 19 days of recordings. Over the same period, the correlation time for channel-1 voltage fluctuations in the REM state declines from 15 to 10 ms (15 to 13 ms in channel-2). When close to term, at 144 days of gestation, the separation of the correlation time between SWS and REM state is about 40 ms for channel-1 and about 22 ms for channel-2. Therefore, the ECoG signal from channel-1 is better than that from channel-2 when used for detecting differentiation of SWS and REM sleep states. The larger contrast between the SWS and REM sleep states computed from channel-1 recordings is possibly due to the cortical positioning of the electrode pairs.

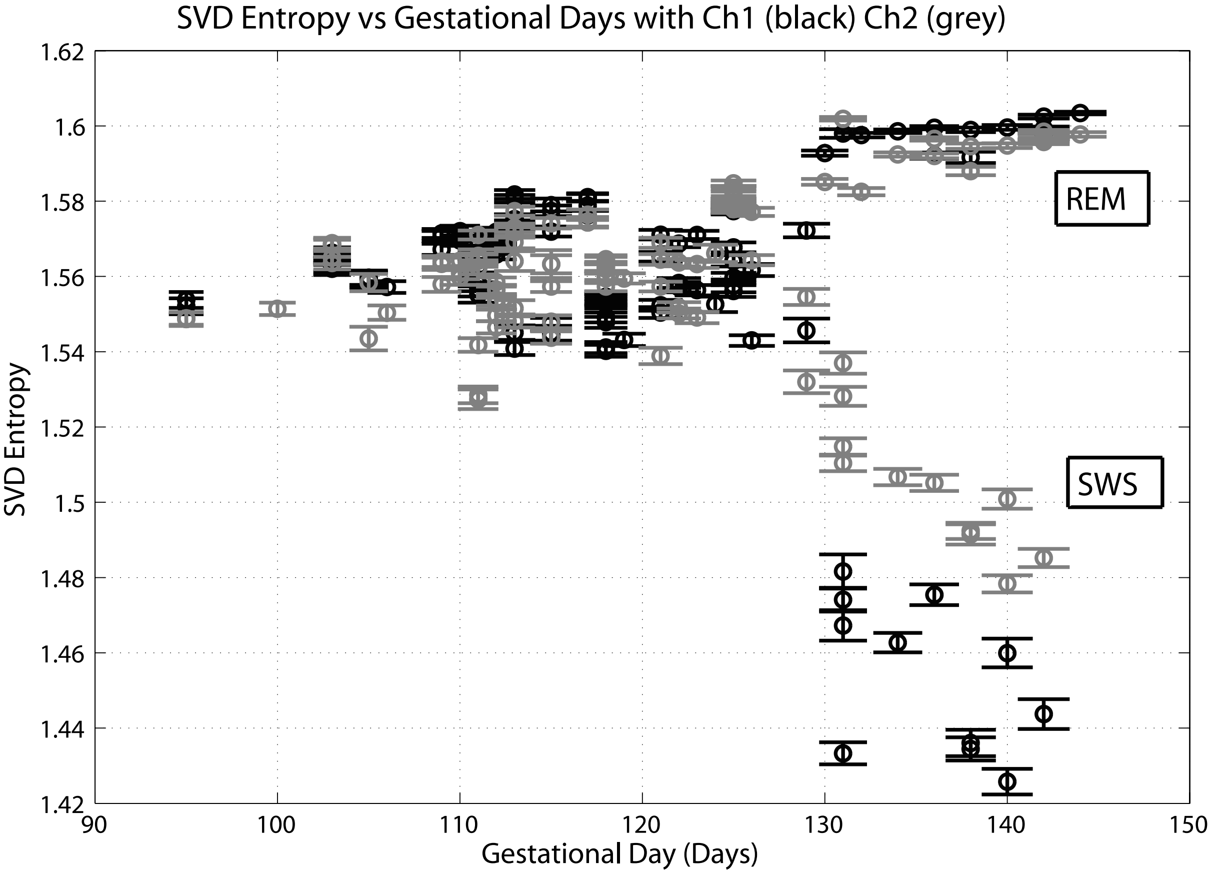

Figure 4.2: Developmental changes of the SVD entropy of the ECoG as a function of gestational age (from 95 to 144 days of gestation). Undifferentiated sleep state is seen before 125 day of gestation and after that, two well-defined sleep states, REM and SWS, are observed. REM sleep state shows larger SVD entropy (two top branches) and SWS sleep state has smaller SVD entropy (two bottom branches). Compared with REM sleep, SWS again displays much more significant development in SVD entropy during sleep cycle maturation after 125 days of gestation.

4.1.3 SVD Entropy

Figure 4.2 shows the SVD entropy changes with increasing gestational age. Consistent with the correlation-time analysis, SVD entropy shows no differentiation between sleep states before day 125. Prior to day 125, SVD entropy is about 1.56 for both channels. After day 125, REM entropy increases slightly, while SWS entropy decreases strongly, particularly in channel-1. Note that the direction of these trends in opposite to that for correlation time (a more correlated temporal fluctuation has less entropy, and vice versa). The pronounced maturational changes in SWS entropy and correlation time imply that electrocotical activity change in SWS state is much more significant than that in REM state.

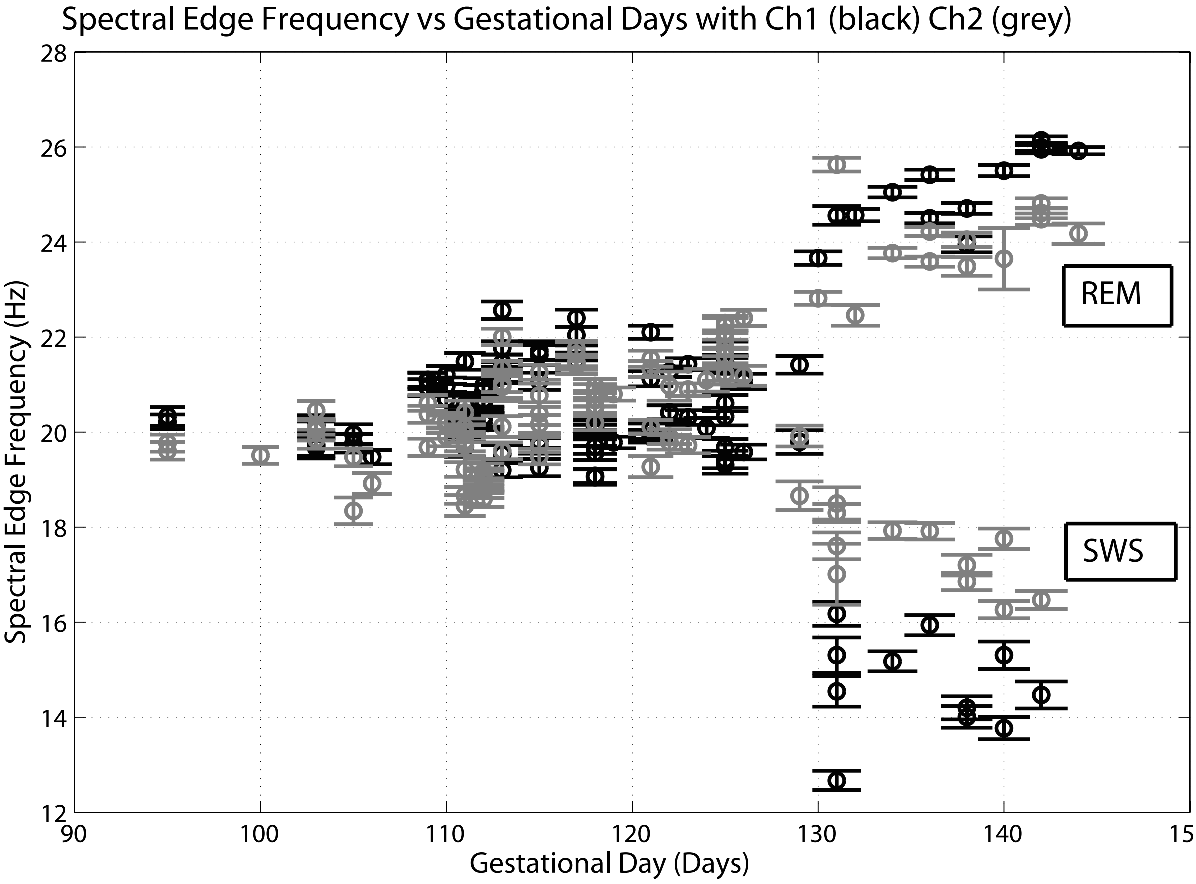

Figure 4.3: Developmental changes of the spectral edge frequency (90% SEF) of the ECoG as a function of gestational age (from 95 to 144 days of gestation). The sleep cycle emerges around day 125. Both REM and SWS states show significant spectral development during subsequent maturation with SWS and REM sleep states shifting to lower-frequencies and higher-frequencies respectively, increasing the edge-frequency contrast between the two states.

4.1.4 Spectral Edge Frequency

Figure 4.3 plots the 90% spectral-edge frequency (SEF) as a function of gestational age. Again, the spectral-edge frequency analysis indicates the beginning of stable SWS and REM sleep states is at 125 days of gestational age. As observed with correlation-time and SVD entropy analysis, there is only one brain state observed from day 95 to day 125. For this early undifferentiated sleep state, the SEF, i.e., the frequency below which 90% of the spectral energy resides, is approximately 20 Hz. After 125 days, two organised sleep states start to emerge. With increasing gestational age, the edge frequency for REM increases to 26 Hz in channel-1 (24 Hz in channel-2), while the edge frequency for SWS decreases to 14 Hz in channel-1 (16 Hz in channel-2). Compared with channel-2, the SEF results from channel-1 give better contrast between SWS and REM sleep states; this is consistent with the correlation time and SVD entropy analysis results.

Starting from day 125, the SEF of SWS decreases rapidly until day 131, then changes of SWS become slower and approach saturation. From 125 to 144 day of gestation, the REM state experiences continuous changes, and, unlike SWS sleep, after 131 day of gestation, the changes of SEF in REM sleep state are still significant.

In summary, all three measures—correlation time, SVD entropy, and SEF—confirm the emergence of cycling between two stable sleep states at about 125-day gestational age (dGA). With increasing gestational age, for SWS state, correlation time increases, and SVD entropy and SEF decrease. For REM state, correlation time decreases with age, while entropy and SEF increase. The increase in entropy and SEF indicates that the REM brain state has a broader spectrum with less synchronized voltage fluctuations. A progressively increasing contrast between the two established SWS and REM states with advancing gestational age is observed. Correlation time, SVD entropy and SEF are all effective in identifying the differentiation of SWS and REM sleep states in developing fetal sheep.

4.2 Power Spectrum Maturation

4.2.1 Stage Classification

In order to investigate the evolution of the frequency content of the ECoG signal over the third-trimester of the fetal sheep, the power spectrum of the ECoG time-series are analysed from 95 to 144 dGA. There are 324 ECoG recordings in total from 15 different fetal sheep. For each gestational age, there are typically several ECoG recordings from the same sheep or from different sheep. Therefore, for all of the files corresponding to a given gestational age, I computed the power spectrum of each ECoG time-series, then averaged over all of the spectra for that day. For each averaged spectrum, I identified the major resonances and recorded the frequency and amplitude of each resonance peak, comparing with those obtained at other gestational ages. If the fetal sheep is at the late-term stage with the two differentiated sleep states, I first classified the ECoG time-series into SWS or REM before computing the power spectra. In the end, an averaged power spectrum for SWS sleep state and an averaged power spectrum for REM sleep state are derived for each gestation age.

Figure 4.4 gives an example illustrating how the averaged power spectrum at each gestational age is acquired. The gestational age is 121 days in this example, and there are a total of 8 ECoG recordings at this gestational age: three from sheep 55, and five from sheep 188. Each ECoG time-series is first categorized into either SWS or REM sleep. For example, in the top-most time-series, the first 150-second epoch belongs to SWS, the last 43-second belongs to REM sleep, and in between, there is 10-second SWS-to-REM transition. I found that for periods of transition, the spectrum contains both SWS and REM components, so I excluded such transitions from further spectral analysis.

Another reason for excluding time-series is the presence of artifacts—we need to ensure the ECoG is artifact-free before starting spectral analysis on it. The second recording from the top shows some artifacts in its ECoG time-series, so I excluded it from further analysis. In Fig. 4.4, all the discarded parts of the ECoG time-series are plotted out with grey and the retained parts in black. Each of the retained ECoG recordings was classified into SWS or REM, and labelled appropriately. As seen in Fig. 4.4, the power spectrum of the entire 503-second ECoG time-series

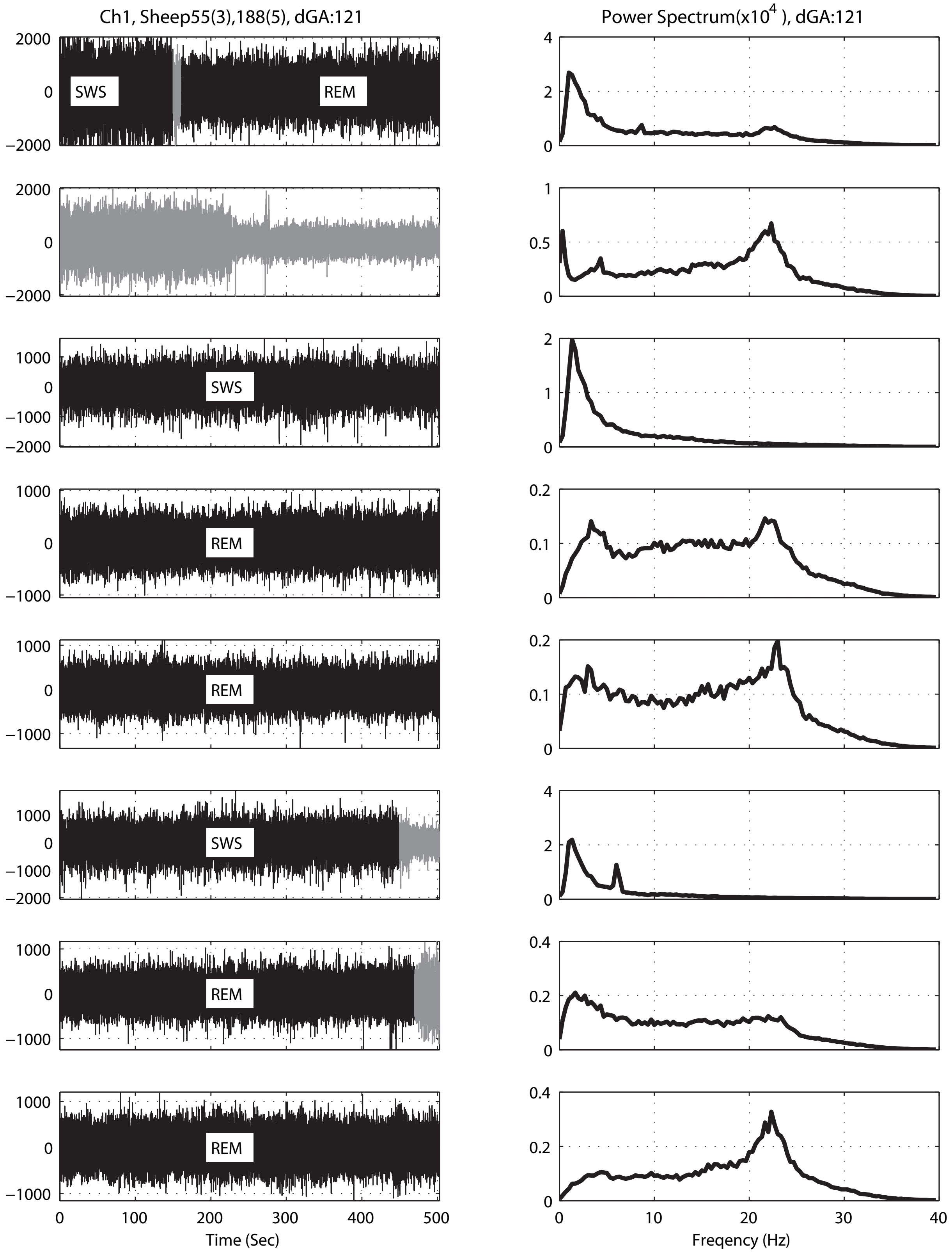

Figure 4.4: Example of SWS and REM sleep-state classification for ECoG time-series at gestational age of 121 day. On the left column, the top three ECoG time series belong to sheep 55 and the bottom five ECoG time-series are from sheep 188. The grey colour marks the part of the ECoG recordings excluded from further power spectral analysis. Both SWS and REM sleep states are plotted out in black. The right column gives the power spectrum analysis results from the entire 503-second ECoG time-series on the left column. This power spectrum is not used for further analysis or study and is used strictly as an auxilliary tool to classify the SWS and REM sleep states.

on the left column are plotted out on the right column. This diagnostic spectrum is helpful for preliminary identification of SWS and REM sleep states.

After the averaged power spectra were attained for each gestational age, I looked for maturational variations of the major resonances focusing on developmental alterations in the frequency and amplitude of the resonances. After close inspection of the spectra for the fetal sheep ECoG records, I decided to subdivide the 50 days of the third trimester into four distinct developmental stages:

Stage I 95–111 dGA (undifferentiated sleep with 15-Hz spindles)
 Three distinct resonances $f^{\mathrm{I}}_{1,2,3} = 2\text{–}3, 6\text{–}8, 15\text{–}16$ Hz
Stage II 109–123 dGA (undifferentiated sleep without spindles)
 Two distinct resonances $f^{\mathrm{II}}_{1,2} = 2\text{–}4, 9\text{–}10$ Hz
Stage III 124–129 dGA (emergence of differentiated sleep states)
 Two SWS resonances $f^{\mathrm{III}}_{1,2}(\mathrm{SWS}) = 2, 10$ Hz
 Two REM resonaces $f^{\mathrm{III}}_{1,2}(\mathrm{REM}) = 3\text{–}4, 11$ Hz
Stage IV 130–144 dGA (maturation of sleep states)
 One SWS resonance $f^{\mathrm{IV}}_{1}(\mathrm{SWS}) = 2$ Hz
 Two REM resonances $f^{\mathrm{IV}}_{1,2}(\mathrm{REM}) = 3\text{–}4, 21\text{–}25$ Hz

4.2.2 Power Spectrum

Early in the third trimester, the ECoG spectra typically display three resonance peaks near 2, 6, and 15 Hz, but, by about day 110, the 15-Hz component (which appears as ripple in the early time-series) disappears. I classify early third-trimester ECoG as stage I (95–111 dGA) if it shows 15-Hz oscillations, or stage II (109–123 dGA) if it does not. The three-day overlap between stages probably arises from natural fetus-to-fetus variations in rates of development.

Figure 4.5 displays the frequency changes of the major resonances over the third-trimester of the fetal sheep. The framed inserts show representative power spectra for each stage; each insert is labelled with its stage (I ... IV) and sleep state. For example, the spectrum for REM sleep state at stage III is labelled as “III (REM)”. The peaks of the major resonances are marked with circles. The frequency and amplitude of significant spectral maxima at each gestational age are summarised in Figs 4.5 and 4.6 respectively.

During stages I and II, no differentiated sleep state can be discerned in fetal sheep. From stage III, two differentiated sleep states, SWS and REM, emerge, so I investigate SWS and REM states independently about their main resonances at stages III and IV. In Fig. 4.5, REM sleep states are plotted in grey and SWS in black.

In stage III, SWS and REM sleep both have two major resonances in their power spectra, but SWS sleep has substantially more low-frequency activity as indicated by its resonance at lower frequency having larger amplitude. Oppositely, during REM sleep, the resonance at higher frequency displays higher amplitude, implying that most REM activity resides in the higher frequency band. The two major resonances of SWS sleep, denoted as $f^{\mathrm{III}}_{1}(\mathrm{SWS})$ and $f^{\mathrm{III}}_{2}(\mathrm{SWS})$ in the figure, locate at about 2 Hz and 10 Hz, while the two major resonances of REM sleep, $f^{\mathrm{III}}_{1}(\mathrm{REM})$ and $f^{\mathrm{III}}_{2}(\mathrm{REM})$, occur at about 3–4 Hz and 11 Hz respectively.

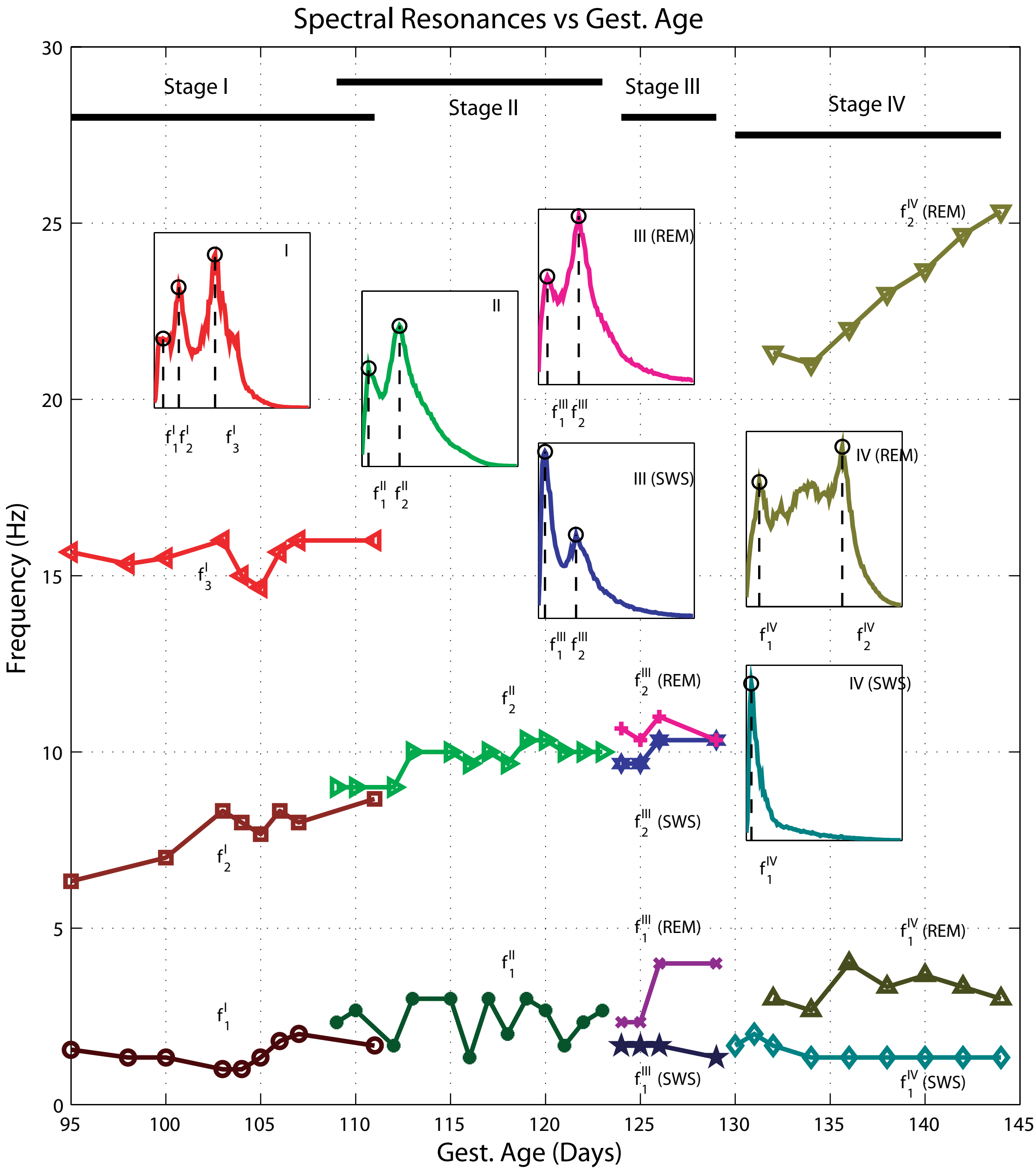

Figure 4.5: Frequency evolution of the power spectrum over the third trimester of the fetal sheep. Based on the frequency variation of the power spectrum, the third trimester of the fetal sheep is divided into four stages I … IV as indicated with the thick lines at the top of the figure. A typical power spectrum at each stage is illustrated in the subplots with stage number denoted at the top right corner. In each spectrum, the peak of the major resonances is marked with a circle. A vertical dashed line extending from the circle downward is used for demonstrating the reading of the corresponding frequency. For frequency denotation, the superscript gives the stage and subscript gives the frequency index. Starting from stage III, two differentiated sleep states, SWS and REM, are detected. In stages III and IV, the frequency and the power spectrum of the REM sleep state are plotted in magenta and yellow respectively, and that of the SWS state in blue and cyan. For the same sleep state, the higher frequency of the resonance, the lighter colour of the line, i.e., for SWS state of stage III, $f_2^{\mathrm{III}}(\mathrm{SWS}) > f_1^{\mathrm{III}}(\mathrm{SWS})$, hence, $f_1^{\mathrm{III}}(\mathrm{SWS})$ is plotted as darker blue and $f_2^{\mathrm{III}}(\mathrm{SWS})$ as lighter blue. This applies to stage I and II too. At stage IV, the resonance with higher frequency during the REM sleep state shifts to a significantly higher frequency value rapidly, see lighter yellow line labelled with $f_2^{\mathrm{IV}}(\mathrm{REM})$.

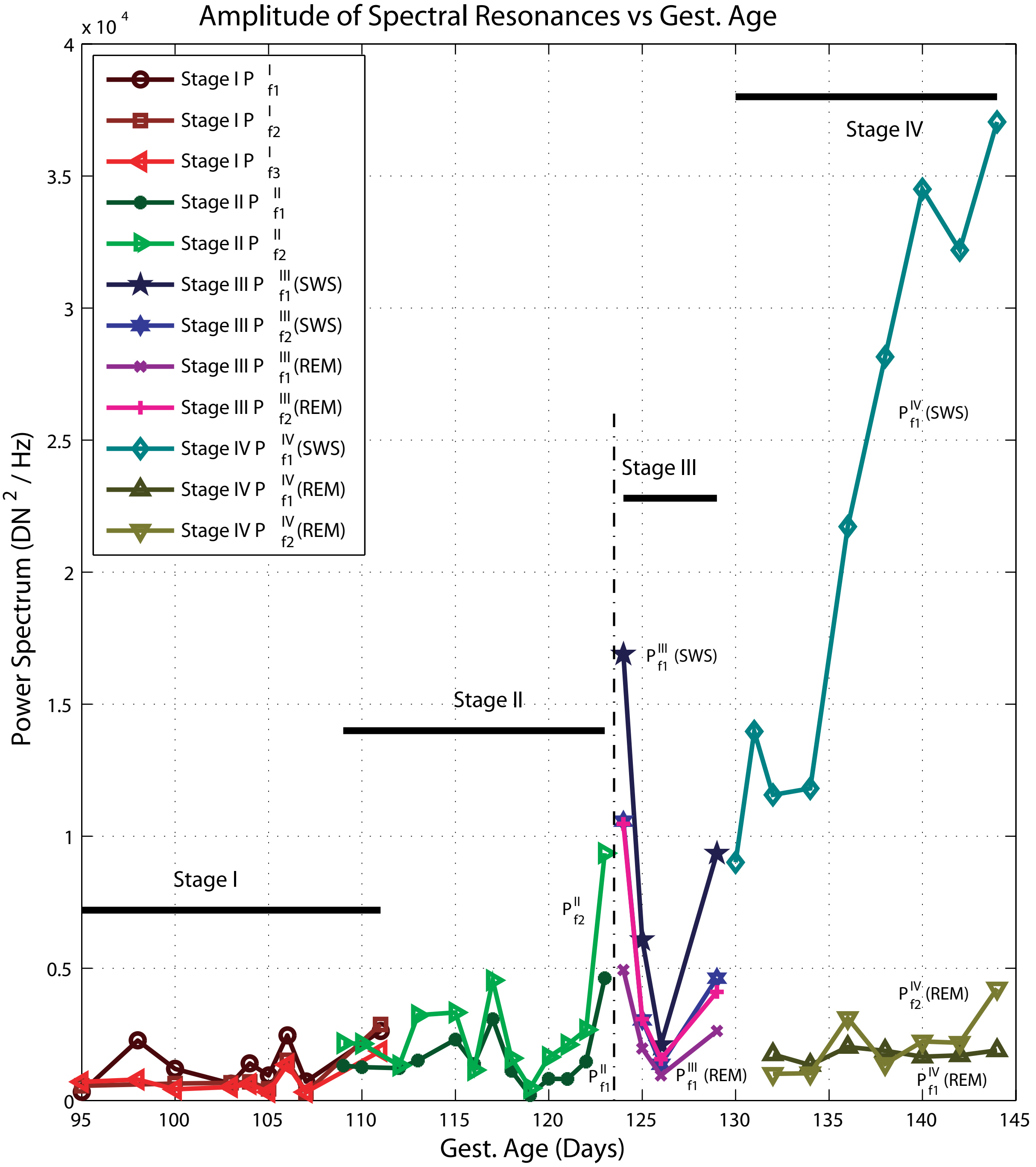

Figure 4.6: Amplitude of the resonance of power spectrum as a function of gestational age. The legend and colour used in this figure is the same as that used in Fig. 4.5. The temporal extent of each stage is indicated with a thick line. In the denotation of the amplitude of the resonance, the subscript gives the corresponding frequency and the superscript gives the stage. A pronounced surge in power appears just before the SWS and REM sleep-state differentiation, reaching maximum at 124 dGA. During stage IV, the amplitude of the sole major resonance at SWS sleep undergoes substantial growth, labelled with $P^{\mathrm{IV}}_{f_1}$(SWS) in the figure.

At stage IV, SWS sleep has only one major resonance, $f_1^{\mathrm{IV}}(\mathrm{SWS}) \approx 2$ Hz. Stage IV REM sleep shows two major resonances: the lower frequency $f_1^{\mathrm{IV}}(\mathrm{REM}) \approx 3$–$4$ Hz remains constant, while the frequency of the upper resonance, $f_2^{\mathrm{IV}}(\mathrm{REM})$, experiences a dramatic increase from 21 Hz to more than 25 Hz over 14 days.

The amplitude variations of the spectral peaks from stage I to IV are shown in Fig. 4.6. At stage I, the amplitude for all three resonances are very similar and roughly $2{\times}10^5$ $\mathrm{DN}^2/\mathrm{Hz}$.

For stage II (109–122 dGA), the amplitude of the two resonances are close, with a largest difference of $4{\times}10^5$ $\mathrm{DN}^2/\mathrm{Hz}$ at 113 dGA. At day 123, both amplitudes start to increase significantly, with $P_{f_2}^{\mathrm{II}}$ rising to $2.3{\times}10^6$ $\mathrm{DN}^2/\mathrm{Hz}$ and $P_{f_1}^{\mathrm{II}}$to $1.1{\times}10^6$ $\mathrm{DN}^2/\mathrm{Hz}$.

At stage III, the amplitude of all resonances first decrease to a minimum and than start to rise again. Throughout stage III, the lower-frequency resonance of SWS dominates: $P_{f_1}^{\mathrm{III}}(\mathrm{SWS}) > P_{f_2}^{\mathrm{III}}(\mathrm{SWS})$, while the reverse is true of REM: $P_{f_1}^{\mathrm{III}}(\mathrm{REM}) < P_{f_2}^{\mathrm{III}}(\mathrm{REM})$. Comparing SWS and REM spectra, I find $P_{f_1}^{\mathrm{III}}(\mathrm{SWS}) > P_{f_2}^{\mathrm{III}}(\mathrm{SWS,REM}) > P_{f_1}^{\mathrm{III}}(\mathrm{REM})$ with the amplitudes of the respective f_2 resonances being rather similar, $P_{f_2}^{\mathrm{III}}(\mathrm{SWS}) \approx P_{f_2}^{\mathrm{III}}(\mathrm{REM})$.

At stage IV, the amplitude of the two resonances of REM sleep, $P_{f_1}^{\mathrm{IV}}(\mathrm{REM})$ and $P_{f_2}^{\mathrm{IV}}(\mathrm{REM})$, are similar at about $5{\times}10^5$ $\mathrm{DN}^2/\mathrm{Hz}$. The amplitude of the only major resonance of SWS sleep, $P_{f_1}^{\mathrm{IV}}(\mathrm{SWS})$, grows sharply from $2.3{\times}10^6$ to $9.3{\times}10^6$ $\mathrm{DN}^2/\mathrm{Hz}$.

Comparing the four stages, stage I is evidently very different to other stages and is characterised by a unique 15–16 Hz spindle-like oscillation that is not found later in the trimester.

Though the two differentiated sleep states, SWS and REM, exist during entire period of stage III, it is during stage IV that the two sleep states undergo most substantial changes to reach their respective maturation. For SWS sleep, the maturation is mainly on the amplitude aspect: there is a four-fold increase in the amplitude for SWS sleep during stage IV. For REM sleep, the maturation is primarily marked by the enlarging frequency band (or frequency separation of the two resonances) with the higher-frequency resonance shifting rapidly to even higher frequencies.

Another interesting finding from my spectral analysis is that a power surge occurs just before differentiation of the SWS and REM sleep states. The surge starts at 122 day of gestation, reaches peak at day 124 and drops back to normal at day 126. This is also seen the average power plot of Fig. 4.8. To us, the physiological mechanism of this power surge is not clear yet, but is suggestive of the fluctuation divergences seen on approach to a phase transition.

The power spectrum analysis result is also plotted out as a stem plot in Fig. 4.7. In this three-dimensional plot, the x-axis (front axis) gives the gestational age of the fetal sheep, the y-axis (left-hand axis) gives the frequency of the major resonances, and the vertical z-axis shows the amplitude of the resonances. This three-dimensional graph nicely demonstrates the frequency and amplitude development of the resonances during the third trimester of the fetal sheep at the same time in a single graph. In this plot, the taller the stem, the larger amplitude of the corresponding resonance. We can easily identify the dramatic amplitude increase at low frequency when the fetal sheep approaches term. A smaller amplitude increase can also be observed for the resonances just before emergence of SWS/REM states at 125 dGA. And at the beginning of the third trimester, the 15-Hz oscillation initially present in the power spectrum, has disappeared by about day 112.

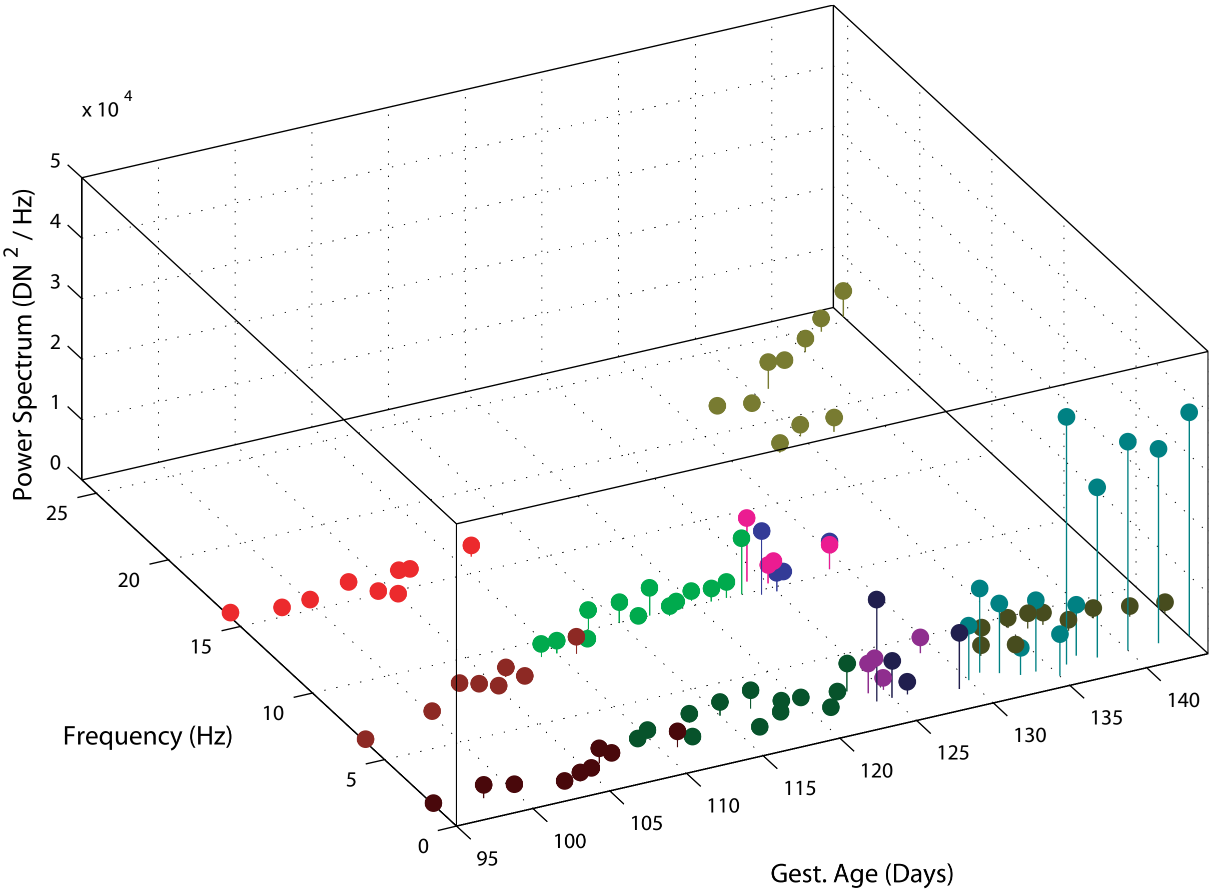

Figure 4.7: Three-dimensional stem-plot of the power-spectral amplitude for fetal sheep ECoG plotted as a function of gestational age (95–144 dGA, front axis) and resonant frequency (left-hand axis). A 15-Hz oscillation is seen during the early stage of the third trimester, and disappears at 112 dGA. When the fetal sheep approaches term, the tallest stems, which imply largest amplitude of the major resonances, are found at a lower frequency, identified as SWS sleep. For the same period of time, a substantial frequency growth is seen in a higher-frequency resonance, which is identified as REM sleep. The colour scheme used in this figure is the same as that used in Fig. 4.5 and 4.6.

Overall, there are two frequencies that are continuously present in the resonances during the entire third trimester of the fetal sheep. The lower frequency is at about 2 Hz and the higher frequency is at about 10 Hz. For the lower-frequency resonance, when the fetus approaches the term, its amplitude increases significantly and becomes SWS as described above. For the higher-frequency resonance, the frequency is at roughly 10 Hz until gestational age of 130 day. After day 130, this frequency suddenly increases to about 20 Hz at day 131, and continuously increases to reach 25 Hz at day 144. This resonance with upper frequency increasing was identified as REM sleep state as described before.

4.2.3 Average Power

In addition to tracking changes in spectral distribution during third-trimester maturation, I also investigated the average power in the raw ECoG time-series. For each ECoG recording, I computed the mean fluctuation power, then averaged these mean power values across all ECoG recordings available for each gestational age, taking the standard deviation of the means as the uncertainty estimate.

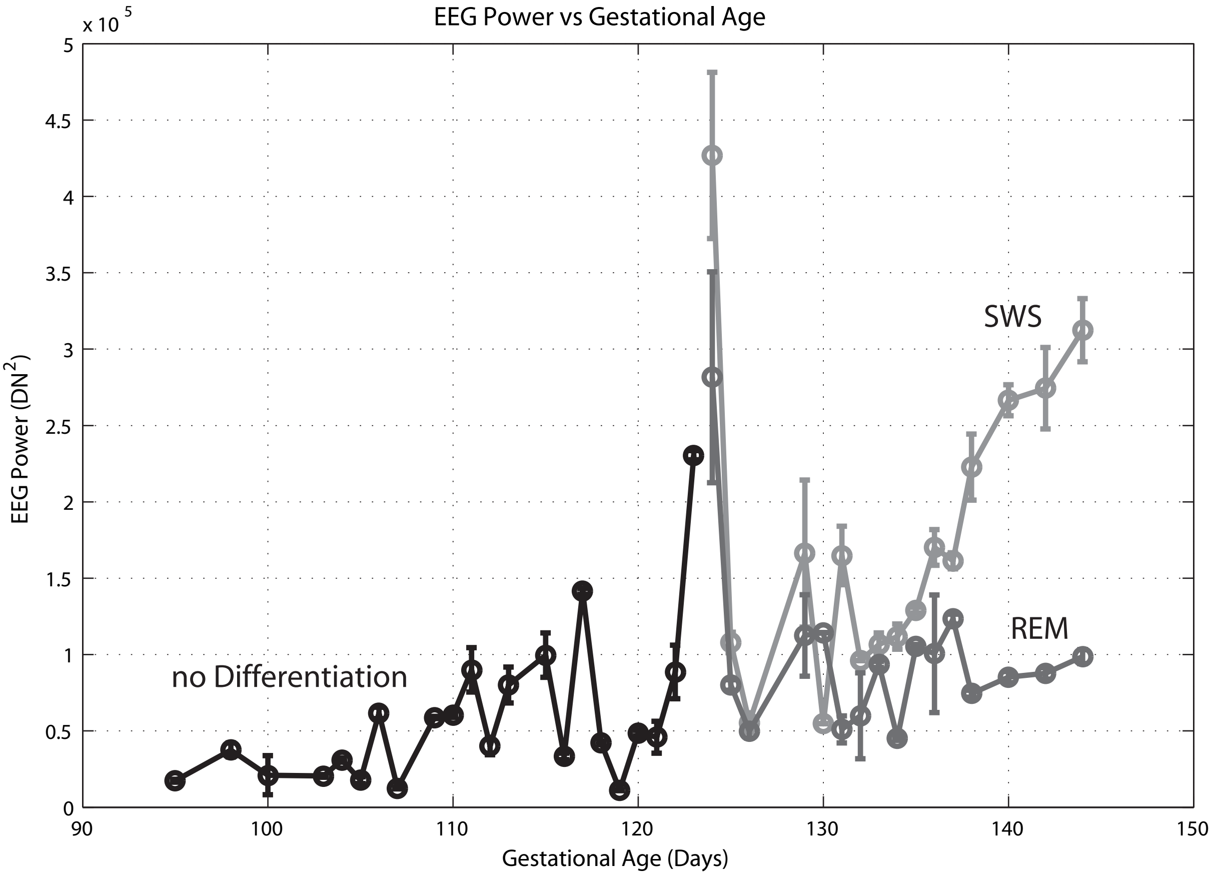

Figure 4.8: Variations of average power during the third trimester of fetal sheep. The fetal sheep gestational age ranges from 95 to 144 dGA. The early non-differentiated sleep state is plotted as black solid line. Starting from 124 day of gestation, the average power for SWS and REM sleep states are plotted out in different colour. Lighter grey solid line and darker grey solid line give the average power of the SWS and REM sleep states respectively from 124 to 144 dGA. The average power shows a dramatic power surge just before the two sleep states (SWS and REM) emerge, peaking at day 124. After the power surge, the average power of the SWS sleep state experiences substantial increase. At 144 day of gestation, the average ECoG fluctuation power for SWS is about three times larger than that of REM sleep.

The results are plotted in Fig. 4.8. The general trend of a gradual increase in ECoG power with age is interrupted with a dramatic lambda-shaped surge in power at about day 124—this event corresponds to the spectral-reonance maximum seen in Fig. 4.6. The surge collapses at day 126, and is replaced by two separate growth curves: one for SWS showing very strong power increase, and another for REM showing more gradual growth. By day 144, SWS fluctuation power has grown to be about three times larger than for REM fluctuation power.

4.3 Summary of Maturational Changes

By analysing correlation time, SVD entropy, and spectral edge frequency (SEF) for fetal sheep aged from 95 to 144 dGA, we detected that the emergence of distinct SWS and REM sleep states occurs at about day 125. Thereafter, both SWS and REM sleep states experience significant maturation until birth. From the power spectrum analysis, we can further divide this sleep maturation process into four stages and each stage has distinct spectral structure.

With the aim of modelling the maturation process of the fetus sleep, I investigated two mathematical models. The first of these is the J. J. Wright Cortical Column Field (`ccf`) model, which is analysed in some detail in the next chapter.

Chapter 5

Cortical Column Field Model

The cortical column field (`ccf`) model is a continuum EEG model developed by Prof J. J. Wright and his group in the Liggins Institute, and Department of Psychological Medicine at the University of Auckland, New Zealand. The `ccf` model can be used to simulate the electrocorticogram of the cat and human, as has been reported by Wright in a series of papers [124, 125, 128].

Recently, Wright [127] applied the `ccf` model to study the generation and control of gamma rhythms at both centimetric and macrocolumnar scales and their interaction. Freeman and colleagues [37, 39, 40] believe that there exist thermodynamic-like phase transitions in the generation and propagation of gamma activity in the cortex. Wright [126] used his continuum model to confirm Freeman's experimental and theoretical findings on gamma synchrony, phase transition, phase cones, and null spikes at the two spatial scales. I explored the `ccf` model at the centimetric scale, and investigated the possibility of its application to the simulation of fetal sheep ECoG.

5.1 State Equations for `ccf`

5.1.1 Cortical Structure Modelling

The cerebral cortex of the brain is modelled as a single-layered square array of 20×20 neural population "elements" in the cortical columnar field model. Figure 5.1 shows the connectivity for a representative matrix of 5×5 elements. Each element includes one excitatory neuron group (labelled "e") and one inhibitory neuron group ("i"). Figure 5.1 also displays the axo-synaptic linkage of excitatory and inhibitory neuron groups within each element. One row of three elements is shaded and plotted at the lower part of the figure. Nonspecific flux (NSF) is assumed to originate from external sources such as the reticular formation, and is applied exclusively to the excitatory neuron groups, while transcortical flux (TCF) is delivered uniformally to both excitatory and inhibitory neuron groups as indicated by the figure.

5.1.2 State Variables

The cortical columnar field (`ccf`) model [124,125,127] is characterised by three pairs of state variables: average membrane potentials, $V_{p,q}(\mathbf{r}, t)$, pulse densities, $Q_{p,q}(\mathbf{r}, t)$, and afferent (incoming) synaptic flux $\varphi_{p,q}(\mathbf{r}, t)$ generated by pulse sources and transmitted along axons to the synaptic receptors. The subscript p or q in these variables represents either excitatory (e) or inhibitory (i) neural populations. Subscript qp indicates synaptic connections *from* neuron population p *to* neuron population q (i.e., a right-to-left flow of action $q \leftarrow p$).

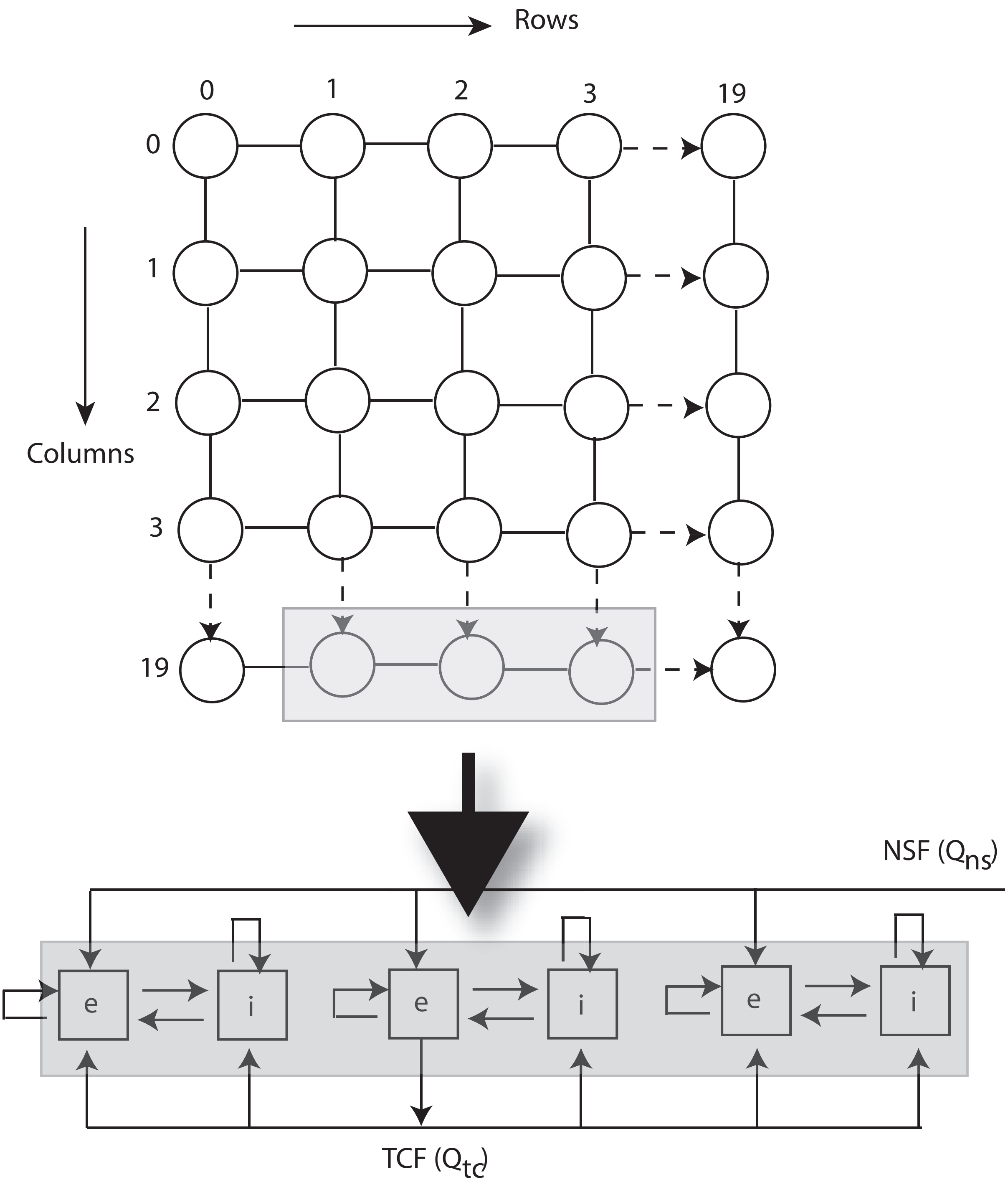

Figure 5.1: Schematic of connectivity in the `ccf` model simulation. The top figure gives a representative cortical structure of grid of elements. The `ccf` model uses a 20×20 grid with cortical rows and columns numbered 0 to 19 left-to-right, and top-to-bottom respectively. The bottom figure shows a portion of one row of the square array. Boxes e are excitatory neuron groups and boxes i are inhibitory neuron group. Nonspecific flux (NSF) comes from reticular formation and acts upon the excitatory neuron groups only. Transcortical flux (TCF) is the lateral spread of excitatory signal to both excitatory and inhibitory neuron groups.

$V_{p,q}(\mathbf{r}, t)$ defines the local field potential, in volts, of neuron populations of type p or q at location $\mathbf{r}$ and at time t. In our work, we assume standard scalp EEG and cortical local field potential (LFP) are equivalent, and that the local field potential measures the electrical activity of the excitatory neural population, i.e., LFP $\equiv V_e(t)$.

$Q_{p,q}(\mathbf{r},t)$ gives the instantaneous point pulse rate (number of spikes per second) or pulse densities of neuron populations of type p or type q located at position of cortical surface ($\mathbf{r}$) at time t. $Q_{p,q}$ has unit s^{-1}. $\varphi_{p,q}(\mathbf{r},t)$ describes the synaptic flux densities and has unit s^{-1}.

The detailed definition of the three pairs of state variables are given in Table 5.1. See Tables 5.1 for a full list of symbol definitions.

Table 5.1: `ccf` Model State Variables

State Variable	**Description**	**(units)**
V_e	Local space-average dendritic potential, excitatory neurons	(V)
V_i	Local space-average dendritic potential, inhibitory neurons	(V)
φ_e	Afferent excitatory pulse density	(s^{-1})
φ_i	Afferent inhibitory pulse density	(s^{-1})
Q_e	Local excitatory pulse density	(s^{-1})
Q_i	Local inhibitory pulse density	(s^{-1})

5.1.3 Afferent Synaptic Flux

The synaptic flux φ_p is generated by pulses Q_p arising at many cortical points $\mathbf{r}'$ and travelling along the axons at velocity ν_p to reach cortical point $\mathbf{r}$ after a delay. Therefore, for a cortical point $\mathbf{r}$, the afferent synaptic flux density $\varphi_p(\mathbf{r},t)$ from all other points $\mathbf{r}'$ are given by equation:

$$\varphi_p(\mathbf{r},t) \;=\; \int_\Omega f\left(\mathbf{r},\mathbf{r}'\right) Q_p\left(\mathbf{r}',t-\left|\mathbf{r}-\mathbf{r}'\right|/\nu_p\right) d^2\mathbf{r}' \tag{5.1}$$

$Q_p(\mathbf{r}',t)$ is the mean pulse density or pulse rates of neurons of type p at position $\mathbf{r}'$. ν_p is the average velocity of axonal conduction. $f(\mathbf{r},\mathbf{r}')$ is the axonal distribution function at cortical point $\mathbf{r}$ and is usually approximated as a 2-dimensional Gaussian distribution [18],

$$f\left(\mathbf{r},\mathbf{r}'\right) \;=\; \frac{1}{2\pi\gamma^2}\exp\left[\frac{-\left|\mathbf{r}-\mathbf{r}'\right|^2}{2\gamma^2}\right] \tag{5.2}$$

where γ is the standard deviation of axonal range. Eq. (5.2) can be used to describe both short-range and long-range connections. The short-range connections include both intracortical excitatory and inhibitory connections, while the long-range connections are exclusively from excitatory sources.

5.1.4 Synaptic Receptor Dynamics

Ion channels regulate the flow of ions across the cell membrane of the neurons. Mass-action interaction of neurotransmitters and receptors modulates the opening/closing of ion channels, controlling ionic flow into the post-synaptic dendritic membrane. Neurotransmitter receptors are able to adapt their properties to continuing changing inputs. The three major neurotransmitter receptors are NMDA, AMPA, GABA$_\mathrm{A}$. The dynamics of receptor adaptation to afferent stimulus is included in the `ccf` model.

The afferent synaptic flux, φ_p, gives rise to a change in membrane polarisation. The postsynaptic impact of φ_p is modified by the ion channel and this process can be approximated with a steady state equation, Eq. (5.3).

$$J^{[R]}(\varphi_p) \;=\; \exp\left[-\lambda^{[R]}\varphi_p\right]\varphi_p \tag{5.3}$$

where [R] is a label standing for one of NMDA, AMPA, or GABA$_{\mathrm{A}}$.

The response of neurotransmitter receptor to a brief afferent stimulus is described by $\Phi^{[R]}(\tau)$ as given in Eq. (5.4),

$$\Phi^{[R]}(\tau) \;=\; \left[\sum_n B_n^{[R]}/\beta_n^{[R]} - \sum_m A_m^{[R]}/\alpha_m^{[R]}\right]^{-1} \times \left[\sum_n B_n^{[R]}\exp\left[-\beta_n^{[R]}\tau\right] - \sum_m A_m^{[R]}\exp\left[-\alpha_m^{[R]}\tau\right]\right] \tag{5.4}$$

In Eq. (5.4), parameters $\lambda^{[R]}, B_n^{[R]}, A_m^{[R]}, \beta_n^{[R]}, \alpha_m^{[R]}$, $m, n = 1, 2, 3$, are derived from three mass-action transmitter/receptor models [32, 48, 62] and values used in the simulation are given in Table 5.2.

Table 5.2: Receptor adaptation for `ccf` model [32, 48, 62]

Parameter	**Description**	**Value (units)**
Receptor adaptation		
$\lambda^{[R]}$	Receptor adaptation pulse-efficacy decay constants	[AMPA] = 0.012 [NMDA] = 0.037 [GABA$_{\mathrm{a}}$] = 0.005 (s)
$B_n^{[R]}$	Receptor onset coefficients	[AMPA]$_1$ = 1.0 [NMDA]$_1$ = 1.0 [GABA$_{\mathrm{a}}$]$_1$ = 1.0 (dimensionless)
$A_n^{[R]}$	Receptor offset coefficients	[AMPA]$_1$ = 0.0004 [AMPA]$_2$ = 0.6339 [AMPA]$_3$ = 0.3657 [NMDA]$_1$ = 0.298 [NMDA]$_2$ = 0.702 [GABA]$_1$ = 0.0060 [GABA]$_2$ = 0.9936 (dimesionless)
$\beta_n^{[R]}$	Receptor onset reciprocal time-constants	[AMPA]$_1$ = 760.0 [NMDA]$_1$ = 50.5 [GABA]$_1$ = 178.0 (s^{-1})
$\alpha_n^{[R]}$	Receptor offset reciprocal time-constants	[AMPA]$_1$ = 21.8 [AMPA]$_2$ = 60.3 [AMPA]$_3$ = 684.0 [NMDA]$_1$ = 0.608 [NMDA]$_2$ = 3.3 [GABA]$_1$ = 11.2 [GABA]$_2$ = 127 (s^{-1})

5.1.5 Postsynaptic Membrane Gain

The ionic reversal potentials modify the response of dendritic membranes to synaptic input. The steady state solution for the average membrane potential, V_q, and the modified afferent synaptic flux, φ_p, is given by Eq. (5.5),

$$M^{[R]}(V_q, \varphi_p) \;=\; g_p^{[R]} \left(\frac{V_p^{\mathrm{rev}} - V_q}{V_p^{\mathrm{rev}} - V_q^{[0]}} \right) J^{[R]} \tag{5.5}$$

where J is the open-channel firing rate defined in Eq. (5.3). The synaptic gain $g_p^{[R]}$ at resting membrane potential is obtained from the work of Thomson and colleagues [111, 112] and given in Table 5.4. V_p^{rev} is the excitatory or inhibitory reversal potential; $V_q^{[0]}$ is the resting membrane potential. The values for V_p^{rev} and V_q^0 are listed in Table 5.6.

5.1.6 Dendritic Time and Space Response

The response of the postsynaptic dendritic membrane potentials to the synaptic inputs is modelled by a biexponential function $\Psi^{[R]}$,

$$\Psi^{[R]}(\tau) \;=\; \frac{a_{qp} b_{qp}}{b_{qp} - a_{qp}} \left(\exp\left(-a_{qp}\tau\right) - \exp\left(-b_{qp}\tau\right)\right) \tag{5.6}$$

a_{qp} and b_{qp} modify the shape of the postsynaptic potentials and control the fall and rise of the postsynaptic potentials respectively. The biexponential function is plotted in Fig. 5.2.

Neurons have complex dendritic arbors. Postsynaptic potentials generated from an enormous number of synapses propagate to the axon hillock (action potential trigger point) where they are summated to initiate an action potential. However, postsynaptic potentials initiated further along the dendritic tree will be attenuated and slowed before reaching the axon hillock after delays due to passive cable properties of the dendrites. So the impulse response function describing postsynaptic potential integration at the soma over a spread of time delay is given by Eq. (5.7),

$$L^j(\tau) \;=\; a^j \exp\left(-a^j \tau\right) \tag{5.7}$$

where the a^j are the rate constants; $j = n, f$ represents near or far dendritic trees respectively. Parameter values a_{qp}, b_{qp} and a^j are listed in Table 5.3. The impulse response function is also displayed in Fig. 5.3.

5.1.7 Action Potential Back-Propagation

The dendritic membrane of pyramidal neurons is active and capable of supporting action potential propagation elicited from their respective initiation locations [61] through dendritic Na$^+$ and K$^+$ channels. Distal dendritic sodium–calcium spikes are able to propagate forward toward the cell body. Sodium action potentials generated at the axon trigger point propagate not only forward along the axon, but also backwards up to the apical dendritic tree. The retrograde signals generated from backpropagating action potentials invading the apical dendritic tree and

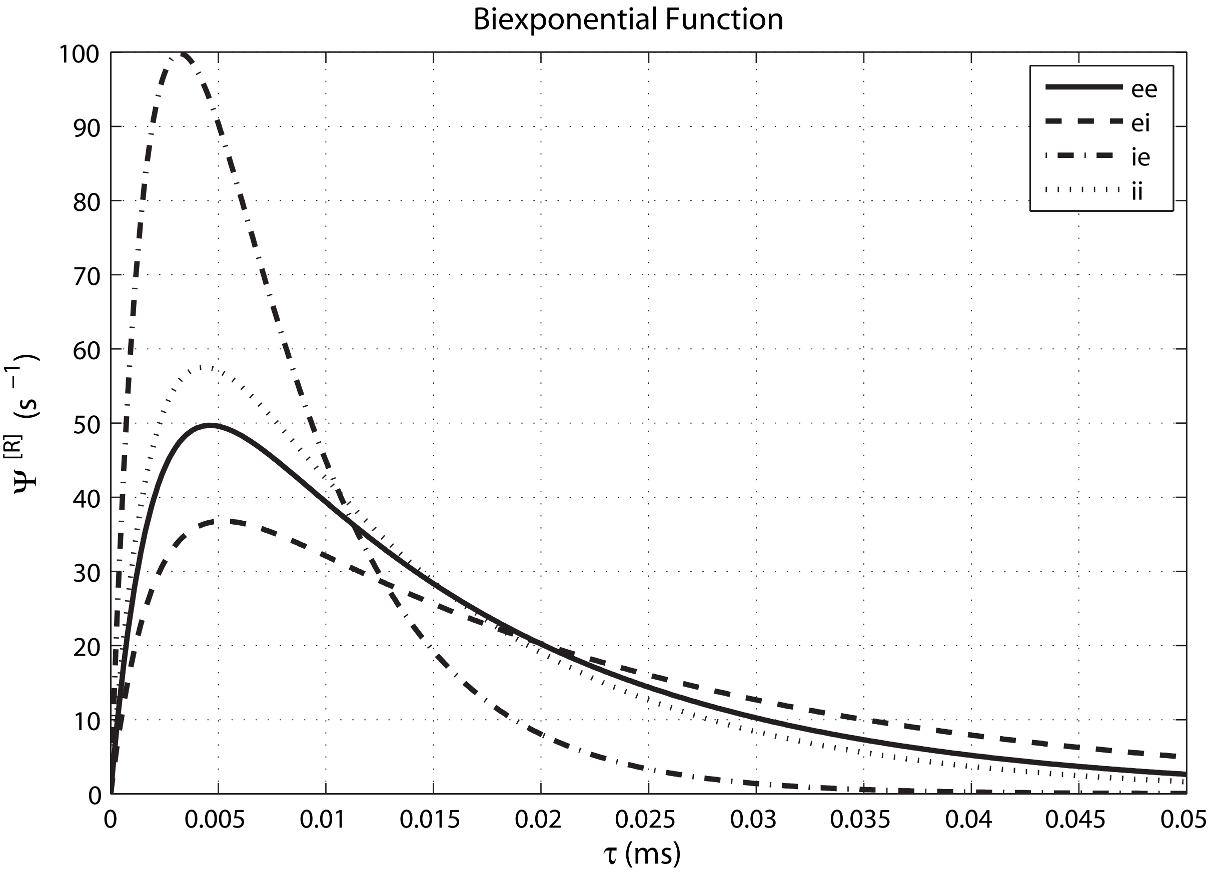

Figure 5.2: The biexponential function describes the rise and fall of postsynaptic membrane potential at the site of synaptic input. The EPSP and IPSP in excitatory cells are plotted with solid and dash curves and labelled as "ee" and "ei". Correspondingly, the dash-dot ("ie") and dot curves ("ii") give the EPSP and IPSP in the inhibitory cells. The rising and decay parameters used for this plot are listed in Table 5.3. All four curves have the same rising rate, but different decay rate.

Table 5.3: Membrane temporal smoothing for `ccf` model [82, 105, 111, 112]

Parameter	**Description**	**Value (units)**
Membrane temporal smoothing		
a_{ee}	EPSP decay in excitatory cells	68 (s^{-1})
b_{qp}	EPSP and IPSP rise	500 (s^{-1})
a_{ei}	IPSP decay in excitatory cells	47 (s^{-1})
a_{ie}	EPSP decay in inhibitory cells	176 (s^{-1})
a_{ii}	IPSP decay in inhibitory cells	82 (s^{-1})
a^j	Time-smoothing attributable to position of near and far synapses on dendritic tree	$a^n = 1000$ (s^{-1}) $a^f = 200$ (s^{-1})

its spines are thought to be crucial to the synaptic integration and brain plasticity required for learning [65, 105].

The activities of proximal dendrites play a bigger role on the generation of an action potential because of proximity to the action potential trigger point, the axon hillock. After the action potential is generated, the retrograde signal depolarises the entire dendritic tree. However, proximal synapses become briefly inactive because of the absolute refractory period following firing, so generation of subsequent action potentials is determined in large weight by the distal

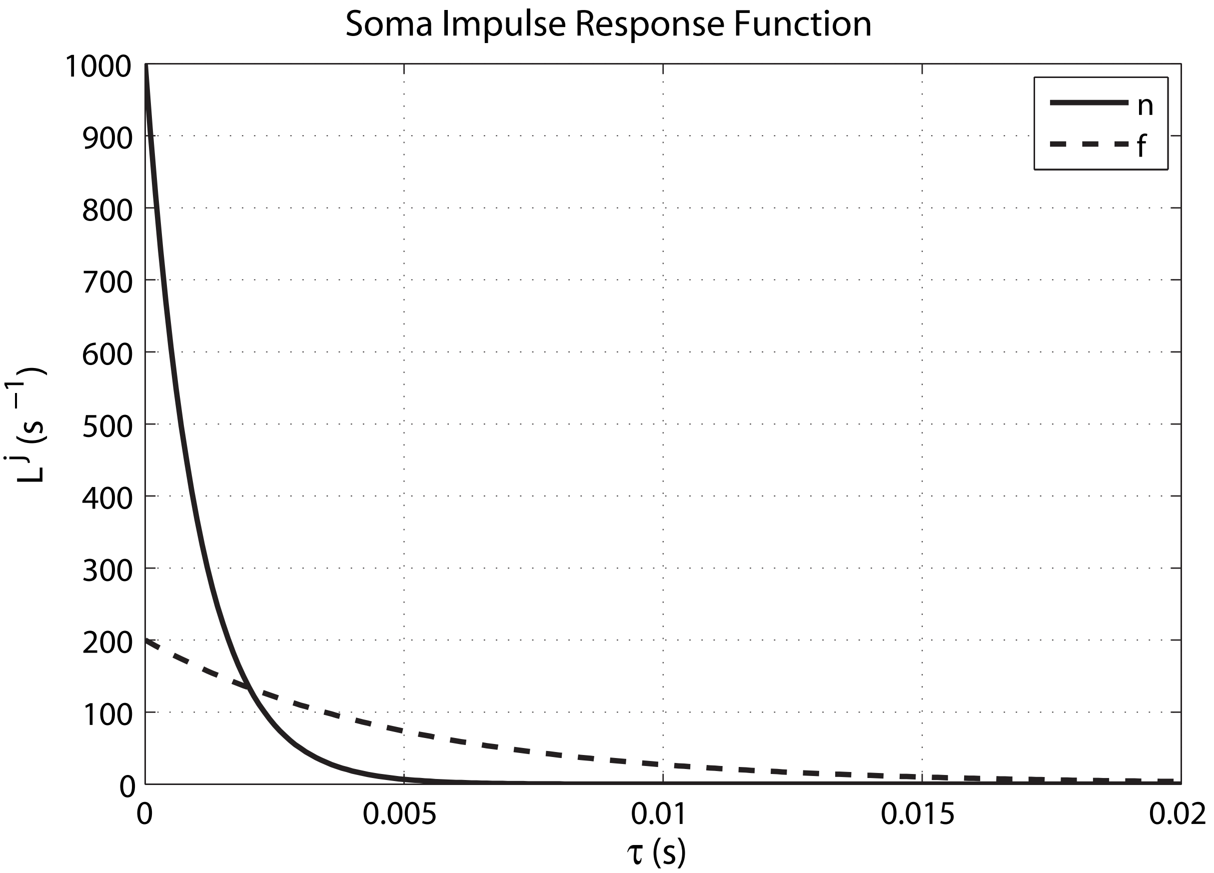

Figure 5.3: Impulse response function describes the relative magnitude of postsynaptic depolarisation reaching the trigger point by cable effect over a spread of arrival times. It takes longer for the postsynaptic depolarisation to transfer to the action potential trigger point from synapses in the far dentritic tree than that from the near dentritic tree, but the postsynpatic potential from the near dendrtic tree (solid curve) decays much faster than that from the far denritic tree (dashed curve). This corresponds to a larger rate constant for the near dendritic tree (1000 s^{-1}) and a smaller rate constant for the far dendritic tree (200 s^{-1}).

dendritic tree.

The effect of the action potential back-propagation can be described in Eq. (5.8) and (5.9),

$$A^f(t) = Q_q/Q_q^{\max} \tag{5.8}$$

$$A^n(t) = 1 - \left(Q_q/Q_q^{\max}\right) \tag{5.9}$$

A^f and A^n give the fraction of far and near neurons which are active and contribute to the generation of the action potentials. $Q_q^{\max}$ is the maximum firing rate of neurons (see Table 5.6).

The fractional distributions of the near and far postsynaptic receptors are $r^{n[R]}$ and $r^{f[R]}$ and follow Eq. (5.10),

$$r^{n[R]} + r^{f[R]} = 1 \tag{5.10}$$

Superscript $[R]$ represents the three major neurotransmitter receptors: fast excitatory glutmate receptor (AMPA), fast inhibitory GABA receptor (GABA$_\mathrm{A}$), and the slow and voltage-dependent glutamate receptor (NMDA). Total excitatory synaptic gain is divided equally between AMPA and NMDA receptors. NMDA receptors are mainly distributed in the distal dendritic tree. Therefore, for simplification in the `ccf` model, NMDA receptors are assumed to be exclusively located on the distal dendritic tree. Other receptors are more uniformly distributed. The values of $r^{n[R]}$ and $r^{f[R]}$ used in the simulation are listed in Table 5.5.

5.1.8 Aggregate Depolarisation

The synaptic influx is modified by synaptic, receptor, and dendritic membrane dynamics, converted into dendritic potentials and subsequently trigger action potentials. The voltage at the trigger point, ψ_q, is given by the triple convolution given in Eq. (5.11),

$$\psi_q(t) \;=\; \sum_p \sum_j \sum_{[R]} N_{qp} A^j r^{j[R]} \left(\left(\left(M^{[R]} * \Phi^{[R]} \right) * \Psi^{[R]} \right) * L^j \right) \tag{5.11}$$

The equation considers convolution and summation over the receptor types ($[R]$), excitatory and inhibitory cells (p), and fractions of quiescent and active cells (A^j), weighted by the average number of synaptic connections (N_{qp}). In the equation, $*$ represents convolution in time, and $j = n, f$ represents near or far dendritic tree.

The local averaged membrane potential is the sum of the resting membrane potential, $V_q^{[0]}$, plus the voltage at the trigger point, ψ_q, and is given in Eq. (5.12),

$$V_q(t) \;=\; V_q^{[0]} + \psi_q \tag{5.12}$$

Table 5.4 lists the parametric values of synaptic number densities, (N_{qp}), used in the simulation. Synaptic number densities, N_{qp} are derived from the work of Liley, Wright and Rennie [64, 82], which is based on the earlier work of Scholl [93], Braienberg and Schüz [18] and Nunez [77]. Table 5.5 gives the values of $r^{j[R]}$, the relative weighting of receptors on near/far dendritic field used in Eq. (5.11).

5.1.9 Action Potential Generation

The firing rate Q of neural population q is assumed to be a sigmoidal function of membrane potential V_q as given in Eq. (5.13) and illustrated in Fig. 5.4.

$$Q_q(t) \;=\; Q_q^{\max} / \left(1 + \exp\left[-\pi \left(V_q - \theta_q \right) / \sqrt{3}\sigma_q \right] \right) \tag{5.13}$$

where Q is the firing threshold and σ_q is its standard deviation. See Table 5.6 for values.

5.1.10 Centimetric Scale Application

The single-layered cortex is approximated by a square array of 20 × 20 elements. In simulation, the state equations are computed numerically over the 20 × 20 grid assuming periodic (i.e., toroidal) boundary conditions. Each element of the grid represents a cortical point $\mathbf{r}$, and $\mathbf{r}'$

Table 5.4: Synaptic connectivities and gains [18, 77, 82, 93, 111, 112]

Parameter	Description	Value (units)
Synaptic numbers and gains		
$N_{ee,cc}$	Excitatory to excitatory corticocortical synapses/cell	3710 (dimensionless)
$N_{ie,cc}$	Excitatory to inhibitory corticocortical synapses/cell	3710 (dimensionless)
$N_{ee,ic}$	Excitatory to excitatory intracortical synapses/cell	410 (dimensionless)
$N_{ei,ic}$	Inhibitory to excitatory intracortical synapses/cell	800 (dimensionless)
$N_{ie,ic}$	Excitatory to inhibitory intracortical synapses/cell	410 (dimensionless)
$N_{ii,ic}$	Inhibitory to inhibitory intracortical synapses/cell	800 (dimensionless)
$N_{ee,ns}$	Synapses per excitatory cell from subcortical sources	100 (dimensionless)
$N_{ie,ns}$	Synapses per inhibitory cell from subcortical sources	0 (dimensionless)
$g_e^{[R]}$	Receptor specific excitatory gain per synapse at rest potential	$[\text{AMPA}] = 1.2 \times 10^{-6}$ (Vs) $[\text{NMDA}] = 1.2 \times 10^{-6}$ (Vs)
$g_i^{[R]}$	Receptor specific inhibitory gain per synapse at rest potential	$[\text{GABA}_\text{A}] = -5.9 \times 10^{-6}$ (Vs)

Table 5.5: Receptor distribution [82, 111, 112]

Parameter	Description	Value (units)
Receptor distribution		
$r_n^{[R]}$	Relative weighting of receptors on near dendritic field	$[\text{AMPA}] = 1 - r^{f[R]}$ $[\text{NMDA}] = 1 - r^{f[R]}$ $[\text{GABA}] = 1 - r^{f[R]}$
$r_f^{[R]}$	Relative weighting of receptors on far dendritic field	$[\text{AMPA}] = 0.50$ $[\text{NMDA}] = 1.0$ $[\text{GABA}] = 0.375$

Table 5.6: Threshold values [82]

Parameter	Description	Value (units)
Threshold values		
$Q_e^{\max}$	Maximum firing rate of excitatory cells	100 (s^{-1})
$Q_i^{\max}$	Maximum firing rate of inhibitory cells	200 (s^{-1})
V_e^{rev}	Excitatory reversal potential	0 (V)
V_i^{rev}	Inhibitory reversal potential	−0.070 (V)
$V_{q,p}^{[0]}$	Resting membrane potential	−0.064 (V)
θ_q	Mean dendritic potential when 50% of neurons firing	−0.035 (V)
σ_q	Standard deviation of neuron firing probability, versus mean dendritic potential	0.0145 (V)

represents any other cortical point. The presynaptic delay between points $\mathbf{r}$ and $\mathbf{r}'$ is given by δ_p,

$$\delta_p = \frac{|\mathbf{r} - \mathbf{r}'|}{\nu_p} \tag{5.14}$$

where ν_p is the axonal propagation speed.

The `ccf` model can be used to simulate the electrical events in the brain at both *centimetric*

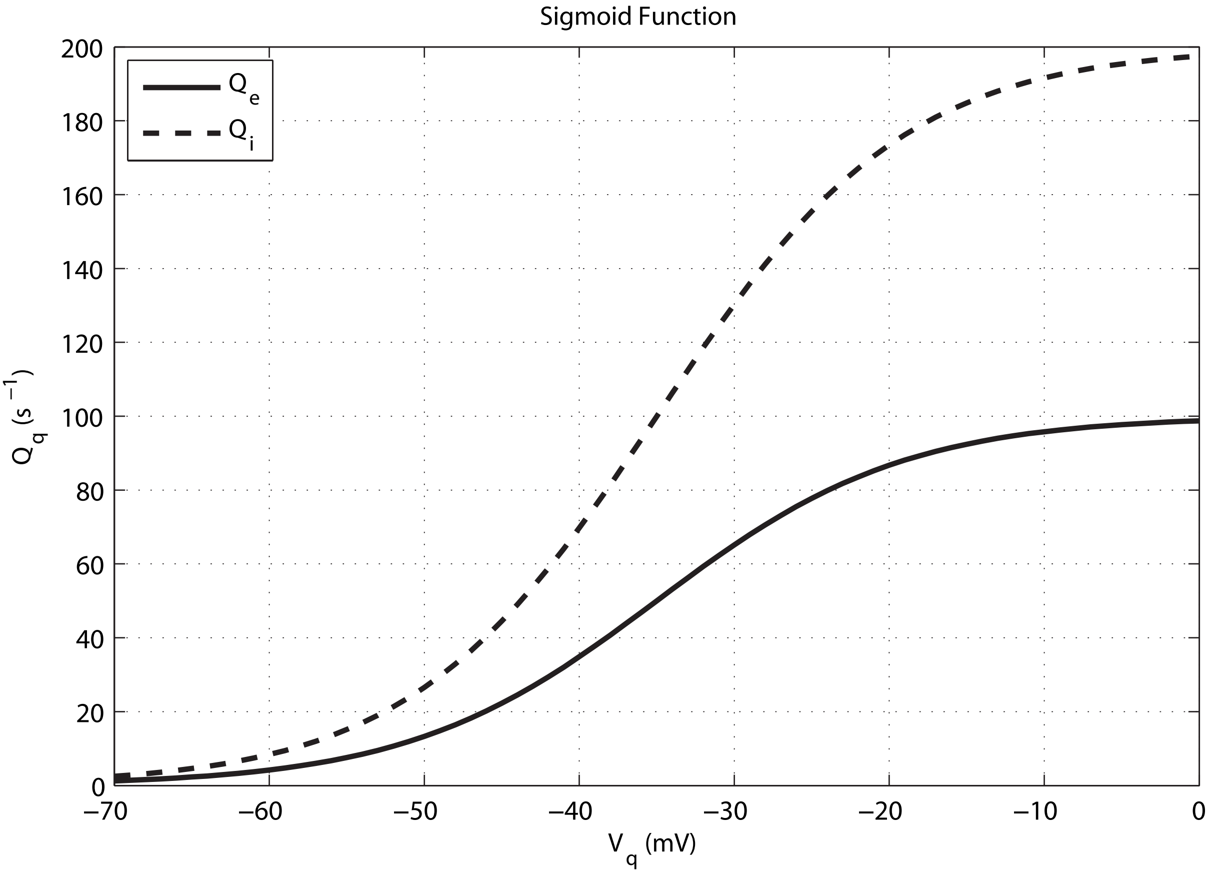

Figure 5.4: Graph of sigmoid function of Eq. (5.13) which describes conversion of membrane potential, V_q, into Q_q the instantaneous average firing rate of the neural population q. Here, the maximum firing rates are $Q_e^{\max} = 100\ \mathrm{s}^{-1}$, $Q_i^{\max} = 200\ \mathrm{s}^{-1}$. The threshold voltage (value at which 50% of the population is firing) is $Q_{e,i} = -35$ mV.

and *macrocolumnar* scales by changing the nearest-neighbour grid spacing $\Delta\mathbf{r}$ of cortical points, delay between the points, δ_p, and excitatory/inhibitory axonal range parameters, γ_e and γ_i (expressed as multiples of the lattice spacing).

Compared with the macrocolumnar scale (mesoscopic scale, about 300 μm diameter [18]), the centimetric scale (macroscopic) is a large, global scale. Because inhibitory axons have a much shorter range than excitatory axons, $\gamma_e \gg \gamma_i$, the inhibitory afferent flux can be approximated as having no significant spatial extension at centimetric scale. Hence, for centimetric-scale simulations, the excitatory afferent flux density φ_e is given by Eq. (5.15),

$$\varphi_e(\mathbf{r},t) \;=\; \int \frac{1}{2\pi\gamma_e^2} \exp\left[\frac{-\left|\mathbf{r}-\mathbf{r}'\right|^2}{2\gamma_e^2}\right] Q_e\left(t-\delta_e\right)\, d^2\mathbf{r}' \tag{5.15}$$

while the inhibitory afferent flux density φ_i is given by Eq. (5.16),

$$\varphi_i(\mathbf{r},t) \;=\; Q_i(\mathbf{r},t) \tag{5.16}$$

To approximate the human cortex on a 20 × 20 grid, the lattice spacing is set at $\Delta x = \Delta y = 0.7$ cm, thus each grid element represents about 0.49 cm^2 of cortex. The propagation delay between nearest elements is $\delta_p = 1.7$ ms, so axonal conduction velocity is roughly 4 m/s in the centimetric scale simulation. $\gamma_e/\Delta x = 4$ and $\gamma_i/\Delta x = 0$ was used in the simulation; these settings correspond to excitatory and inhibitory cortico-cortical connection ranges of $4\Delta x = 2.8$ cm and 0 cm respectively.

5.1.11 Transcortical Flux (TCF) and Nonspecific Flux (NSF)

Transcortical flux (TCF) is defined as the afferent synaptic flux transmitted by the cortico-cortical fibers. Nonspecific flux (NSF) is the excitatory synaptic flux delivered wholly to the excitatory cortical cells from the reticular activation system. Transcortical flux and nonspecific flux connections are shown in Fig. 5.1. The unit for both of transcortical flux and nonspecific flux is spikes per second.

At *centimetric scale*, the elements are linked by excitatory cortico-cortical connections and we can approximate the inhibitory and short-range intracortical connections as being local to each element. Therefore, at centimetric scale, the nonspecific afferent flux is the only control parameter and is introduced uniformly to all elements, but only to excitatory neuron population within each element, and is defined as variable $\varphi_{ee,ns}$.

At *macrocolumnar scale*, the 20×20 elements are also connected by both intracortical excitatory and inhibitory connections. The connection field is a “Mexican hat” shape with diameter of approximately 300 μm. So at macrocolumnar scale, there are *two* control parameters: transcortical flux and nonspecific flux. Transcortical flux is delivered to all elements and to both excitatory and inhibitory neuron population in each element of the cortical field in a spatially uniform manner. Similar to the centimetric scale, the nonspecific flux is only applied to the excitatory neuron population in each element. This is consistent with the physiological fact that most long-range upward axons originating from subcortical excitatory neurons terminate on the dendritic trees of pyramidal excitatory neurons in the cortex.

5.2 Cortical Column Field Model Simulation

5.2.1 Technical Details of Cortical Column Field Model

The cortical column field model treats the cortex as an equally-spaced array of cortical columns which comprise the several layers of cortex. The thalamus can also be modelled as an array of columns.[1] Each cortical column or element includes a mass of excitatory neurons and a mass of inhibitory neurons with couplings between them. In the model, input signals are pulse densities generated by the program itself. Gaussian white noise can be applied to the whole cortex field when needed. Output signals are mean pulse densities (Q_e, Q_i) and local potentials (V_e, V_i) for each element.

Figure 5.5 gives the file structure for `ccf` simulation. The `ccfv6-64` file is the 64-bit executable that simulates the cortical field. The `ncc` script tells `ccfv6-64` to read the default file `ncc.def`. If necessary, parameters can be redefined in the `ncc` script file, overriding the default definitions contained in `ncc.def`. The output file format be chosen to be either `.eivw`, an `ASCII` text listing of Q_e, Q_i, V_e, V_i values at nominated grid points, or `.fits`, a compressed

---

[1] Although couplings between cortex and thalamus can be simulated by the `ccf` model, I did not explore cortico-thalamic model behaviours in my thesis investigations.

binary listing of V_e and V_i. `FITS` (Flexible Image Transport Standard) is an image compression algorithm designed by `NASA`.[2]

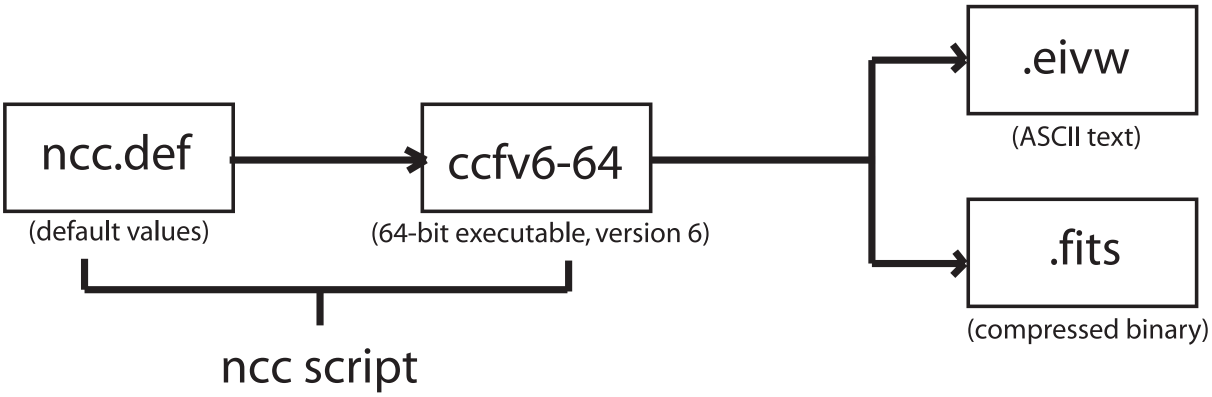

Figure 5.5: File structure of `ccf` model simulation. The default parameters values used for the simulation are defined in the text file `ncc.def`. Default values can be overridden in the `ncc` script file. The `ncc` script tells executable file `ccfv6-64` to read default values stored in file `ncc.def`. Two formats are available for the output file: `.eivw` and `.fits`.

The surface of the cortex is "lumped" into a 20×20 grid of neural elements. The boundary condition is toroidal in our simulations, which is appropriate for the simulation of the events at the scale of the whole brain (centimetric scale). Significant parameters required for the simulations include noise amplitude, time-step, grid resolution, dimensions for the cortex, and inputs to the cortex.

The steady state for each simulation was determined experimentally by running the simulation without external noise stimulus. Each simulation was considered to have reached steady state after a settling time of 200 seconds. Here, "steady state" is defined to be a final state with negligible power other than at DC or in one of the oscillation states.

Simulation time-step δt was set at 0.1 ms. All simulations were run at centimetric scale. Typically, a simulation consisted of a 200-s "settling in" period, followed by, say, ~1 to 10 s of active recording from either all 400 grid points, or from a specified subset of elements. During the simulation, nonspecific inputs Q_{ns} were delivered at constant positive values uniformly to the excitatory neuron cells within all elements of the entire matrix. The amplitude of the nonspecific input can be set at any value over the range 0 to 1000 s^{-1}. A zero-mean asynchronous Gaussian white noise [72] of small amplitude (standard deviation of 0.001) was applied to every element of the 20 by 20 grid uniformlly. These white noise signals are added to the constant nonspecific input Q_{ns} signal. Transcortical flux (Q_{tc}) was set to zero throughout. The output variables, excitatory potential (V_e), inhibitory potential (V_i), excitatory pulse rate (Q_e), and inhibitory pulse rate (Q_i), were recorded from one or more cortical elements.

The source code of `ccf` was written in `ANSII C` by Mr Nick Hawthorn, Medical School of Auckland University, following algorithm design specifications provided by Prof Jim Wright. There are a total of 12,847 lines of `C` code in the current version-6 release. Running on a 64-bit server (e.g., `Tesla` at Waikato University), a 200-second `ccf` simulation takes about 90 minutes. For each second of active `ccf` recording, the `eivw` output file at each grid element is about 923 KB

---

[2] Source codes for the `FITS` subroutine library are freely available from the `NASA` website `http://heasarc.gsfc.nasa.gov/docs/heasarc/fits.html`.

in size. In order to investigate the entire cortical field, recordings for all 400 grid elements are needed. For a 1-second 400-grid-elements recording, the `eivw` text file occupies about 365 MB, while the size of the `fits` compressed binary file is about 63 MB. Because of the smaller size of the `fits` file, we choose to output the results in `fits` format when 400-grid-elements results are needed.

5.2.2 Time Series Simulation

Running in centimetric mode, the cortex was stimulated with noise applied to all 20 by 20 grid elements. The level of cortical arousal was determined by setting the non-specific flux (Q_{ns}) at a value lying between 0 and 1000 s^{-1}; the transcortical flux (Q_{tc}) was set at 0 s^{-1}. The time series of mean pulse density (Q_e, Q_i) and local field potential (V_e, V_i) for excitatory and inhibitory elements located at any grid point can be recorded in the `eivw` or `fits`[3] output file, for subsequent processing in `Matlab`. This post-processing applies time- and frequency-domain analysis to the mean pulse densities and local field potentials: average power, power-law determination, cross-spectra, and spatial Fourier analysis.

We recorded the local field potentials for a one-second simulation for all 20 by 20 grid points in the cortical field. Figures 5.6 and 5.8 show the time series for V_e and V_i at nine different grid points for two different levels of subcortical drive: $Q_{ns} = 400\ \mathrm{s}^{-1}$ (Figures 5.6 and 5.7) and $Q_{ns} = 500\ \mathrm{s}^{-1}$ (Figures 5.8 and 5.9). It is evident that the cortical response changes dramatically at the higher level of stimulation, resulting in a coherent whole-of-cortex oscillation of frequency ~57 Hz lying within the so-called EEG gamma band (30–80 Hz). After performing a large number of simulation runs for different values of Q_{ns} stimulation, I determined that the critical level of drive for gamma onset is $Q_{ns}^{\mathrm{crit}} = 478.8793\ \mathrm{s}^{-1}$ (to four decimal places). Below this critical value, the cortex is in a random fluctuation state that does not exhibit any coherent structure, see Figs 5.6 (single-point time series) and 5.7 (20×20 grid display snapshots at 0.25-s intervals).

From Fig. 5.6, we can see for Q_{ns} of 400 s^{-1}, V_e fluctuates between -42.5322 and -42.531 mV, and V_i fluctuates between -56.333 and -56.3322 mV. The fluctuations of V_e at different grid points are not synchronised, nor are the fluctuations between V_e and V_i at the *same* grid point. In addition, no obvious up or down movement of the cortical sheet is observed in Fig. 5.7.

For Q_{ns} of 500 s^{-1}, the cortical field is now in gamma resonance mode. From Fig. 5.8, the time series of V_e and V_i recorded at all nine grid points are oscillating in the same well-defined single frequency. The oscillations of V_e at different grid points are in phase, as are the oscillations of V_i at different grid points. But the oscillations of V_e and V_i are *not* in phase: V_e and V_i are approximately 180° out of phase. Figure 5.9 indicates the whole cortex sheet is moving up and down. Compared with the movement of the whole cortex, the fluctuation at each grid point is very small and can be ignored. Therefore, we can deduce the behaviour of the resonant cortex by investigating the behaviour of any single grid point. In the following studies, we focused on the recordings of V_e and V_i at grid point (10, 10).

---

[3] Although the `fits` file only contains (V_e, V_i) time-series pairs, the corresponding (Q_e, Q_i) pulse densities can be retrieved via the sigmoidal mapping of Eq. (5.13).

The emergence of the gamma resonance is visualized in the 1-s $V_{e,i}$ and companion $Q_{e,i}$ time series of Figs 5.10 and 5.11. A range of Q_{ns} stimulation levels that bracket and closely approach the threshold value was selected: $Q_{ns} = 0$, 200, 400, …, 900 s^{-1}. Q_{ns} of 0, 200, and 400 s^{-1} is below the resonance area; $Q_{ns} = 478.88$ s^{-1} is just above and very close to critical value; and $Q_{ns} = 900$ s^{-1} is well above the gamma resonance region. Within the resonance region, with Q_{ns} increasing, the amplitude of the global oscillation also increases, reaching maximum amplitude at about $Q_{ns} = 540$ s^{-1}. Further increases in Q_{ns} cause the oscillation amplitude to diminish, and finally lead the cortex sheet out of the resonance area. For $Q_{ns} = 900$ s^{-1}, the fluctuation amplitude grows slowly with time, suggesting that the cortex is in an unstable state.

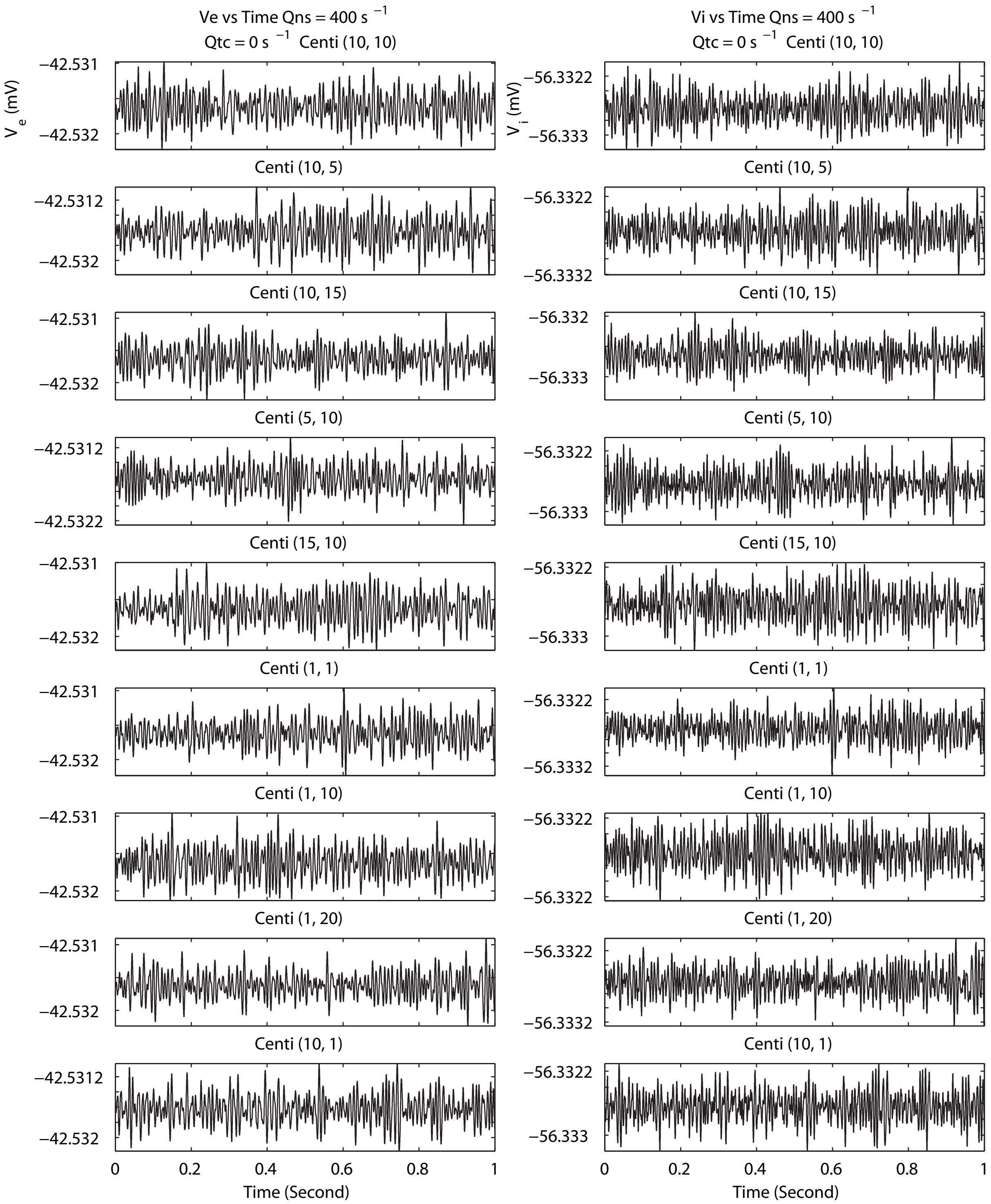

Figure 5.6: Time series of local field potential of excitatory (V_e, left panels) and inhibitory (V_i, right panels) element for $Q_{ns} = 400$ s^{-1}, $Q_{tc} = 0$ s^{-1} at centimetric scale. Q_{ns} is below the critical value, and the cortex remains in an uncorrealated state. From top to bottom, the recorded (row, column) grid points of the cortical field are (10, 10), (10, 5), (10, 15), (5, 10), (15, 10), (1, 1), (1, 10), (1, 20), and (10, 1); here we are using `Matlab`'s unity-based indexing rather than the zero-based indexing of Fig. 5.1. In total, nine recordings from different grid positions are shown. Grid point (10, 10) is centrally located in the cortical field.

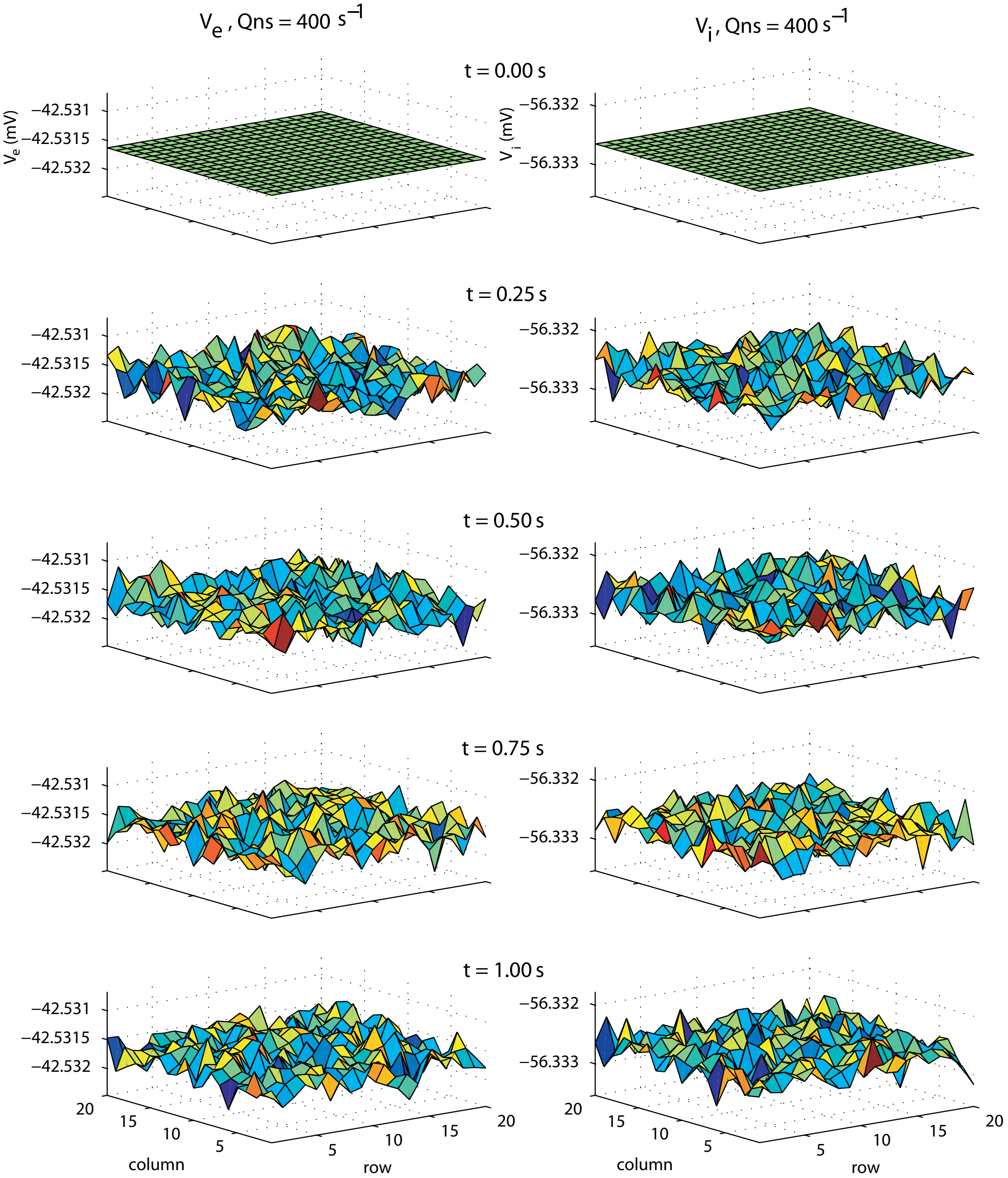

Figure 5.7: Snapshots of local field potential V_e and V_i of the entire cortical sheet for $Q_{ns} = 400$ s^{-1}. The snapshots are taken at time 0, 0.25, 0.50, 0.75, and 1.00 second. Snapshots of V_e are shown at the left column, snapshots of V_i are shown at the right column.

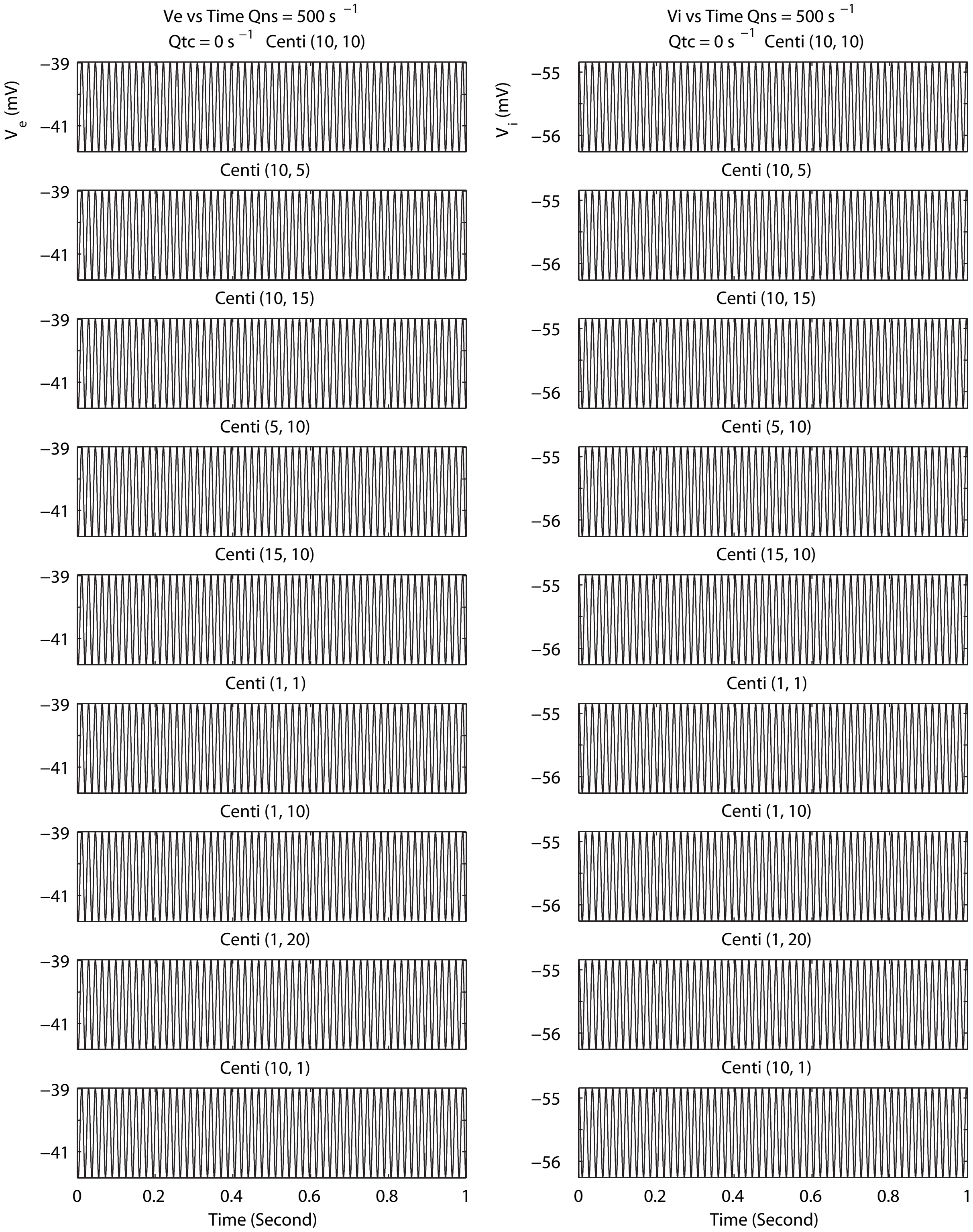

Figure 5.8: Time series for V_e and V_i for $Q_{ns} = 500$ s^{-1}, and $Q_{tc} = 0$ s^{-1} at centimetric scale. Q_{ns} is now above the critical value and the cortex has entrained into a coherent whole-of-cortex resonant mode of frequency ∼57 Hz. The selected grid points are the same as those shown in Fig. 5.6.

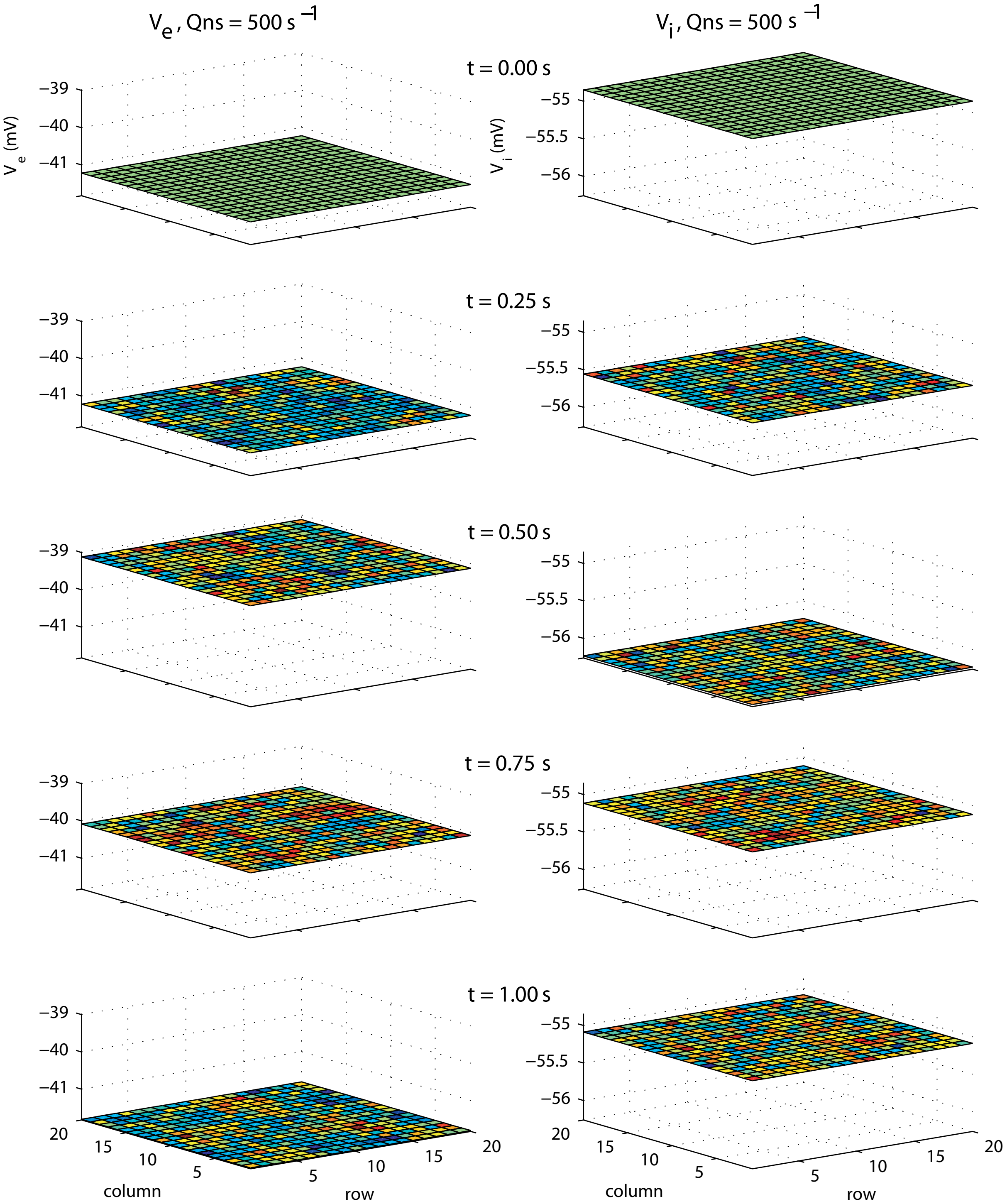

Figure 5.9: Snapshots of local field potential V_e and V_i of the entire cortical sheet for $Q_{ns} = 500$ s^{-1}. The snapshots are taken at time 0, 0.25, 0.50, 0.75, and 1.00 second. In contrast to Fig. 5.7 the field potentials at all grid positions now oscillate coherently, but with a constant phase difference between V_e (left panels) and V_i (right).

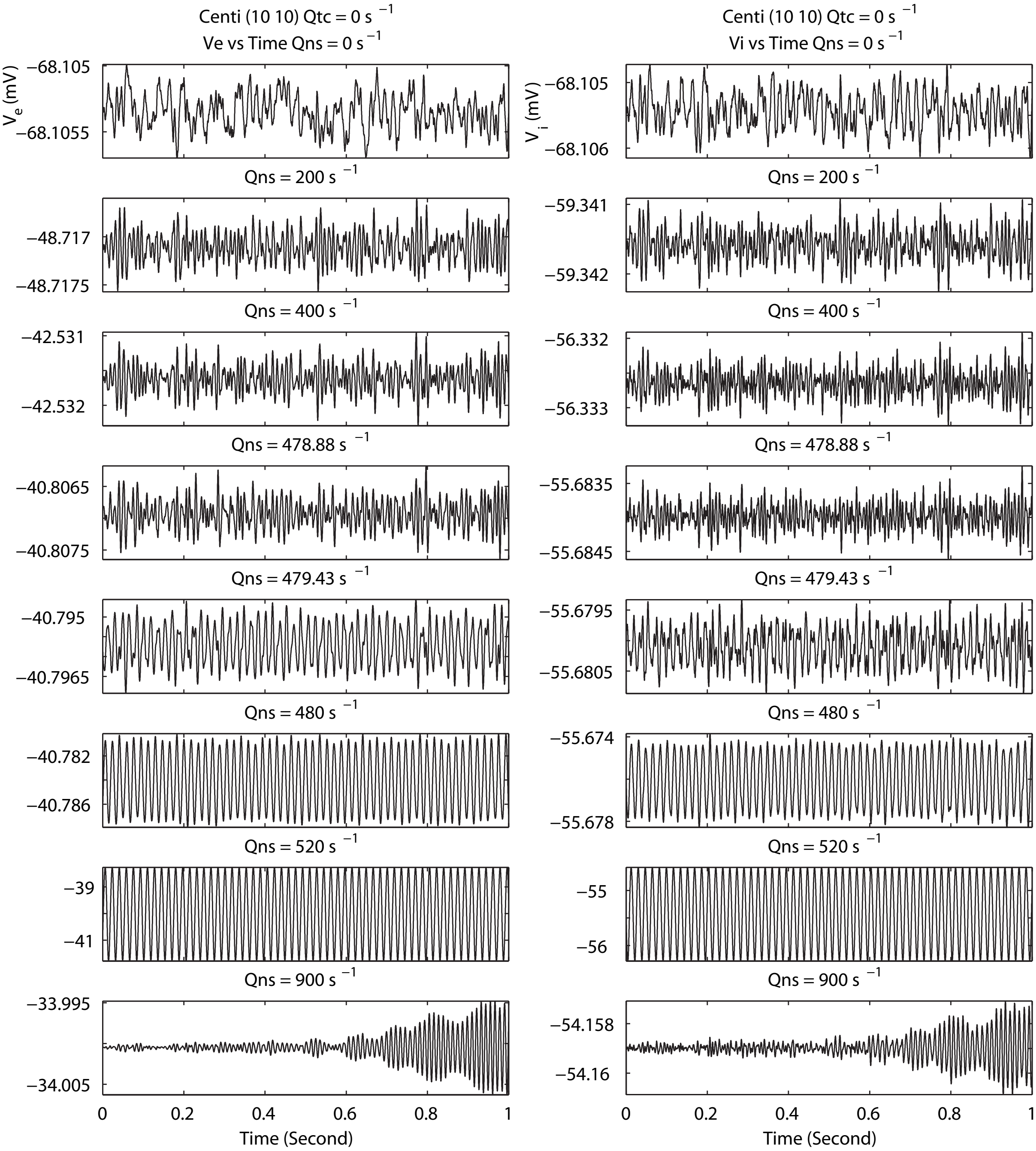

Figure 5.10: Time series of local field potentials for V_e (left) and V_i (right) at grid point (10, 10) simulated at different values of nonspecific input flux (Q_{ns}). From top to bottom, the one second time series of V_e and V_i are recorded at Q_{ns} of 0, 200, 400, 478.88, 479.43, 480, 520, and 900 s^{-1} respectively. Q_{ns} of 900 s^{-1} is above and out of the resonance area. See Fig. 5.11 for the corresponding $Q_{e,i}$ vs time firing-rate time series.

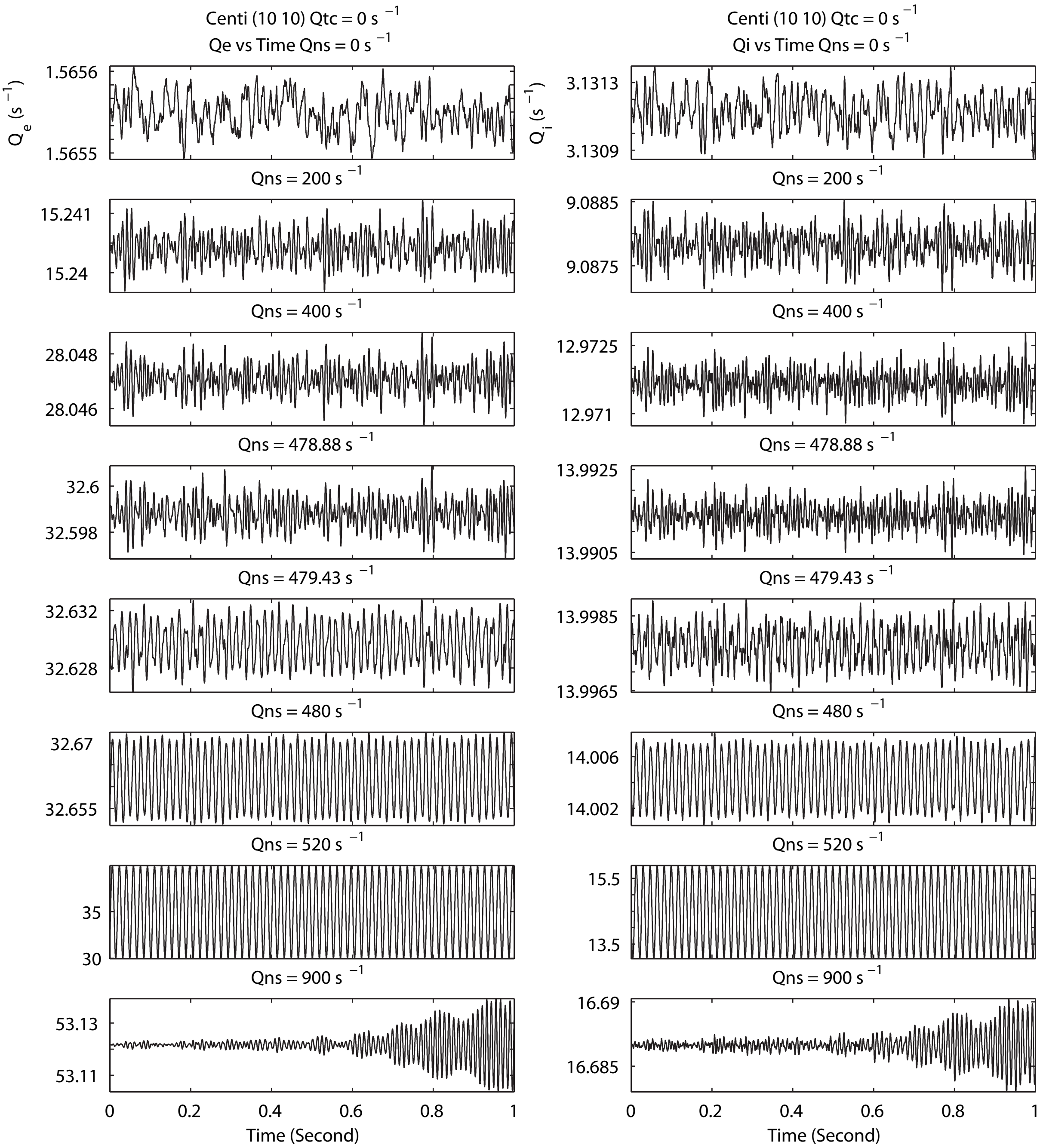

Figure 5.11: Time series showing firing rates of excitatory and inhibitory populations at grid point (10, 10) corresponding to the voltage traces shown in Fig. 5.10.

5.2.3 Fluctuation Power and Power Law

The average fluctuation power is computed for the excitatory and inhibitory membrane potential (V_e and V_i) obtained from the 1-s simulation (following a 200 s settling time) at centimetric scale. The voltage fluctuation is first calculated by deducting the voltage mean over the one-second time-series data. The instantaneous power was then computed.

$$\begin{aligned} \widetilde{V}_{e,i} &= V_{e,i} - \langle V_{e,i} \rangle & (5.17) \\ P^{av}_{e,i} &= \frac{1}{T}\int_0^T \widetilde{V}^2_{e,i}\, dt \rightarrow \frac{1}{N}\sum_{k=1}^{N}\left(\widetilde{V}_{e,i}\right)^2_k & (5.18) \end{aligned}$$

where k is sample number, $T = 1$ s, and $N = 10000$ for time-step of 0.1 ms.

Figure 5.12 gives the average power of the excitatory and inhibitory voltage fluctuations for the element at row 10, column 10. The Q_{ns} used for the analysis ranges from 0 to 1000 s^{-1}. The values of Q_{ns} indicated by circles and letters in this figure are given in Table 5.7.

In Fig. 5.12, the solid and dashed lines give the average power of the excitatory and inhibitory neuron populations respectively. The average power analysis result shows when Q_{ns} approaches the critical point, the average power of both the excitatory and inhibitory cells increases dramatically. In the vicinity of the critical point, small increases in Q_{ns} cause the fluctuation power of the excitatory neuron cell to increase rapidly from about 5×10^{-8} mV^2 to about 1 mV^2, with similar dramatic increases also observed for inhibitory fluctuation activity. During the gamma oscillations, the average power of both excitatory and inhibitory cells is much larger than that seen for when the system is non-resonant and incoherent. Gamma power is maximum when nonspecific input Q_{ns} equals 540 s^{-1} (see point **q** in Fig. 5.12). When Q_{ns} continues to increase and pass beyond the gamma oscillation area, the fluctuation power falls back sharply to the typically low values seen prior to gamma onset.

Neuronal activity in the cortex is highly irregular. Power laws are commonly found at many scales from single neuron to large-scale measurement of EEG, and the power-law exponent varies with scale. We studied the power law of the `ccf` model at the centimetric scale. We assume that the power-law has the form:

$$P_{ave}(Q_{ns}) \sim AQ^k_{ns} \tag{5.19}$$

where Q_{ns} is the nonspecific afferent flux, P_{ave} is the average power, k is the power-law exponent, A is parameter. The value of k is estimated via a set of log-log least-squares linear fits of the average power.

The presence and character of the power-law form was investigated for the raw average power. For Q_{ns} between 50 and 478 s^{-1}, the fit of a power-law form $P_{ave} \sim Q^{2/3}_{ns}$ for the excitatory element was found. For inhibitory elements, the fit of a power-law form $P_{ave} \sim Q^{-1/3}_{ns}$ was obtained. The results are shown in Fig. 5.13.

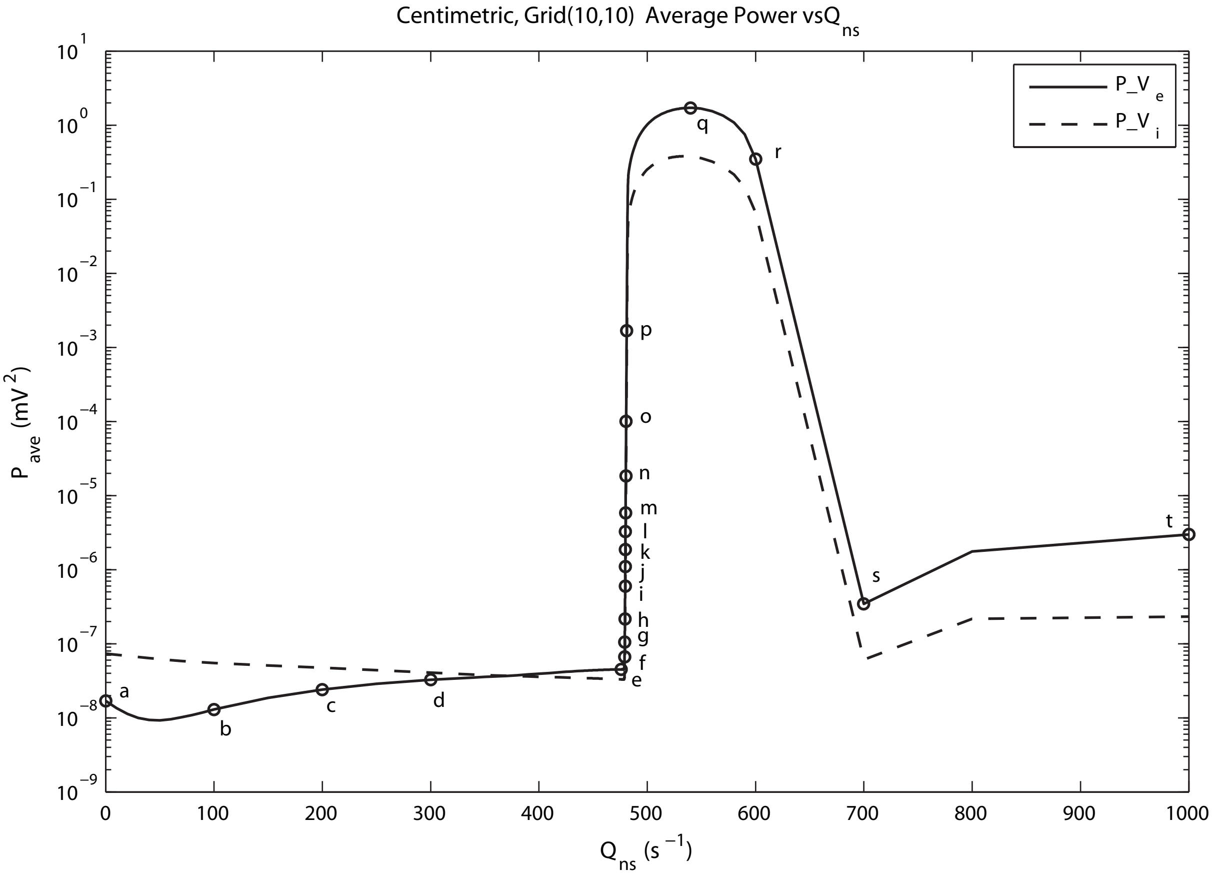

Figure 5.12: Average power of voltage fluctuations for excitatory and inhibitory neuron populaltions at row 10, column 10 for Q_{ns} ranging from 0 to 1000 s^{-1} at centimetric scale. The Q_{ns} values labelled with circles and letters are given in Table 5.7.

5.2.4 Phase Plot and Gamma Oscillation

As shown above, when the subcortical drive varies from 0 to 500 s^{-1}, the `ccf` model cortex experiences a transition from damped oscillation to an autonomous oscillation (limit cycle). The critical value of nonspecific afferent input (Q_{ns}) for this transition is 478.8793 s^{-1}. Below this critical value, when nonspecific input is small, both excitatory and inhibitory firing rate (Q_e and Q_i) show damped oscillations that decay promptly to steady state. When nonspecific afferent flux crosses the threshold value, both excitatory and inhibitory firing rate oscillate in the gamma frequency band. A gamma resonance is defined as oscillation with a peak frequency in the 30- to 80-Hz range in our simulation.

Figure 5.14 presents a sequence of phase plots of inhibitory firing rate versus excitatory firing rate. The values of nonspecific afferent flux used in this figure are Q_{ns} = [0:50:450, 476, 479.6, 479.8, 480, 481:1:485, 490, 495, 500, 510:10:530, 540, 550:10:600, 700, 800, 1000] s^{-1}.[4] There are 35 phase plots shown in this figure, corresponding to 35 nonspecific flux values. Maximum amplitude for gamma oscillation occurs at Q_{ns} = 540 s^{-1}. Therefore, in Fig. 5.14, we set the display scale factor for this maximum oscillation amplitude case at unity, and scale the other phase plots for better view. (Values of the scale factor used are listed in the figure caption.)

---

[4] We have used `Matlab` colon notation here, thus [0:50:450] is an abbreviation for [0 50 100 150 . . . 450]

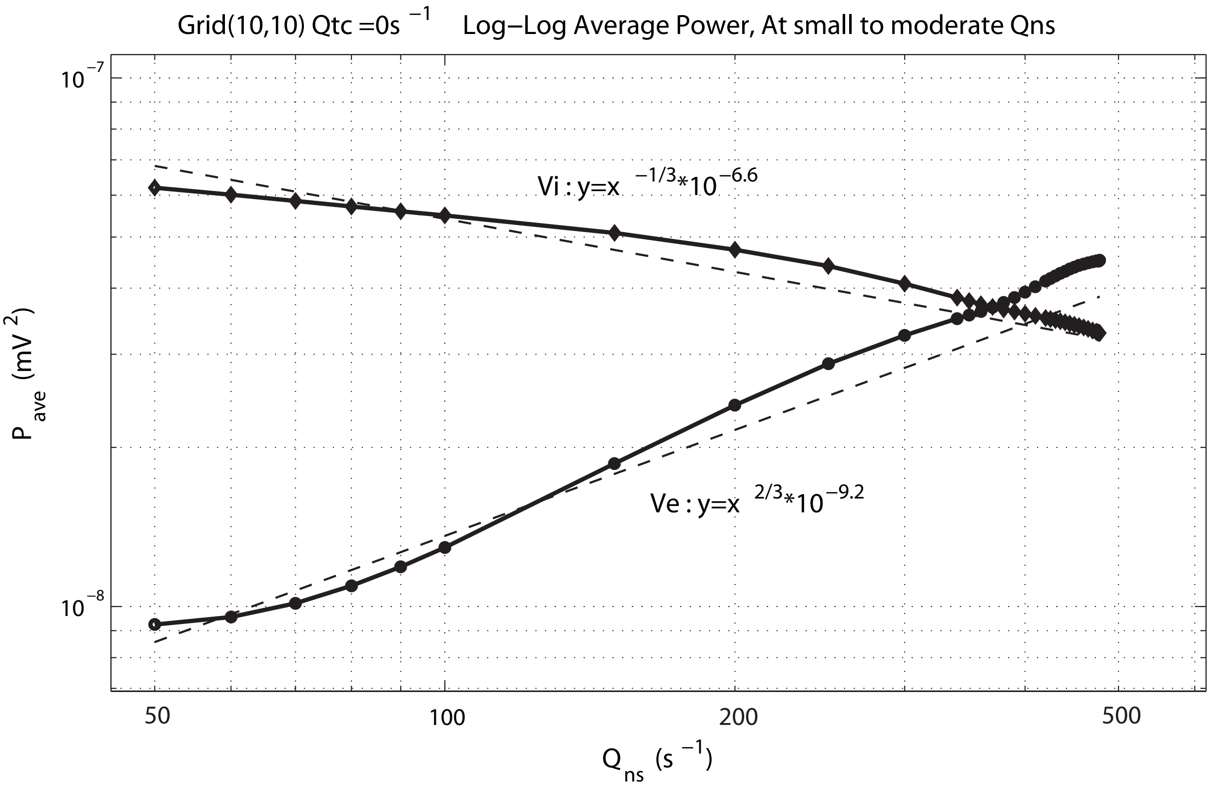

Figure 5.13: Loglog graph of average power vs Q_{ns} and fitting. Q_{ns} ranges from 50 to 478 s^{-1}. The raw average power of excitatory and inhibitory elements are given in solid lines and was fitted linearly on the log-log axes. Dashed lines show the fit here. The slope determines the exponent of an associated power-law. For excitatory elements: $P_{ave} \sim Q_{ns}^{2/3}$. For inhibitory elements: $P_{ave} \sim Q_{ns}^{-1/3}$.

Below gamma threshold, with increasing nonspecific afferent influx, the firing rates for both Q_e and Q_i also increase until Q_{ns} reaches its critical value, Q_{ns}^{crit}. For $Q_{ns}^{\text{crit}} \leq Q_{ns} \leq 600$ s^{-1}, the gamma oscillation prevails. In this range, at the beginning, with Q_{ns} continuously increasing, the firing rate reaches maximum at $Q_{ns} = 540$ s^{-1}. For $Q_{ns} > 540$ s^{-1}, the firing rates begin to *decrease*. When Q_{ns} is above 600 s^{-1}, the gamma resonance disappears and the oscillation is unstable (see Fig. 5.11, bottom panels).

A zoomed view of the gamma oscillation area in Fig 5.14 is displayed in Fig. 5.15. Selected phase plots are labelled with a letter; the labels and their corresponding Q_{ns} values are given in Table 5.7.

Table 5.7: Values of Q_{ns} used for phase plots labelled with letters in Fig 5.14 and Fig. 5.15

Letter	**a**	**b**	**c**	**d**	**e**	**f**	**g**	**h**	**i**	**j**
Q_{ns} (s^{-1})	0	100	200	300	476	479	479.2	479.4	479.6	479.7

Letter	**k**	**l**	**m**	**n**	**o**	**p**	**q**	**r**	**s**	**t**
Q_{ns} (s^{-1})	479.8	479.9	480	480.2	480.5	481	540	600	700	1000

The phase plots for the excitatory and inhibitory membrane potentials (V_e and V_i) are closely similar to those for firing rates (Q_e and Q_i), so are not shown here.

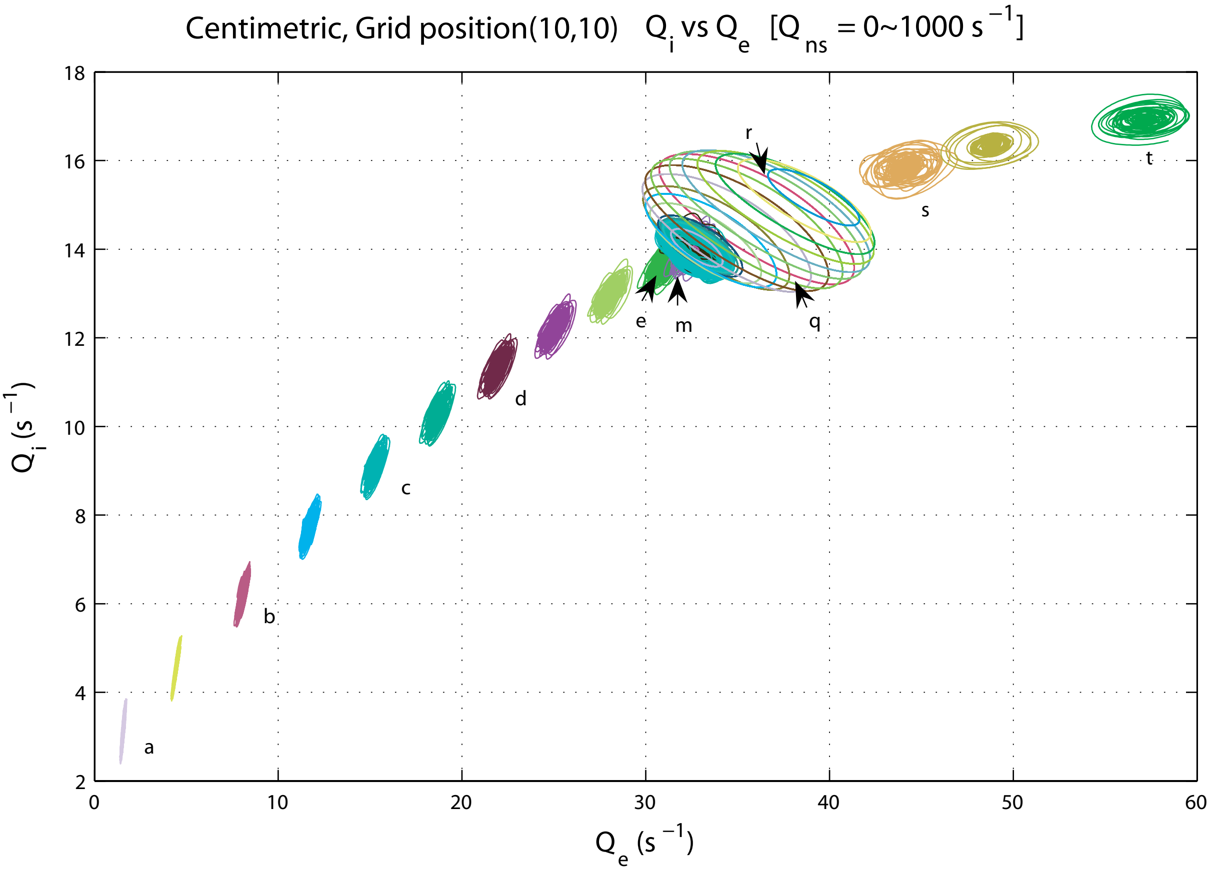

Figure 5.14: Q_e vs Q_i phase plots of inhibitory and excitatory firing rate for stepped increases in Q_{ns} stimulation. The critical value of nonspecific afferent flux (Q_{ns}) to generate gamma oscillation is 478.8793 s^{-1}. Values of Q_{ns} used in the plot are [0:50:450, 476, 479.6, 479.8, 480, 481:1:485, 490, 495, 500, 510:10 530, 540, 550:10:600, 700, 800, 1000] s^{-1}. The scale factors used for plotting the phase plots when $0 \leq Q_{ns} \leq 480$ s^{-1} are [2670, 2019, 1433, 1154, 1008, 921, 837, 767, 716, 699, 712, 411, 308, 203]. For $Q_{ns} \geq 481$ s^{-1} (i.e., for curves **p** to **t**), the phase plots are displayed in their real size (that is, their scale factors are one).

5.2.5 Phase Relation of Gamma Oscillation

The phase difference between excitatory and inhibitory neuron cells in a single element are computed (in radius or degrees) by Eq. (5.20),

$$\Theta = 2\pi \frac{|l_+|}{|l_+| + |l_-|} \text{ or } 360^\circ \frac{|l_+|}{|l_+| + |l_-|} \tag{5.20}$$

where $|l_+|$ and $|l_-|$ are the respective lag from zero in the leading and lagging direction to the first peaks in the lag cross-correlation function, $\texttt{xcorr}(\widetilde{Q}_e, \widetilde{Q}_i)$.

Figure 5.16 gives the calculated results of the phase difference between the excitatory and inhibitory populations at the row-10, column-10 element. The phase difference given in Fig. 5.16 shows the phase advance of excitatory cells relative to inhibitory cell within one element. From the figure, we can see before the gamma oscillation starts, the phase difference between Q_e and Q_i increases very slowly from about $-10°$ to about $+30°$ with Q_e leading. But when Q_{ns} approaches the point of gamma onset, the phase difference of Q_e and Q_i experiences a very abrupt increase: just before transition, Q_e leads Q_i about 30°. After gamma oscillation has

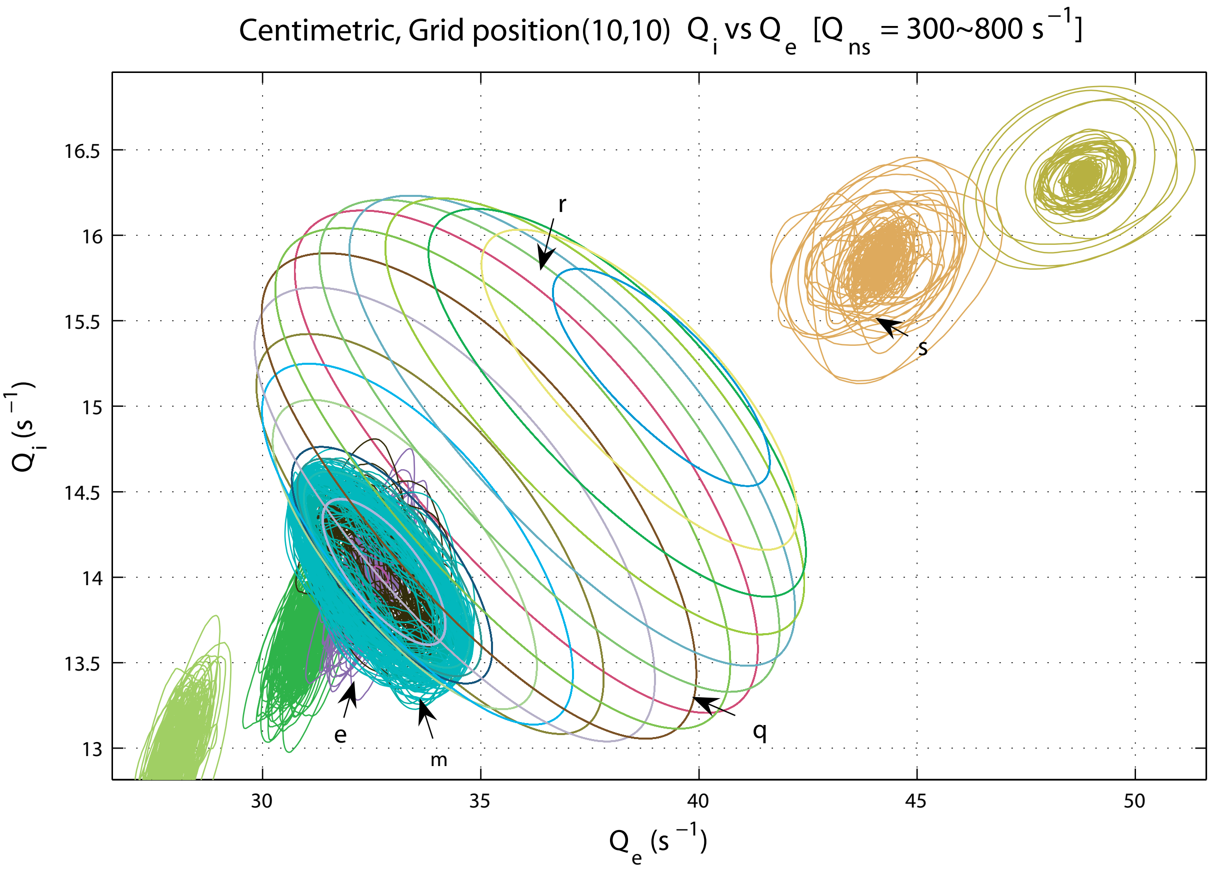

Figure 5.15: Amplified view of gamma oscillation area in Fig. 5.14. The Q_{ns} values for the phase plots labelled with letter **e**, **m**, **q**, **r**, **s** are listed in Table 5.7.

been established, Q_e leads Q_i about 130°. Beyond the gamma oscillation area, the leading of Q_e over Q_i drops back to about 60°.

Figure 5.17 shows 20 phase plots for selected Q_{ns} values. All the subplots in Fig. 5.17 have been scaled to occupy the same window size. The abscissa for $\widetilde{Q}_e$ is from -8 to 8 s^{-1} and the ordinate for $\widetilde{Q}_i$ is from -2 to 2 s^{-1}. Plot **q** (Q_{ns}=540 s^{-1}) shows the axes values and labels. The display scale-factor for each subplot is indicated at its bottom left corner. The phase plot in subplot **q** has a scale-factor one. From Fig. 5.17, we can see the changing of the phase difference between Q_e and Q_i as Q_{ns} changes. At the beginning, the phase plot of Q_i and Q_e points to the right, which corresponds a small Q_e leading. With Q_{ns} increase, the phase plot changes its orientation. When Q_{ns} approaches gamma onset (subplot **f**), the phase plot abruptly rotates counterclockwise, and the limit cycle gradually emerges (subplots **i**, **j**). The phase plots are replotted in a single row in Fig. 5.18 to aid inspection of the phase-plot direction change and consequently the phase relation between Q_e and Q_i.

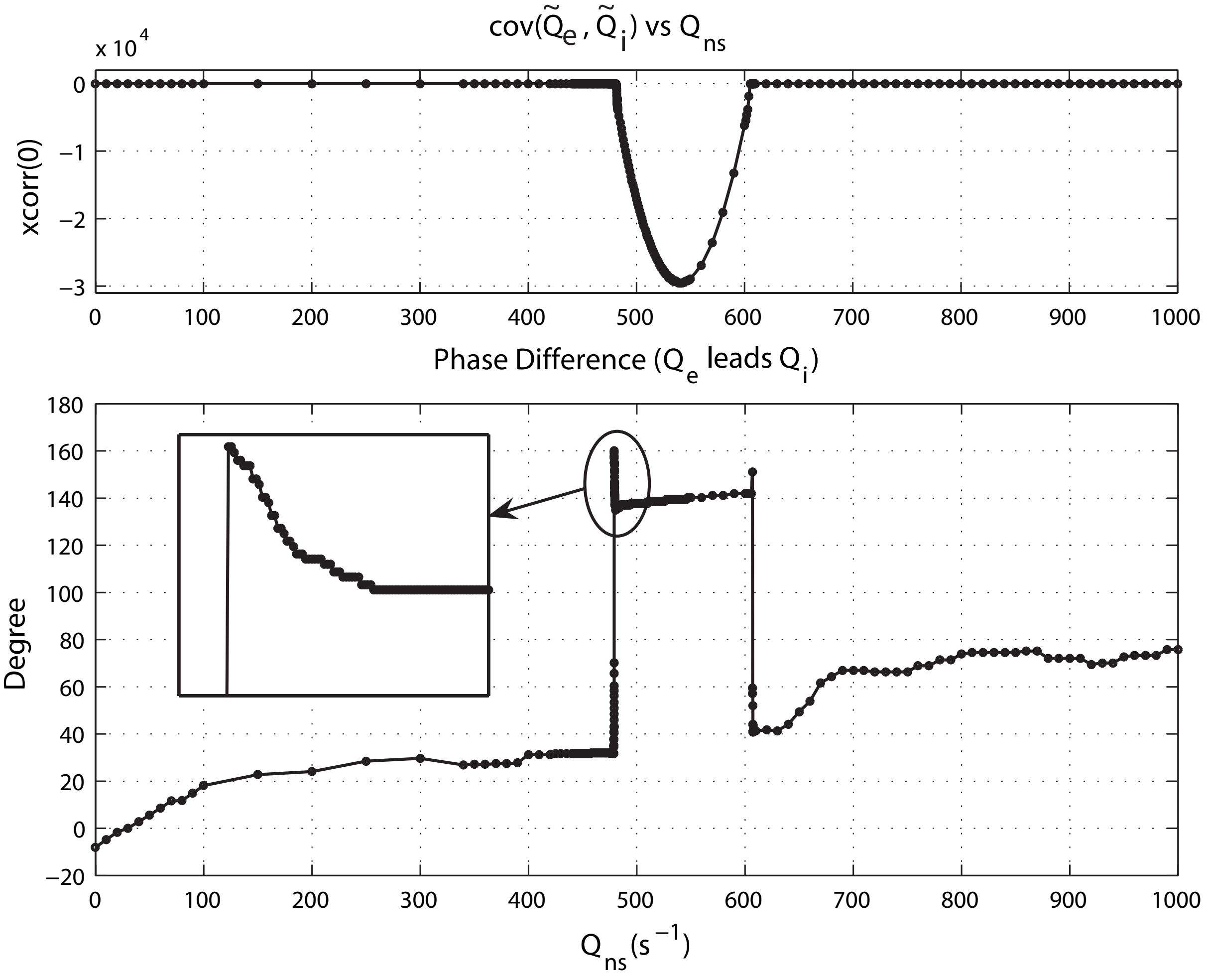

Figure 5.16: (a) Covariance (cross-correlation at zero lag) of excitatory and inhibitory firing rates in terms of Q_{ns}. (b) Phase difference between excitatory and inhibitory neuron cells with varying Q_{ns}. For the resonance region $478 \lesssim Q_{ns} \lesssim 600$ s^{-1}, the Q_e and Q_i oscillations are ∼140° out of phase, leading to the negative covariance trend shown in the upper graph.

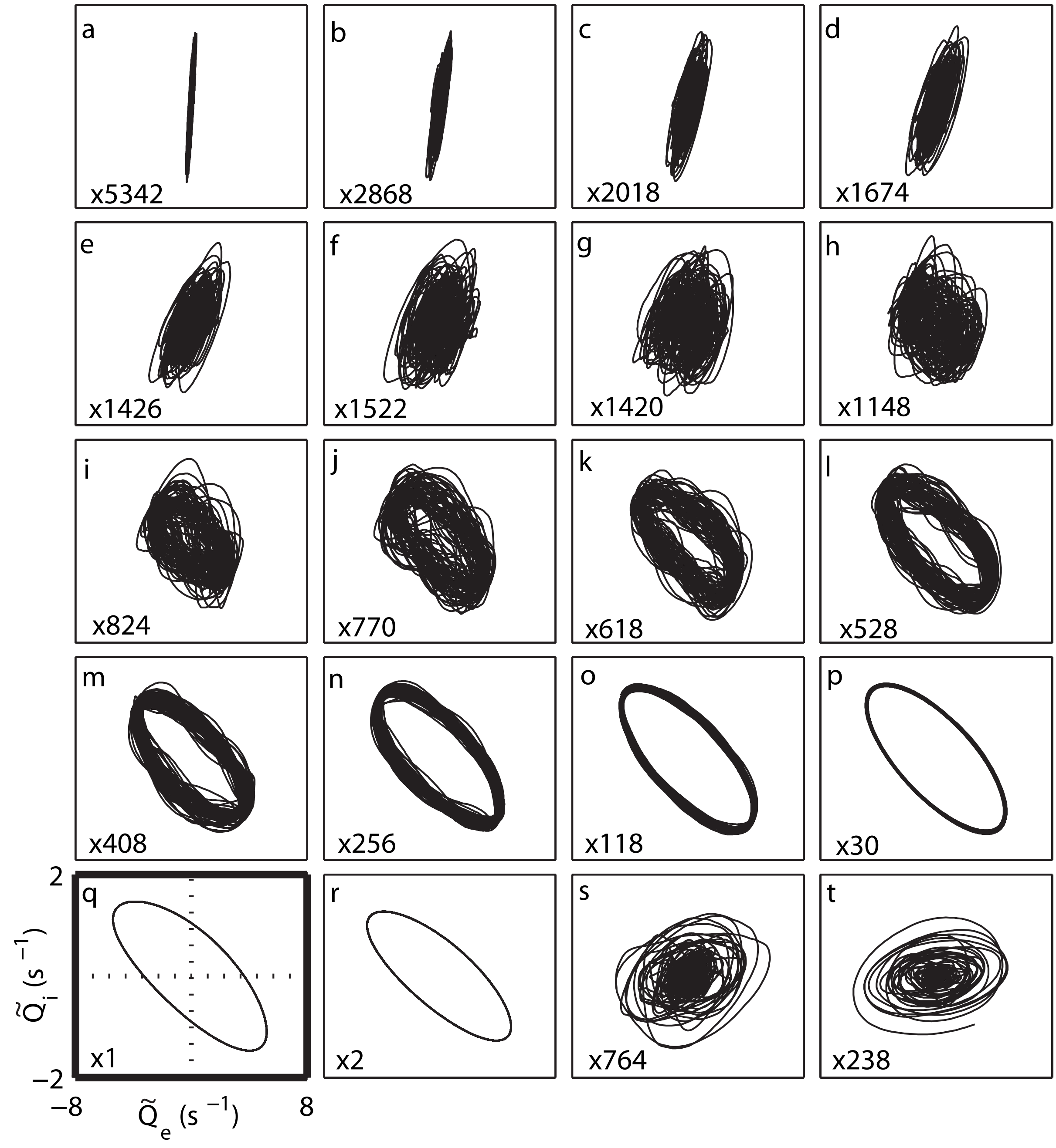

Figure 5.17: Gallery of phase plots showing fluctuations in Q_e, Q_i firing rates for selected Q_{ns} values. The Q_{ns} value for each subplot can be found in Table 5.7 by checking the corresponding letter labelled at its top left corner. The orientation of the phase plot determines the phase relationship (lead or lag) between Q_e and Q_i. The gamma threshold Q_{ns}^{crit} is 478.8793 s^{-1}, which is between subplot **e** (Q_{ns} = 476 s^{-1}) and **f** (Q_{ns} = 479 s^{-1}). During the prevalence of the gamma oscillation in the cortex, the phase of Q_i leads Q_e.

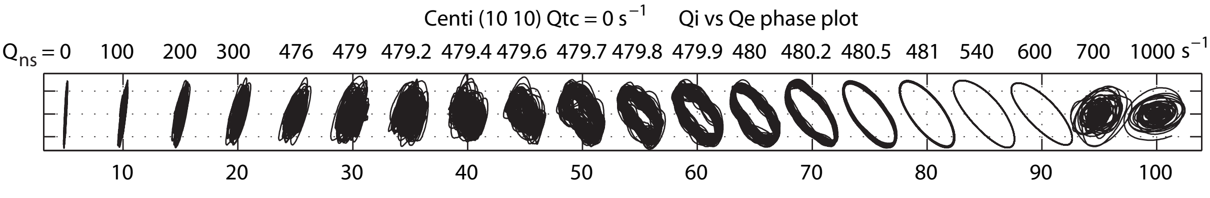

Figure 5.18: Gallery of phase plots for selected Q_{ns} values plotted in one row. The corresponding Q_{ns} value for each phase plot is labelled on its top.

5.2.6 Power Spectral Density

Power spectral analyses performed for 10-s simulation recordings of V_e and V_i are presented in Figs 5.19, 5.20, and 5.21. The cross-spectrum of V_e and V_i was achieved by calculating the Fourier transform of the cross-correlation of V_e and V_i and is shown in Fig. 5.19. It can be seen that before reaching the resonance area, there are multiple peaks existing in the cross spectrum. At $Q_{ns} = 0$ s^{-1}, there are five peaks present in the cross spectrum including one near DC. When Q_{ns} is 50 s^{-1}, the relative amplitudes of the lower-frequency peaks decrease while those at the higher frequencies increase. The peak at DC and the second peaks disappear at Q_{ns} of 100 s^{-1}. For $Q_{ns} > 100$ s^{-1}, the peak at 85 Hz dominates, but the relative amplitude of the peak at 117 Hz rises rapidly. Hence, when Q_{ns} reaches 450 s^{-1} which is close to to criticality point, two significant peaks (85 Hz and 117 Hz) exist in the cross-spectrum. When the cortex enters resonance, a single well-defined single gamma frequency 57 Hz is observed.

The spectra of V_e and V_i were obtained by calculating the Fourier transform of the auto-correlation of the V_e and V_i. The fluctuations spectra of V_e and V_i are similar to their cross-spectrum and are shown in Fig. 5.20 and 5.21 respectively. The spectra of V_e and V_i also have five peaks when Q_{ns} is 0 s^{-1}. When Q_{ns} increases, the relative amplitude of the peaks at lower frequencies decrease and the amplitude of the peaks at higher frequencies increase. Thus, as nonspecific afferent input (Q_{ns}) increases, the multiple peaks move to higher frequencies over several frequency bands. Both spectra for V_e and V_i shows a single frequency peak at 57 Hz at $Q_{ns} = 500$ s^{-1}, which is beyond the critical point and within the resonance area (limit cycle).

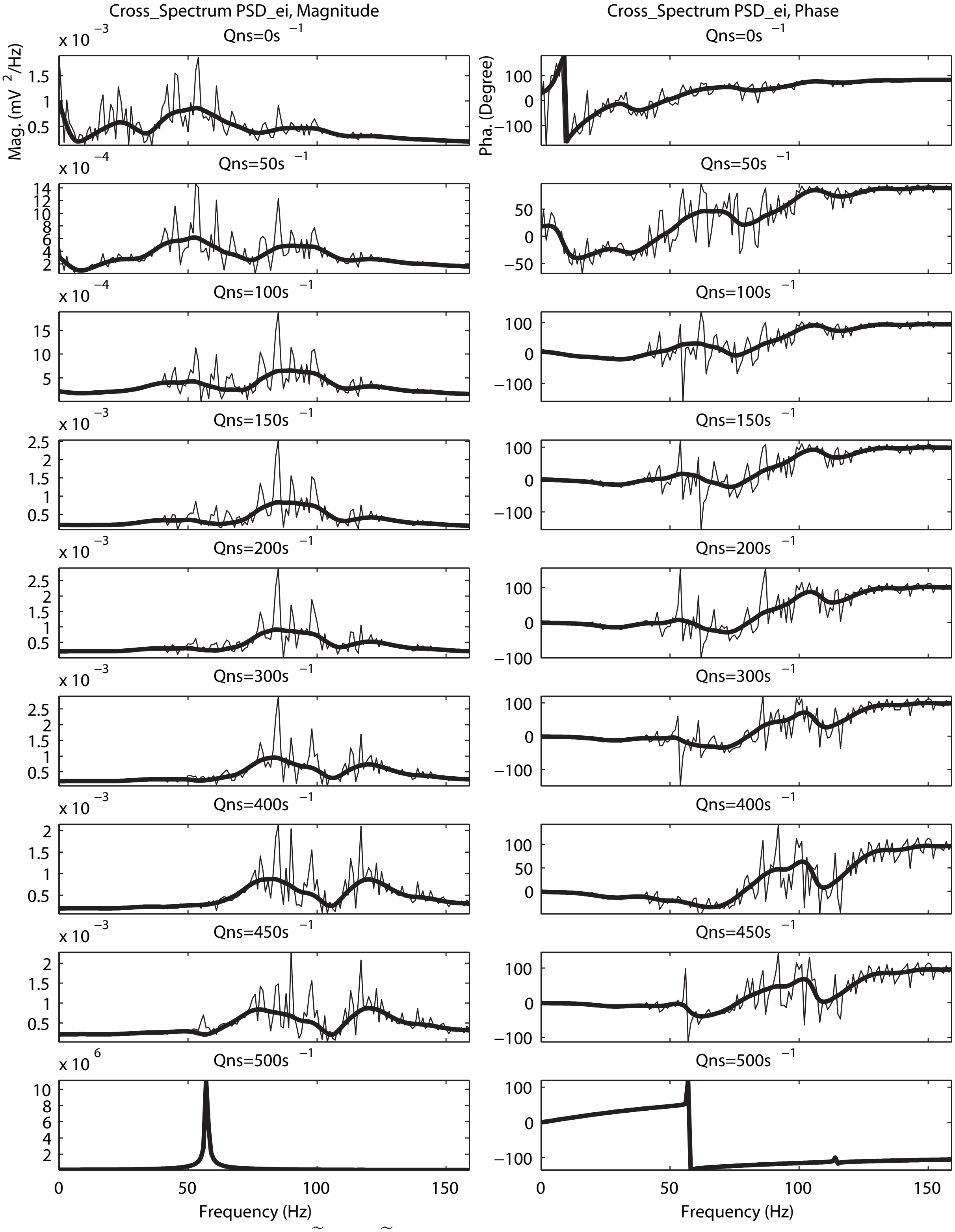

Figure 5.19: Cross spectrum of $\widetilde{V}_e$ and $\widetilde{V}_i$ at centimetric scale. From top to bottom, Q_{ns} is 0, 50, 100, 150, 200, 300, 400, 450, and 500 s^{-1}. Left column is the magnitude of the cross spectrum and right column is the phase of the cross spectrum. Note the extremely abrupt change in magnitude and phase characteristics when Q_{ns} is stepped from below (450 s^{-1}) to above (500 s^{-1}) gamma threshold. Thin lines: raw spectra; thick lines: smoothed spectra obtained using Whittaker filter.

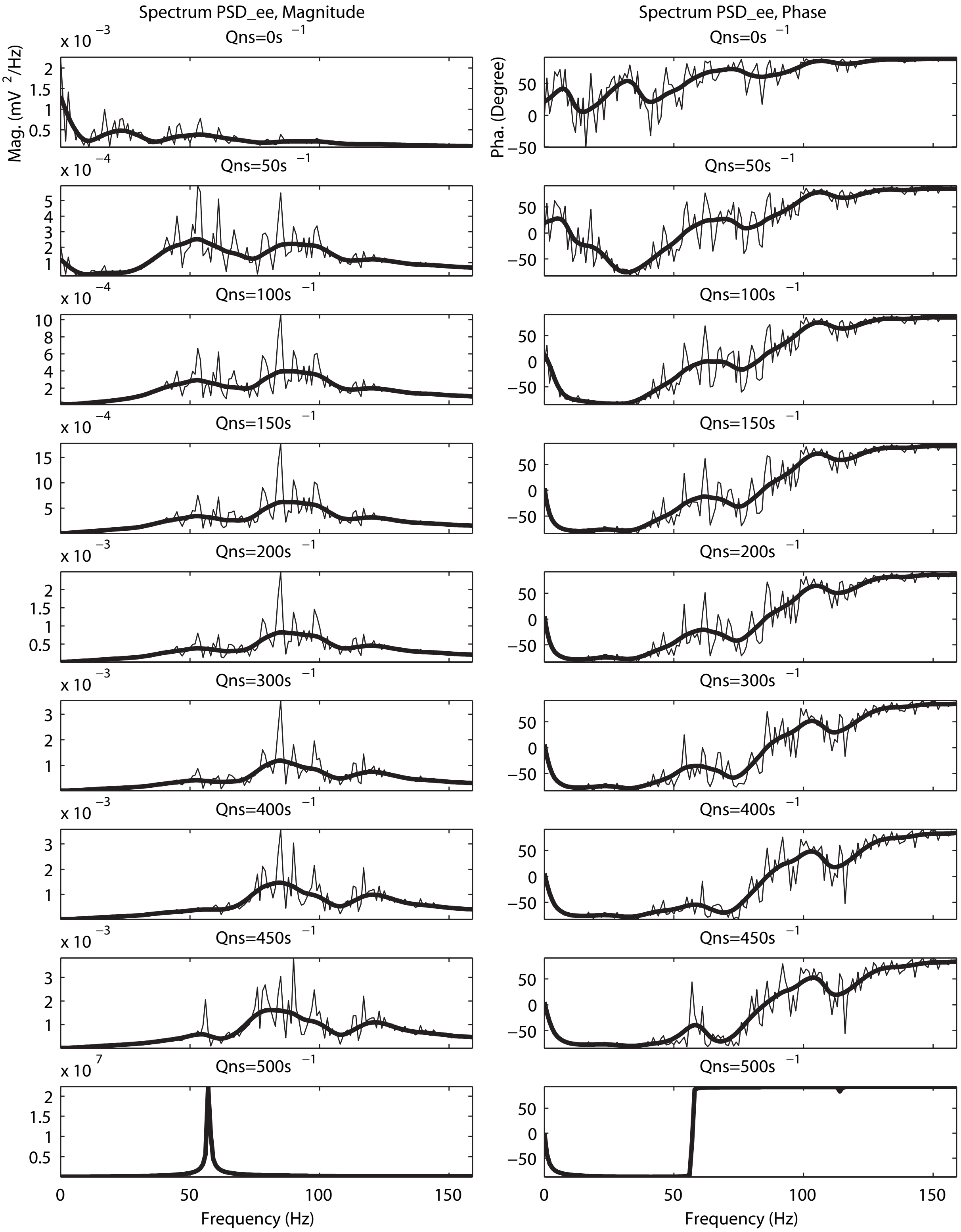

Figure 5.20: Spectrum of $\widetilde{V}_e$ at centimetric scale. From top to bottom, Q_{ns} is 0, 50, 100, 150, 200, 300, 400, 450, and 500 s^{-1}. Left column gives the magnitude of the spectrum and right column gives the phase of the spectrum.

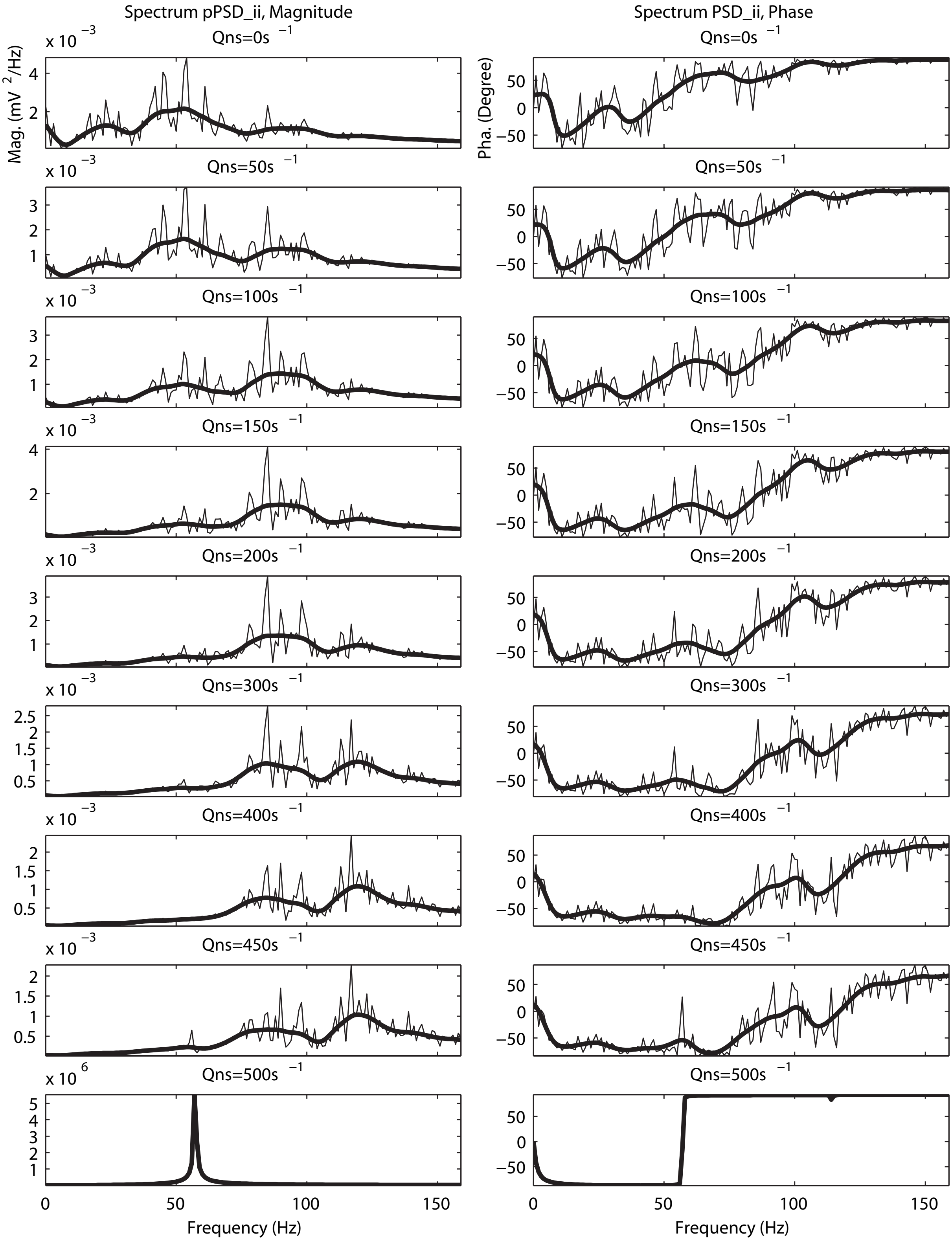

Figure 5.21: Spectrum of $\widetilde{V}_i$ at centimetric scale. From top to bottom, Q_{ns} is 0, 50, 100, 150, 200, 300, 400, 450, and 500 s^{-1}. Left column gives the magnitude of the spectrum and right column gives the phase of the spectrum. The magnitude and phase spectra are very similar to those obtained for the $\widetilde{V}_e$ spectra shown in Fig. 5.20.

5.2.7 Spatial Fourier Spectrum

The spatial Fourier spectra of local field potentials of the excitatory and inhibitory elements of the entire 20 by 20 grid points were computed using simulation results at different nonspecific afferent input (Q_{ns}) to study development of spatial periodicity of the cortical field. Figure 5.22 displays the spatial Fourier spectrum of the excitatory and inhibitory local field potentials for Gaussian noise generated by seed(1, 3). For $Q_{ns} \leq 478$ s^{-1}, we see the emergence of elliptical features in the spatial spectra, suggesting two distinct spatial frequencies oriented in mutually orthogonal directions. These could arise from standing or travelling waves of cortical activity. The ellipse formed at $Q_{ns} = 400$ s^{-1} has semiminor and semimajor axes of about 3 and 5 pixels, corresponding to spatial frequencies of 0.21 and 0.36 waves/cm, with wavelengths of ∼4.8 and 2.8 cm respectively.

In `ccf` simulation, Gaussian white noise is generated through a random number generator first reported by G. Marsaglia [72], which has a period of $2^{144} \approx 10^{43}$. Two integers seeds are needed to initialise the random number generator. The ranges for the two seeds are $0 \leq$ seed1 ≤ 31328 and $0 \leq$ seed2 ≤ 30081. New noise values are computed at each time step for each element in the cortical field.

To confirm that the spatial patterns in the subthreshold cortex are robust, and not artifacts caused by inadvertent spatial correlations in the particular noise sequence chosen, we repeated the spectral analysis with different choices of random seed. Figure 5.23 shows the results for seed(2000, 2000). The same elliptical features appear in the $V_{e,i}$ spectra as are seen in Fig. 5.23. Although the orientations differ, the size of the ellipses appear unchanged, implying that the emergent spatial frequencies are a robust property of the subthreshold cortex that is independent of the Gaussian noise stimulus.

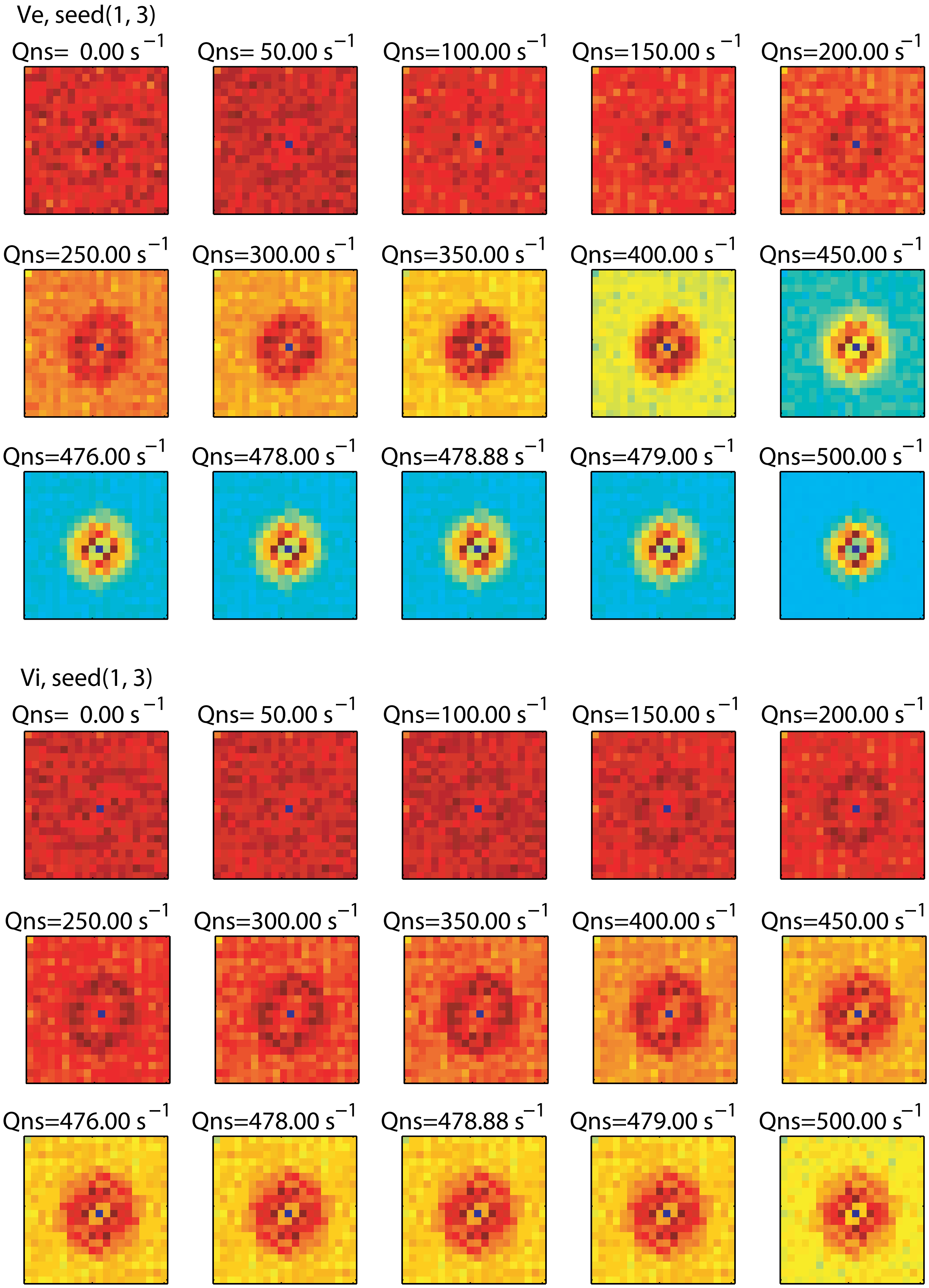

Figure 5.22: Spatial Fourier spectrum of local field potential of the excitatory and inhibitory elements (V_e, V_i) for the entire 20 by 20 cortex field with noise generated by noise seed(1, 3). The 15 values of Q_{ns} used in the 15 panels from top left and bottom right are 0, 50, 100, 150, 200, 250, 300, 350, 400, 450, 476, 478, 478.88, 479, and 500 s^{-1}. Given that a 20×20 grid repsents a 14×14-cm cortex, a length of 10 pixels in the Fourier spectrum corresponds to a spatial frequency of 0.71 waves/cm.

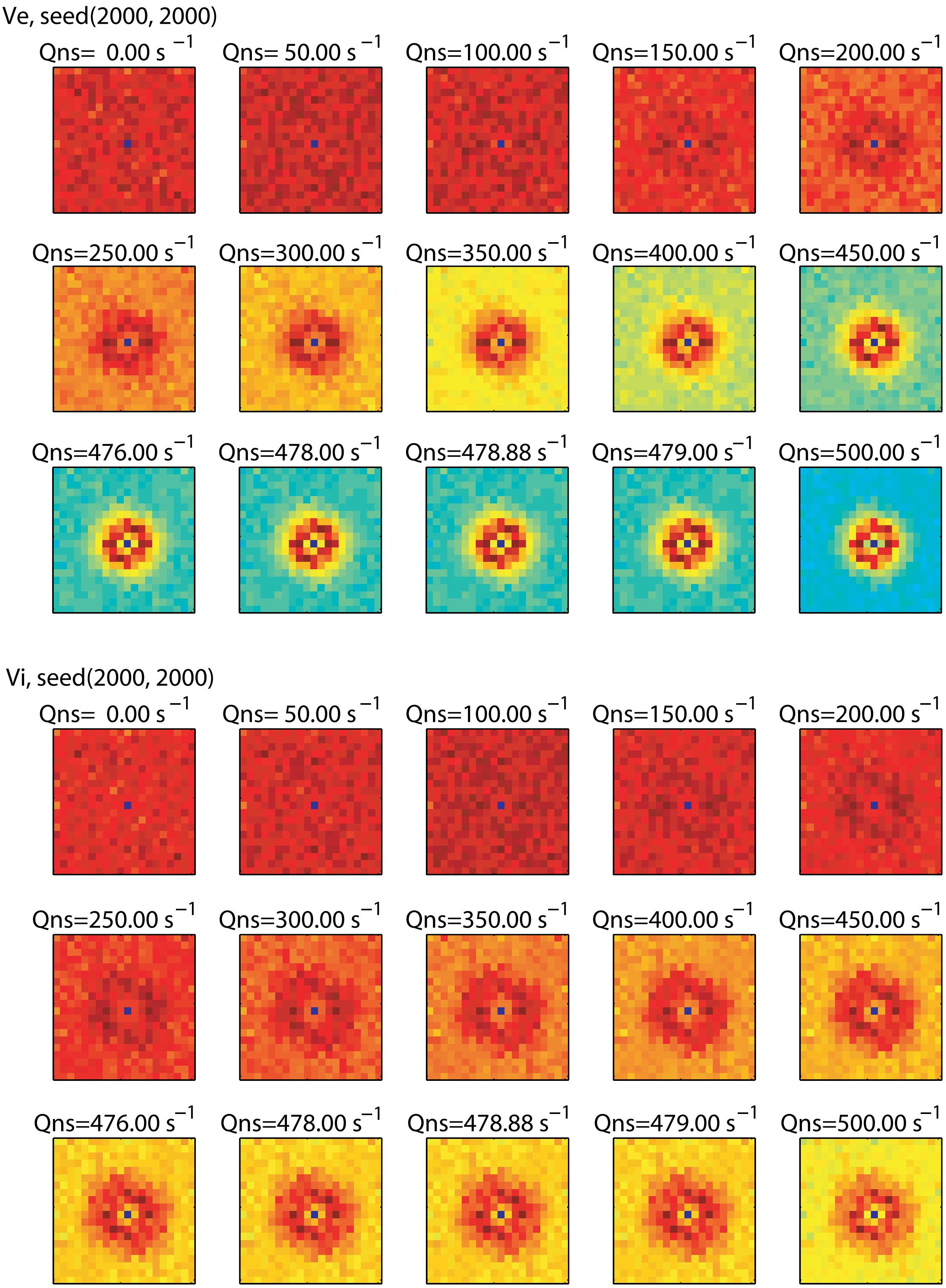

Figure 5.23: Spatial Fourier spectrum of V_e (top) and V_i (bottom) with noise generated by noise seed(2000, 20000). The Q_{ns} values in this figure are the same as those in Fig. 5.22.

5.3 Summary of `ccf` Investigation

The `ccf` model is a biophysically-motivated mathematical description of the cortex whose parameters are based on experimental results. By adjusting the parameters, `ccf` is capable of simulating some aspects of mammalian brains, including human and other animal species such as cat. As a first step towards exploring possible application to fetal sheep maturation, I developed familiarity with the model by investigating the properties of the excitatory and inhibitory elements in the cortical field during transition into the gamma resonance caused by the increased nonspecific afferent flux at the centimetric scale (global scale) of the `ccf` model. The major results, including time series, phase plots, average power, power law association, power spectral density, and spatial spectrum of the cortical field before and after the critical point of the gamma transition, have been described in the previous sections of this chapter.

The `ccf` model is a huge program with over 12,000 lines of `C` code. We found that a single 200-second simulation takes about 90 minutes on a 64-bit server. A one-second simulation of the full 20 by 20 cortical grid results in a 356 MB `eivw` file, containing time series of the four state variables: Q_e, Q_i, V_e, and V_i; file size can be reduced to 63 MB per second of simulation time by storing in `fits` (compressed binary) format. These huge file sizes make it difficult to record simulation results for extended periods. This also causes problems for analysis: using a personal computer (`Pentium` 4 CPU, 2.80 GHz, 504 MB `RAM`). I was not able to read in a one-second simulation of the full 20 × 20 grid. Instead, I needed to observe and analyse the one-second results on the 64-bit Linux server (`Tesla`) in our department.

From my work over several months, I find the `ccf` model to be a huge, biophysically sophisticated, but unwieldy platform to work with. Compared with the simpler Waikato mean field cortical model (described in Chapter 6), `ccf` is a more biophysically complete model with many more physiological mechanisms and features such as the receptor dynamics and retrograde propagation into the dentritic tree. Therefore, the `ccf` model is capable of simulating more physiological phenomena and brain dynamics. But it is so complicated and has so many input parameters that it is difficult to understand the program to a level sufficient to enable customization of parameters for specific simulation purposes. It also needs a large amount of hard-disk storage for the simulation outputs, and a very fast computer with capacious memory resources to analyse the results. Compared with `ccf`, the Waikato mean-field model is a nimbler, more flexible, and portable model with fewer simulation parameters. The model is comparatively easy to understand and has far less stringent hardware resource requirements. For these reasons, I have opted to use the Waikato cortical model, rather than `ccf`, for the fetal sheep simulations.

One important feature of the `ccf` model is the incorporation of the back-propagation effect. The retrograde signal from the soma to the dendritic tree will effect the generation of the action potential. The back-propagation effect is considered to be crucial to the synaptic integration and brain plasticity, especially the high frequency gamma oscillation. In order to simulate the high-freqency resonances found in the early immature EEG, I first try to incorporate the back-propagation effect into the Waikato cortical model. The standard Waikato mean-field equations and the incorporated Waikato cortical model, and their possible application to fetal sheep, are described in the next two chapters.

Chapter 6

Generalising the Waikato Mean Field Model for Back-Propagation Effects

The standard Waikato mean field model is a continuum description of the population-averaged properties of the cerebral cortex. The Waikato model was developed by Professor Moira Steyn-Ross and Associate Professor Alistair Steyn-Ross in 1999 at the School of Engineering of the University of Waikato [100–102]. Since then, the model has been extended to include additional physiological effects to make it a more complete computational model capable of simulating a larger range of cortical dynamics [99, 103, 104, 122, 123]. In this chapter, the Waikato mean field model is modified by introducing dendritic back-propagation effects into the continuum state equations by partitioning the dendrites into near (proximal) and far (distal) dendrites. The retrograde signal from the active dendritic back-propagation facilitated by the presence of the voltage-gated channels within dendrites will affect the initiation and propagation of action potentials at the soma. A linear stability analysis is performed for the near-far dendritic mean-field model.

6.1 Cortical Model with Near-Far Dendrites

6.1.1 Introduction

The human cerebral cortex contains about 10 billion (10^{10}) neurons organised into complex networks of local and long-range circuits. A typical brain neuron has connections with at least 1,000 other neurons. The Waikato mean field model treats the cortex as a 2-dimensional homogeneous and continuous cortical sheet composed of a large number of macrocolumns. The macrocolumn is the fundamental element of the cortical sheet; each macrocolumn contains approximately 100,000 (10^5) neurons of which 85% are excitatory and 15% are inhibitory, and occupies volume of about 1 mm^3.

Inhibitory neurons are small and have a random, symmetric distribution of dendrite and axon orientations. Excitatory neurons are larger. The axons and dendrites of excitatory neurons are parallel to each another and perpendicular to the scalp. Therefore, the cortical and scalp potentials measured by ECoG and EEG are mostly generated by excitatory neurons. So we assume the measured EEG and ECoG signal is proportional to fluctuations in the excitatory population soma voltage, V_e. Similar to the mean field continuum method of Liley [63], we use a set of coupled differential equations to describe the excitatory and inhibitory soma potentials and synaptic fluxes of a neuron population within a macrocolumn as a function of time and space. For the propagation of the action potential to the terminal of the neuron along the axon, a damped standard wave equation is used following Robinson [86].

6.1.2 Slow-Soma and Fast-Soma Cortical Model

When the neuron is at rest, that is before the neuron is stimulated to transmit an electrical impulse, the membrane potential of the neuron is held at a relatively stable value, called resting potential. The resting potential is a polarised state: the inside of the neuron is negative relative to the outside of the neuron because of unevenly distributed charges originating from sodium, potassium, and chloride ions. In our model, the resting voltage is set at $V_{e,i} = -64$ mV for both excitatory and inhibitory neuron populations.

Incoming synaptic flux from presynaptic neurons perturbs the soma voltage away from rest. The resulting soma voltages of the excitatory and inhibitory populations are expressed as the convolution of synaptic flux with the respective soma membrane response functions,

$$V_e(t) = V_e^{\text{rest}} + L_e(t) \otimes [\rho_e U_{ee}(t) + \rho_i U_{ie}(t)] \tag{6.1}$$

$$V_i(t) = V_i^{\text{rest}} + L_e(t) \otimes [\rho_e U_{ei}(t) + \rho_i U_{ii}(t)] \tag{6.2}$$

where L_b is the exponential soma-impulse response,

$$L_b(t) = \frac{1}{\tau_b} e^{-t/\tau_b}, \quad t > 0, \quad b \in \{e, i\} \tag{6.3}$$

in which τ_b is the soma time-constant for neuron of type b (e for excitatory or i for inhibitory). In Eqs (6.1) and (6.2), $\rho_{e,i}$ is the synaptic strength with unit mV·s. For excitatory post-synaptic potential (EPSP), $\rho_e > 0$, and for inhibitory post-synaptic potential (IPSP), $\rho_i < 0$. U is the postsynaptic response rate with unit s^{-1}. U_{ee} and U_{ei} are the excitatory postsynaptic response rates, while U_{ie} and U_{ii} are the inhibitory postsynaptic response rates. Our Waikato cortical model has two versions: "slow soma" and "fast soma". The postsynaptic response rates of the "slow soma" and "fast soma" variants are given in Eqs (6.4) and (6.5) respectively [104],

$$\begin{aligned} U_{ab}(t) &= \psi_{ab}(t) \cdot [H_{ab}(t) \otimes M_{ab}(t)] \\ &= \psi_{ab}(t) \int_0^t H_{ab}\left(t - t'\right) M_{ab}(t')\, dt' \quad a, b \in \{e, i\} \quad (\text{"slow soma"}) \end{aligned} \tag{6.4}$$

$$\begin{aligned} U_{ab}(t) &= H_{ab}(t) \otimes [\psi_{ab}(t) \cdot M_{ab}(t)] \\ &= \int_0^t H_{ab}\left(t - t'\right) \psi_{ab}(t') M_{ab}(t')\, dt' \quad a, b \in \{e, i\} \quad (\text{"fast soma"}) \end{aligned} \tag{6.5}$$

Here, ψ_{ab} is a dimensionless weighting function which scales the effectiveness of the synaptic input flux M_{ab}. ψ_{ab} is proportional to the difference of the soma voltage V_b and the relevant ionic reversal potential V_a^{rev}, and given in Eq. (6.6),

$$\psi_{ab}(t) = \frac{V_a^{\text{rev}} - V_b(t)}{V_a^{\text{rev}} - V_b^{\text{rest}}}, \quad a, b \in \{e, i\} \tag{6.6}$$

where b stands for either e or i. V_e^{rev} is the reversal potential of the excitatory receptors (`AMPA`), and has a value of 0 mV. For the reversal potential of the inhibitory receptors (`GABA`), $V_i^{\mathrm{rev}} = -70$ mV. This weighting function ψ_{ab} is unity when the neuron is at rest, and zero when the membrane potential matches the reversal potential.

An impulse arriving at a synapse from an activated neuron (presynaptic neuron) triggers the release of neurotransmitters into the synaptic cleft. The neurotransmitter binds to the receptor of the channel-shaped molecules in the membrane of the receiving (postsynaptic) neuron, opening the ion channel to allow charge to enter or leave the postsynaptic neuron, causing a momentary change in its membrane potential. The excitatory postsynaptic potential (EPSP) is a positive-going voltage change that increases the probability that the postsynaptic neuron will fire an action potential. The inhibitory postsynaptic potential (IPSP) is a negative-going voltage change that decreases the chance of action potential generation.

The dendrite impulse response function H_{ab} describes the shape of the momentary postsynaptic potential (PSP) as given in Eq. (6.7) for $t > 0$,

$$H_{ab}(t) = \begin{cases} \frac{\alpha\beta}{\beta-\alpha}\left(e^{-\alpha t} - e^{-\beta t}\right) & \alpha \neq \beta \\ \gamma^2 t e^{-\gamma t} & \alpha = \beta = \gamma \end{cases} \tag{6.7}$$

The shape of the dendrite impulse response function can be modelled either as a biexponential function for $\alpha \neq \beta$, or as an alpha function when $\alpha = \beta$. α, β, and γ are positive constants.

The separation between "fast-soma" and "slow-soma" limits is based on how fast the soma voltage changes during the period of dendritic integration. For "slow soma", if the response of the soma voltage is much slower than the dendritic integration, the weighting function ψ_{ab} approximately remains constant during the dendritic integration period. So the slow-arriving weighting function, ψ_{ab}, can be incorporated in Eq. (6.4) *after* the convolution of dendrite impulse response H_{ab} and input flux M_{ab}. For "fast soma", if the response speed of the soma voltage is similar to that of the dendritic integration, the fast-arriving weighting function, ψ_{ab}, is applied to the input flux M_{ab} first, that is, *before* the convolution of H_{ab} and M_{ab}. The integral form of the post-synaptic response rates of "slow soma" and "fast soma" are listed in Eqs (6.4) and 6.5.

The raw input flux coming from neuron of type a into neuron of type b is defined as M_{ab} and given in Eq. (6.8).

$$M_{ab} = N_{ab}^{\alpha}\phi_{ab}^{\alpha}(t) + N_{ab}^{\beta}\phi_{ab}^{\beta}(t) + N_{eb}^{\mathrm{sc}}\phi_{eb}^{\mathrm{sc}}, \quad a, b \in \{e, i\} \tag{6.8}$$

N_{ab} is the number of one-way synaptic connections from a *to* b (i.e., $a \rightarrow b$). The superscripts of N_{ab}, α, β, and sc represent longe-range (cortico-cortical connections from other macrocolumns), short-range (connections within one macrocolumn), and subcortical (input from subcortical structure such as thalamus and brain stem) synaptic connections respectively. ϕ_{ab}^{α} is the long-range cortico-cortical presynaptic flux-rate from $a \rightarrow b$, ϕ_{ab}^{β} is the short-range presynaptic flux-rate, and ϕ_{ab}^{sc} is the flux-rate coming from subcortex. In our model, there are no distant inhibitory connections from other macrocolumns. Hence,

$$N_{ib}^{\alpha} = N_{ib}^{\mathrm{sc}} = 0 \tag{6.9}$$

$$\phi_{ib}^{\alpha} = \phi_{ib}^{\mathrm{sc}} = 0 \tag{6.10}$$

Following Robinson [86], we assume both long-range and short-range fluxes ϕ_{ab}^{α} and ϕ_{ab}^{β} propagate obeying a 2-dimensional synaptic distribution function. The pair of damped wave equations are given in Eqs (6.11) and (6.12).

$$\left[\left(\frac{\partial}{\partial t} + \nu_{eb}^{\alpha}\Lambda_{eb}^{\alpha}\right)^2 - (\nu_{eb}^{\alpha})^2 \nabla^2\right] \phi_{eb}^{\alpha}(\vec{r},t) = (\nu_{eb}^{\alpha}\Lambda_{eb}^{\alpha})^2 Q_e(\vec{r},t), \quad b \in \{e,i\} \tag{6.11}$$

$$\left[\left(\frac{\partial}{\partial t} + \nu_{ab}^{\beta}\Lambda_{ab}^{\beta}\right)^2 - \left(\nu_{ab}^{\beta}\right)^2 \nabla^2\right] \phi_{ab}^{\beta}(\vec{r},t) = \left(\nu_{ab}^{\beta}\Lambda_{ab}^{\beta}\right)^2 Q_a(\vec{r},t), \quad a,b \in \{e,i\} \tag{6.12}$$

where Λ_{ab}^{α} and Λ_{ab}^{β} is the inverse-length scale for long-range and short-range axonal connections respectively. Λ_{ab}^{α} and Λ_{ab}^{β} have units of cm^{-1}. ν_{eb}^{α} is the long-range axonal conduction speed with unit cm s^{-1}; ν_{ab}^{β} is the short-range axonal conduction speed.

In Eqs (6.11) and (6.12), Q_a is the empirical sigmoid mapping from membrane voltage V_a to firing rate of neuron of type a,

$$Q_a(\vec{r},t) = \frac{Q_a^{\max}}{1 + \exp\left[-C\left(V_a(\vec{r},t) - \theta_a\right)/\sigma_a\right]}, \quad a \in \{e,i\} \tag{6.13}$$

in which θ_a is the population-average threshold voltage for neuronal firing, σ_a measures the spread of the sigmoid function, $Q_a^{\max}$ is the maximal firing rate for the macrocolumn population, and the constant $C = \pi/\sqrt{3}$ [82].

The subcortical flux, ϕ_{eb}^{sc}, is defined in Eq. (6.14) with a fixed term, and a stochastic term.

$$\phi_{eb}^{\mathrm{sc}}(\vec{r},t) = sQ_e^{\max} + \gamma\sqrt{sQ_e^{\max}}\xi_m(\vec{r},t), \quad m = 1,2 \tag{6.14}$$

where γ is a constant dimensionless noise scale-factor. ξ_m are a pair of Gaussian-distributed, zero-mean, spatio-temporal white-noise sources that are delta-correlated in time and space.

$$\langle \xi_m(\vec{r},t)\rangle = 0, \tag{6.15}$$

$$\left\langle \xi_m(\vec{r},t)\xi_n(\vec{r}')\right\rangle = \delta_{mn}\delta(t-t')\delta(\vec{r}-\vec{r}') \tag{6.16}$$

6.1.3 Near-Far Cortical Model

Based on the Waikato "fast soma" cortical model, the back propagation effect was incorporated into our model for the first time based on the idea of Wright [126, 127]. The membrane of the proximal dendritic tree is depolarised by the retrograde propagation after an action potential is released at the soma. In our model, "near" synapses refer to those synapses within the zone of back propagation and "far" synapses to those synapses more distal in the dendritic trees.

The impact of the transmission of total synaptic flux to the trigger point depends upon cable delays in the near and far dendritic trees, and on the fraction of the neurons which have recently fired. Hence, the fraction of neurons responding primarily to near or far synapses are defined in Eqs (6.17) and (6.18) respectively,

$$A_b^n \; = \; 1 - \bar{Q}_b/Q_b^{\max} \tag{6.17}$$

$$A_b^f \; = \; \bar{Q}_b/Q_b^{\max} \tag{6.18}$$

A_b^n and A_b^f stands for near and far dendritic fractions respectively. As stated before, $Q_b^{\max}$ is the maximum firing rate of the neuron of type b (b is e or i). $\bar{Q}_b$ is the pulse density (or firing rate) of neuron b at steady state.

The convolution equations of the excitatory and inhibitory soma voltages then can be redefined to create the near-far Waikato cortical model in Eqs (6.19) and (6.20),

$$V_e(t) \; = \; V_e^{\text{rest}} + A_b^n L_e^n(t) \otimes [\rho_e U_{ee}(t) + \rho_i U_{ie}(t)] + A_b^f L_e^f(t) \otimes [\rho_e U_{ee}(t) + \rho_i U_{ie}(t)] \tag{6.19}$$

$$V_i(t) \; = \; V_i^{\text{rest}} + A_b^n L_e^n(t) \otimes [\rho_e U_{ei}(t) + \rho_i U_{ii}(t)] + A_b^f L_e^f(t) \otimes [\rho_e U_{ei}(t) + \rho_i U_{ii}(t)] \tag{6.20}$$

The definitions of $V_{e,i}$, $\rho_{e,i}$, and U_{ab} are the same as before. The impulse response of the soma, $L_b^j(t)$, for neuron of type b (e or i) are given in Eq. (6.21),

$$L_b^j(t) \; = \; d_j e^{-d_j t}, \quad t > 0; \quad b \in \{e, i\}, \quad j \in \{n, f\} \tag{6.21}$$

in which d_j are rate constants of the soma receiving stimulus from dendrites j. $j = n, f$ indicates synapses located in the near and far dendritic trees respectively. Thus, the impulse response functions L_b^n and L_b^f describe the cable delay in the near and far dendritic trees. In order to simplify the results of the steady states analysis, the rate constants (d_j) are used here, instead of time constant (τ_b) as in Eq. (6.3). The rate constant is the inverse of the time constant.

By modifying the definition of postsynaptic response rate, U_{ab} (a, $b \in e$, i), the near-far effects can be applied to both the slow- and fast-soma versions of the Waikato cortical model. Therefore, the near-far slow-soma model and near-far fast-soma model can be expressed in Eqs (6.22) and (6.23).

$$\begin{aligned} V_b(t) \; = \; & V_b^{\text{rest}} + A_b^n L_b^n(t) \otimes \{\rho_e \psi_{eb}(t) \cdot [H_{eb}(t) \otimes M_{eb}(t)] + \rho_i \psi_{ib}(t) \cdot [H_{ib}(t) \otimes M_{ib}(t)]\} \\ & + A_b^f L_b^f(t) \otimes \{\rho_e \psi_{eb}(t) \cdot [H_{eb}(t) \otimes M_{eb}(t)] + \rho_i \psi_{ib}(t) \cdot [H_{ib}(t) \otimes M_{ib}(t)]\} \end{aligned}$$

slow-soma with near-far dendritic tree (6.22)

$$\begin{aligned} V_b(t) \; = \; & V_b^{\text{rest}} + A_b^n L_b^n(t) \otimes \{\rho_e H_{eb}(t) \otimes [\psi_{eb}(t) \cdot M_{eb}(t)] + \rho_i H_{ib}(t) \otimes [\psi_{ib}(t) \cdot M_{ib}(t)]\} \\ & + A_b^f L_b^f(t) \otimes \{\rho_e H_{eb}(t) \otimes [\psi_{eb}(t) \cdot M_{eb}(t)] + \rho_i H_{ib}(t) \otimes [\psi_{ib}(t) \cdot M_{ib}(t)]\} \end{aligned}$$

fast-soma with near-far dendritic tree (6.23)

6.1.4 State Variables and Parameter Values

State variables for slow-soma and fast-soma models are listed in Table. 6.1. The definition of dendritic flux response, U_{ab}, for slow-soma and fast-soma model is different. For slow-soma model, $U_{ab} = \psi_{ab} \cdot [H_{ab} \otimes M_{ab}] = \psi_{ab} \cdot \Phi_{ab}$. For fast-soma, the order of $\cdot$ (product) and $\otimes$ (convolution) operations is reversed, $U_{ab} = H_{ab} \otimes [\psi_{ab} \cdot M_{ab}]$.

Table 6.1: State variables for Waikato near-far dendrite slow- and fast-soma mean field model [104]

State variables	Description	Unit
V_e, V_i	Soma voltage	mV
U_{ee}, U_{ei}, U_{ie}, U_{ii}	Dendritic flux response	s^{-1}
ϕ^{α}_{ee}, ϕ^{α}_{ei}	Long-range flux input	s^{-1}
ϕ^{β}_{ee}, ϕ^{β}_{ei}, ϕ^{β}_{ie}, ϕ^{β}_{ii}	Short-range flux input	s^{-1}

Table 6.2: Other system variables for Waikato near-far dendrite slow- and fast-soma model [104]

Variables	Description	Unit
M_{ab}	Total flux input	s^{-1}
Q_a	Firing rate	s^{-1}
H_{ab}	Dendritic impulse function	s^{-1}
L_b	Soma impulse function	s^{-1}
ψ_{ab}	Reversal-potential weight	-
Φ_{ab}	Slow-soma convolved flux	s^{-1}
ϕ^{sc}_{eb}	Subcortical flux	s^{-1}

6.2 Stability Analysis for Near-Far Fast-Soma Cortical Model

6.2.1 Summary of Fast-Soma DEs with Near-Far Dendrites

The complete set of equations describing the population averages of soma potential, synaptic fluxes and axonal wave propagation, as a function of space and time, are listed in Eqs (6.24)–(6.32) below:

Soma potentials

$$\frac{1}{d}\frac{\partial V_b(t)}{\partial t} = -V_b(t) + V_b^{\text{rest}} + \frac{1}{d}\left[W_b^f(t) + W_b^n(t)\right] + \frac{A_b^n d_n + A_b^f d_f}{d}\left[\rho_e U_{eb}(t) + \rho_i U_{ib}(t)\right] + D_j \nabla^2 V_b \tag{6.24}$$

where $d = d_n + d_f$, $b \in \{e, i\}$, and $j \in \{1, 2\}$. Here, d_n and d_f are the rate constants for the near and far dendritic tree.

Synaptic fluxes

$$\frac{1}{d_f}\frac{dW_b^f(t)}{dt} = -W_b^f(t) + d_n A_b^f\left[\rho_e U_{eb}(t) + \rho_i U_{ib}(t)\right] \tag{6.25}$$

Table 6.3: Standard parameters used in the Waikato mean field model [104]

Parameter	Description	Standard values (Unit)
$\tau_{e,i}$	Membrane time constants	0.050, 0.050 (s)
$V_{e,i}^{\text{rev}}$	Reversal potential for AMPA, GABA channels	0, −70 (mV)
$V_{e,i}^{\text{rest}}$	Cell resting potential	−60, −60 (mV)
$\rho_{e,i}$	Synaptic gain at resting potential	(2.4, −5.9) × 10 $^{-3}$ (mV · s)
β_{ee}, β_{ie}	PSP rise-rate in excitatory neurons	500, 500 (s^{-1})
β_{ei}, β_{ii}	PSP rise-rate in inhibitory neurons	500, 500 (s^{-1})
α_{ee}	EPSP decay-rate in excitatory neurons	68 (s^{-1})
α_{ei}	EPSP decay-rate in inhibitory neurons	176 (s^{-1})
α_{ie}	IPSP decay-rate in excitatory neurons	47 (s^{-1})
α_{ii}	IPSP decay-rate in inhibitory neurons	82 (s^{-1})
N_{eb}^{α}	Long-range $e \to b$ axonal connectivity	3710 (dimensionless)
N_{eb}^{β}	Local $e \to b$ axonal connectivity	410 (dimensionless)
N_{ib}^{β}	Local $i \to b$ axonal connectivity	800 (dimensionless)
s	Control parameter for subcortical synaptic flux	0.1 (dimensionless)
ν_{eb}^{α}	Long-range $e \to b$ axonal speed	140 (cm s^{-1})
ν_{eb}^{β}, ν_{ib}^{β}	Local $e \to b$, $i \to b$ axonal speed	20, 20 (cm s^{-1})
Λ_{eb}^{α}	Inverse-length scale for long-range $e \to b$ axons (slow-soma model)	4 (cm^{-1})
Λ_{eb}^{α}	Inverse-length scale for long-range $e \to b$ axons (fast-soma model)	1 (cm^{-1})
Λ_{eb}^{β}, Λ_{ib}^{β}	Inverse-length scale for long-range $e \to b$, $i \to b$ axons	50, 50 (cm^{-1})
$Q_{e,i}^{\max}$	Maximum firing rate	100, 200 (s^{-1})
$\theta_{e,i}$	Threshold voltage for firing	−52, −52 (mV)
$\sigma_{e,i}$	Standard deviation for threshold	5, 5 (mV)

$$\frac{1}{d_n}\frac{dW_b^n(t)}{dt} \;=\; -W_b^n(t) + d_f A_b^n\left[\rho_e U_{eb}(t) + \rho_i U_{ib}(t)\right] \tag{6.26}$$

$$\left(\frac{d}{dt} + \alpha_{ab}\right)\left(\frac{d}{dt} + \beta_{ab}\right) U_{ab}(t) \;=\; \alpha_{ab}\beta_{ab}\psi_{ab}(t) M_{ab}(t), \quad a, b \in \{e, i\} \tag{6.27}$$

where

$$M_{ab}(t) \;=\; N_{ab}^{\alpha}\phi_{ab}^{\alpha}(t) + N_{ab}^{\beta}\phi_{ab}^{\beta}(t) + N_{eb}^{\text{sc}}\phi_{eb}^{\text{sc}} \tag{6.28}$$

Long-range wave equations

$$\left[\left(\frac{\partial}{\partial t} + \nu_{eb}^{\alpha}\Lambda_{eb}^{\alpha}\right)^2 - \left(\nu_{eb}^{\alpha}\right)^2 \nabla^2\right] \phi_{eb}^{\alpha}\left(\vec{r}, t\right) \;=\; \left(\nu_{eb}^{\alpha}\Lambda_{eb}^{\alpha}\right)^2 Q_e\left(\vec{r}, t\right), \quad b \in \{e, i\} \tag{6.29}$$

Short-range wave equations

$$\left[\left(\frac{\partial}{\partial t} + \nu_{ab}^{\beta}\Lambda_{ab}^{\beta}\right)^2 - \left(\nu_{ab}^{\beta}\right)^2 \nabla^2\right] \phi_{ab}^{\beta}\left(\vec{r}, t\right) \;=\; \left(\nu_{ab}^{\beta}\Lambda_{ab}^{\beta}\right)^2 Q_a(\vec{r}, t), \quad a, b \in \{e, i\} \tag{6.30}$$

Subcortical flux

$$\phi_{eb}^{\mathrm{sc}}(\vec{r},t) \;=\; sQ_e^{\max} + \gamma\sqrt{sQ_e^{\max}}\,\xi_m(\vec{r},t)\,, \quad m \;=\; 1,2 \tag{6.31}$$

Voltage-to-firing rate sigmoid

$$Q_a(\vec{r},t) \;=\; \frac{Q_a^{\max}}{1+\exp\left[-\pi/\sqrt{3}\left(V_a(\vec{r},t)-\theta_a\right)/\sigma_a\right]}, \quad a \in \{e,i\} \tag{6.32}$$

$\vec{r}$ is the 2-D position vector. In Eq. (6.24), the diffusion effects of gap junctions are included in differential equations of the soma voltages as a Laplacian scaled by excitatory and inhibitory coefficients D_1 and D_2. The mean-field treatment of the gap junctions and the incorporation of diffusive terms into the Waikato mean-field model are first introduced in the 2007 paper by M. Steyn-Ross et al [103]. The definitions for all other variables were given earlier in Section 6.1.

6.2.2 Steady States

To find the equilibrium states of the noiseless homogenous cortex, the first and second order of time and space derivatives are set to zero ($\partial/\partial t \;=\; 0$ and $\nabla^2 \;=\; 0$) in the set of differential equations (6.24)–(6.30). The subcortical stochastic noise terms are also set to zero ($\xi_m(\vec{r},t) = 0$) in Eq. (6.31). The obtained state variables at the equilibrium state are given in a set of coupled nonlinear algebraic equations (6.33)–(6.42). Inspecting these equations, we see the soma voltage at the equilibrium state, V_b^0, cannot be solved analytically. Hence, we utilise a numerical method to solve the set of coupled nonlinear algebraic equations to obtain the V_e^0, V_i^0, Q_e^0, and Q_i^0. According to our computation, the steady states of the near-far dendritic tree model is the same as that of fast-soma and slow-soma models.

$$Q_a^0 \;=\; \frac{Q_a^{\max}}{1+\exp\left[-\pi/\sqrt{3}\left(V_a^0-\theta_a\right)/\sigma_a\right]} \tag{6.33}$$

$$\left(\phi_{eb}^{\alpha}\right)^0 \;=\; Q_e^0 \tag{6.34}$$

$$\left(\phi_{ab}^{\beta}\right)^0 \;=\; Q_a^0 \tag{6.35}$$

$$\left(\phi_{eb}^{\mathrm{sc}}\right)^0 \;=\; sQ_e^{\max} \tag{6.36}$$

$$\psi_{ab}^0 \;=\; \frac{V_a^{\mathrm{rev}}-V_b^0}{V_a^{\mathrm{rev}}-V_b^{\mathrm{rest}}} \tag{6.37}$$

$$M_{ab}^0 \;=\; N_{ab}^{\alpha}\left(\phi_{ab}^{\alpha}\right)^0 + N_{ab}^{\beta}\left(\phi_{ab}^{\beta}\right)^0 + N_{eb}^{\mathrm{sc}}\left(\phi_{eb}^{\mathrm{sc}}\right)^0 \tag{6.38}$$

$$U_{ab}^{0} = \psi_{ab}^{0} M_{ab}^{0} \tag{6.39}$$

$$\left(W_b^f\right)^0 = d_n A_b^f \left[\rho_e U_{eb}^0 + \rho_i U_{ib}^0\right] \tag{6.40}$$

$$\left(W_b^n\right)^0 = d_f A_b^n \left[\rho_e U_{eb}^0 + \rho_i U_{ib}^0\right] \tag{6.41}$$

$$V_b^0 = V_b^{\text{rest}} + \frac{1}{d}\left[\left(W_b^f\right)^0 + \left(W_b^n\right)^0\right] + \frac{A_b^n d_n + A_b^f d_f}{d}\left[\rho_e U_{eb}^0 + \rho_i U_{ib}^0\right] \tag{6.42}$$

To explore the distribution of equilibrium states available to the cortex, we choose subcortical afferent flux ϕ_{eb}^{sc} as the control parameter. Equation (6.36) shows ϕ_{eb}^{sc} at equilibrium state is a function of subcortical drive s ($0 \leq s \leq 1$). So by changing subcortical drive s, we can vary the subcortical afferent flux ϕ_{eb}^{sc}.

6.2.3 First-Order Partial Differential Equations

The second-order differential equations (6.27)–(6.30) were rewritten as pairs of coupled first-order differential equations. The final set of 26 first-order differential equations in time are shown in equations (6.43)–(6.68).

$$\frac{1}{d}\frac{\partial V_e}{\partial t} = -V_e + V_e^{\text{rest}} + \frac{1}{d}\left[W_e^f + W_e^n\right] + \frac{A_e^n d_n + A_e^f d_f}{d}\left[\rho_e U_{ee} + \rho_i U_{ie}\right] + D_1 \nabla^2 V_e \tag{6.43}$$

$$\frac{1}{d}\frac{\partial V_i}{\partial t} = -V_i + V_i^{\text{rest}} + \frac{1}{d}\left[W_i^f + W_i^n\right] + \frac{A_i^n d_n + A_i^f d_f}{d}\left[\rho_e U_{ei} + \rho_i U_{ii}\right] + D_2 \nabla^2 V_i \tag{6.44}$$

$$\frac{1}{d_f}\frac{dW_e^f}{dt} = -W_e^f + d_n A_e^f \left[\rho_e U_{ee} + \rho_i U_{ie}\right] \tag{6.45}$$

$$\frac{1}{d_n}\frac{dW_e^n}{dt} = -W_e^n + d_f A_e^n \left[\rho_e U_{ee} + \rho_i U_{ie}\right] \tag{6.46}$$

$$\frac{1}{d_f}\frac{dW_i^f}{dt} = -W_i^f + d_n A_i^f \left[\rho_e U_{ei} + \rho_i U_{ii}\right] \tag{6.47}$$

$$\frac{1}{d_n}\frac{dW_i^n}{dt} = -W_i^n + d_f A_i^n \left[\rho_e U_{ei} + \rho_i U_{ii}\right] \tag{6.48}$$

$$\frac{dU_{ee}}{dt} = A_{ee} \tag{6.49}$$

$$\frac{dA_{ee}}{dt} = -\left(\alpha_{ee}+\beta_{ee}\right)A_{ee}+\alpha_{ee}\beta_{ee}\left[\psi_{ee}\left(N_{ee}^{\alpha}\phi_{ee}^{\alpha}+N_{ee}^{\beta}\phi_{ee}^{\beta}+N_{ee}^{sc}\phi_{ee}^{sc}\right)-U_{ee}\right] \tag{6.50}$$

$$\frac{dU_{ei}}{dt} = A_{ei} \tag{6.51}$$

$$\frac{dA_{ei}}{dt} = -\left(\alpha_{ei}+\beta_{ei}\right)A_{ei}+\alpha_{ei}\beta_{ei}\left[\psi_{ei}\left(N_{ei}^{\alpha}\phi_{ei}^{\alpha}+N_{ei}^{\beta}\phi_{ei}^{\beta}+N_{ei}^{sc}\phi_{ei}^{sc}\right)-U_{ei}\right] \tag{6.52}$$

$$\frac{dU_{ie}}{dt} = A_{ie} \tag{6.53}$$

$$\frac{dA_{ie}}{dt} = -\left(\alpha_{ie}+\beta_{ie}\right)A_{ie}+\alpha_{ie}\beta_{ie}\left[\psi_{ie}N_{ie}^{\beta}\phi_{ie}^{\beta}-U_{ie}\right] \tag{6.54}$$

$$\frac{dU_{ii}}{dt} = A_{ii} \tag{6.55}$$

$$\frac{dA_{ii}}{dt} = -\left(\alpha_{ii}+\beta_{ii}\right)A_{ii}+\alpha_{ii}\beta_{ii}\left[\psi_{ii}N_{ii}^{\beta}\phi_{ii}^{\beta}-U_{ii}\right] \tag{6.56}$$

$$\frac{d\phi_{ee}^{\alpha}}{dt} = B_{ee} \tag{6.57}$$

$$\frac{dB_{ee}}{dt} = -2\nu_{ee}^{\alpha}\Lambda_{ee}^{\alpha}B_{ee}-\left(\nu_{ee}^{\alpha}\right)^2\left[\left(\Lambda_{ee}^{\alpha}\right)^2-\nabla^2\right]\phi_{ee}^{\alpha}+\left(\nu_{ee}^{\alpha}\Lambda_{ee}^{\alpha}\right)^2Q_e \tag{6.58}$$

$$\frac{d\phi_{ei}^{\alpha}}{dt} = B_{ei} \tag{6.59}$$

$$\frac{dB_{ei}}{dt} = -2\nu_{ei}^{\alpha}\Lambda_{ei}^{\alpha}B_{ei}-\left(\nu_{ei}^{\alpha}\right)^2\left[\left(\Lambda_{ei}^{\alpha}\right)^2-\nabla^2\right]\phi_{ei}^{\alpha}\left(\vec{r},t\right)+\left(\nu_{ei}^{\alpha}\Lambda_{ei}^{\alpha}\right)^2Q_e \tag{6.60}$$

$$\frac{d\phi_{ee}^{\beta}}{dt} = C_{ee} \tag{6.61}$$

$$\frac{dC_{ee}}{dt} = -2\nu^{\beta}_{ee}\Lambda^{\beta}_{ee}C_{ee} - \left(\nu^{\beta}_{ee}\right)^2\left[\left(\Lambda^{\beta}_{ee}\right)^2 - \nabla^2\right]\phi^{\beta}_{ee} + \left(\nu^{\beta}_{ee}\Lambda^{\beta}_{ee}\right)^2 Q_e \tag{6.62}$$

$$\frac{d\phi^{\beta}_{ei}}{dt} = C_{ei} \tag{6.63}$$

$$\frac{dC_{ei}}{dt} = -2\nu^{\beta}_{ei}\Lambda^{\beta}_{ei}C_{ei} - \left(\nu^{\beta}_{ei}\right)^2\left[\left(\Lambda^{\beta}_{ei}\right)^2 - \nabla^2\right]\phi^{\beta}_{ei} + \left(\nu^{\beta}_{ei}\Lambda^{\beta}_{ei}\right)^2 Q_e \tag{6.64}$$

$$\frac{d\phi^{\beta}_{ie}}{dt} = C_{ie} \tag{6.65}$$

$$\frac{dC_{ie}}{dt} = -2\nu^{\beta}_{ie}\Lambda^{\beta}_{ie}C_{ie} - \left(\nu^{\beta}_{ie}\right)^2\left[\left(\Lambda^{\beta}_{ie}\right)^2 - \nabla^2\right]\phi^{\beta}_{ie} + \left(\nu^{\beta}_{ie}\Lambda^{\beta}_{ie}\right)^2 Q_i \tag{6.66}$$

$$\frac{d\phi^{\beta}_{ii}}{dt} = C_{ii} \tag{6.67}$$

$$\frac{dC_{ii}}{dt} = -2\nu^{\beta}_{ii}\Lambda^{\beta}_{ii}C_{ii} - \left(\nu^{\beta}_{ie}\right)^2\left[\left(\Lambda^{\beta}_{ii}\right)^2 - \nabla^2\right]\phi^{\beta}_{ii} + \left(\nu^{\beta}_{ii}\Lambda^{\beta}_{ii}\right)^2 Q_i \tag{6.68}$$

The first-order nonlinear system above can then be rewritten in matrix form in Eq. 6.69.

$$\frac{d\vec{X}\left(\vec{r}, t\right)}{dt} = F \tag{6.69}$$

where $\vec{X}$ is a 26-element column vector: $\vec{X} = [V_e\ V_i\ W_e^f\ W_e^n\ W_i^f\ W_i^n\ U_{ee}\ A_{ee}\ U_{ei}\ A_{ei}\ U_{ie}\ A_{ie}$ $U_{ii}\ A_{ii}\ \phi^{\alpha}_{ee}\ B_{ee}\ \phi^{\alpha}_{ei}\ B_{ei}\ \phi^{\beta}_{ee}\ C_{ee}\ \phi^{\beta}_{ei}\ C_{ei}\ \phi^{\beta}_{ie}\ C_{ie}\ \phi^{\beta}_{ii}\ C_{ii}]^T$. Every variable in vector $\vec{X}$ is a function of space $\vec{r}$ and time t.

$\vec{X}$ can be expressed as its equilibrium state $\vec{X}^0$ plus a small disturbance $\delta\vec{X}$.

$$\vec{X}(\vec{r}, t) = \vec{X}^0 + \delta\vec{X}(\vec{r}, t) \tag{6.70}$$

After linearising Eq. (6.69) about steady state, we obtain a matrix equation for the disturbance,

$$\frac{d}{dt}\delta\vec{X}(\vec{r}, t) = \hat{J}\,\delta\vec{X}(\vec{r}, t) \tag{6.71}$$

where $\hat{J}$ is the 26×26 Jacobian matrix evaluated at equilibrium point $\vec{X}^0$.

The spatial Fourier transform was then taken to δX,

$$\widetilde{\delta X}(\vec{q}, t) = \int_{-\infty}^{\infty} \delta X(t) e^{-i\vec{q}\cdot\vec{r}}\, d\vec{r} \tag{6.72}$$

where $\widetilde{\delta X}$ is the spatial Fourier transform of δX. $\vec{q}$ is its 2-D wave number vector ($q = |\vec{q}|$ is the wavenumber). The ∇^2 terms (relating to gap junction diffusion effects and axonal wave equations), after spatial Fourier transformation, generate $-q^2$ terms in the Jacobian matrix $\hat{J}$.

6.2.4 Eigenvalue Analysis

The composition of the Jacobian matrix is shown in Eq. (6.73). The address of each element is given by listing the row number and then the column number. Only the 68 non-zero terms of the Jacobian matrix are given in equations (6.74)–(6.143); the remaining 608 terms, not listed here, are equal to zero.

$$\hat{J} = \begin{bmatrix} J_{1,1} & J_{1,2} & J_{1,3} & J_{1,4} & \cdots & J_{1,26} \\ J_{2,1} & J_{2,2} & J_{2,3} & J_{2,4} & \cdots & J_{2,26} \\ & & & & \vdots & \\ J_{25,1} & J_{25,2} & J_{25,3} & J_{25,4} & \cdots & J_{25,26} \\ J_{26,1} & J_{26,2} & J_{26,3} & J_{26,4} & \cdots & J_{26,26} \end{bmatrix} \tag{6.73}$$

$$J_{1,1} = -d\left(1 + D_1 q^2\right) \tag{6.74}$$
$$J_{1,3} = 1 \tag{6.75}$$
$$J_{1,4} = 1 \tag{6.76}$$
$$J_{1,7} = \rho_e \left(A_e^n d_n + A_e^f d_f\right) \tag{6.77}$$
$$J_{1,11} = \rho_i \left(A_e^n d_n + A_e^f d_f\right) \tag{6.78}$$

$$J_{2,2} = -d\left(1 + D_2 q^2\right) \tag{6.79}$$
$$J_{2,5} = 1 \tag{6.80}$$
$$J_{2,6} = 1 \tag{6.81}$$
$$J_{2,9} = \rho_e \left(A_i^n d_n + A_i^f d_f\right) \tag{6.82}$$
$$J_{2,13} = \rho_i \left(A_i^n d_n + A_i^f d_f\right) \tag{6.83}$$

$$J_{3,3} = -d_f \tag{6.84}$$
$$J_{3,7} = d_n d_f A_e^f \rho_e \tag{6.85}$$
$$J_{3,11} = d_n d_f A_e^f \rho_i \tag{6.86}$$

$$J_{4,4} = -d_n \tag{6.87}$$
$$J_{4,7} = d_n d_f A_e^n \rho_e \tag{6.88}$$
$$J_{4,11} = d_n d_f A_e^n \rho_i \tag{6.89}$$

$$\begin{aligned} J_{5,5} &= -d_f && (6.90)\\ J_{5,9} &= d_n d_f A_i^f \rho_e && (6.91)\\ J_{5,13} &= d_n d_f A_i^f \rho_i && (6.92)\end{aligned}$$

$$\begin{aligned} J_{6,6} &= -d_n && (6.93)\\ J_{6,9} &= d_n d_f A_i^n \rho_e && (6.94)\\ J_{6,13} &= d_n d_f A_i^n \rho_i && (6.95)\end{aligned}$$

$$J_{7,8} = 1 \quad (6.96)$$

$$\begin{aligned} J_{8,1} &= \alpha_{ee}\beta_{ee}\left(\frac{\partial\widetilde{\psi_{ee}}}{\partial\widetilde{V}_e}\right)^0 \left[\left(N_{ee}^{\alpha}+N_{ee}^{\beta}\right)\widetilde{Q_e}^0 + N_{ee}^{\mathrm{sc}}\,\mathrm{s}\,Q_e^{\max}\right] && (6.97)\\ J_{8,7} &= -\alpha_{ee}\beta_{ee} && (6.98)\\ J_{8,8} &= -\left(\alpha_{ee}+\beta_{ee}\right) && (6.99)\\ J_{8,15} &= \alpha_{ee}\beta_{ee}\widetilde{\psi_{ee}}^0 N_{ee}^{\alpha} && (6.100)\\ J_{8,19} &= \alpha_{ee}\beta_{ee}\widetilde{\psi_{ee}}^0 N_{ee}^{\beta} && (6.101)\end{aligned}$$

$$\begin{aligned} J_{9,10} &= 1 && (6.102)\\ & && (6.103)\end{aligned}$$

$$\begin{aligned} J_{10,2} &= \alpha_{ei}\beta_{ei}\left(\frac{\partial\widetilde{\psi_{ei}}}{\partial\widetilde{V}_i}\right)^0 \left[\left(N_{ei}^{\alpha}+N_{ei}^{\beta}\right)\widetilde{Q_e}^0 + N_{ei}^{\mathrm{sc}}\,\mathrm{s}\,Q_e^{\max}\right] && (6.104)\\ J_{10,9} &= -\alpha_{ei}\beta_{ei} && (6.105)\\ J_{10,10} &= -\left(\alpha_{ei}+\beta_{ei}\right) && (6.106)\\ J_{10,17} &= \alpha_{ei}\beta_{ei}\widetilde{\psi_{ei}}^0 N_{ei}^{\alpha} && (6.107)\\ J_{10,21} &= \alpha_{ei}\beta_{ei}\widetilde{\psi_{ei}}^0 N_{ei}^{\beta} && (6.108)\end{aligned}$$

$$\begin{aligned} J_{11,12} &= 1 && (6.109)\\ & && (6.110)\end{aligned}$$

$$
\begin{aligned}
J_{12,1} &= \alpha_{ie}\beta_{ie}\left(\frac{\partial\widetilde{\psi_{ie}}}{\partial\widetilde{V}_e}\right)^0 N_{ie}^{\beta}\,\widetilde{Q_i}^0 && (6.111)\\
J_{12,11} &= -\alpha_{ie}\beta_{ie} && (6.112)\\
J_{12,12} &= -\left(\alpha_{ie}+\beta_{ie}\right) && (6.113)\\
J_{12,23} &= \alpha_{ie}\beta_{ie}\widetilde{\psi_{ie}}^0 N_{ie}^{\beta} && (6.114)
\end{aligned}
$$

$$
J_{13,14} = 1 \qquad (6.115)
$$

$$
\begin{aligned}
J_{14,2} &= \alpha_{ii}\beta_{ii}\left(\frac{\partial\widetilde{\psi_{ii}}}{\partial\widetilde{V}_i}\right)^0 N_{ii}^{\beta}\,\widetilde{Q_i}^0 && (6.116)\\
J_{14,13} &= -\alpha_{ii}\beta_{ii} && (6.117)\\
J_{14,14} &= -\left(\alpha_{ii}+\beta_{ii}\right) && (6.118)\\
J_{14,25} &= \alpha_{ii}\beta_{ii}\widetilde{\psi_{ii}}^0 N_{ii}^{\beta} && (6.119)
\end{aligned}
$$

$$
J_{15,16} = 1 \qquad (6.120)
$$

$$
\begin{aligned}
J_{16,1} &= \left(\nu_{ee}^{\alpha}\Lambda_{ee}^{\alpha}\right)^2\left(\frac{\partial\widetilde{Q_e}}{\partial\widetilde{V}_e}\right)^0 && (6.121)\\
J_{16,15} &= -\left(\nu_{ee}^{\alpha}\right)^2\left[\left(\Lambda_{ee}^{\alpha}\right)^2+q^2\right] && (6.122)\\
J_{16,16} &= -2\nu_{ee}^{\alpha}\Lambda_{ee}^{\alpha} && (6.123)
\end{aligned}
$$

$$
J_{17,18} = 1 \qquad (6.124)
$$

$$
\begin{aligned}
J_{18,1} &= \left(\nu_{ei}^{\alpha}\Lambda_{ei}^{\alpha}\right)^2\left(\frac{\partial\widetilde{Q_e}}{\partial\widetilde{V}_e}\right)^0 && (6.125)\\
J_{18,17} &= -\left(\nu_{ei}^{\alpha}\right)^2\left[\left(\Lambda_{ei}^{\alpha}\right)^2+q^2\right] && (6.126)\\
J_{18,18} &= -2\nu_{ei}^{\alpha}\Lambda_{ei}^{\alpha} && (6.127)
\end{aligned}
$$

$$
J_{19,20} = 1 \qquad (6.128)
$$

$$
\begin{aligned}
J_{20,1} &= \left(\nu_{ee}^{\beta}\Lambda_{ee}^{\beta}\right)^2 \left(\frac{\partial \widetilde{Q}_e}{\partial \widetilde{V}_e}\right)^0 && (6.129)\\
J_{20,19} &= -\left(\nu_{ee}^{\beta}\right)^2 \left[\left(\Lambda_{ee}^{\beta}\right)^2 + q^2\right] && (6.130)\\
J_{20,20} &= -2\nu_{ee}^{\beta}\Lambda_{ee}^{\beta} && (6.131)
\end{aligned}
$$

$$J_{21,22} = 1 \qquad (6.132)$$

$$
\begin{aligned}
J_{22,1} &= \left(\nu_{ei}^{\beta}\Lambda_{ei}^{\beta}\right)^2 \left(\frac{\partial \widetilde{Q}_e}{\partial \widetilde{V}_e}\right)^0 && (6.133)\\
J_{22,21} &= -\left(\nu_{ei}^{\beta}\right)^2 \left[\left(\Lambda_{ei}^{\beta}\right)^2 + q^2\right] && (6.134)\\
J_{22,22} &= -2\nu_{ei}^{\beta}\Lambda_{ei}^{\beta} && (6.135)
\end{aligned}
$$

$$J_{23,24} = 1 \qquad (6.136)$$

$$
\begin{aligned}
J_{24,2} &= \left(\nu_{ie}^{\beta}\Lambda_{ie}^{\beta}\right)^2 \left(\frac{\partial \widetilde{Q}_i}{\partial \widetilde{V}_i}\right)^0 && (6.137)\\
J_{24,23} &= -\left(\nu_{ie}^{\beta}\right)^2 \left[\left(\Lambda_{ie}^{\beta}\right)^2 + q^2\right] && (6.138)\\
J_{24,24} &= -2\nu_{ie}^{\beta}\Lambda_{ie}^{\beta} && (6.139)
\end{aligned}
$$

$$J_{25,26} = 1 \qquad (6.140)$$

$$
\begin{aligned}
J_{26,2} &= \left(\nu_{ii}^{\beta}\Lambda_{ii}^{\beta}\right)^2 \left(\frac{\partial \widetilde{Q}_i}{\partial \widetilde{V}_i}\right)^0 && (6.141)\\
J_{26,25} &= -\left(\nu_{ii}^{\beta}\right)^2 \left[\left(\Lambda_{ii}^{\beta}\right)^2 + q^2\right] && (6.142)\\
J_{26,26} &= -2\nu_{ii}^{\beta}\Lambda_{ii}^{\beta} && (6.143)
\end{aligned}
$$

For these non-zero Jacobian terms, elements with superscript 0 implies computing the variable value at its equilibrium point. These terms are given in equations (6.144)–(6.147). In these equations, $a, b \in \{e, i\}$.

$$\widetilde{\psi_{ab}}^{\,0} = \frac{V_a^{\mathrm{rev}} - \widetilde{V_b}^{\,0}}{V_a^{\mathrm{rev}} - V_b^{\mathrm{rest}}} \qquad (6.144)$$

$$\left(\frac{\partial\widetilde{\psi_{ab}}}{\partial\widetilde{V_b}}\right)^0 = \frac{-1}{(V_a^{\mathrm{rev}} - V_e^{\mathrm{rest}})} \tag{6.145}$$

$$\widetilde{Q_a}^0 = \frac{Q_a^{\mathrm{max}}}{1+\exp\left[-\pi/\sqrt{3}\left(\widetilde{V_a}^0 - \theta_a\right)/\sigma_a\right]} \tag{6.146}$$

$$\left(\frac{\partial\widetilde{Q_a}}{\partial\widetilde{V_a}}\right)^0 = \frac{\pi}{\sqrt{3}\sigma_a Q_a^{\mathrm{max}}}\,\widetilde{Q_a}^0\, e^{-\frac{\pi}{\sqrt{3}\sigma_a}\left(\widetilde{V_a}^0-\theta_a\right)} \tag{6.147}$$

The 26 eigenvalues are computed by `Matlab` function `eig`($\hat{J}$). Only the dominant eigenvalues, Λ^{dom}, are retained and the dispersion curve is plotted as a function of wavenumber q. Here, the dominant eigenvalue is defined as the eigenvalue whose real part is *least negative* or *most positive.* In general, the dominant eigenvalue Λ^{dom} is a complex quantity with real and imaginary parts as defined in Eq. (6.148).

$$\begin{aligned}\Lambda^{\mathrm{dom}}(q) &= \alpha(q) \pm i\omega(q)\\ \alpha &= \mathrm{Re}\left[\Lambda^{\mathrm{dom}}\right]\\ \omega &= \left|\mathrm{Im}\left[\Lambda^{\mathrm{dom}}\right]\right|\end{aligned} \tag{6.148}$$

α is the real part of Λ^{dom}, which determines the rate of exponential growth ($\alpha > 0$) or decay ($\alpha < 0$) of the perturbation away from steady state. ω is the absolute value of the imaginary part of Λ^{dom} and it determines the frequency of temporal oscillation. The values of α and ω predict whether stationary or dynamic patterns will be generated in the cortical sheet.

1. When $\alpha(q) < 0$ across a full range of q, small perturbations on the cortical sheet will die away, and the homogeneous cortex remains stable. There are no patterns or oscillations formed in the cortical sheet.
2. When $\alpha > 0$ and $\omega = 0$, a static instability occurs at some non-zero wavenumber q. The homogenous cortex will destabilise and generate a stationary **Turing pattern** of wavelength $2\pi/q$.
3. When $\alpha > 0$ and $\omega \neq 0$, if $q = 0$, the cortex is in a state of dynamic instability and the entire cortex oscillates in uniform synchrony at frequency ω. This synchronised oscillation is **Hopf oscillation**.
4. When $\alpha > 0$ and $\omega \neq 0$, if $q \neq 0$, **travelling waves** will form in the cortical sheet and propagate with a phase speed of $\nu = \omega/q$.

6.2.5 Stability Predictions

In order to investigate the effect of inhibitory diffusion strength on the stability of near-far dendritic tree fast-soma model, both real and imaginary parts of the dominant eigenvalue, Λ^{dom}, are plotted as a function of wavenumber. The inhibitory diffusion strength, D_2 is varied from 0 (i.e., no diffusive coupling) to 0.03 cm^2. Excitatory diffusion strength D_1 is set at 1% of D_2, that is $D_1 = D_2/100$. The resulting dispersion curves are shown in Fig. 6.1. In this figure, subcortical drive s is set at 0.1. That means subcortical efferent flux $\phi_{sc} = 10\ \text{s}^{-1}$. The rate constants of near and far dendritic trees (d_n and d_f) are both set at 20 s^{-1}.

When there is no inhibitory diffusion coupling, the cortex shows instability ($\alpha > 0$) for wavenumber $q/2\pi > 0.35$ waves/cm. With increased inhibitory diffusion strength, the spatial frequency range of cortical instability decreases. For $D_2 = 0.02\ \text{cm}^2$, cortical instability occurs when spatial frequency, $q/2\pi$, lies in the range 0.4~0.67 waves/cm. This instability reaches maximum at $q/2\pi \approx 0.5$ waves/cm with corresponding temporal frequency $\omega/2\pi \approx 29$ Hz. When inhibitory diffusion strength is set to $D_2 = 0.03\ \text{cm}^2$, the real part of the dominant eigenvalue, α, is less than zero over the full wavenumber range, so any perturbations are expected to decay away enabling the cortex to settle into a stable state.

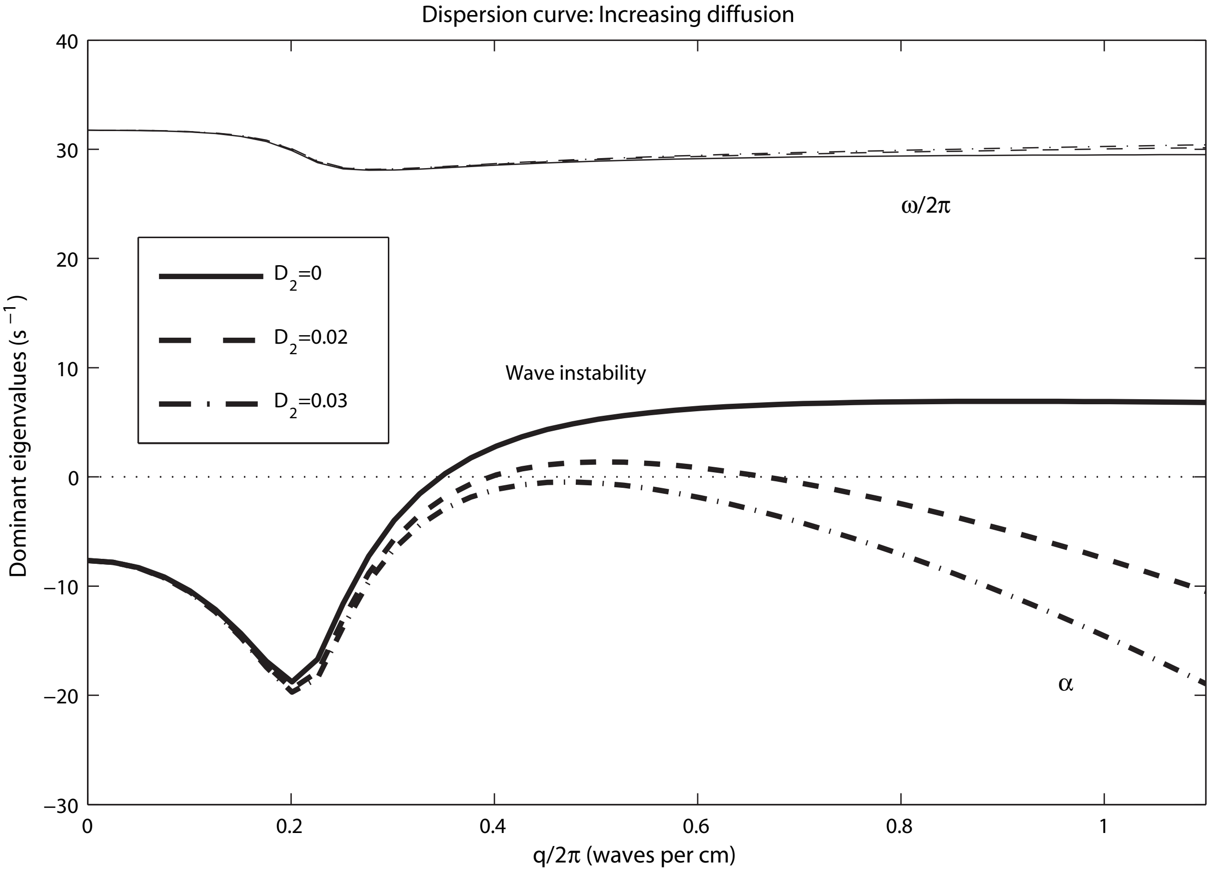

Figure 6.1: Near-far dendritic tree fast-soma dispersion curves for varying inhibitory diffusion strength D_2. The subcortical drive $s = 0.1$ is fixed in this figure. Rate constants $d_n = d_f = 20\ \text{s}^{-1}$. Three pairs of dominant eigenvalues are displayed for $D = [0,\ 0.02,\ 0.03]\ \text{cm}^2$. The real parts of Λ^{dom} are labelled with α and plotted with thick lines. The three thin lines are the corresponding imaginary parts of Λ^{dom} divided by 2π and labelled as $\omega/2\pi$. The homogeneous steady states are the same for the three dispersion curves: $(V_e^0, V_i^0) = (-59.41, -59.41)$ mV and $(Q_e^0, Q_i^0) = (6.37, 12.74)\ \text{s}^{-1}$.

Dispersion curves for altering levels of subcortical drive, $s = [0.1,\ 0.3,\ 0.5]$, are displayed in Fig. 6.2, with inhibitory diffusion strength D_2 fixed at 0.03 cm^2. As in Fig. 6.1, both rate constants, d_n and d_f, are set to 20 s^{-1}. Larger subcortical drive leads to cortical instability over a larger range of wavenumbers. For subcortical drive $s = 0.1$, the cortex is stable for all wavenumbers. For subcortical drive of 0.3 and 0.5, two kinds of dynamic instability can coexist in the cortex. At wavenumber $q = 0$, a Hopf oscillation occurs with a frequency of about

35 Hz for $s = 0.5$. Like Fig. 6.1, travelling waves appear at non-zero q, because $\alpha > 0$ and $\omega \neq 0$. The phase speed $\omega/q \approx 60$ cm/s at wavenumber $q/2\pi \approx 0.5$ waves/cm and temporal frequency $\omega/2\pi \approx 30$ Hz. From the curve of ω-vs-q, the group speed defined as $\nu_g = d\omega/dq$ is approximately zero, which implies 30-Hz standing waves of wavelength about 2 cm. The dynamic spatiotemporal patterns across the cortex is likely to be determined by interference between the 30-Hz standing wave and the Hopf oscillation.

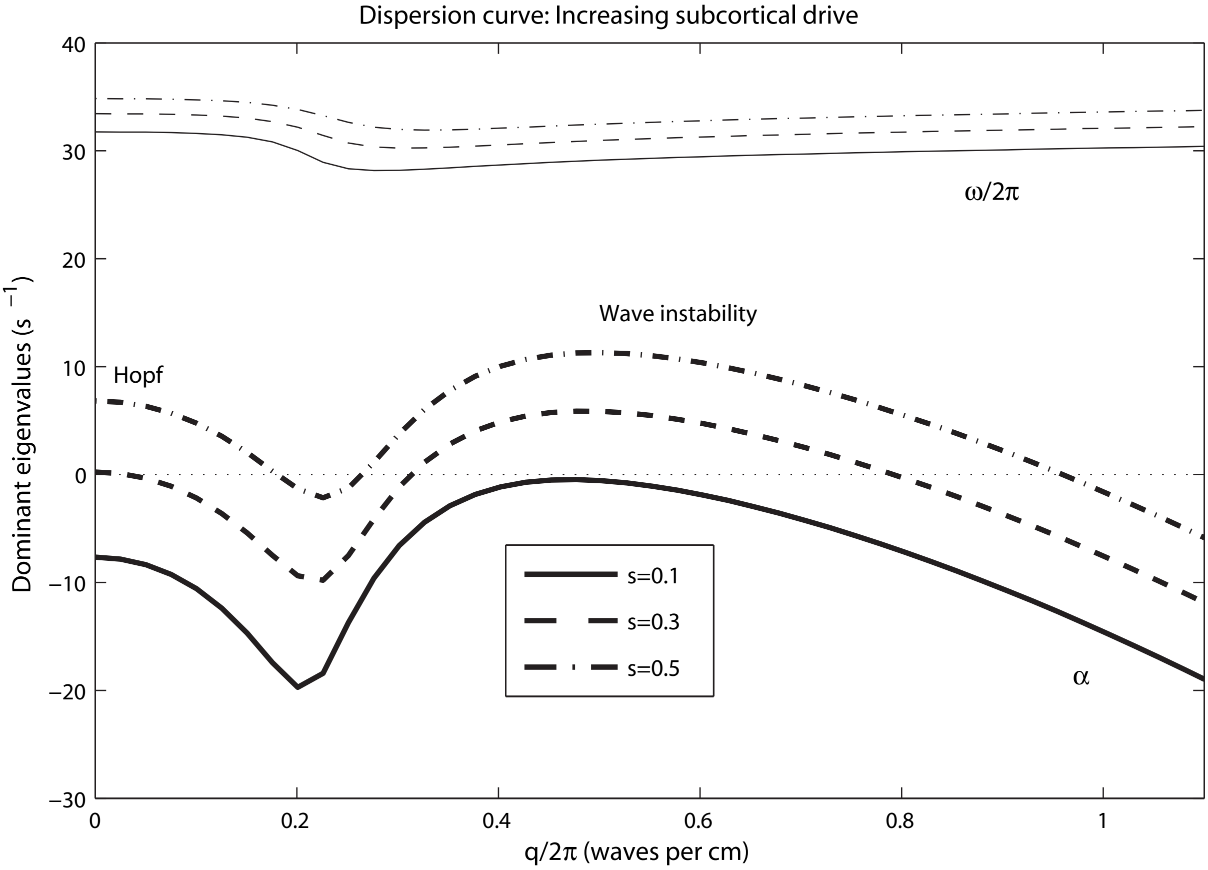

Figure 6.2: Near-far dendritic tree fast-soma dispersion curves when increasing subcortical drive $s = [0.1,\ 0.3,\ 0.5]$ with inhibitory diffusion fixed at $D_2 = 0.03$ cm^2. For the three increasing levels of subcortical drive, the corresponding homogeneous steady-state firing rates of the excitatory and inhibitory neuron populations are $Q_e^0 = [6.37, 7.28, 8.10]$ s^{-1} and $Q_i^0 = [12.74, 14.55, 16.20]$ s^{-1} respectively. The values of d_n and d_f are the same as those in Fig. 6.1.

The influence of the rate constants for the near and far dendritic trees (d_n and d_f) on cortical stability are also investigated and illustrated in Figs 6.3 and 6.4. In Fig. 6.3, we fix the rate-constant of the far dendritic tree d_f at a constant value and vary the rate constant of near dendritic tree across three values $d_n = [20,\ 23,\ 25]$ s^{-1}. Usually the rate constant of far dendritic tree d_f is smaller than the rate constant of near dendritic tree d_n [127]. Therefore, we set d_f to 20 s^{-1}. Fig. 6.3 shows that reducing the rate constant of near dendritic tree, d_n, to 20 s^{-1}, can completely eliminate the cortical instability. Increasing d_n to 23 s^{-1}, a 31-Hz travelling wave with spatial frequency of 0.5 cm^{-1} appears. Further increasing rate constant d_n to 25 s^{-1} evokes a $q = 0$ (i.e., whole of cortex) Hopf oscillation of 34 Hz.

For Fig. 6.4, the rate-constant of near dendritic tree d_n is fixed at 25 s^{-1}, and the stability behaviour of the cortex is explored for three values of rate constant of far dendritic tree $d_f =$

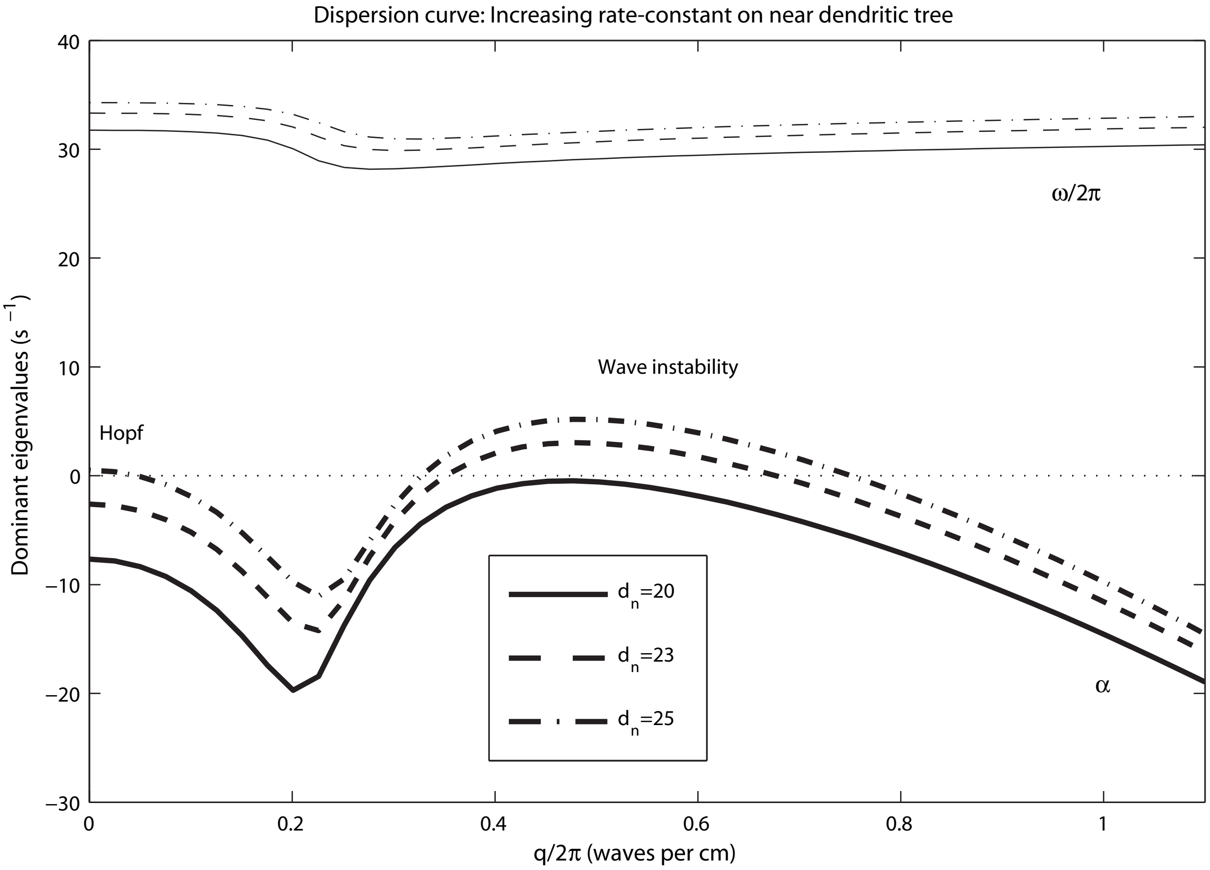

Figure 6.3: Stability curves generated by changing rate constant of near dendritic tree (d_n). The rate constant of near dendritic tree $d_n = [20,\ 23,\ 25]\ \mathrm{s}^{-1}$ and rate constant of far dendritic tree d_f is set at $20\ \mathrm{s}^{-1}$. The inhibitory diffusion strength $D_2 = 0.03\ \mathrm{cm}^2$ and subcortical drive $s = 0.1$. The steady-state soma voltages and firing rates are $(V_e^0, V_i^0) = (-59.41, -59.41)$ mV and $(Q_e^0, Q_i^0) = (6.37, 12.74)\ \mathrm{s}^{-1}$.

$[20,\ 23,\ 25]\ \mathrm{s}^{-1}$. The three stability curves are very similar and show coexistance of 34-Hz Hopf-oscillation and 32-Hz travelling wave of spatial frequency $0.5\ \mathrm{cm}^{-1}$. Comparing Figs 6.3 and 6.4, the rate-constant of the near dendritic tree d_n has a much larger influence on cortical stability than the rate-constant of the far dendritic tree d_f. A small increase in d_n can significantly change the cortical stability and easily drive the cortex from a completely stable state into an unstable state with Hopf oscillation and travelling waves. On the contrary, varying d_f does not cause obvious changes in cortical stability of the cortex. The stronger influence of d_n on the cortical stability is possibly due to its larger value. Larger rate constant of the near dendritic tree leads a larger change in the relative magnitude of the postsynaptic depolarisation when reaching to the trigger point, and therefore a larger influence on the action potential generation, and consequentially the states of the entire cortex.

From our results, the cortex basically keeps the same Hopf oscillation frequency and the same travelling wave, irrespective of the settings for d_n or d_f.

From the eigenvalue stability analysis, we can predict the brain dynamics with the back-propagation effect incorporated into the cortical model. From the above description, I found when changing the diffusion strength and subcortical drive, the stability prediction of the near-far dendritic tree model is not too dissimilar from that of the original slow-soma model. That means similar brain dynamics happens when varying the same model parameters. And the original

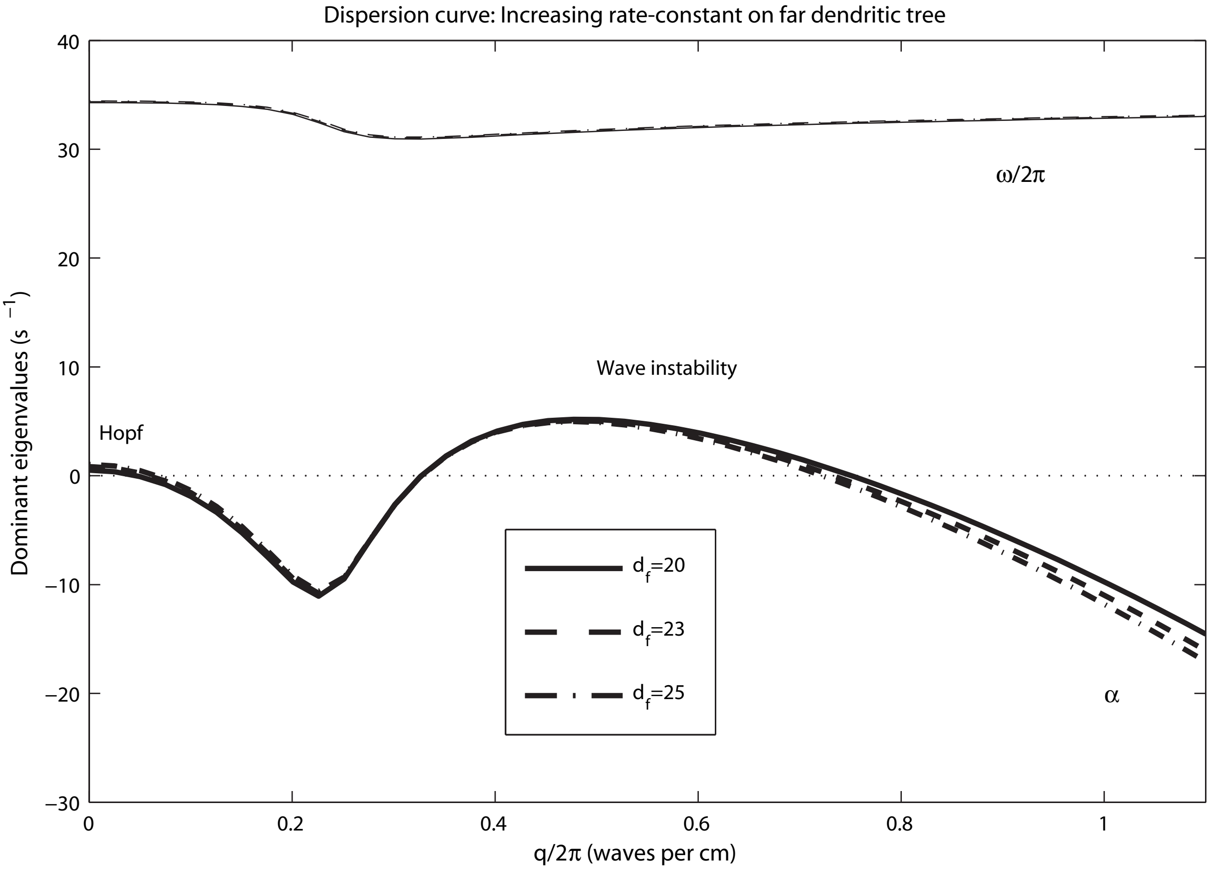

Figure 6.4: Dominant eigenvalue distribution influenced by rate constant of far dendritic tree d_f. The utilised rate constants of far dendritic tree are $d_f = [20,\ 23,\ 25]$ s^{-1}. In this figure, $d_n = 25$ s^{-1}, $D_2 = 0.03$ cm^2, and $s = 0.1$. The steady-state firing rates and soma voltages are the same as those in Fig. 6.3.

slow-soma model has been very well studied by our group and already been used for simulating different sleep phenomena in adult, such as sleep cycle [99], K-complex [122]. Therefore, I decided to simulate aspects of fetal sheep maturation using the original (and much simpler) Waikato slow-soma equations. My preliminary simulation studies are described in next chapter. The extended near-far Waikato cortical model may be useful for simulating the high-frequency resonances in the immature fetal sheep EEG, so listed in the Future Work section of the final chapter.

Chapter 7

Applying Waikato Slow-Soma Model to Fetal Sheep Maturation

The discontinuous or intermittent EEG wave is the hallmark of the early immature cortex and comprises two basic states: bursting activities and quiet intervals. During this immature stage, GABA is excitatory and depolarises the neuron. The disappearance of discontinuity of the EEG waves parallels the excitatory-to-inhibitory switch-over of GABA neurotransmitter effect. In this chapter, I simulate the discontinuous EEG wave by customising the Waikato slow-soma parameters to fit the picture in the immature cortex. Steady states are computed for the immature cortex with excitatory GABA considered. Cortical stability is investigated for the case of reductions in the rate constants of the IPSP. Finally, the pulsing and bursting activities and quiet states in the discontinuous EEG waves are simulated, and the gap junction diffusion effect is also investigated for the immature cortex.

7.1 Model Parameters Customisation

The development of sleep-like states in the fetus has been well studied and defined experimentally and clinically for both human and animal [8,27,78]. Before well-defined sleep states emerge, the EEG signal is discontinuous. This definition is based on the evolution of the visually apparent "continuity" of the EEG tracing. The discontinuous EEG signal has already been observed at conceptional age of 24 weeks in human preterm babies [96]. For sheep fetus, discontinuous ECoG tracings are observed at 91 days of gestation, which corresponds to the human brain at about 26–28 weeks of gestation [74]. For our fetal sheep data, the discontinuous ECoG signal exists at 95 days of gestation, which is the youngest fetal sheep data we obtained from Auckland University (see Fig. 3.3 in Chapter 3).

During EEG maturation, the flatter periods of EEG trace gradually become shorter, and the periods of burst activity extend, eventually merging to form a "continuous" EEG trace. The ending of the discontinuous EEG signal and beginning of well-defined sleep states happens at full term for human babies. For fetal sheep, we found that EEGs evolve from the discontinous patterns into well-defined differentiated sleep states of SWS and REM at about gestational age 125 days, approximately 20 days before full term. In rodent, the maturity of the brain during the first two weeks of postnatal life corresponds approximately to the maturity of human brain at term [21]. This suggests that brain maturity of rat at term is roughly comparable to that of humans at the beginning of the last trimester.

7.1.1 Early Oscillations and GABA Excitation (V_i^{rev})

The cellular and network mechanisms of the spontaneous intermittent (discontinuous) activities in immature cortical structures (hippocampus and neocortex) are called ENOs (early network oscillations) and GDPs (giant depolarising potentials). These early oscillations have been extensively studied in rodents [12, 84]. In adult nervous system, GABA is the major inhibitory neurotransmitter [58] which activates GABA_A receptors and causes hyperpolarisation of mature neurons. In contrast, in immature rodent brain, GABA *depolarises* immature cortical neurons by elevated intracellular chloride concentration following late development of chloride transporter KCC2, a crucial molecule for generation of inhibitory GABAergic Cl^- currents. Studies reveal that the disappearance of the early spontaneous activity, cortical ENOs ($\sim$0.01 Hz) and cortical GDPs ($\sim$0.1 Hz, lasting $\sim$300 ms), is closely paralleled by the maturation of GABAergic inhibition [12, 41, 59].

Excitatory actions of GABA depend on three parameters: resting membrane potential ($V_{e,i}^{\text{rest}}$), reversal potential of GABA (V_i^{rev}), and threshold of action potential generation ($\theta_{e,i}$). Rheims and colleagues [83] determined $V_{e,i}^{\text{rest}}$ and V_i^{rev} in the same neuron by noninvasive cell-attached recordings of N-methyl-D-aspartate (NMDA) and GABA channels in the postnatal first two weeks of immature rodent brain slices. They also measured action potential (AP) activation threshold, $\theta_{e,i}$, through random synaptic stimulation to cells for the same-aged rat puppy. Their results displayed that at the early age of rodent neocortex in vitro, all three parameters increase. To simplify parameter customisation in my simulation, I fix the parameters V_i^{rev} and $\theta_{e,i}$ and only vary the resting membrane potential $V_{e,i}^{\text{rest}}$ to approximate the GABA excitatory effect in the immature neuron.

7.1.2 Inhibitory PSP (γ_i)

The rise and decay time of IPSPs also changes during postnatal development in rat [46]. Measuring single stimulus shock-evoked IPSPs from newborn (P0–P7) to adult ($>$ P30) shows both rise and decay time constants of IPSPs decrease, with the decrease being most significant during the first two postnatal weeks. In our Waikato mean field "slow-soma" model, the IPSP is modelled as an alpha function, defined in Eq. (6.7), with rate constant γ_i, which is the inverse of the time constant. For my EEG maturation simulation, the rate constant γ_i is *decreased* to explore the effects of the inhibitory postsynaptic membrane response on the electrical activity of the immature cortex.

Other parameters also experiencing significant change during this period include gap junction density, axonal conduction speed, and number of long-/short-range connections.

7.1.3 Gap Junction Connectivity (D_2)

Gap junctions are widespread in the immature developing mammalian brain and contribute to the primitive form of synchronised spontaneous activity [11, 41], which is important for neurogenesis, neuronal maturation, synaptogenesis, and neural circuit formation. For mammals, gap junction coupling is most extensive and widespread before and during the time of synapse formation in many brain regions. Gap junction *uncoupling* occurs during postnatal weeks 1 to

3 in the rat when the chemical synaptic transmission matures and NMDA receptor activation is completed.

Arumugam and collegues [9] found the electrical coupling of neurons via gap junction increases in rat hypothalamus during the first two postnatal weeks and then decreases during the third and fourth weeks. This transient increase of gap junction coupling is widely observed in mammalian central nervous system during embryonic and/or early postnatal development [13]. The subsequent coupling decrease marks the transition from immature brain structure, with synchronised spontaneous activity modulated by both immature synapses and gap junctions, to the mature brain structure where chemical synaptic transmission dominates. During the present modelling, the inhibitory and excitatory diffusion strengths of the gap junctions, D_2 and D_1, already incorporated in the standard Waikato model, are investigated for their impact on immature brain dynamics.

7.1.4 Axonal Conduction Speed (v)

Sergejew [97] summarised callosal (relating to corpus callosum, a great commissure between the two cerebral hemispheres) conduction velocity in the fetal sheep brain from 75 days of gestation (dGA) to 70 days after birth (full term is $\sim$150 days of gestation). The axonal conduction velocity for adult is also given for comparison. The axonal conduction velocity increases very slowly from 75 dGA to birth (150 dGA), but increases dramatically from birth to 30 days after birth. After that the increase of conduction velocity becomes slow again. At 70 days after birth, the axonal conduction velocity is almost the same as the conduction velocity of adult. The myelogenesis of fetal sheep cortex is also summarised by Sergejew and replotted here in Fig. 7.1. Myelination commences at about 100 dGA and matures at about 140 dGA. Considering that the sleep cycle emerges at about 125 dGA, the increase in axonal conduction speed occurs primarily *after* the sleep cycle has developed. In our present early EEG simulation, the axonal conduction velocity v was not modified and the default value of 140 cm/s was retained.

Another interesting fact I found from Fig. 7.1 is that a divergence of conduction velocity from different fibers occurs at about 120 day of gestation. This divergence may be responsible for the emergence of the two distinct sleep states. (This assumption could be tested by further simulation after incorporating the variation of conduction velocity into the model.)

7.1.5 Synaptic Connectivity (N)

In mammals such as rat and humans, synaptogenesis occurs in two phases, first progressive, then regressive [52, 71]. The synaptic densities of the cerebral cortex reach peak at postnatal day 30 in rat and postnatal 8–12 months in humans. O'Kusky and colleagues [79] measured the total number of synapses and the synaptic density in the hypoglossal nucleus (the motor nucleus innervating the muscles of the tongue) of the rat from birth to postnatal day 30 and in young adults. The total number of synapses increased 843% from birth to postnatal day 20, then decreased 30% in adults, while the *synaptic density* (synapses per volume) increased 131% from birth to postnatal day 20, and then decreased 45% in adults. For both *asymmetric* and *symmetric* synapses, similar developmental changes are observed for total number of synapses

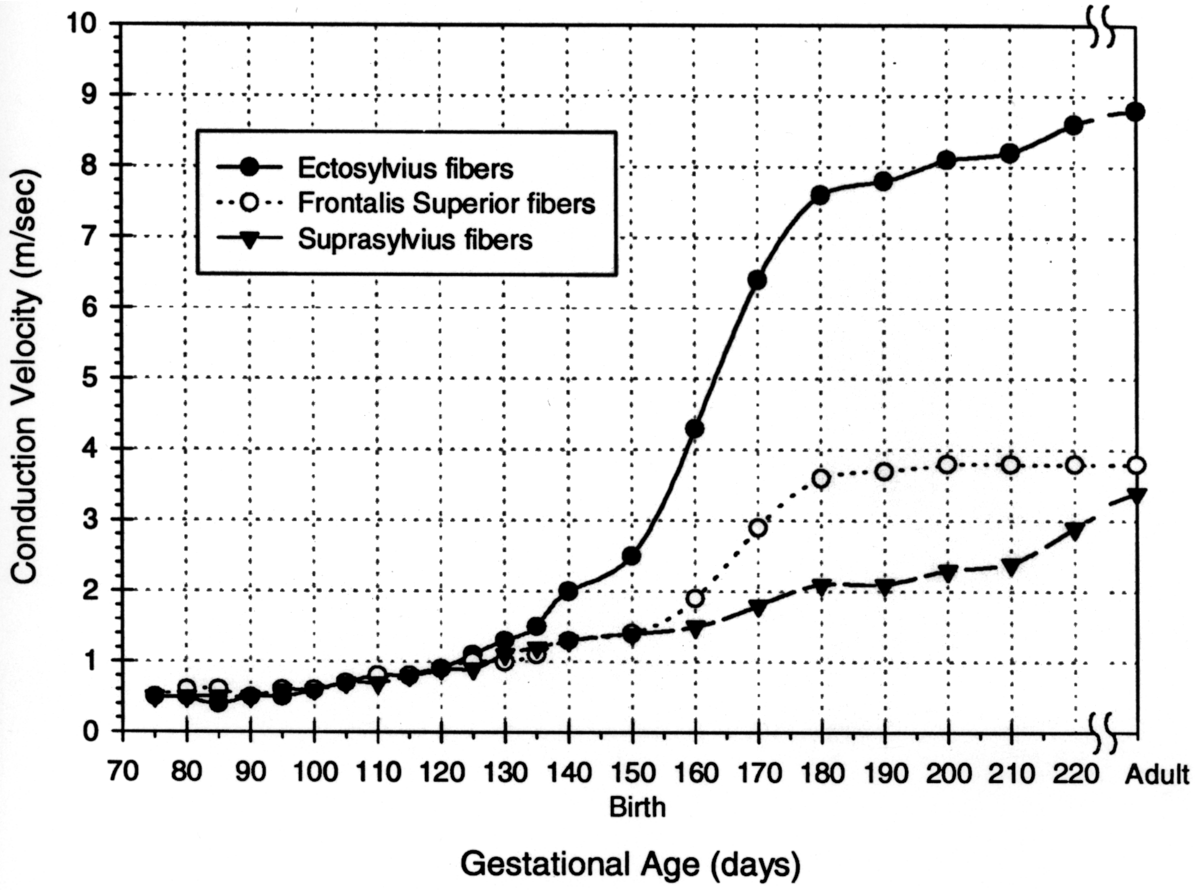

Figure 7.1: Axonal conduction speed for fetal sheep reproduced from Sergejew's PhD thesis [97]. The conduction velocity starts to increase dramatically only after about 140∼150 day of gestational age.

and synaptic density. The variations of the synaptic connectivity during the brain development is also considered in the simulation.

7.2 Fetal Sheep Simulation

7.2.1 Method

The Waikato mean-field slow-soma model assumes the cortex is homogenous, and that each macrocolumn consists of an excitatory neuron population and an inhibitory neuron population. The model consists of 14 stochastic partial differential equations which are first-order in time and second-order in space. After considering the parameter symmetries (eight pairs), the model can be simplified to eight coupled first-order differential equations. The considered parameter symmetries include $V_e^{\text{rest}} = V_i^{\text{rest}}$; $\tau_e = \tau_i$; $\gamma_{ee} = \gamma_{ei}$; $\gamma_{ie} = \gamma_{ii}$; $N_{ee}^{\alpha} = N_{ei}^{\alpha}$; $N_{ee}^{\beta} = N_{ei}^{\beta}$; $N_{ie}^{\beta} = N_{ii}^{\beta}$; $\Lambda_{ee} = \Lambda_{ei}$. This simplification was detailed in Prof. Moira Steyn-Ross's 2007 paper [103]. Setting all the time and space derivatives to zero, we can obtain the steady states of the cortical system. Linearising the system about its equilibrium state and Fourier transforming the eight differential equations, the eigenvalues of the 8×8 Jacobian matrix are then computed to evaluate the stability of the cortex. In the simulation, we also assume that the excitatory soma membrane potential approximately corresponds to the electrical signal recorded from the cortex (ECoG) or scalp (EEG).

To date, the Waikato mean-field cortical model has been applied to studying *adult* brain phenomena. Therefore, in order to model immature brain dynamics, we need to customise the relevant adult model parameters on the basis of physiology of the immature cortex. The relevant variations in model parameters occurring during development of the immature brain have been detailed individually in the previous section. Here I give a brief summary describing how I incorporate these customisations into the slow-soma Waikato model.[1]

First, for the steady states analysis, the variation of the synaptic connections during the early brain development is considered by decreasing the numbers of corticocortical and intracortical synaptic connections (N_{eb}^{α} and N_{ab}^{β}) in the Waikato mean-field slow-soma model. GABA excitatory effect is investigated by decreasing the resting membrane potential ($V_{e,i}^{\mathrm{rest}}$) to the value of GABA reversal potential (V_i^{rev}), -70 mV.

Second, we know that the rate constant of the inhibitory PSPs (γ_i) dramatically effects the stability properties of the cortex, though not its steady states. In immature neuron, this rate constant is significantly smaller than in its mature counterpart because of slower rise and decay time of the IPSPs. The effect of smaller rate constant on the stability of the immature cortex is investigated by reducing the γ_i from its default value, 58.6 s^{-1}, to 8.6 s^{-1}. Following the stability investigation, the simulation is carried out in two cases: 25 s^{-1} and 18.6 s^{-1} to explore the development of the bursting patterns for discontinuous EEG during its maturation.

Third, both inhibitory and excitatory diffusion strength of the gap junction (D_2 and D_1) have no influence on the steady states of the cortical system, but they do alter the stability of the cortical system and its propensity to form nonhomogeneous spatial patterns in the cortex—from previous study by the Waikato cortical modelling group, we know that gap junctions are responsible for Turing pattern formation in the cortex [104]. Here, I will investigate how gap junction diffusion alters the dynamics of the immature cortex.

7.2.2 Simulation Goal

Visually, the early immature EEG activity has a "discontinuous" appearance with two components—high-amplitude discrete bursting activity intermixed with low-amplitude quiet activity. This early discontinuous activity is universal, existing in every cortical structure for various mammals. One essential feature of the maturation of the EEG activity is the gradual emergence of continuous activity that replaces the earlier intermittent bursts. The maturation of the inhibitory GABA is paralleled by the emergence of the continuous oscillations in various frequency bands. Cellular-level study also shows that excitatory GABA is responsible for the generation of giant depolarisation potentials (GDPs), the network-driven synaptic events in the immature cortex [12].

For the discontinuous EEG, the discrete activity is characterised by a low intrinsic frequency (< 0.5 Hz). At the earliest age, the bursting component is brief and with higher-amplitude, and usually only one brief burst. During maturation, the duration of each burst episode increases and the amplitude decreases, with each burst showing several deflections (more than one component).

Based on the brief description above, my simulation concentrates on the main feature of the discontinuous EEG—the intermittent burst activity, the hallmark of the early immature

---

[1] The default modelling parameters used in the simulation are listed in Table 6.3.

EEG. The bursting activity is investigated when making the inhibitory neuron excitatory with suitable adjustments of the cell resting potentials as stated before. Another requirement for my simulation is the existence of transition from the transient bursting state to the quiet state.

7.2.3 Steady States

In the present steady states study, the resting membrane potential, $V_{e,i}^{\text{rest}}$, is chosen as the control parameter. The long-range and short-range synaptic connectivity are reduced to 80% and 72% of their respective default values. The distribution of the steady states, Q_e^0, Q_i^0, V_e^0, and V_i^0, as a function of resting membrane potential, is shown in Fig. 7.2. In this figure, the resting membrane potential is varied from -73 mV to -63 mV, which includes the GABA excitatory-inhibitory switching point. A three-roots region is observed for $V_{e,i}^{\text{rest}}$ lying between -72.2 mV and -66.2 mV. In the three steady-states region, the top branch is the high-firing state and the bottom branch is the low-firing state. Because the GABA reversal potential is -70 mV, when the resting membrane potential is below -70 mV, GABA is excitatory and *depolarises* the neuron in the immature cortex. As mentioned above, the steady-states distribution is independent of both the IPSP rate constant and the diffusion strength of gap junctions.

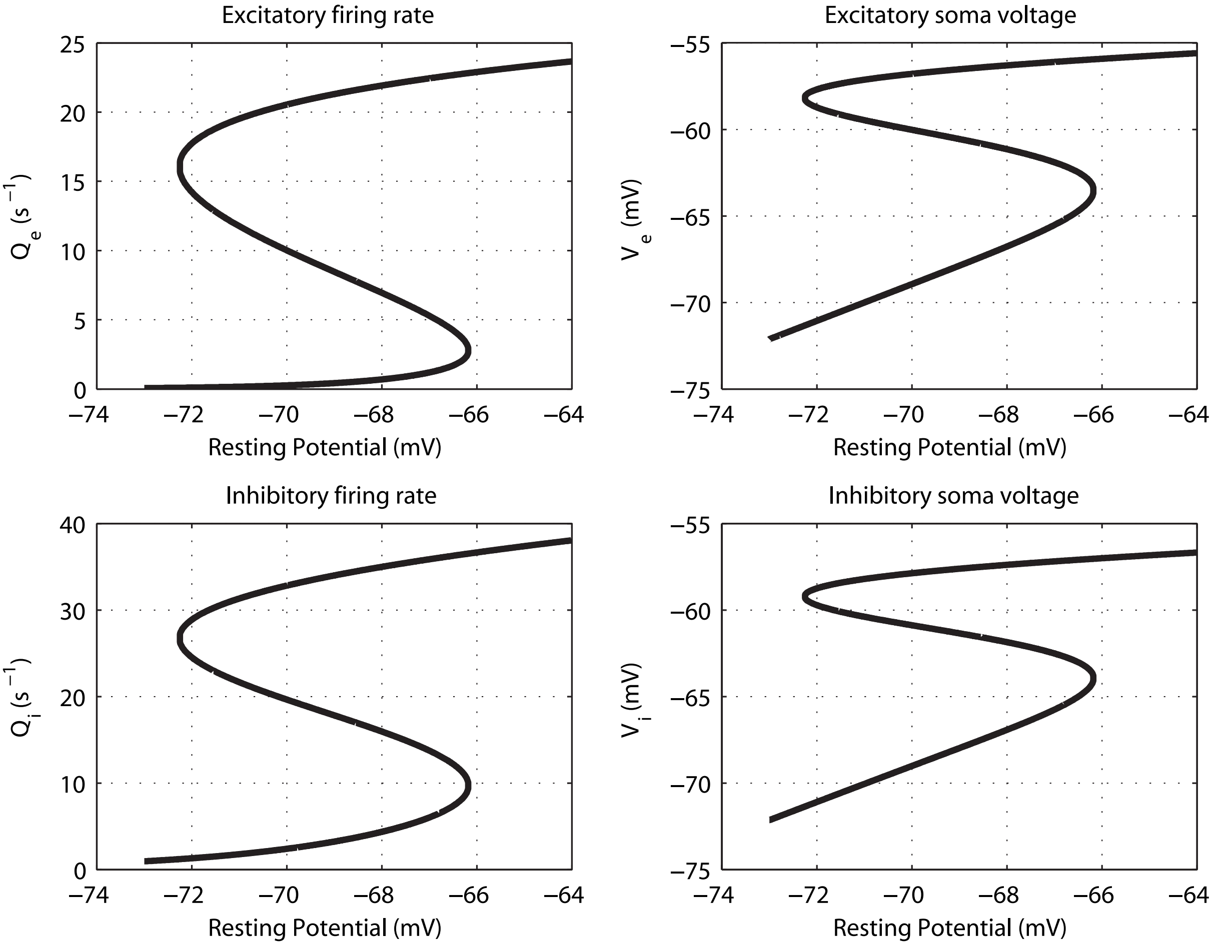

Figure 7.2: Steady states as a function of the resting membrane potential. Long-range synaptic connectivity, $N_{eb}^{\alpha} = 2968$; local synaptic connectivity, $N_{eb}^{\beta} = 295$ and $N_{ib}^{\beta} = 576$. Multiple steady states arise when the resting membrane potential is in the range of -72.2 to -66.2 mV. The GABA excitatory-inhibitory switch-over occurs at -70 mV.

7.2.4 Stability Analysis

After computing the steady states of the immature cortex, I investigate their stability when the IPSP rate constant decreases due to slower rise and decay times of IPSPs. The results are shown in Fig. 7.3. Six cases are displayed: $\gamma_i = 58.6$, 28.6, 25, 18.6, 12, and 8.6 s^{-1}, with smaller rate constants corresponding to increasing *immaturity*.

When $\gamma_i = 58.6\ \mathrm{s}^{-1}$, both top and bottom branches are stable and only the middle branch is unstable. Decreasing γ_i tends to destabilise the top branch. For example, reducing γ_i to 25 s^{-1} destabilises the top branch from the left-hand side, while the bottom branch remains stable. Further reductions in γ_i cause the range of instability on the top branch to extend to less negative resting potentials.

As γ_i reduced to 12 s^{-1}, the bottom branch also begins to destabilise, and further reductions in γ_i expand the extent of instability to the right (top branch) and left (bottom branch).

I also found that when altering γ_i from 58.6 s^{-1} to 8.6 s^{-1}, the middle branch becomes increasingly unstable, as signalled by the fact that the dominant eigenvalue at each point on the middle branch has a real part that becomes increasingly positive (not shown).

7.2.5 Simulation

We assume the excitatory soma membrane potential corresponds to the recorded EEG. In order to explore the dynamical activity in the immature brain, the cortex is modelled as a 25-×25-cm square sheet with 60 sample points on each direction giving 3600 sample points in total. The Euler algorithm is adopted to solve the full set of differential equations with time-step $\Delta t = 0.4$ ms. The simulation starts by initialising the firing rates, Q_e and Q_i, and soma voltages, V_e and V_i, at their respective lower branch steady-state values (see '×' points in Fig. 7.3).

In this model, I use a white-noise kick to model the early transient stimulus coming from the subcortex or other perturbations inside the neocortex itself, such as spontaneous synaptic activity. At the beginning of the simulation, a sharp, spatially-white kick is applied to all grid points of the cortical sheet; the kick lasts for 0.4 ms (i.e., for a single time step). Two γ_i values: 25 s^{-1} and 18.6 s^{-1}, are investigated for the brain dynamics. The gap junction effect is also studied in the simulation.

$\gamma_i = 18.6\ \mathrm{s}^{-1}$: Pulsing Activity

For our modified cortical model, I find that setting $\gamma_i = 18.6\ \mathrm{s}^{-1}$ generates the early pulse activity of the discontinuous EEG. The simulation result without considering gap junction diffusion effects is shown in Fig. 7.4 (a). After setting inhibitory neurons for excitatory GABA with $V_{e,i}^{\mathrm{rest}} = -70$ mV, a quick kick generates a pulsing EEG wave. The pulse lasts about 0.5 s with a quiet interval of about 4 s and a pulse amplitude of $\sim$15 mV. When considering gap junction diffusion effect, see Fig. 7.5 (a), $D_2 = 1.05\ \mathrm{cm}^2$ and $D_1 = D_2/100$, the pulses change direction with the quiet state on top and the pulse acting downward.

Comparing Fig. 7.4 (a) and Fig. 7.5 (a), one significant difference for the quiet state is that after introducing gap junction diffusion, small amplitude oscillations appear in the quiet state with a frequency roughly of 2 Hz, similar to that seen in the discontinuous EEG of fetal sheep, where the quiet interval is not completely silent, but contains some low-amplitude oscillations.

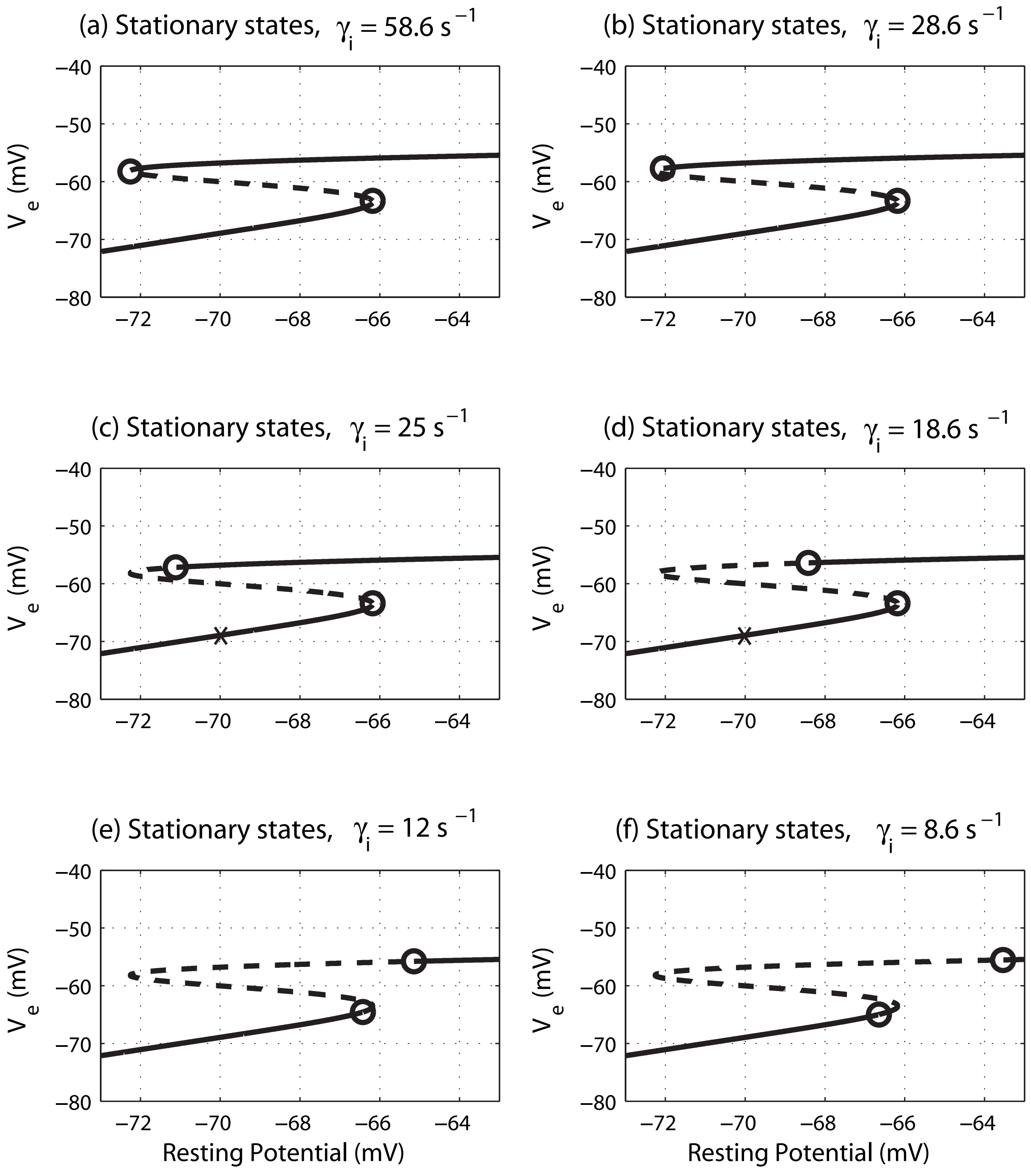

Figure 7.3: Steady states with stability results for different γ_i (a) 58.6 s^{-1}, (b) 28.6 s^{-1}, (c) 25 s^{-1}, (d) 18.6 s^{-1}, (e) 12 s^{-1}, (f) 8.6 s^{-1}. Solid-line: stable region; dashed-line: unstable region. The two cross marks (×) in (c) and (d) label the starting points of the simulation.

The "discontinuous" appearance of early immature EEG is caused mainly by the relative amplitude difference in the two states.

The corresponding real discontinuous EEG signals recorded in the early-term fetal sheep (ID 065) are given in Fig. 7.4 (b) and Fig. 7.5 (b). A general similarity is apparent between the simulated EEG and the actual recorded fetal sheep EEG. Comparing Fig. 7.4 (a) and (b), it can be seen that although the simulated EEG successfuly generated the EEG pulses, the simulated EEG wave did not reproduce any small fluctuations in the quiet state. For the downward pulsing activity of Fig. 7.5, the actual recorded fetal sheep EEG has a much higher oscillation frquency, about 20 Hz, than the oscillation frequency, 2 Hz, in the simulated fetal sheep EEG. In this real recorded fetal sheep EEG trace, an upward pulse is also observed at about 10.7 s.

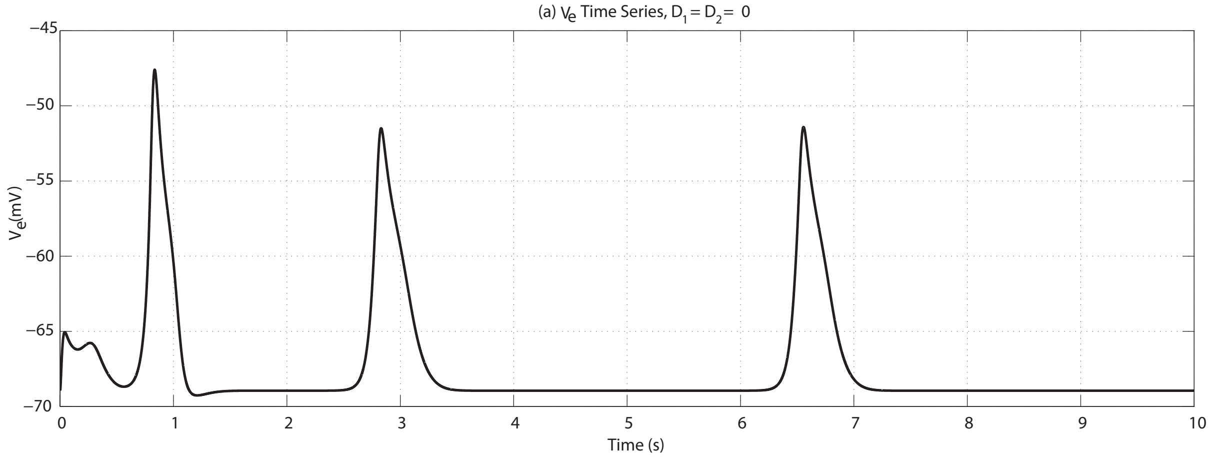

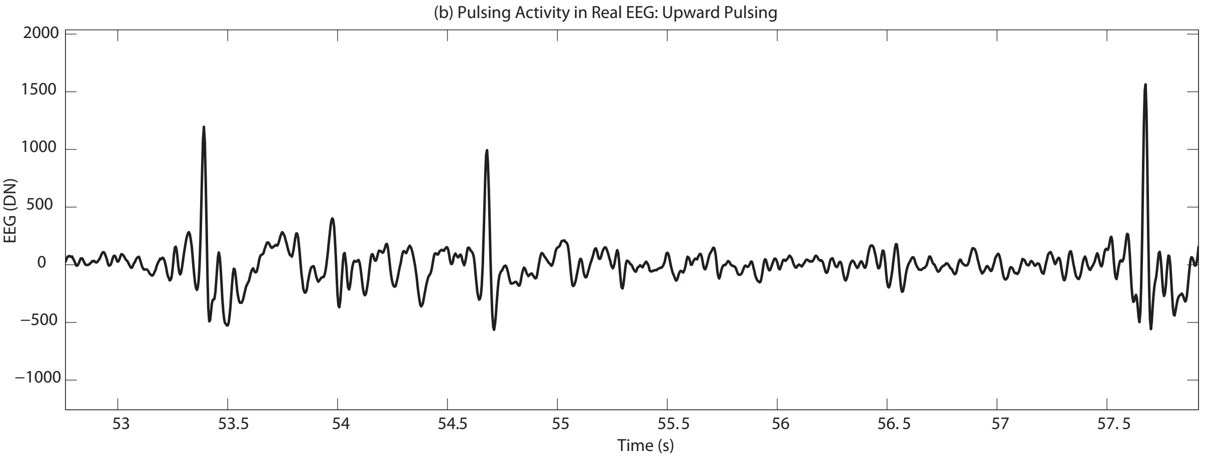

Figure 7.4: Simulated and real fetal sheep EEG without considering gap junction diffusion effect when $\gamma_i = 18.6\ \mathrm{s}^{-1}$. (a) Simulated results with diffusion strength $D_2 = D_1 = 0$. (b) Real electrocortical activity recorded from fetal sheep of 95 dGA. Both simulated and real EEG traces compose of upward pulse-like activity. The quiet state in the experimental results has small-amplitude fluctuations, which are not seen over the quiet state in the simulated results.

$\gamma_i = 25\ \mathrm{s}^{-1}$: Bursting Activity

For the more mature discontinuous EEG, the bursting activity develops more components—several low-frequency deflections. In order to simulate this bursting activity in the older discontinuous EEG, I set the rate constant γ_i at a higher value of 25 s^{-1}. The simulation results are shown in Fig. 7.6 (a) and Fig. 7.7 (a). As before, Fig. 7.6 (a) shows the result without gap junction diffusion effect and Fig. 7.7 (a) is the result after incorporating gap junctions.

The cortex is started on the bottom branch of the steady states at $V_{e,i}^{\mathrm{rest}} = -70$ mV. After giving a sharp kick at the beginning of the simulation for 0.4 ms, the cortex remains activated for about 0.5 s, and then settles down at the quiet state as shown in Fig. 7.6 (a). The bursting activity contains oscillatory components of frequency ∼3 Hz. The quiet state is completely silent in this simulation.

(a) V_e Time Series, D_2=1/1.05, D_1= D_2 /100

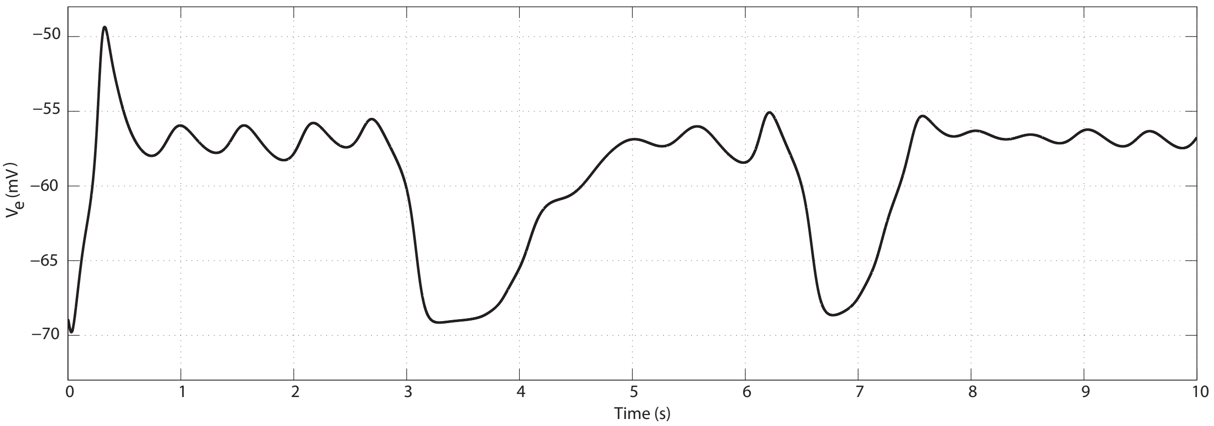

(b) Pulsing Activity in Real EEG: Downward Pulsing

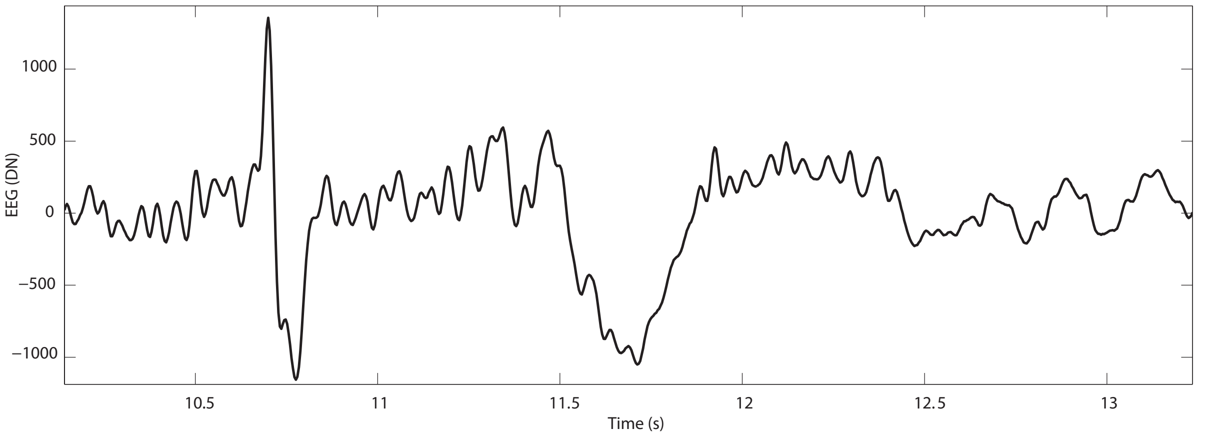

Figure 7.5: Simulated and real fetal sheep EEG after considering gap junction diffusion effect when $\gamma_i = 18.6$ s^{-1}. (a) Simulated discontinuous downward pulsing activity with gap junction incorporated into the cortical model: $D_2 = 1/300$ cm^2 and $D_1 = D_2/100$. With gap junction integrated into the cortical network, oscillation is generated in the cortex. (b) Actual EEG trace with downward pulsing activity recorded from fetal sheep aged at 100 dGA. There are two downward pulsings in this real fetal sheep electrocortical wave trace. The small oscillation fluctuations are very well simulated, though its oscillation frequency is about ten times slower than that in the real case. This is limited by the maximum oscillation frequency the Waikato slow-soma model can generate. An upward pulse is also observed just before the first downward pulsing.

When a small amount of gap junction coupling is added, the EEG wave develops several multi-component bursting activities with quiet interval in between to separate the bursts. This result is shown in Fig. 7.7 (a). In this figure, the inhibitory diffusion strength is fixed at $D_2 = 1/300$ cm^2 and the excitatory diffusion strength is $D_1 = D_2/100$. Gap junctions are abundant in the early age of the immature cortex, but its function in the generation of the early network oscillation is not known. Because gap junctions enhance electrical coupling between neurons, it is plausible that such coupling could generate synchronous membrane potential oscillations. In our current simulation, before gap junction is added to the immature neuronal network, no oscillation is generated as seen in Fig. 7.6 (a). After the gap junction is incorporated into the model, slow oscillations are aroused in the cortex, suggesting that gap junctions can support the generation of oscillatory states in the cortex.

For the bursting activity, the real fetal sheep EEGs measured from sheep 065 are given in Fig. 7.6 (b) and Fig. 7.7 (b). Comparing the simulated and the real EEG, the simulated multi-component bursting activity lasts longer than that in the real fetal sheep EEG. Furthermore, in the simulated EEG, there is no small oscillation in the quiet state, while for the real EEG, small fluctuations are seen. After the gap junction effect is introduced in the simulated EEG, the bursting activity and the quiet state last approximately equal length. Again, during the quiet state of the simulated results, no fluctuation is produced. In the real fetal sheep EEG, the bursting activity lasts much shorter than that in the simulated EEG. Compared with the simulated EEG, the contrast between the bursting state and the quiet state in the real EEG is also small.

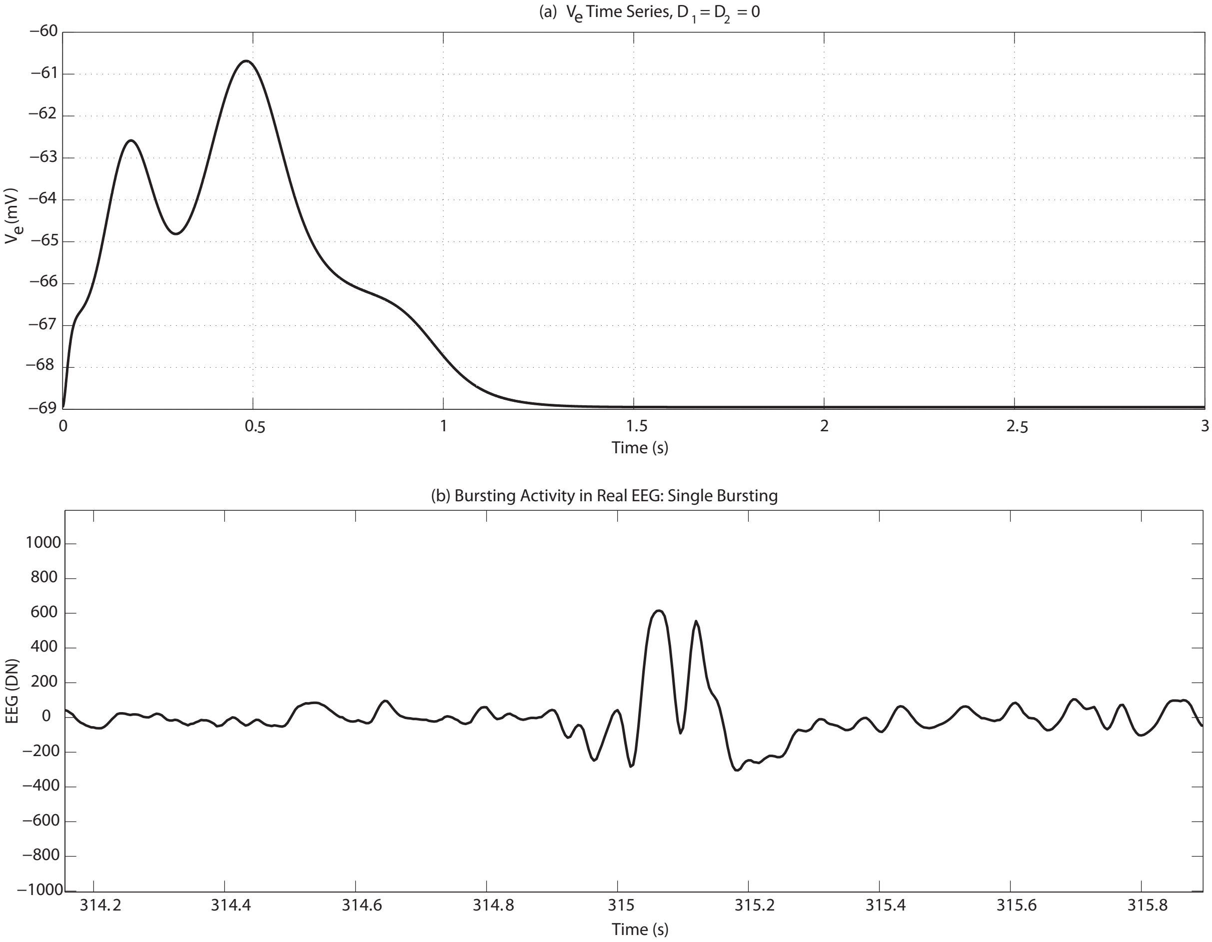

Figure 7.6: Simulated and experimental EEG bursting activity when $\gamma_i = 25\ \mathrm{s}^{-1}$ and gap junction diffusion effect is not considered. (a) Simulated bursting activity with $D_2 = D_1 = 0$. (b) Experimental results recorded from fetal sheep of day 111 of gestation. The bursting activity in the simulated result is very similiar with that in the experimental result. The quiet state in the real fetal sheep EEG has small flutuations, while the quiet state in the simulated signal is completely silent.

7.3 Summary

In summary, in this chapter, the immature discontinuous EEG is successfully simulated in a qualitative way. The basic features of the discontinuous EEG wave—two distinct states: pulsing/bursting activity and quiet state—are realised in our immature cortical model. Furthermore,

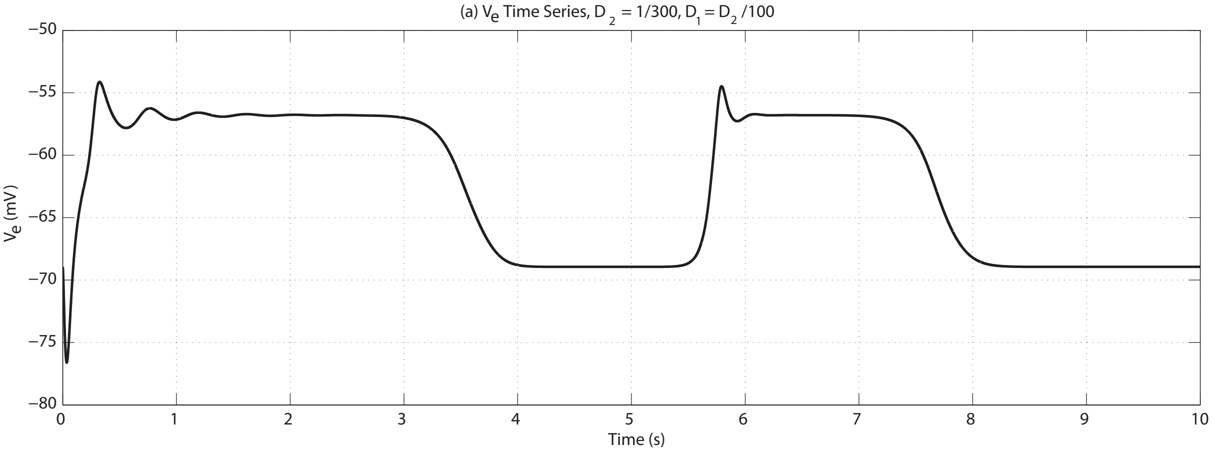

(a) V_e Time Series, $D_2 = 1/300$, $D_1 = D_2/100$

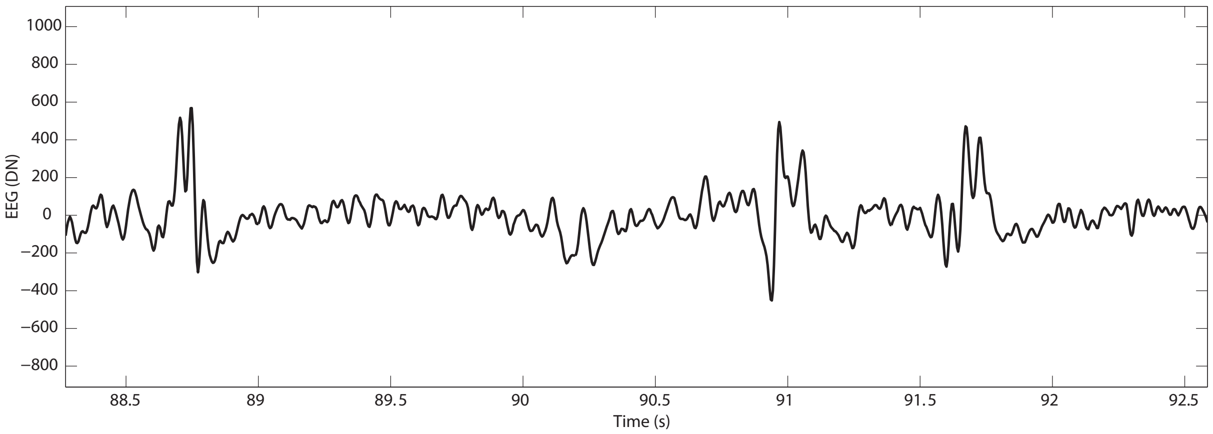

(b) Bursting Activity in Real EEG: Several Burstings

Figure 7.7: Simulated and real EEG signal when gap junction is incorporated into the Waikato cortical model and $\gamma_i = 25\ \mathrm{s}^{-1}$. (a) Simulated electrocortical wave obtained with the gap junction diffusion strength $D_2 = 1/300\ \mathrm{cm}^2$ and $D_1 = D_2/100$. With gap junction incorporated into the cortical network, oscillation is generated in the cortex. (b) Experimental results recorded from fetal sheep aged at 111 day of gestation. Small fluctuations are spotted in the quiet state of the real fetal sheep EEG trace and not seen in the quiet state of the corresponding simulated results. Three bursting activities are captured in the experimental results. The duration of each bursting activity in the experimental signal is shorter than that in the simulated signal.

two types of discontinuous EEG activity—pulsing and bursting—are observed in our simulation results. Gap junction diffusion effect is also investigated for the immature cortex. When rate constant $\gamma_i = 18.6\ \mathrm{s}^{-1}$, small amplitude oscillations in the quiet state are generated. A cortical network oscillation due to gap junction is seen for rate constant $\gamma_i = 25\ \mathrm{s}^{-1}$.

This is the first time that modelling of the immature discontinuous EEG wave has been attempted by incorporating GABA excitatory effect into a mean field cortical model. The partially successful modelling of the immature discontinuous EEG wave and exploration of the gap junction diffusion effects on the cortical dynamics at different maturation stages expand our knowledge and understanding of the immature brain and its maturation. This piece of work is significant and worthwhile to be published.

Chapter 8

Summary and Future Work

8.1 Summary

The work completed in this thesis comprises three major components—study of the maturational changes of the fetal sheep ECoG, investigation of `ccf` and Waikato cortical models, and modelling of discontinuous EEG wave in the immature cortex. I summarise the major results as follows.

Analysis of the Fetal Sheep ECoG

I introduced EEG signal analysis techniques used for the fetal sheep EEG analysis, which include power, correlation time, power spectral density, SVD entropy, spectral edge frequency. Following this introduction, I described the EEG recording techniques adopted in the University of Auckland, elucidating surgical instrumentation, data acquisition, and structure of the data files.

The third-trimester (95 to 144 day of gestation) of the fetal sheep is then divided into early and late third-trimester based on the appearance of the ECoG signal and the emergence of sleep cycles. For the early third-trimester fetal sheep, the ECoG appears discontinuous with intermittent high-voltage bursts and low-voltage intervals separating the bursts. When the fetal sheep reaches late third-trimester, the two well-defined sleep states—high-voltage SWS and low-voltage REM—occur and the sleep cycle starts. I found that for the SWS-to-REM transition, there is a power surge just before the transition and the change of state itself is rather quick, lasting about 30 s. In contrast, for the REM-to-SWS transition, no power surge is observed and the change is much slower, lasting $\sim$200 s. These observations suggest that the transition between the SWS and REM sleep state is a cortical phase transition, in which the SWS-to-REM transition is first-order (abrupt), while the REM-to-SWS transition is second-order (gradual).

Maturational Changes in Fetal Sheep ECoG

By analysing correlation time, SVD entropy, spectral edge frequency of the ECoG time-series, I investigated the maturational development of the fetal sheep during its third-trimester gestation. All three analysis techniques demonstrate that the two distinct sleep states, SWS and REM, emerge at about day 125 of gestation. Close examination of the frequency and amplitude variations in the power spectrum of the ECoG signal shows that the third trimester can be subdivided into four stages:

Stage I 95–111 dGA (undifferentiated sleep with 15-Hz spindles)
Stage II 109–123 dGA (undifferentiated sleep without spindles)
Stage III 124–129 dGA (emergence of differentiated sleep states)
Stage IV 130–144 dGA (maturation of sleep states)

One of the important findings is that a 15–16 Hz spindle-like ECoG wave exclusively exists at the first stage and is not seen at later stages. Another important finding is that just before the two distinct sleep states emerge, there is a significant surge in brain activity that peaks at day 124. After the differentiation of the sleep states, both SWS and REM states continue to exhibit substantial changes in frequency and amplitude.

Cortical Column Field Model

In order to simulate discontinuous EEG activity in the immature cortex, I needed to choose an appropriate cortical model. As a starting point, I experimented with the cortical column field (`ccf`) model developed by Professor J. J. Wright at the University of Auckland. Working with the `ccf` model at centimetric scale, I examined the time-series, fluctuation power, power law relation, gamma oscillation, phase relation between the exitatory and inhibitory cells, power spectral density, and spatial Fourier spectrum. My experiences with this model persuaded me that although biophysically sophisticated, `ccf` is too big and unwieldy to be suitable for my immature cortex simulation. Hence, I decided to use the Waikato mean-field model.

Waikato Near-Far Cortical Model

Dendritic back-propagation effects are important for the generation and propagation of the action potential at the soma. Borrowing ideas from Wright's `ccf` model, and guided by Prof M Steyn-Ross, I incorporated this effect into the Waikato mean-field fast-soma model to form an improved cortical model: the Waikato `near-far` fast-soma cortical model. The state equations are given out; steady states and the Jacobian matrix are then computed. The stability predictions are carried out by varying gap junction diffusion strength and subcortical drive. Furthermore, the influence of the rate constants of the near dendritic tree and far dendritic tree on the cortical stability is explored separately. I concluded that the stability properties of the near-far dendritic tree model are not too dissimilar from that of the slow-soma model.

Immature EEG Simulation

The original Waikato slow-soma mean-field model has been well-studied by the Waikato group, so I determined to proceed with my simulation by adapting the Waikato slow-soma model. The first step was to customise the modelling parameters in terms of the physiology of the immature cortex. GABA excitatory effect is a major event at this immature stage and its switching from excitatory to inhibitory foretells the maturation of the inhibitory neuron network in the cortex. The GABA excitatory effect was integrated into the model by lowering the resting membrane potential to the level of GABA reversal potential. Moreover, the alterations of the long- and short-range synaptic connections and the rate constants of the IPSPs during the early stage of cortical development were also considered. With the new set of modelling parameters, the steady states were calculated and the stability of the cortex was investigated. The discontinuous EEG waves were then simulated for two values of the γ_i rate constant and two distinct states—bursting activity and quiet state—are successfully generated by the model. Furthermore, two different types of burstings—single component and multi-component—are realised when γ_i equals 18.6 s^{-1} and 25 s^{-1} respectively. The introduction of gap junctions into the model leads to small-amplitude oscillations in the quiet state at $\gamma_i = 18.6\ \mathrm{s}^{-1}$, and possible slow cortical oscillation at $\gamma_i = 25\ \mathrm{s}^{-1}$.

8.2 Future Work

Axonal Speed

The axonal speed of the long- and short-range connections experiences substantial increase during the process of cortical development (see Fig. 7.1), but this change was not considered in the work reported in this thesis. As discussed in the previous chapter (Chapter 7), the divergence of the axonal speed at ∼120 dGA may cause the differentiation of SWS and REM sleep states. In the future, it would be worthwhile customising the corresponding modelling parameters and investigating the effect that increases in axonal speed have on the generation of distinct sleep states in the maturing cortex.

Near-Far Fast-Soma Model

Currently, I use the Waikato slow-soma model for the simulation of the discontinuous EEG. However, the slow-soma approach is unable to produce EEG rhythms faster than ∼5 Hz. From my fetal sheep ECoG analysis, I know there are higher-frequency rhythms present in the immature cortex, such as the 15–16 Hz spindles (see Chapter 3). It is impossible to model these fast spindle-like oscillations using the slow-soma model. Therefore, the Waikato *fast-soma* model is required for the simulation of the fast rhythmic EEG. Furthermore, back-propagation effects as incorporated into the near-far version of the fast-soma model should be investigated for improved modelling of immature EEG waves.

Appendix A

ECoG Time-Series for Fetal Sheep

The original recorded time-series are important for the analysis of the fetal sheep ECoG. By first visually inspecting the time-series, possible artefacts can be spotted easily. Therefore, the time-series with artefacts can be excluded from further analysis. By comparing time-series recorded from different-aged fetal sheep, the early-term discontinuous EEG and late-term continuous EEG can be immediately differentiated. For the late-term fetal sheep ECoG, time-series with sleep state transition can also be easily identified visually.

This appendix presents a full catalogue of all 324 ECoG time-series recorded at the Liggins Institute at Auckland University from 15 fetal sheep as they aged from 95 to 144 days since gestation. Recordings are ordered by gestational age. Each page contains 20 ECoG traces, with channel-1 plotted on the left column and channel-2 on the right. The left margin shows fetal age and sheep ID, with successive recording sessions indicated with a subscript index. For example, at gestational age 105 (see p. 145), three recordings were made from sheep 65 (65_0, 65_1, 65_2), and nine were obtained from sheep 298 (298_1, 298_2, $\ldots$, 298_9). The mapping from catalogue entry to the corresponding data file on `CD-ROM` is obtained by reading the catalogue numbers from right-to-left. Thus the last entry on p. 145 is mapped as follows:

`106 267`$_1$ → `1 267 106` → `P1267106.ACQ`

Note that for same sheep, the recording index starts at zero, while for others, the index starts at one (the reason for this inconsistency in Liggins file naming is unknown).

The standard recording length for each session is 502.78 second, though for a minority of sessions, the recording length is shorter (394.396 s), e.g., the first 18 pairs of traces (95 65_0 to 13 031_9) are 394 s in length.

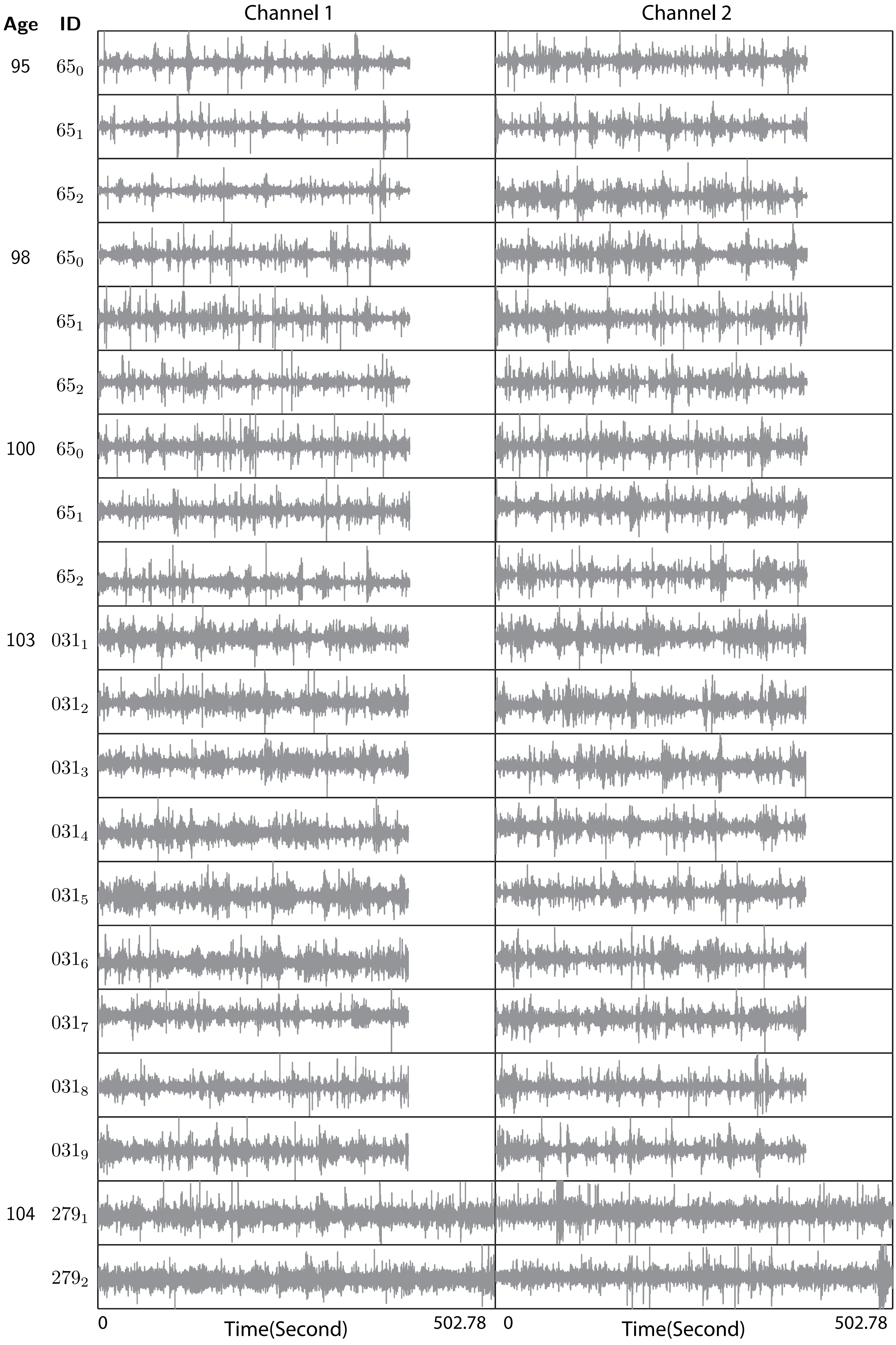
Age
ID
Channel 1
Channel 2
95
65_0
65_1
65_2
98
65_0
65_1
65_2
100
65_0
65_1
65_2
103
031_1
031_2
031_3
031_4
031_5
031_6
031_7
031_8
031_9
104
279_1
279_2
0
Time(Second)
502.78
0
Time(Second)
502.78

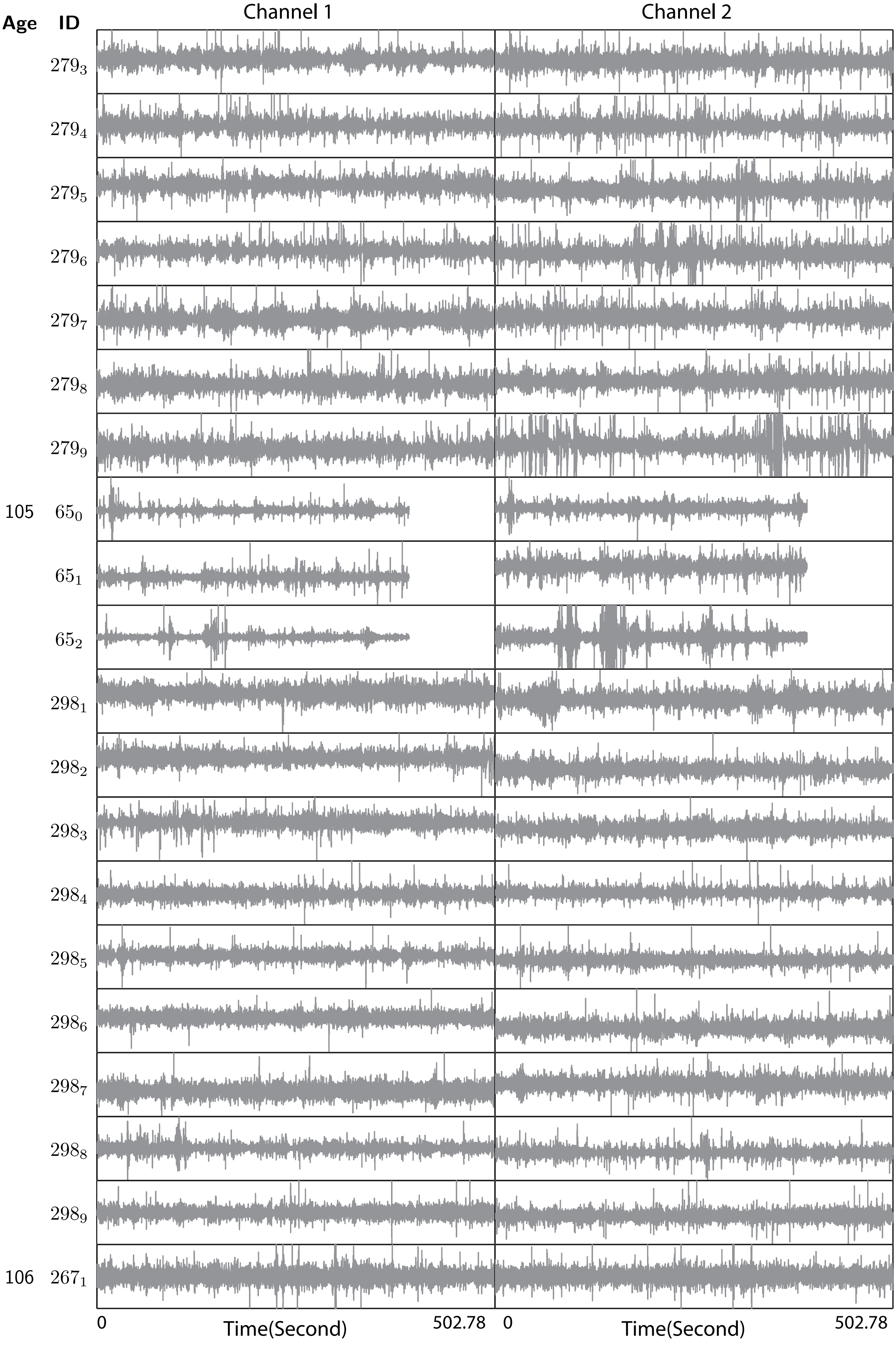
Age
ID
Channel 1
Channel 2
279_3
279_4
279_5
279_6
279_7
279_8
279_9
105
65_0
65_1
65_2
298_1
298_2
298_3
298_4
298_5
298_6
298_7
298_8
298_9
106
267_1
0
Time(Second)
502.78
0
Time(Second)
502.78

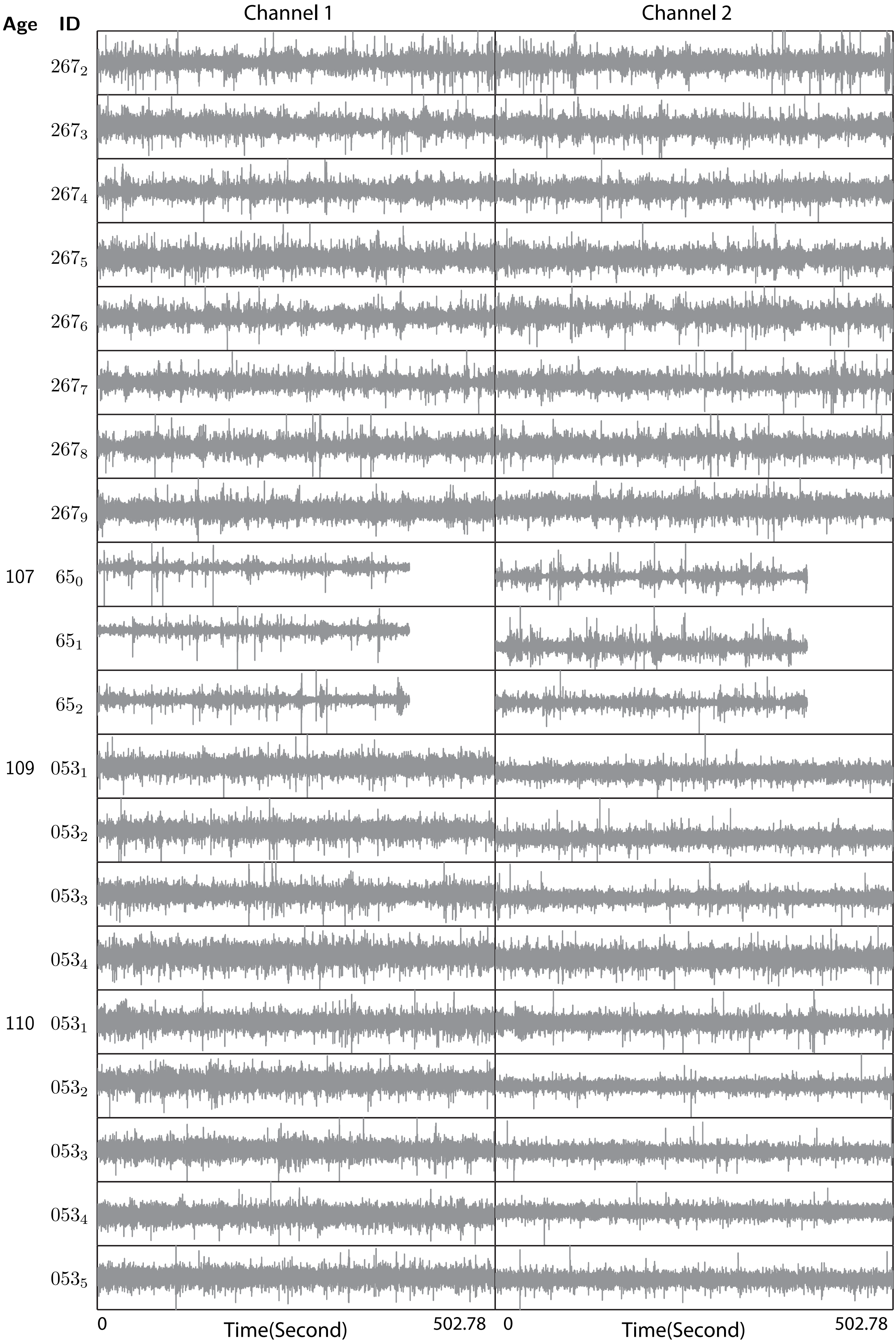
Age
ID
Channel 1
Channel 2
267_2
267_3
267_4
267_5
267_6
267_7
267_8
267_9
107
65_0
65_1
65_2
109
053_1
053_2
053_3
053_4
110
053_1
053_2
053_3
053_4
053_5
0
Time(Second)
502.78
0
Time(Second)
502.78

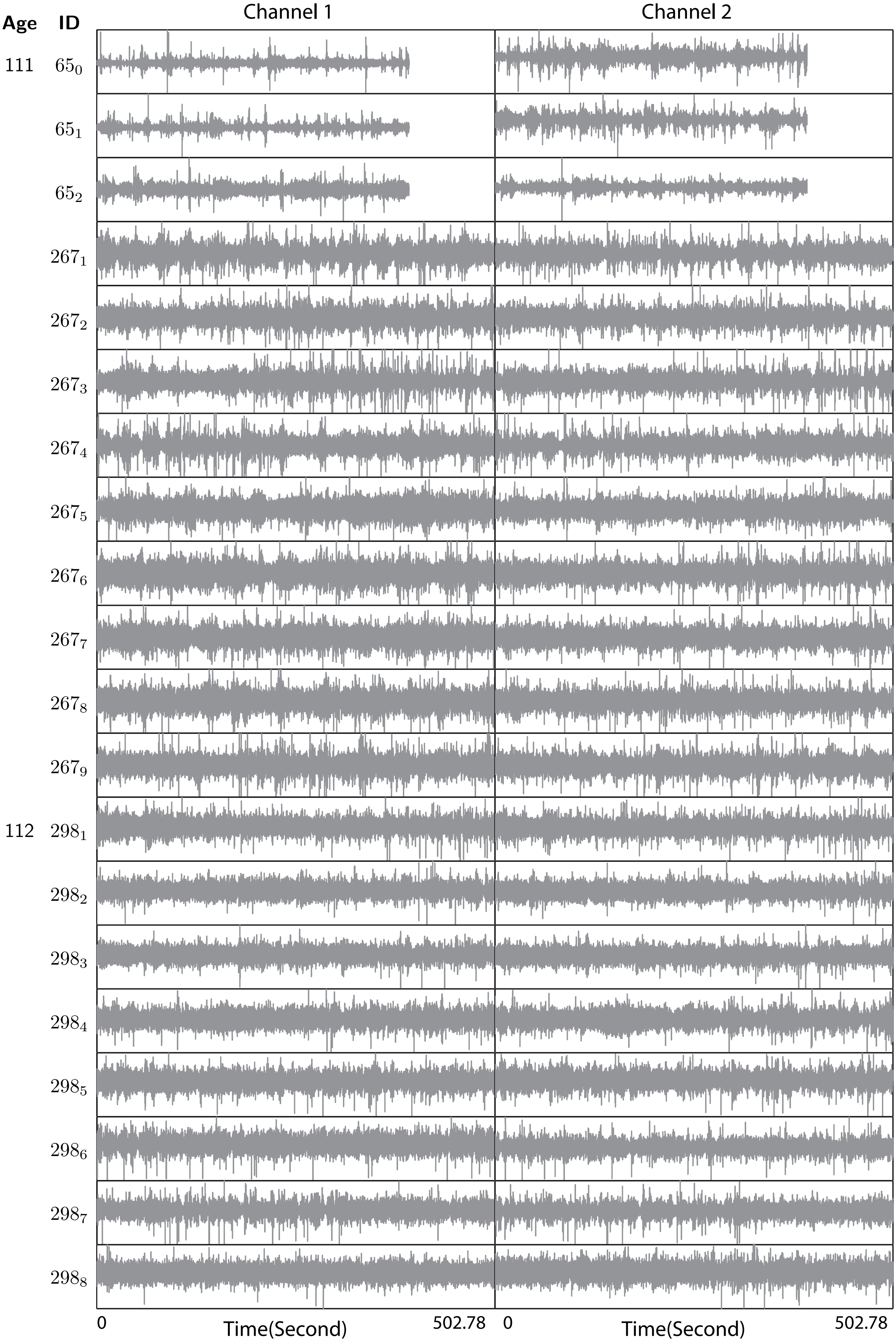
Age
ID
Channel 1
Channel 2
111
65$_0$
65$_1$
65$_2$
267$_1$
267$_2$
267$_3$
267$_4$
267$_5$
267$_6$
267$_7$
267$_8$
267$_9$
112
298$_1$
298$_2$
298$_3$
298$_4$
298$_5$
298$_6$
298$_7$
298$_8$
0
Time(Second)
502.78
0
Time(Second)
502.78

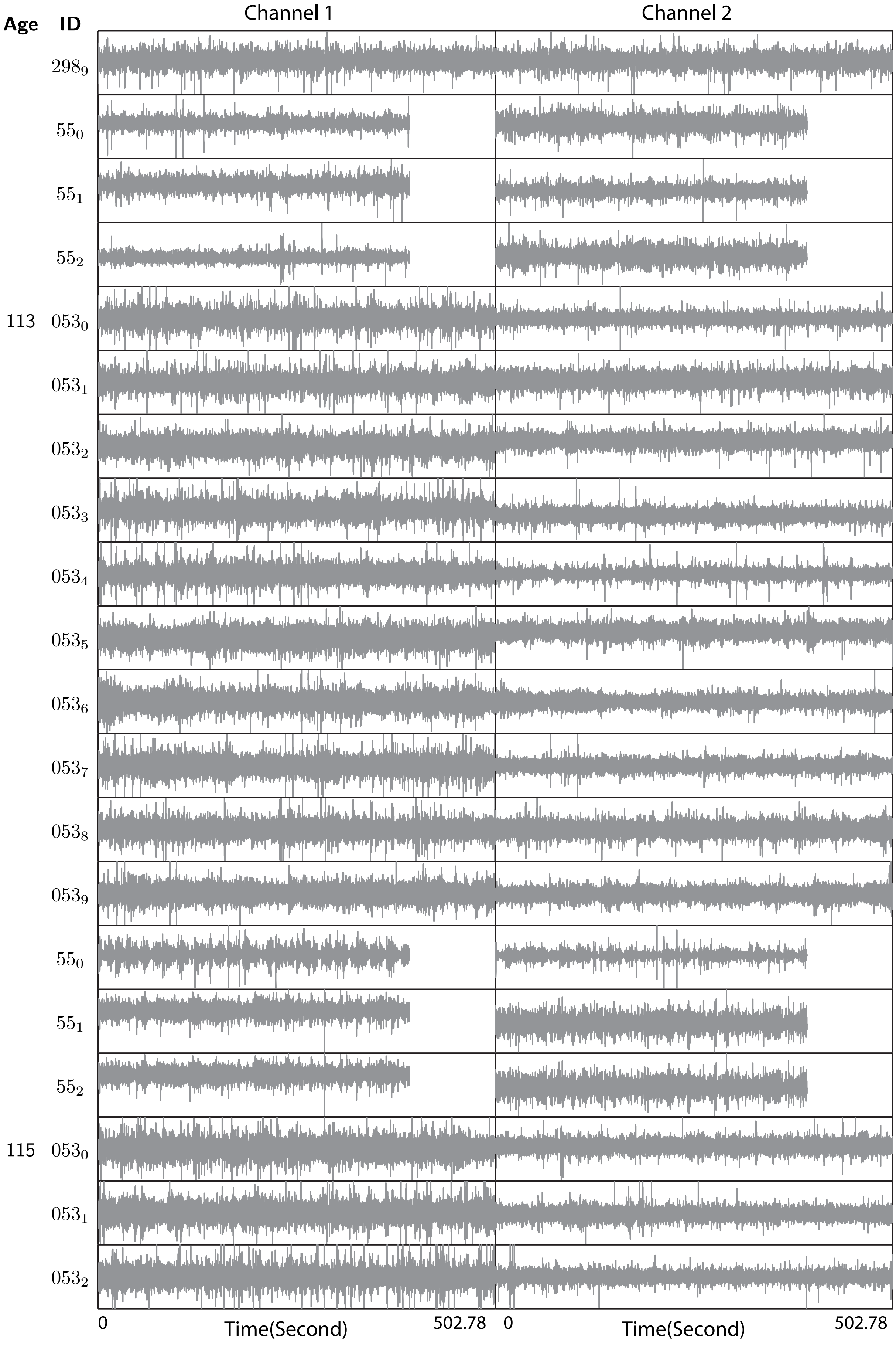
Age
ID
Channel 1
Channel 2
298_9
55_0
55_1
55_2
113 053_0
053_1
053_2
053_3
053_4
053_5
053_6
053_7
053_8
053_9
55_0
55_1
55_2
115 053_0
053_1
053_2
0
Time(Second)
502.78
0
Time(Second)
502.78

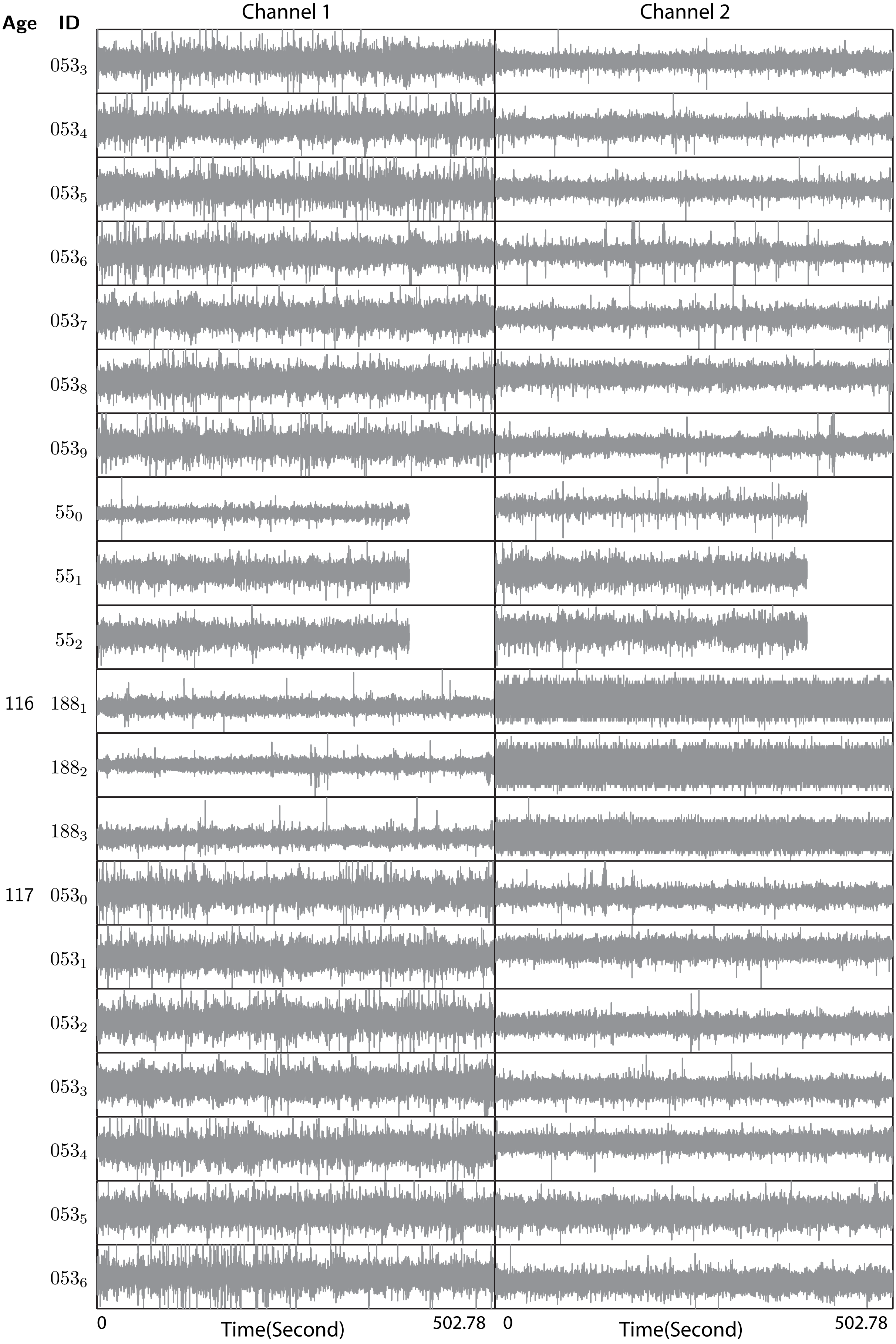
Age
ID
Channel 1
Channel 2
053_3
053_4
053_5
053_6
053_7
053_8
053_9
55_0
55_1
55_2
116
188_1
188_2
188_3
117
053_0
053_1
053_2
053_3
053_4
053_5
053_6
0
Time(Second)
502.78
0
Time(Second)
502.78

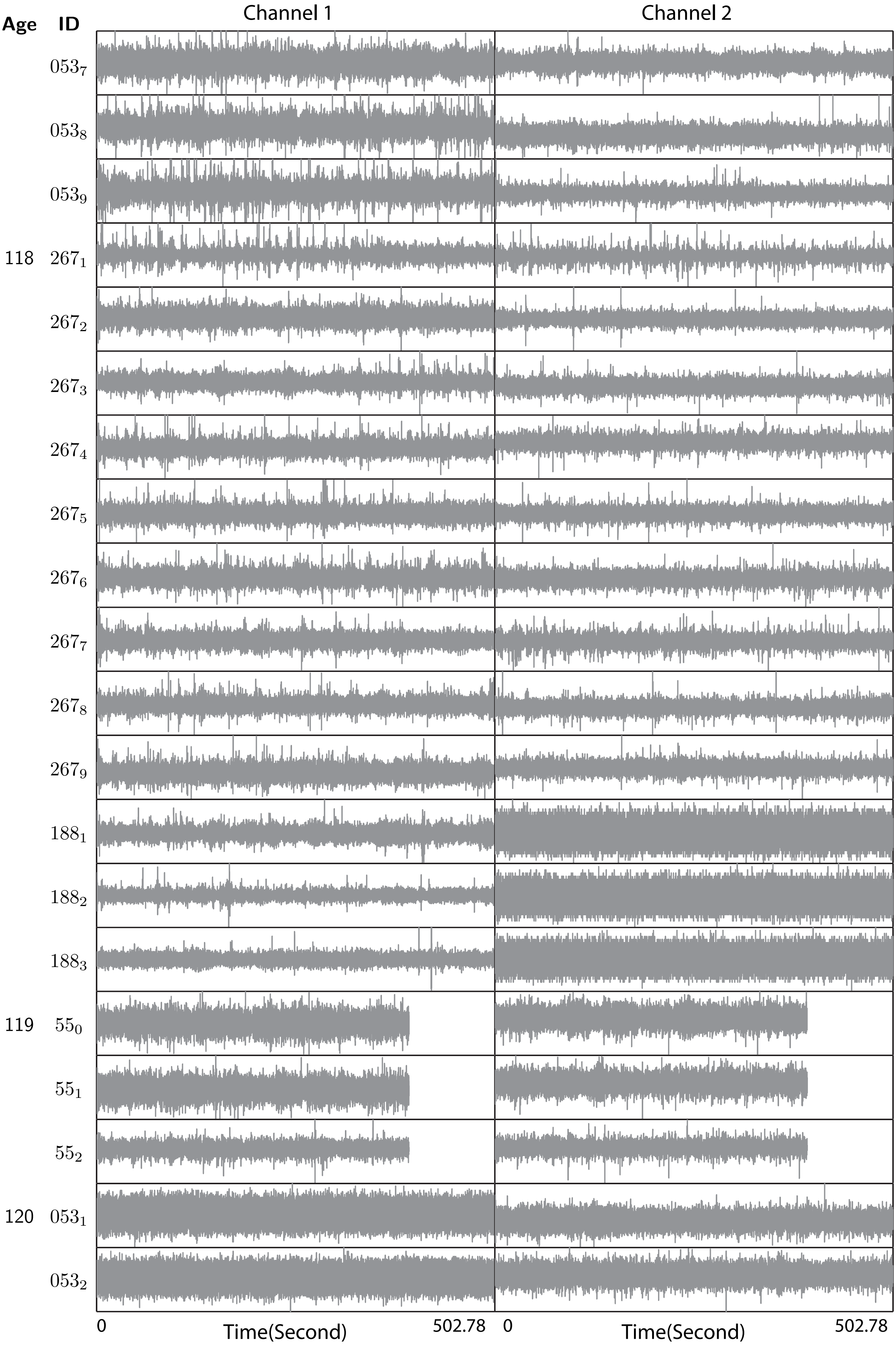
Age
ID
Channel 1
Channel 2
053_7
053_8
053_9
118
267_1
267_2
267_3
267_4
267_5
267_6
267_7
267_8
267_9
188_1
188_2
188_3
119
55_0
55_1
55_2
120
053_1
053_2
0
Time(Second)
502.78
0
Time(Second)
502.78

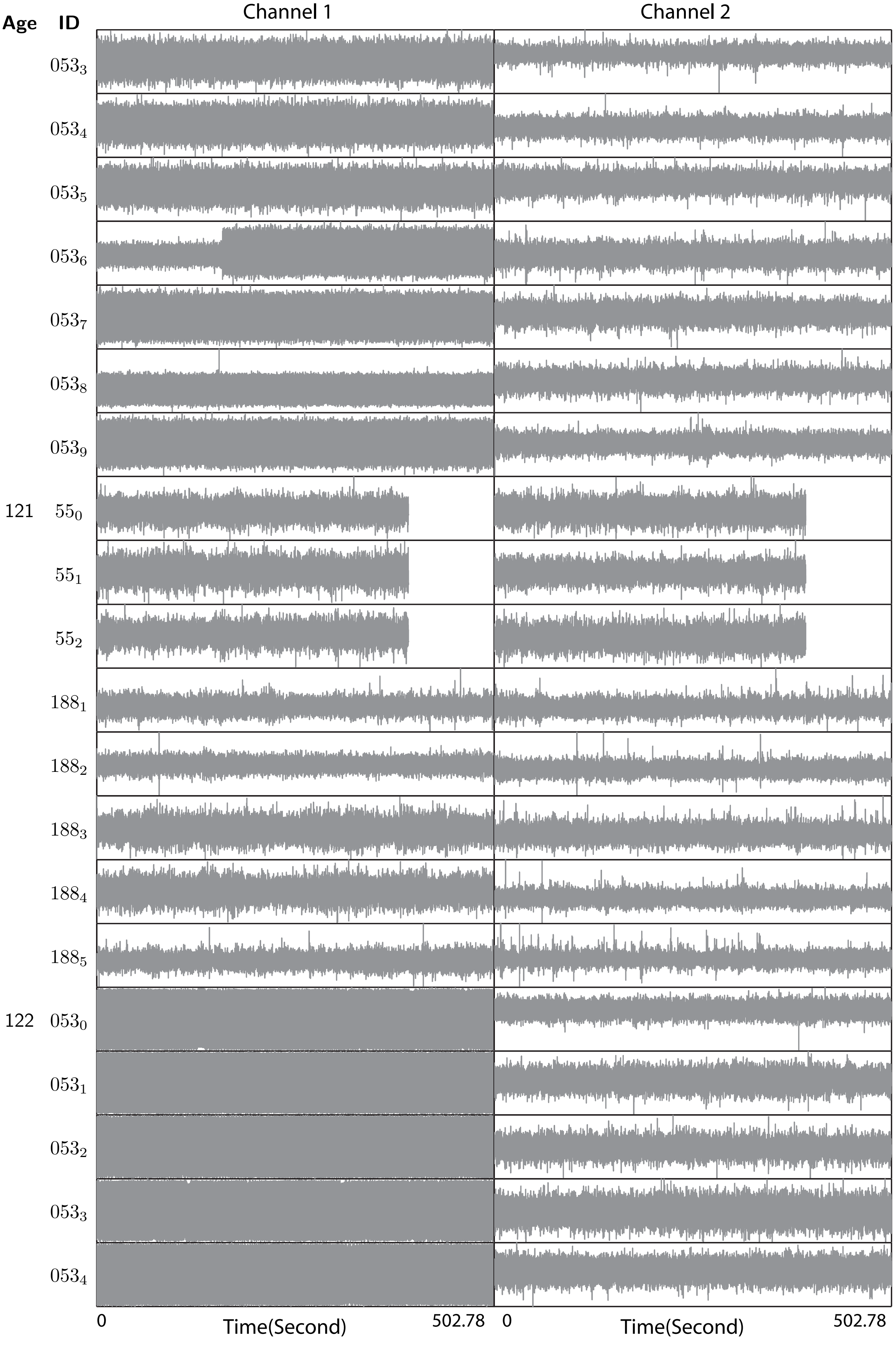
Age
ID
Channel 1
Channel 2
053_3
053_4
053_5
053_6
053_7
053_8
053_9
121
55_0
55_1
55_2
188_1
188_2
188_3
188_4
188_5
122
053_0
053_1
053_2
053_3
053_4
0
Time(Second)
502.78
0
Time(Second)
502.78

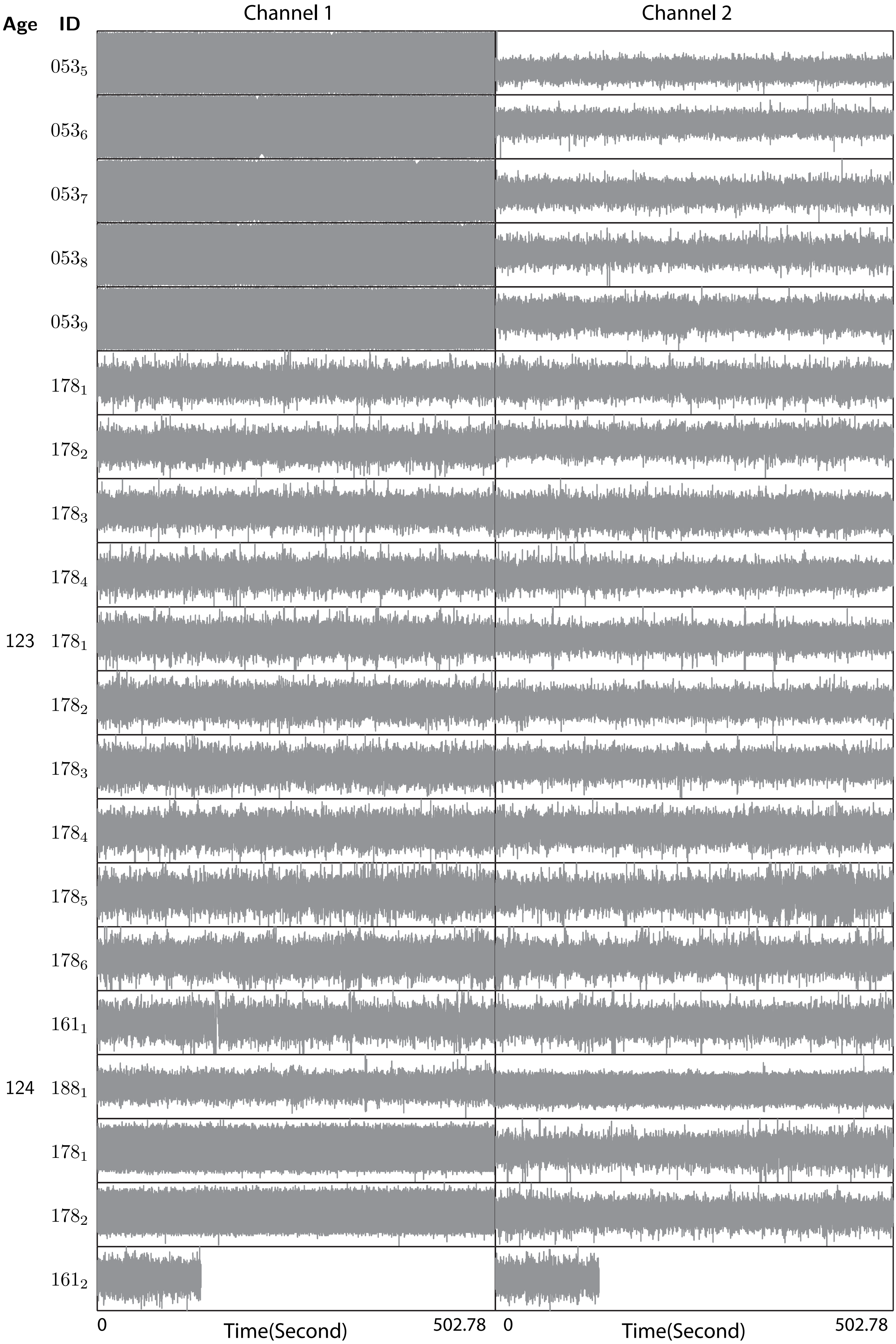
Age
ID
Channel 1
Channel 2
053_5
053_6
053_7
053_8
053_9
178_1
178_2
178_3
178_4
123
178_1
178_2
178_3
178_4
178_5
178_6
161_1
124
188_1
178_1
178_2
161_2
0
Time(Second)
502.78
0
Time(Second)
502.78

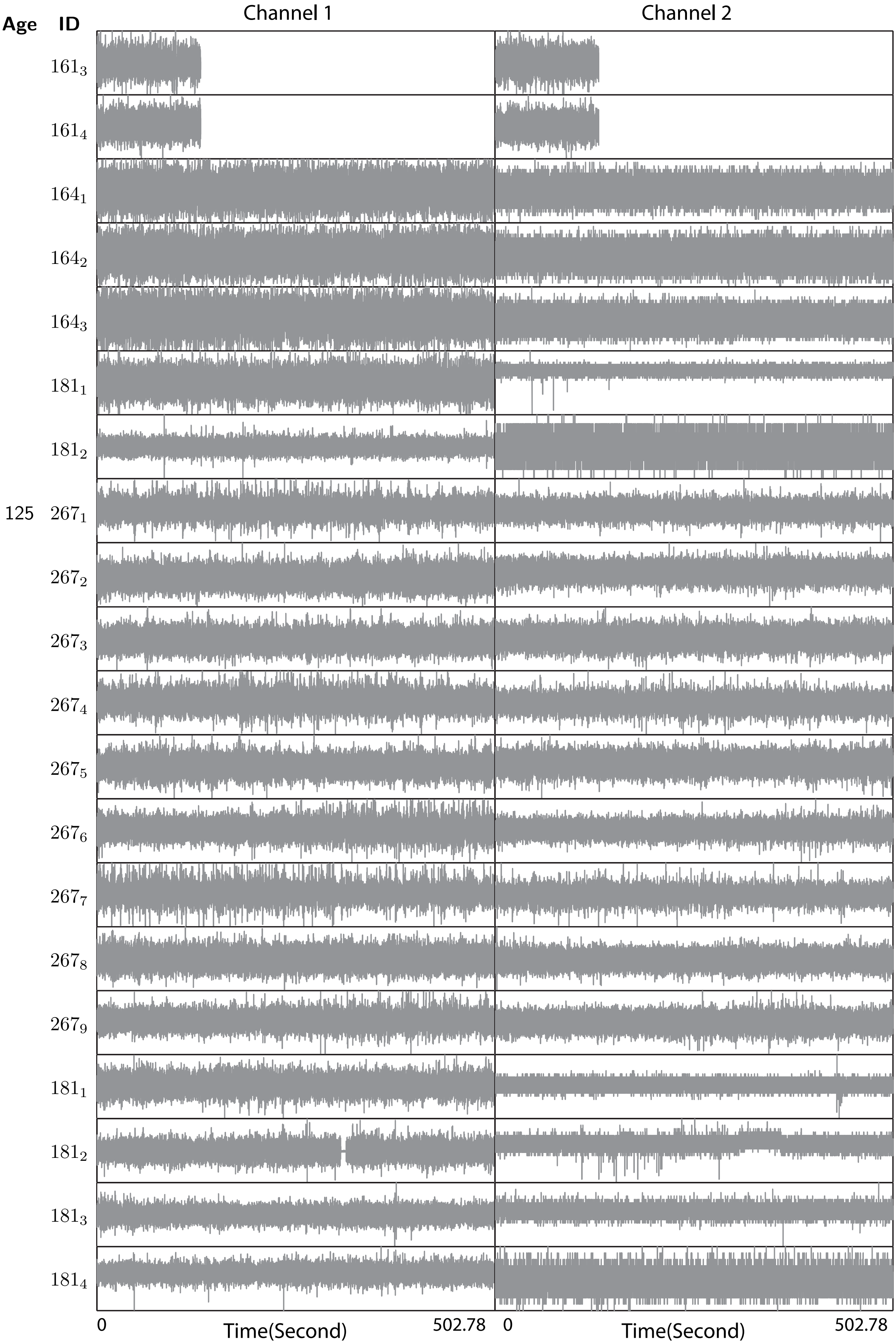
Age
ID
Channel 1
Channel 2
161_3
161_4
164_1
164_2
164_3
181_1
181_2
125
267_1
267_2
267_3
267_4
267_5
267_6
267_7
267_8
267_9
181_1
181_2
181_3
181_4
0
Time(Second)
502.78
0
Time(Second)
502.78

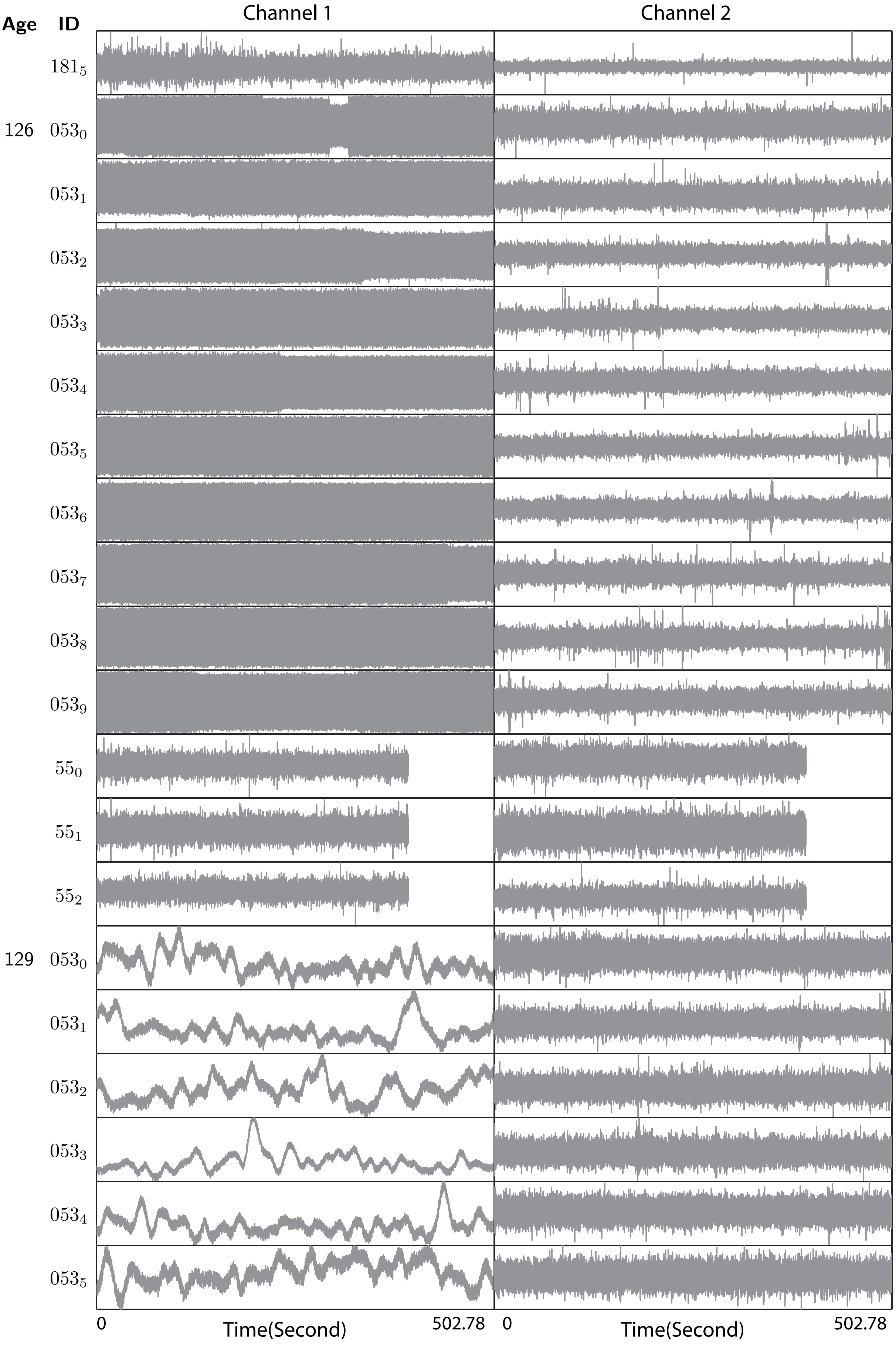
Age
ID
Channel 1
Channel 2
181_5
126
053_0
053_1
053_2
053_3
053_4
053_5
053_6
053_7
053_8
053_9
55_0
55_1
55_2
129
053_0
053_1
053_2
053_3
053_4
053_5
0
Time(Second)
502.78
0
Time(Second)
502.78

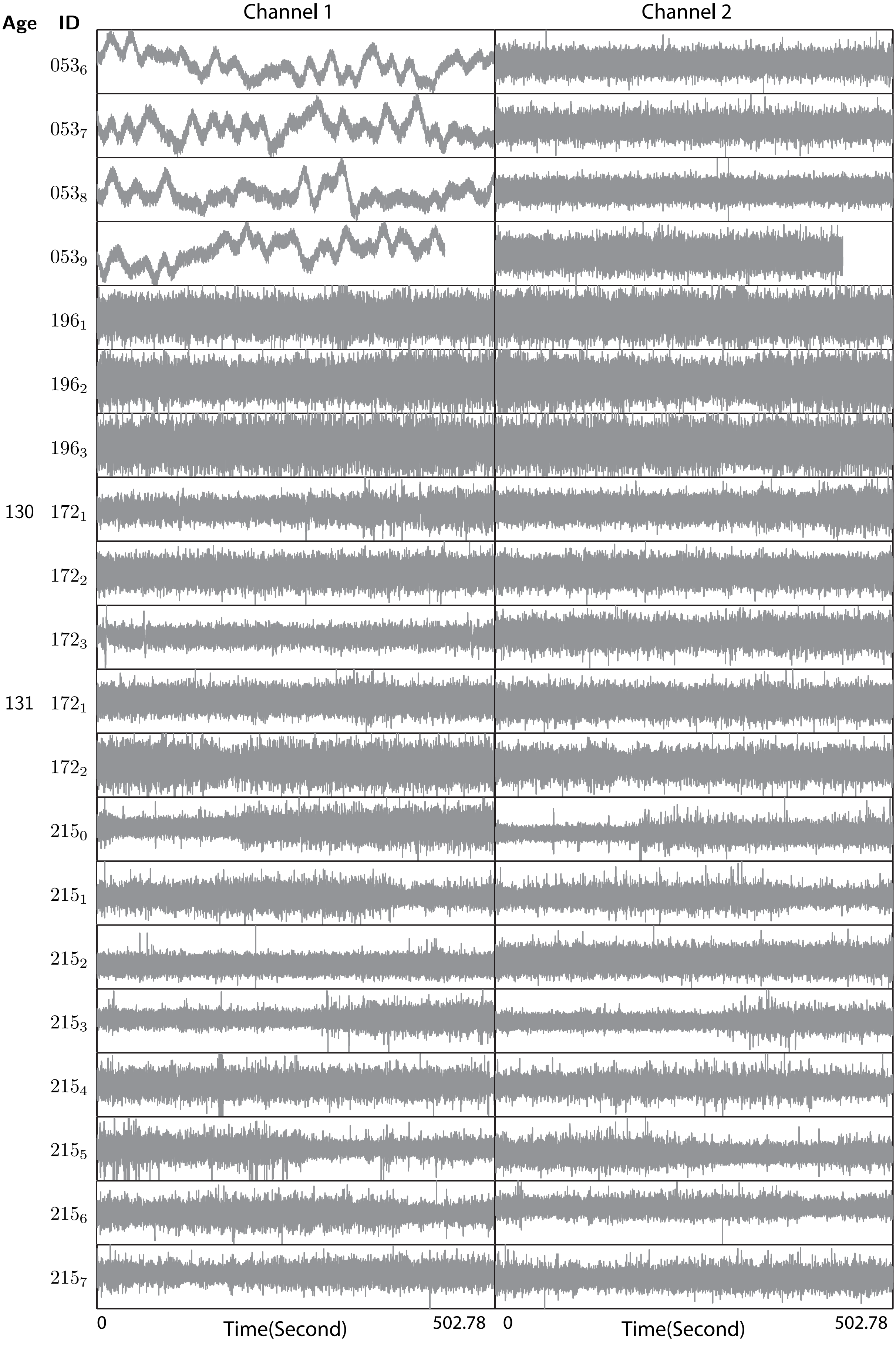
Age
ID
Channel 1
Channel 2
053_6
053_7
053_8
053_9
196_1
196_2
196_3
130
172_1
172_2
172_3
131
172_1
172_2
215_0
215_1
215_2
215_3
215_4
215_5
215_6
215_7
0
Time(Second)
502.78
0
Time(Second)
502.78

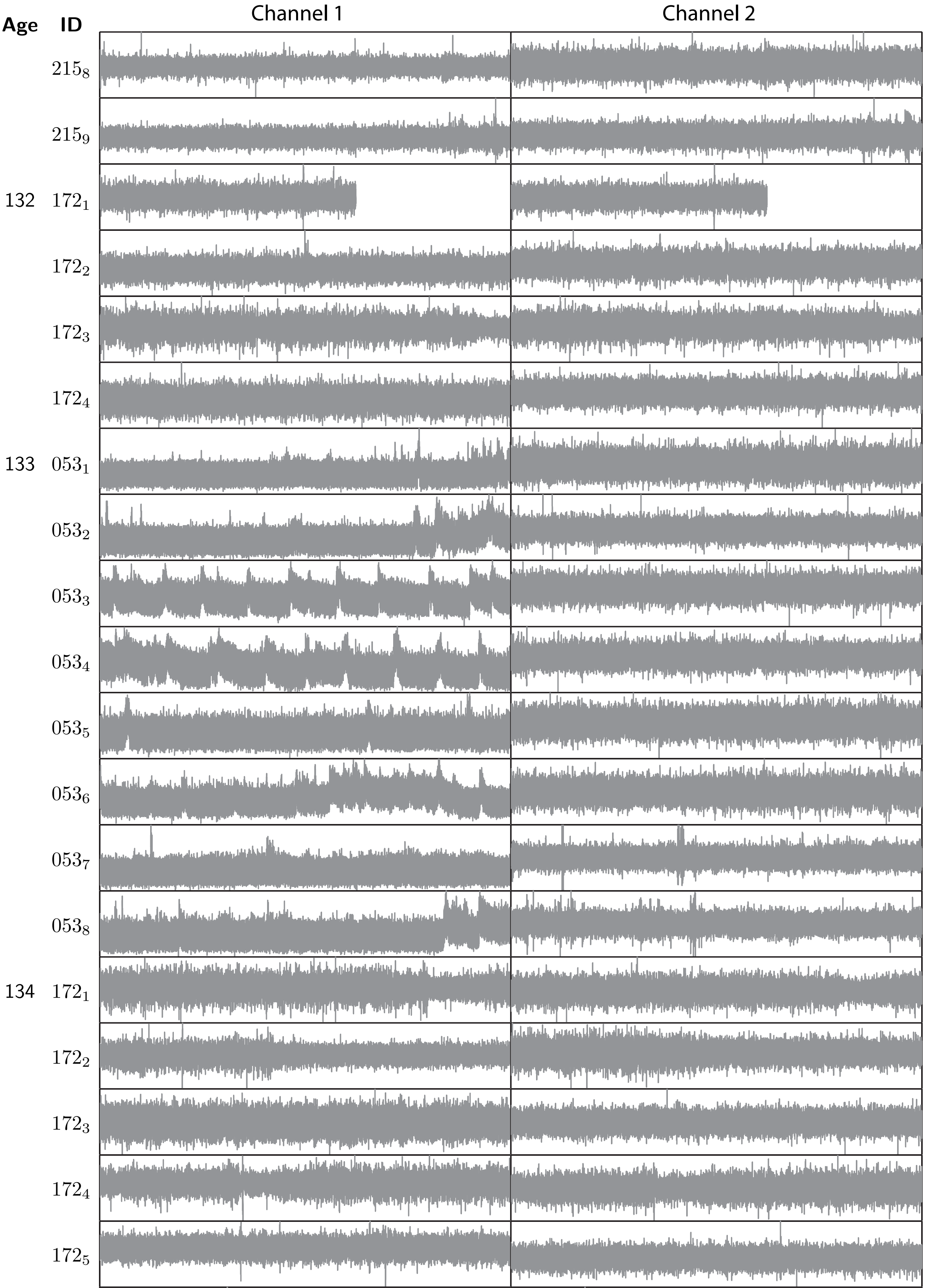
Age
ID
Channel 1
Channel 2
215₈
215₉
132
172₁
172₂
172₃
172₄
133
053₁
053₂
053₃
053₄
053₅
053₆
053₇
053₈
134
172₁
172₂
172₃
172₄
172₅
172₆
0
Time(Second)
502.78
0
Time(Second)
502.78

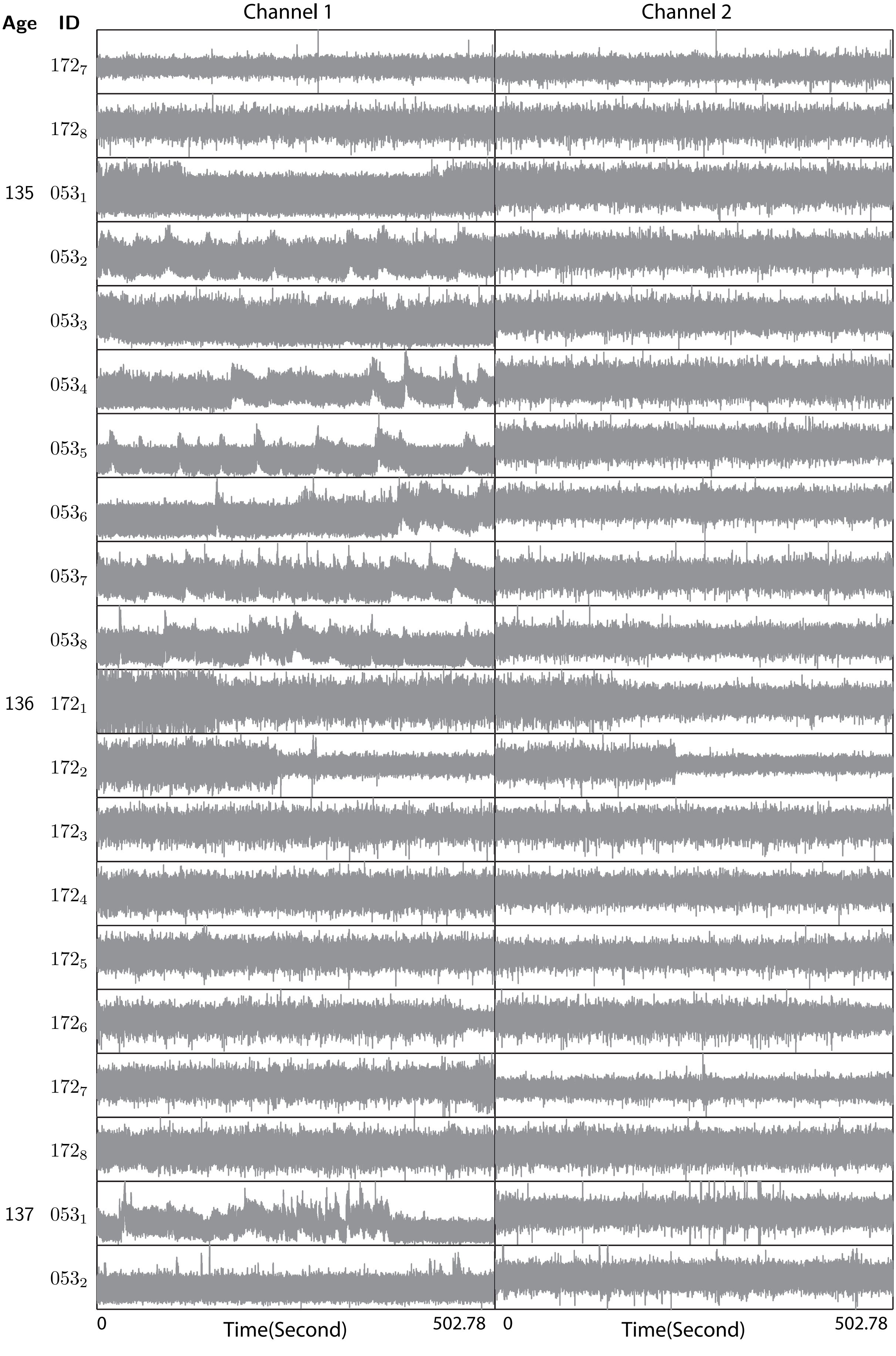
Age
ID
Channel 1
Channel 2
172_7
172_8
135
053_1
053_2
053_3
053_4
053_5
053_6
053_7
053_8
136
172_1
172_2
172_3
172_4
172_5
172_6
172_7
172_8
137
053_1
053_2
0
Time(Second)
502.78
0
Time(Second)
502.78

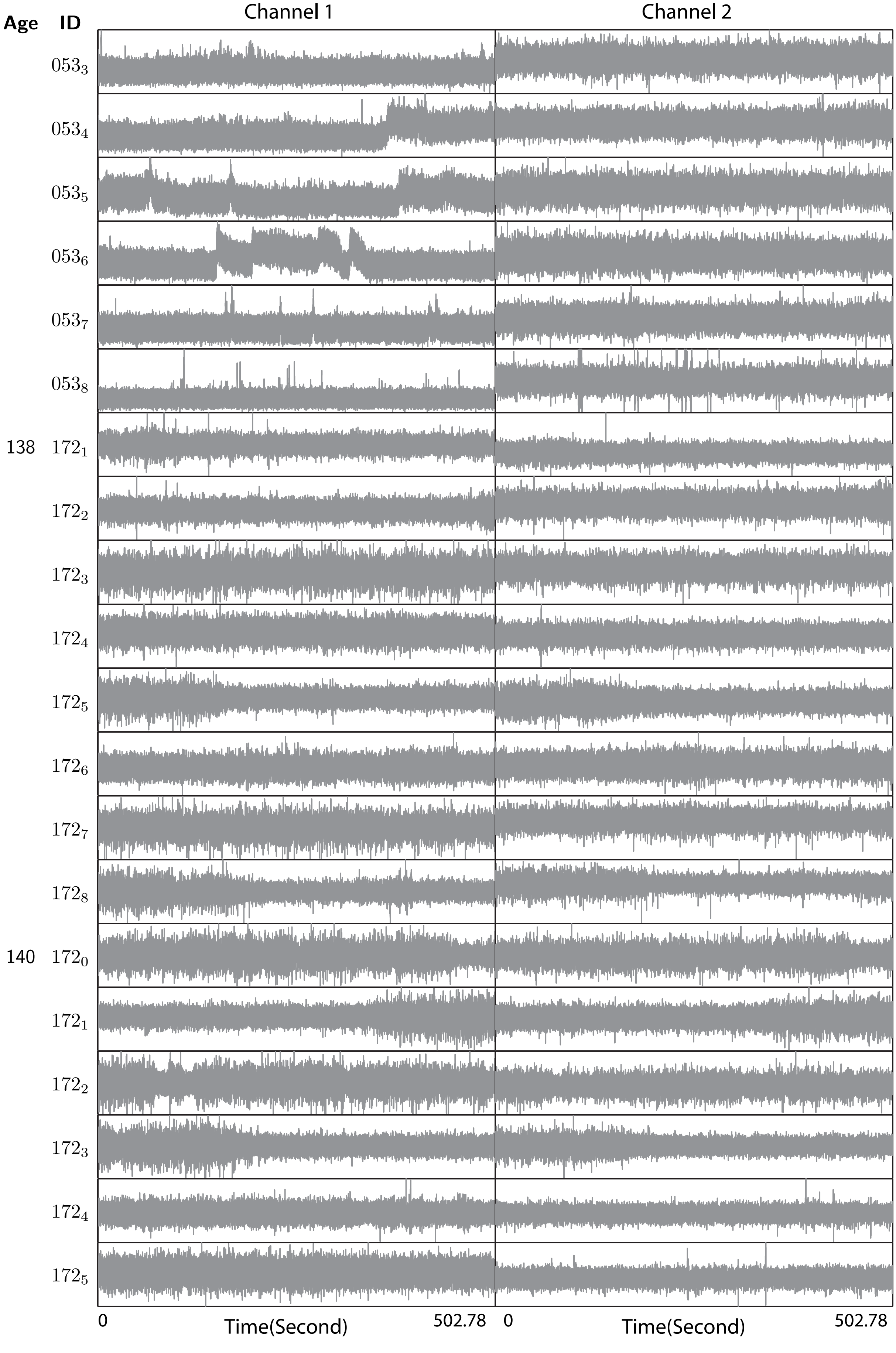
Age
ID
Channel 1
Channel 2
053_3
053_4
053_5
053_6
053_7
053_8
138
172_1
172_2
172_3
172_4
172_5
172_6
172_7
172_8
140
172_0
172_1
172_2
172_3
172_4
172_5
0
Time(Second)
502.78
0
Time(Second)
502.78

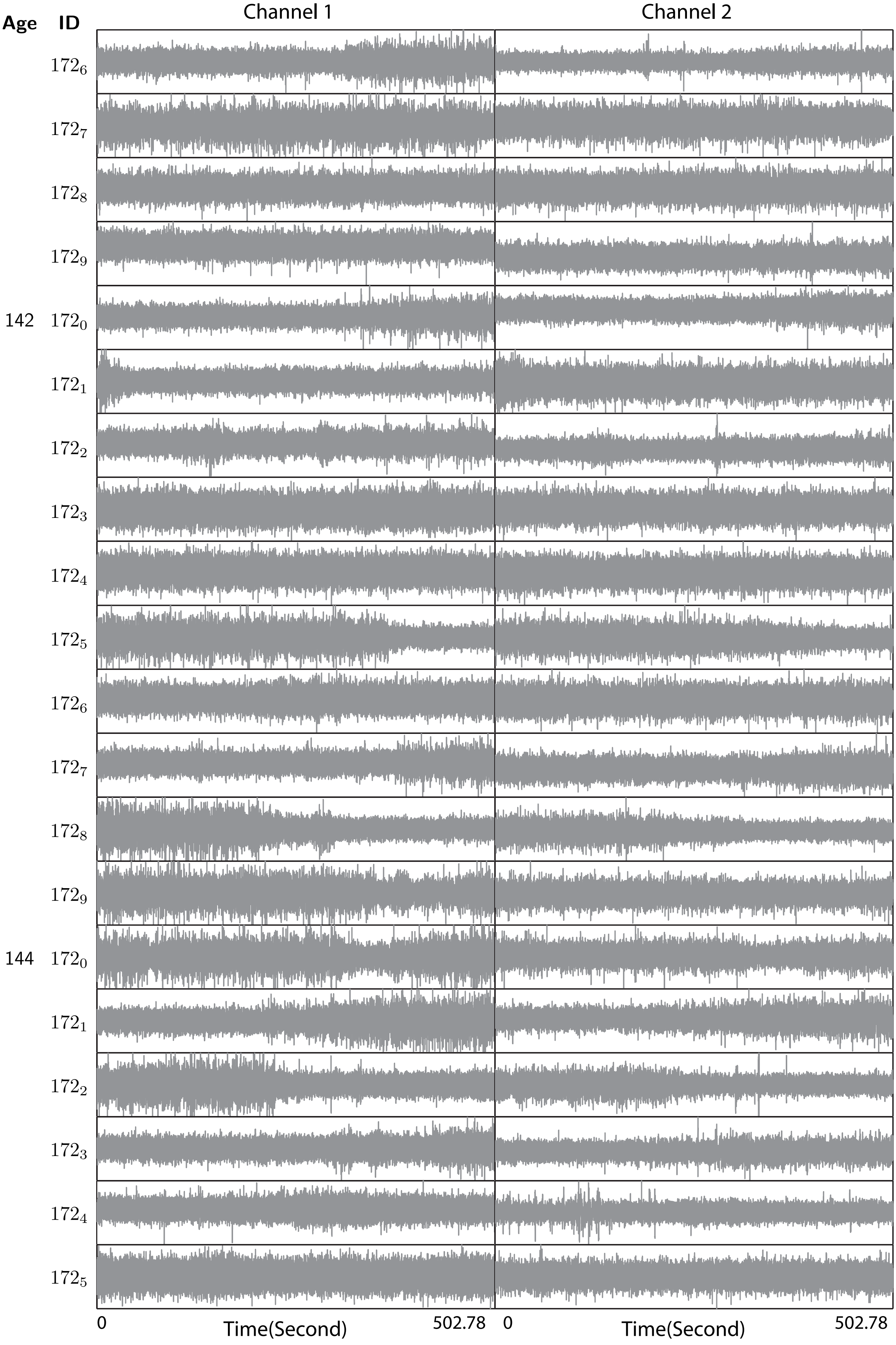
Age
ID
Channel 1
Channel 2
172_6
172_7
172_8
172_9
142
172_0
172_1
172_2
172_3
172_4
172_5
172_6
172_7
172_8
172_9
144
172_0
172_1
172_2
172_3
172_4
172_5
0
Time(Second)
502.78
0
Time(Second)
502.78

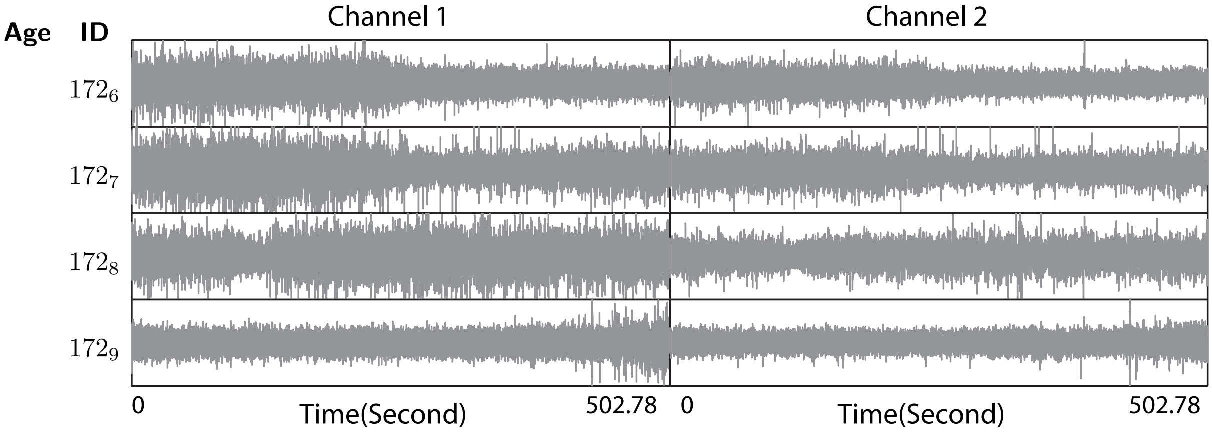
Age
ID
Channel 1
Channel 2
172_6
172_7
172_8
172_9
0
Time(Second)
502.78
0
Time(Second)
502.78

Appendix B

REM and SWS State Transitions

In our 234 fetal sheep recordings aged from 95 to 144 gestational days, I identified 14 ECoG recordings as SWS-to-REM sleep state transition, and 8 ECoG recordings as REM-to-SWS transition. Average power, correlation time, and SVD entropy analysis are conducted for each ECoG recording showing a sleep-state transition, and the results are displayed in this Appendix.

On each page, the top figure gives the ECoG recording from channel-1 and its analysis results, the bottom figure gives the corresponding ECoG recording and its analysis results from channel-2. In each figure, the title gives the information of the sleep-state transition, the sheep ID, fetus age, recording session number, and recording channel. For example, in the first figure of this appendix, the ECoG time-series with a SWS-to-REM sleep state transition is recorded from channel-1 during recording session 6 on fetus with ID 172 at gestational age of 144 days. The time-series in the first subplot has unit of raw digital number (DN). The correlation time in the third subplot has unit of ms. The unit of average power is DN^2 and SVD entropy is dimensionless.

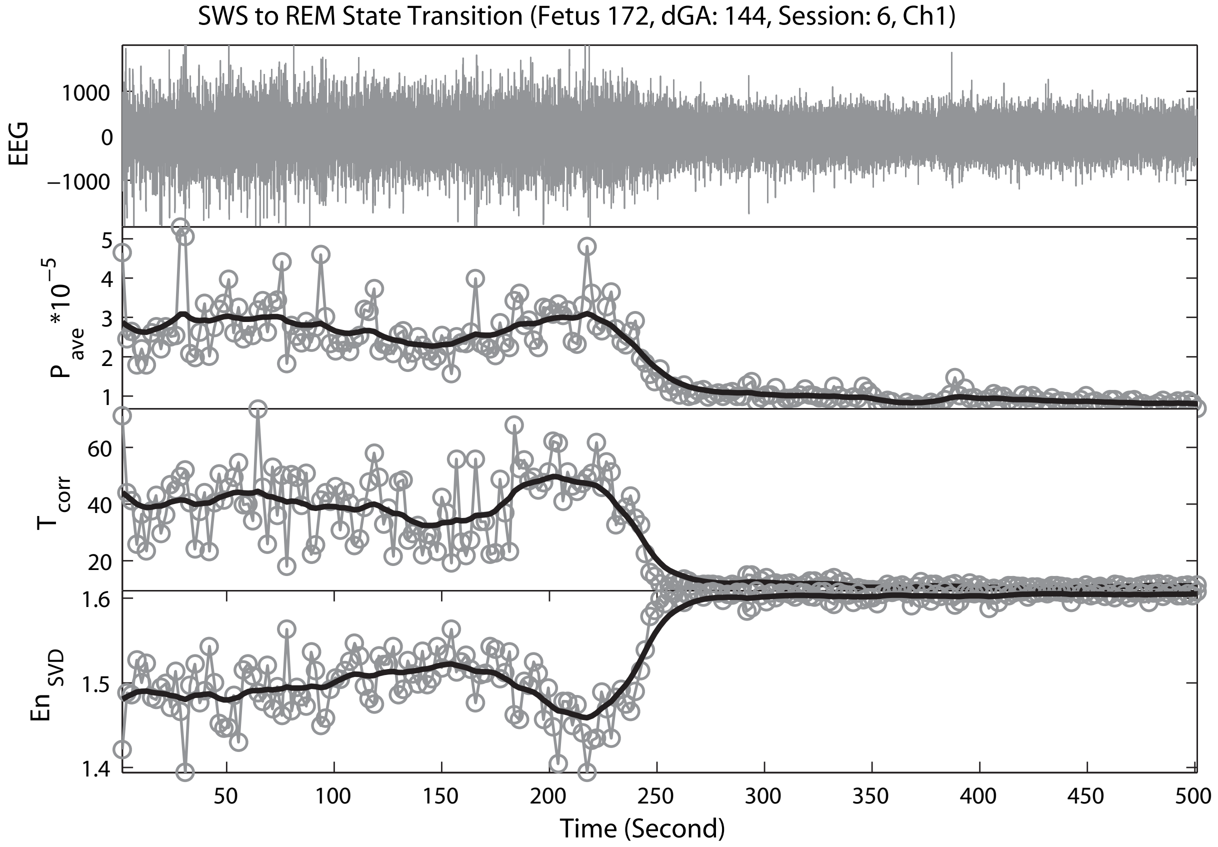
SWS to REM State Transition (Fetus 172, dGA: 144, Session: 6, Ch1)
EEG
1000
0
−1000
$P_{ave}*10^{-5}$
5
4
3
2
1
T_{corr}
60
40
20
En_{SVD}
1.6
1.5
1.4
50
100
150
200
250
300
350
400
450
500
Time (Second)

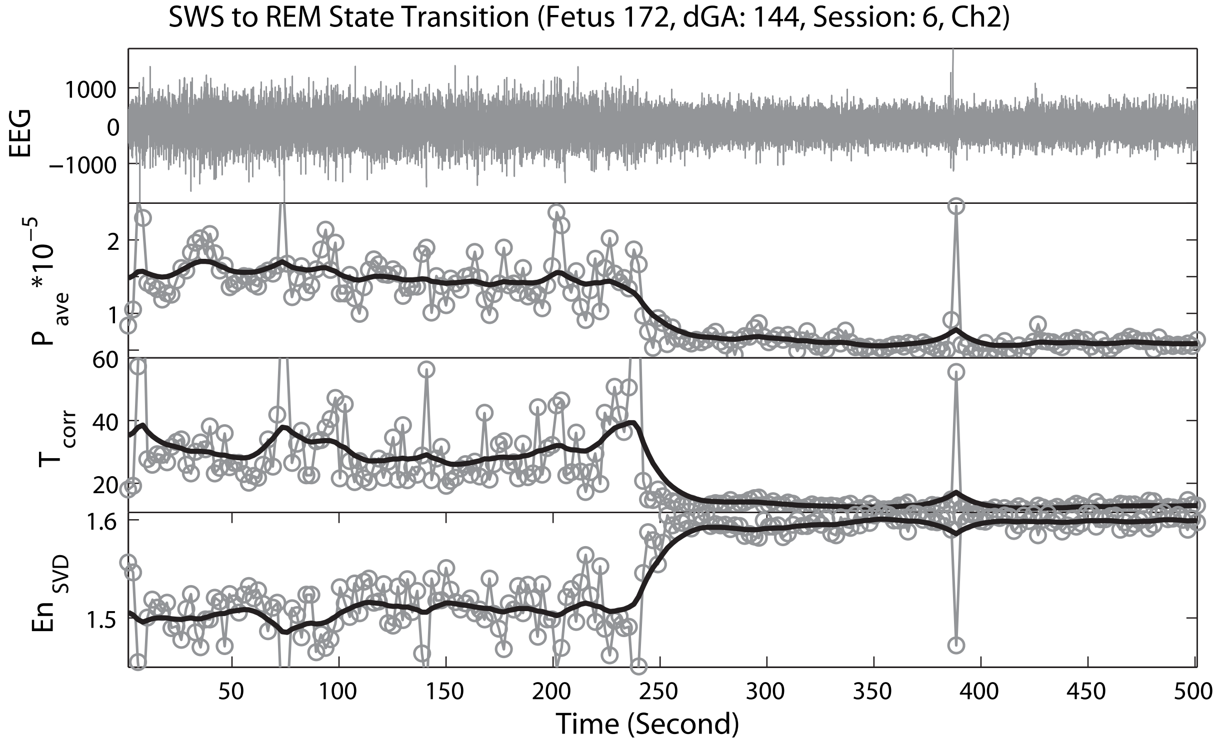
SWS to REM State Transition (Fetus 172, dGA: 144, Session: 6, Ch2)
EEG
1000
0
−1000
$P_{ave}*10^{-5}$
2
1
T_{corr}
60
40
20
En_{SVD}
1.6
1.5
50
100
150
200
250
300
350
400
450
500
Time (Second)

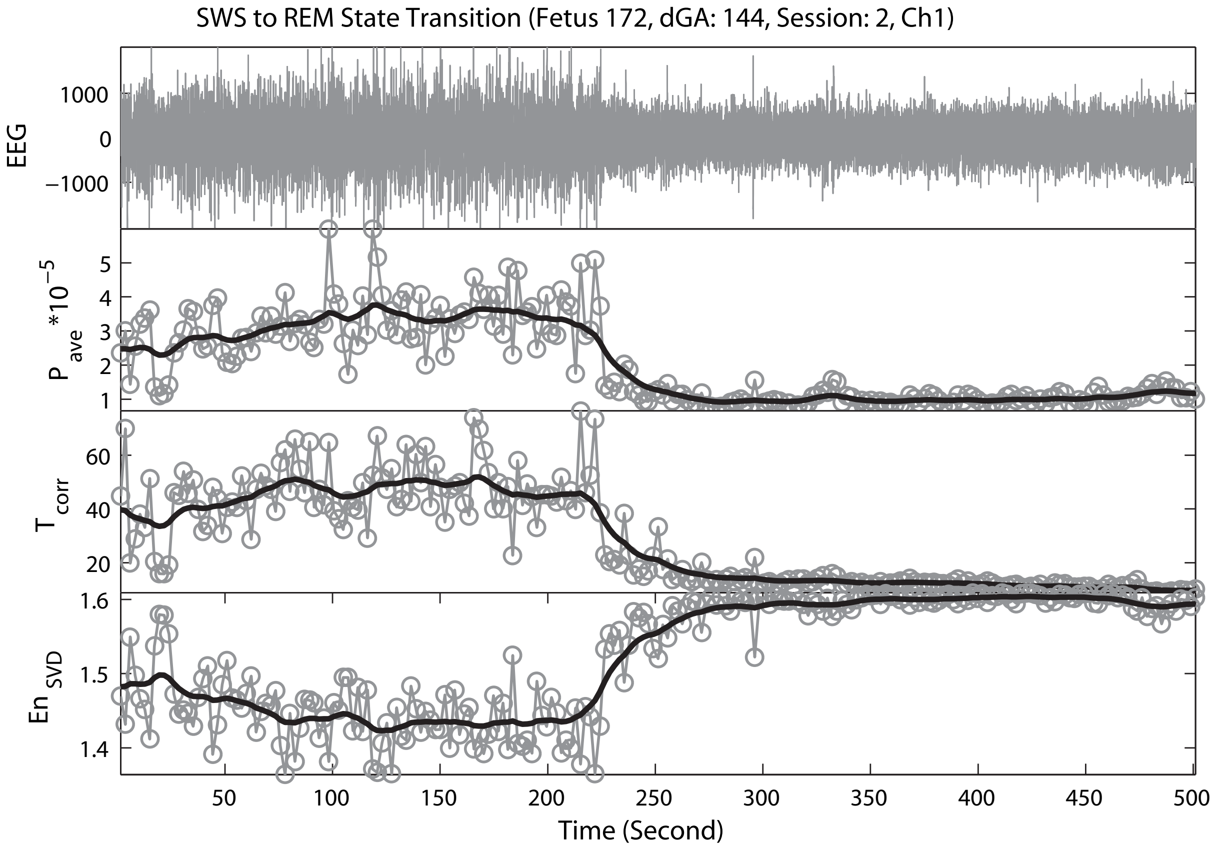
SWS to REM State Transition (Fetus 172, dGA: 144, Session: 2, Ch1)
EEG
1000
0
−1000
$P_{ave}*10^{-5}$
5
4
3
2
1
T_{corr}
60
40
20
En_{SVD}
1.6
1.5
1.4
50
100
150
200
250
300
350
400
450
500
Time (Second)

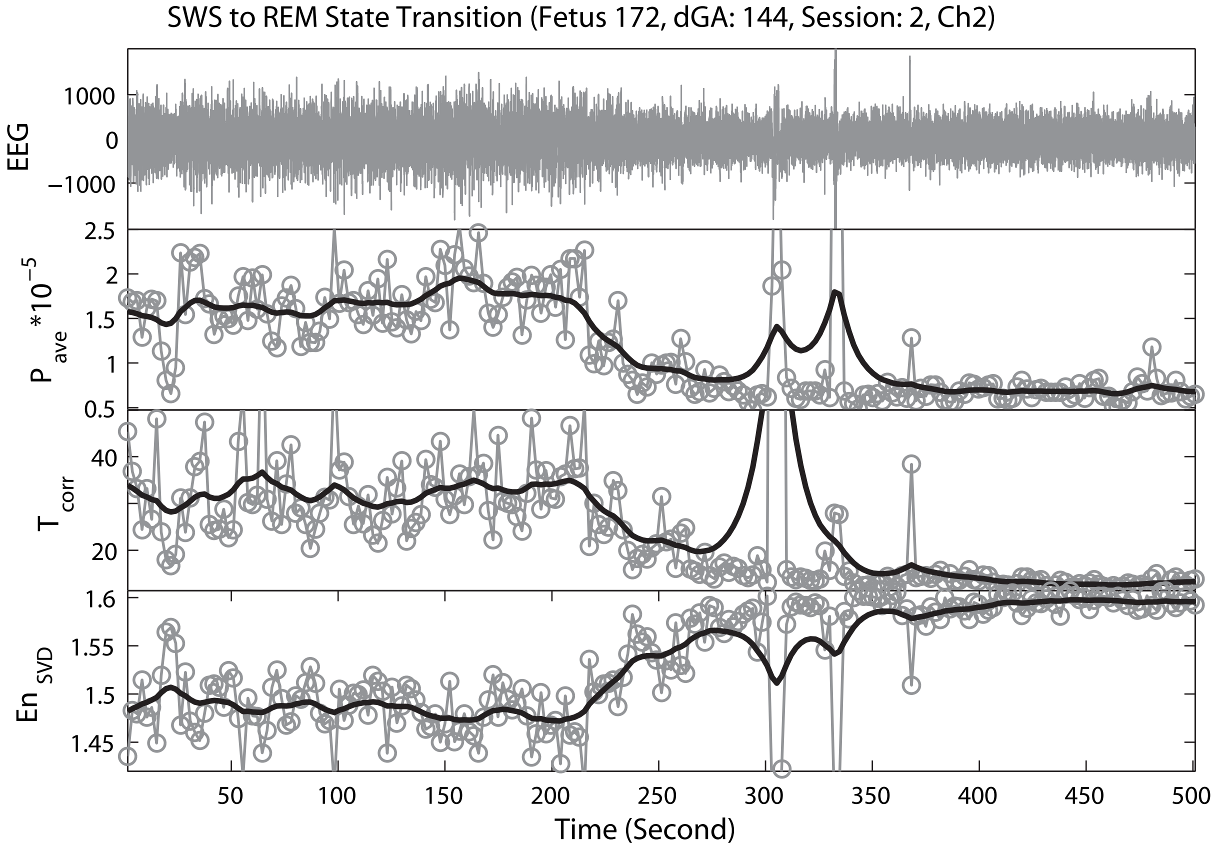
SWS to REM State Transition (Fetus 172, dGA: 144, Session: 2, Ch2)
EEG
1000
0
−1000
$P_{ave}*10^{-5}$
2.5
2
1.5
1
0.5
T_{corr}
40
30
20
En_{SVD}
1.6
1.55
1.5
1.45
50
100
150
200
250
300
350
400
450
500
Time (Second)

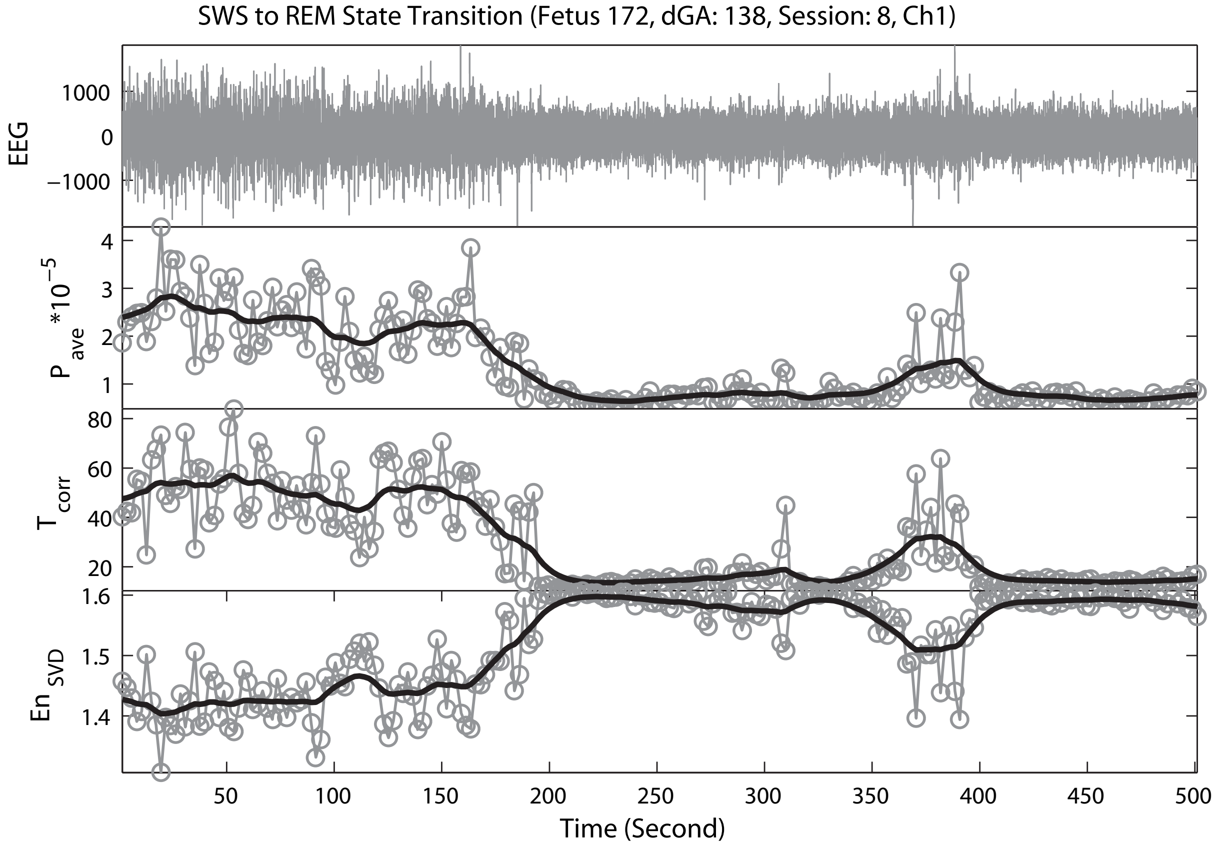
SWS to REM State Transition (Fetus 172, dGA: 138, Session: 8, Ch1)
EEG
1000
0
−1000
$P_{ave}*10^{-5}$
4
3
2
1
T_{corr}
80
60
40
20
En_{SVD}
1.6
1.5
1.4
50
100
150
200
250
300
350
400
450
500
Time (Second)

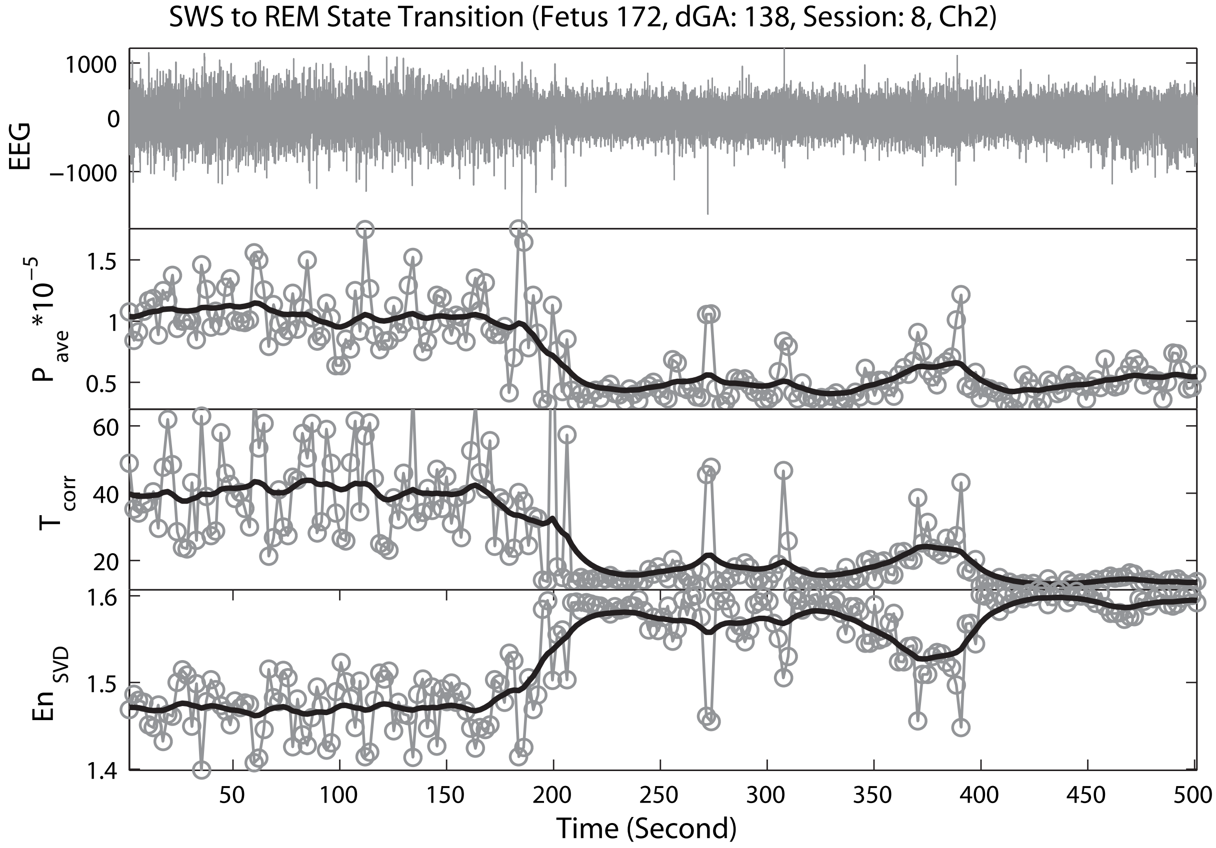
SWS to REM State Transition (Fetus 172, dGA: 138, Session: 8, Ch2)
EEG
1000
0
−1000
$P_{ave}*10^{-5}$
1.5
1
0.5
T_{corr}
60
40
20
En_{SVD}
1.6
1.5
1.4
50
100
150
200
250
300
350
400
450
500
Time (Second)

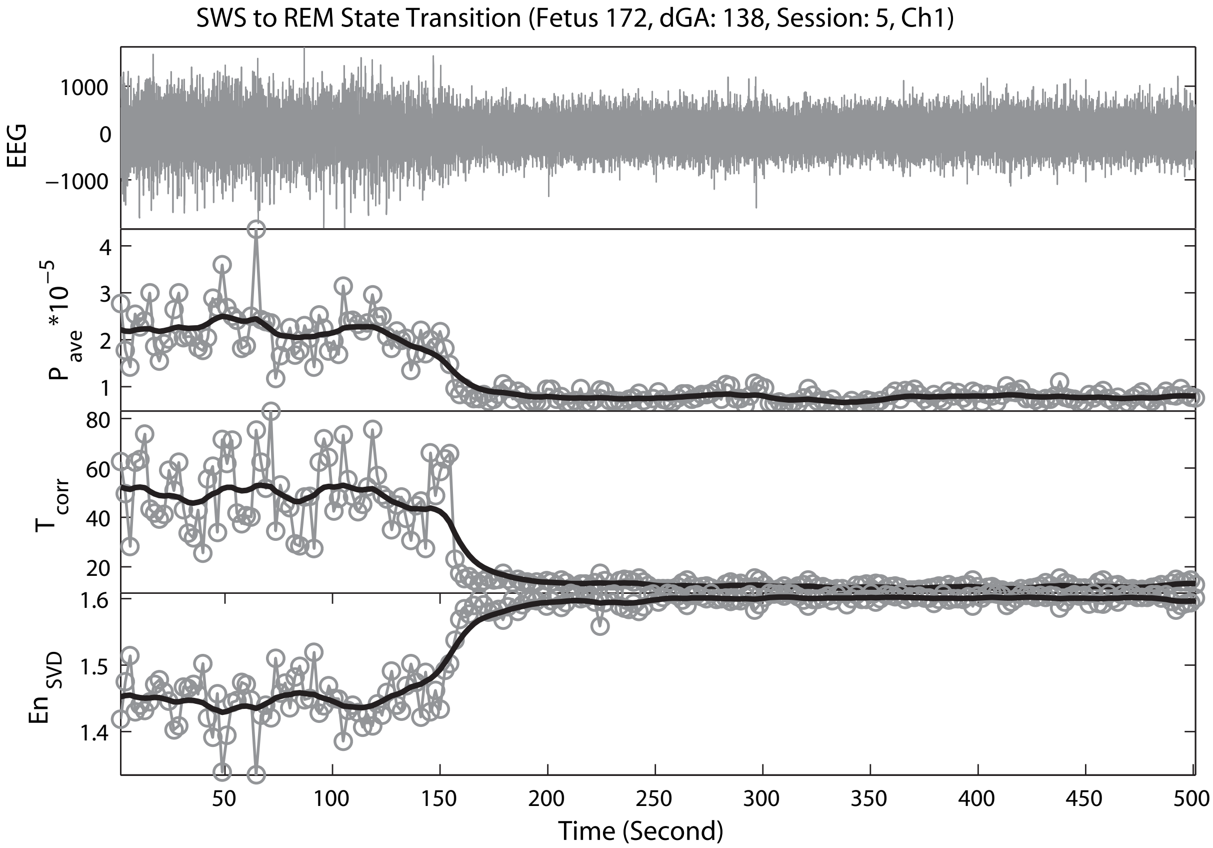
SWS to REM State Transition (Fetus 172, dGA: 138, Session: 5, Ch1)
EEG
1000
0
−1000
P_{ave}*10^{-5}
4
3
2
1
T_{corr}
80
60
40
20
En_{SVD}
1.6
1.5
1.4
50
100
150
200
250
300
350
400
450
500
Time (Second)

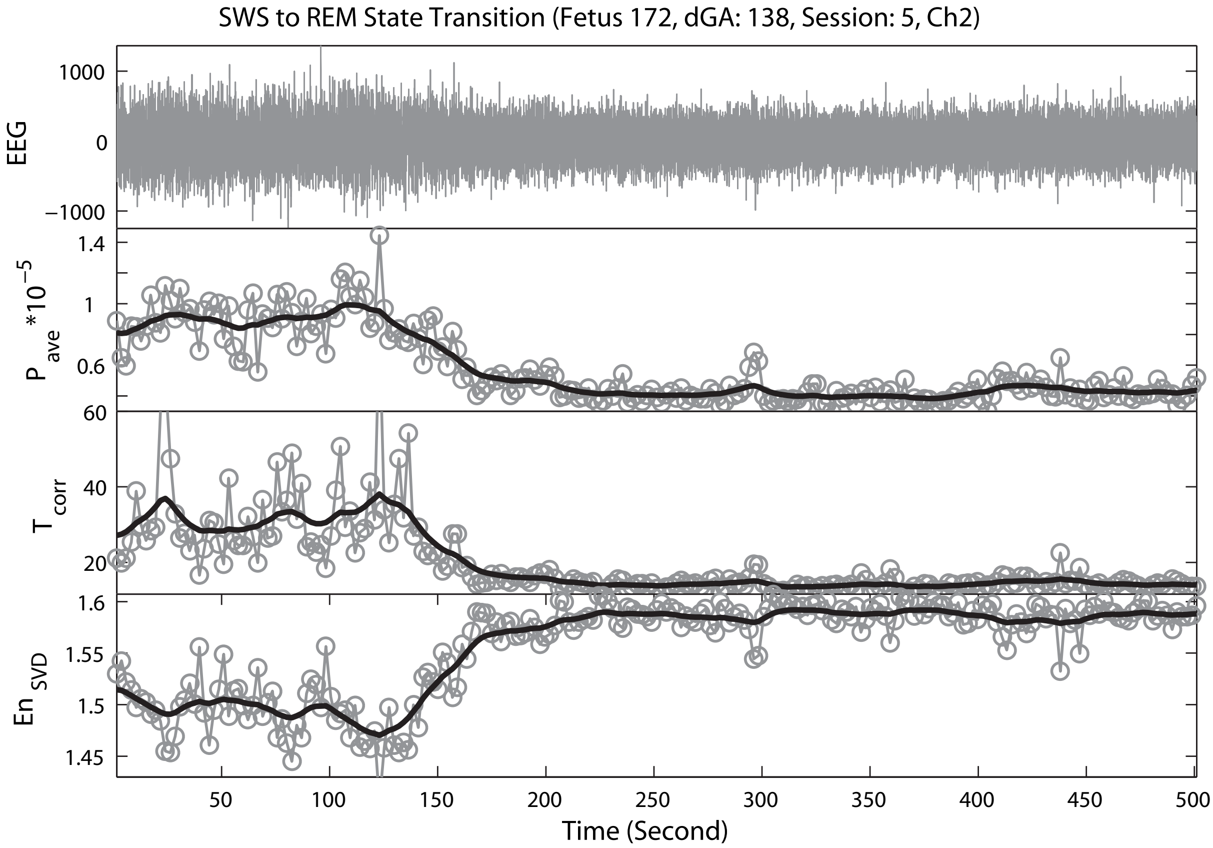
SWS to REM State Transition (Fetus 172, dGA: 138, Session: 5, Ch2)
EEG
1000
0
−1000
P_{ave}*10^{-5}
1.4
1
0.6
T_{corr}
60
40
20
En_{SVD}
1.6
1.55
1.5
1.45
50
100
150
200
250
300
350
400
450
500
Time (Second)

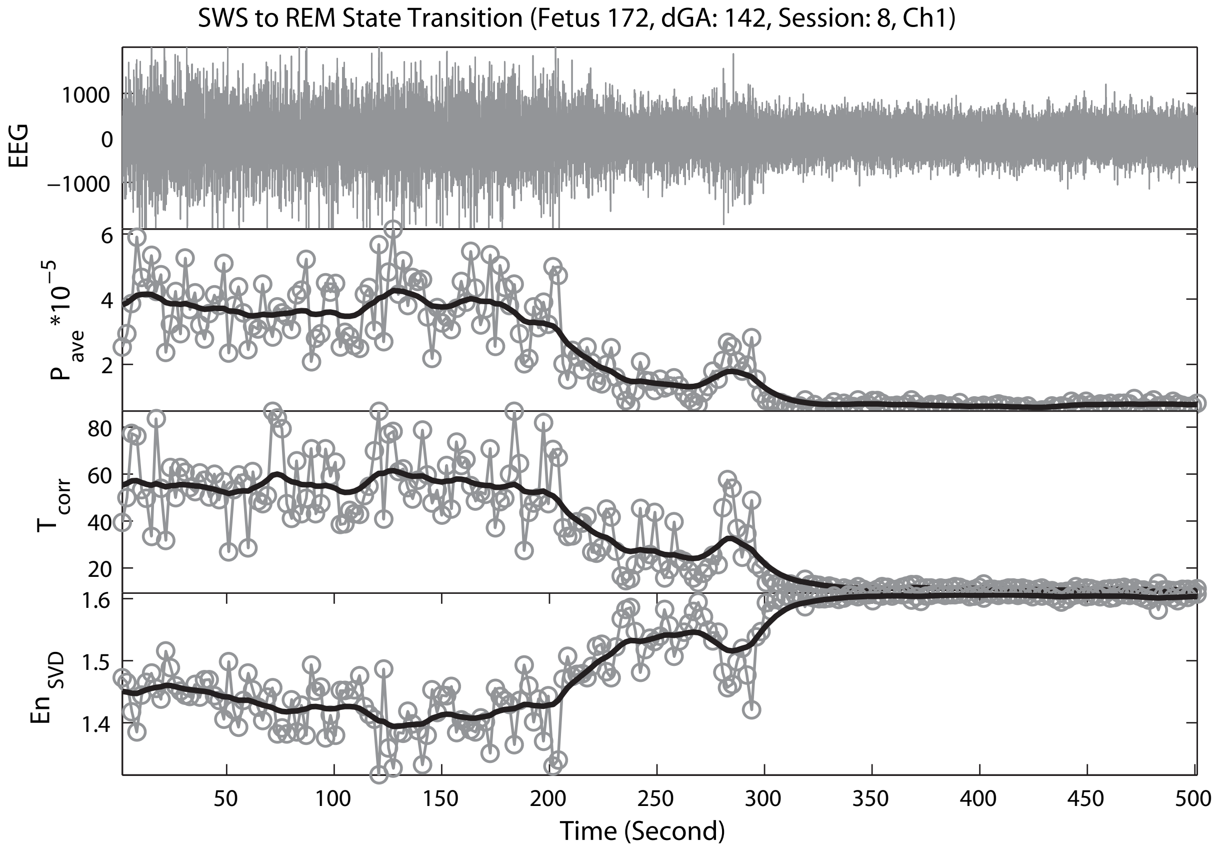
SWS to REM State Transition (Fetus 172, dGA: 142, Session: 8, Ch1)
EEG
1000
0
−1000
$P_{ave}*10^{-5}$
6
4
2
T_{corr}
80
60
40
20
En_{SVD}
1.6
1.5
1.4
50
100
150
200
250
300
350
400
450
500
Time (Second)

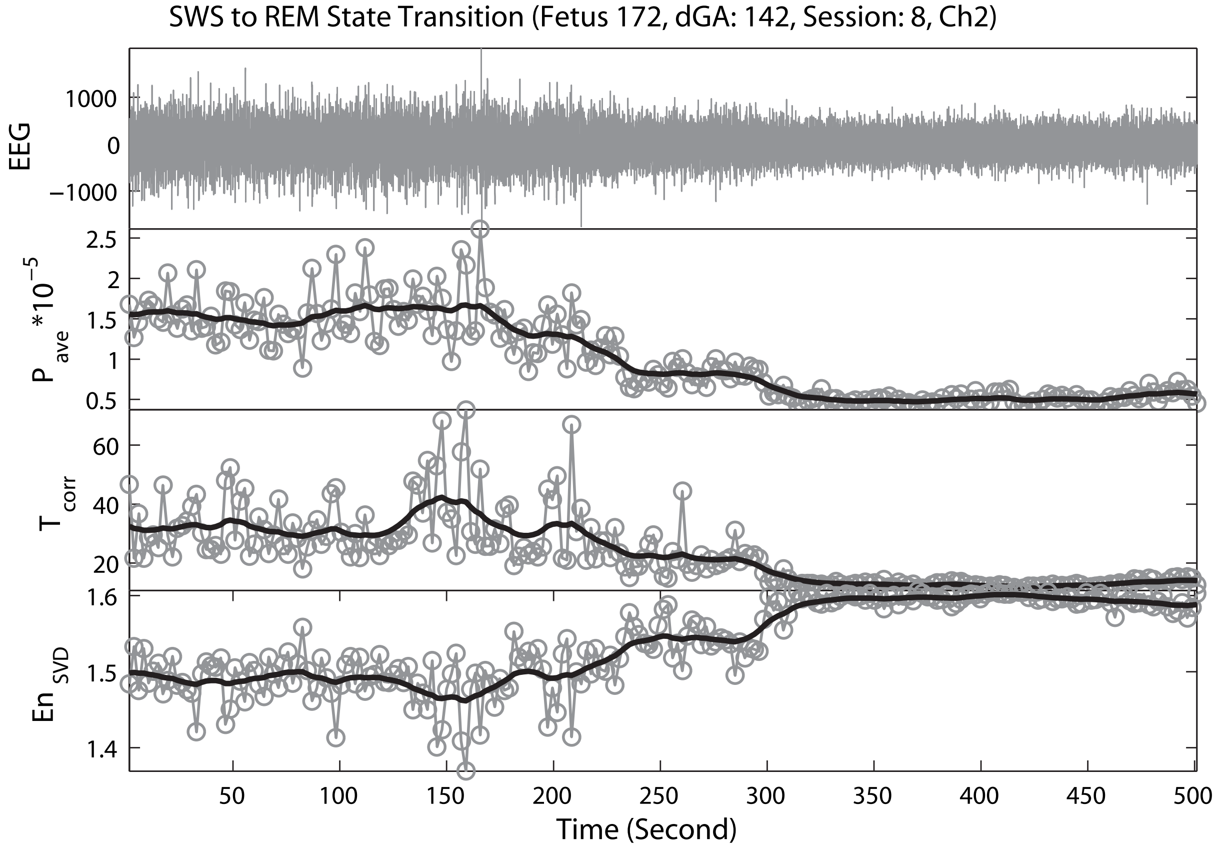
SWS to REM State Transition (Fetus 172, dGA: 142, Session: 8, Ch2)
EEG
1000
0
−1000
$P_{ave}*10^{-5}$
2.5
2
1.5
1
0.5
T_{corr}
60
40
20
En_{SVD}
1.6
1.5
1.4
50
100
150
200
250
300
350
400
450
500
Time (Second)

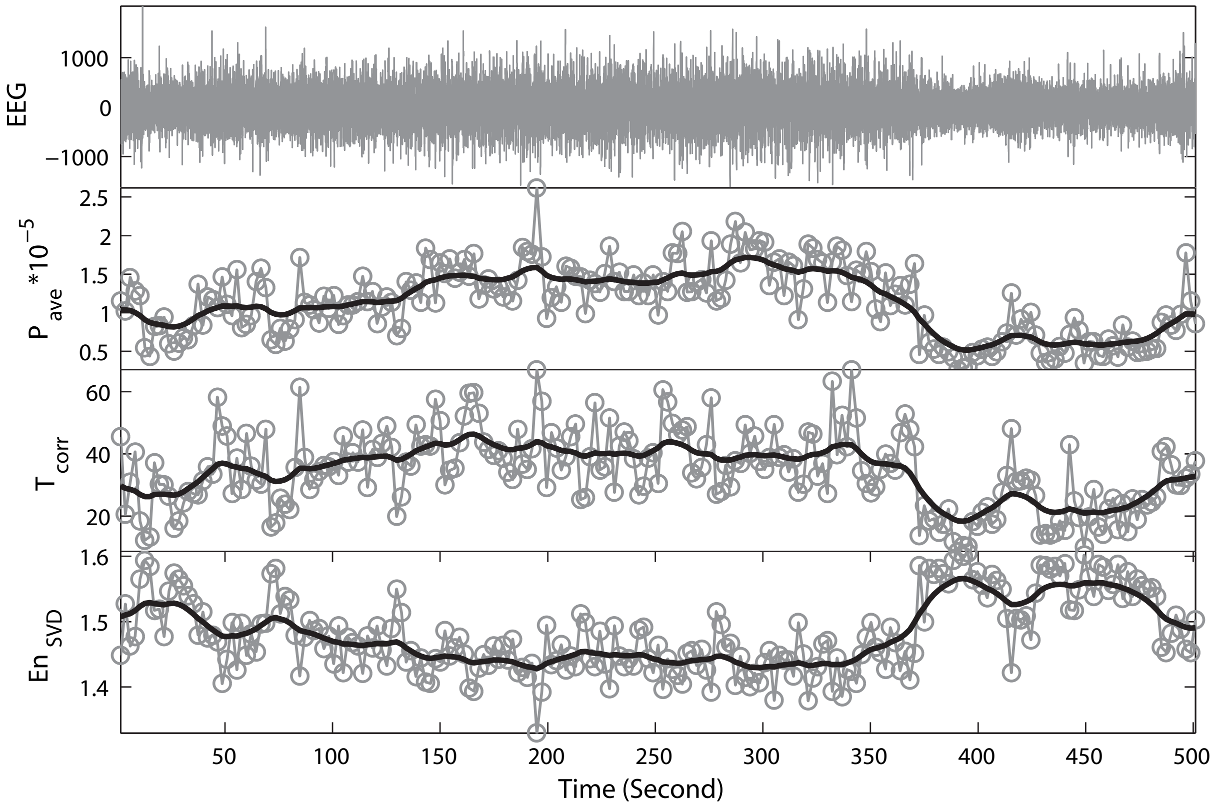

SWS to REM State Transition (Fetus 215, dGA: 131, Session: 1, Ch1)

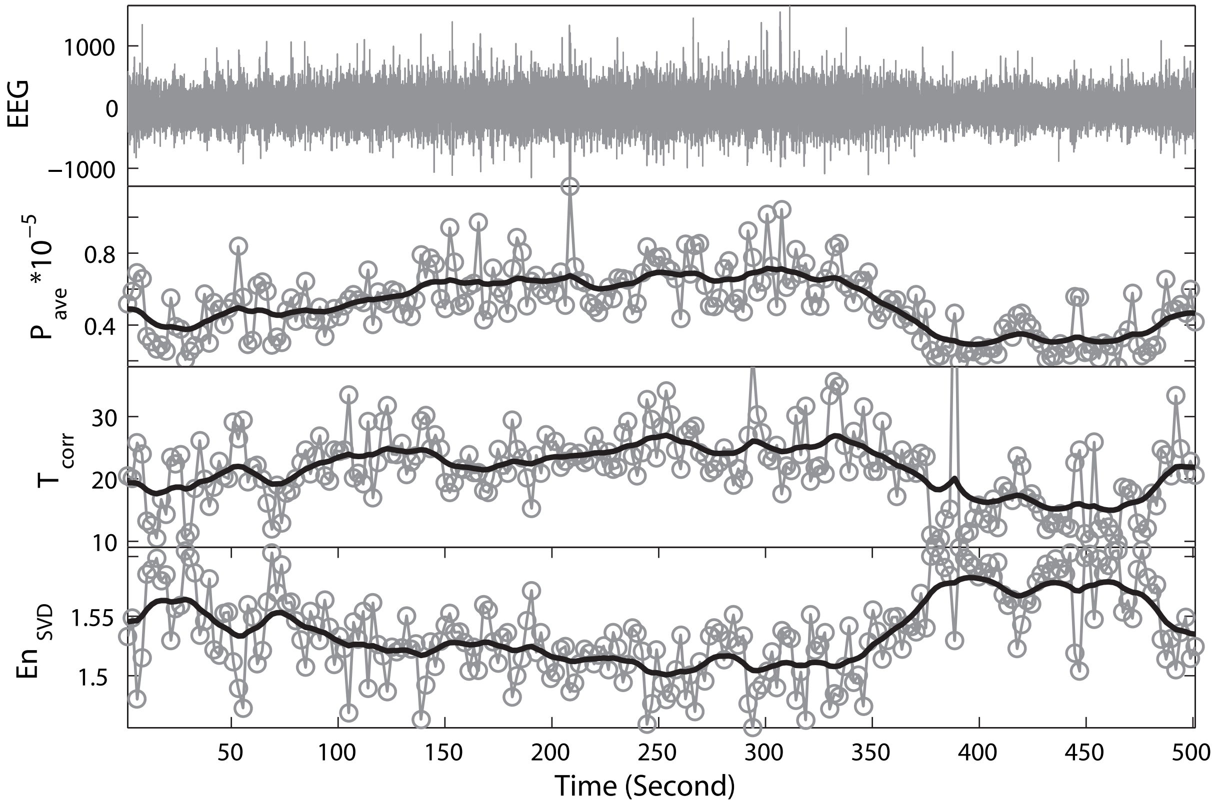

SWS to REM State Transition (Fetus 215, dGA: 131, Session: 1, Ch2)

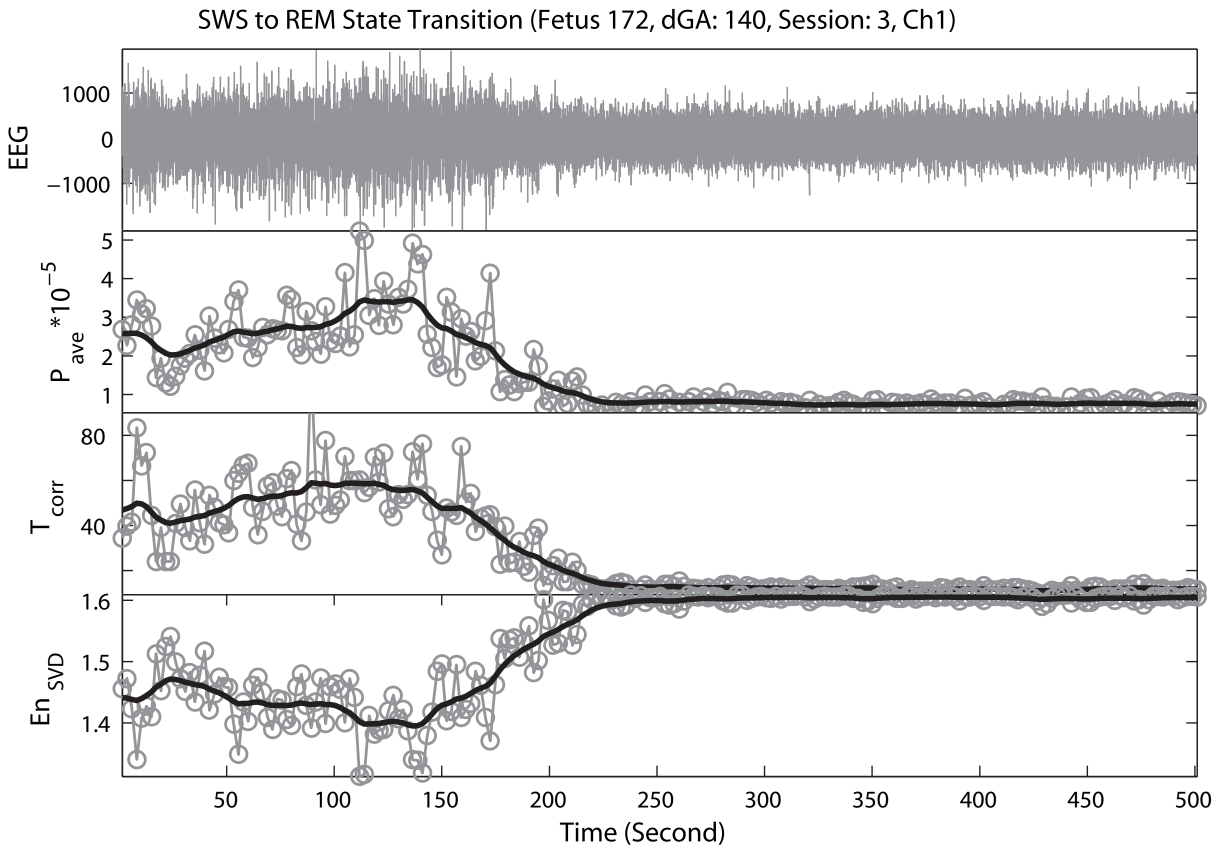
SWS to REM State Transition (Fetus 172, dGA: 140, Session: 3, Ch1)
EEG
1000
0
−1000
$P_{ave}*10^{-5}$
5
4
3
2
1
T_{corr}
80
40
En_{SVD}
1.6
1.5
1.4
50
100
150
200
250
300
350
400
450
500
Time (Second)

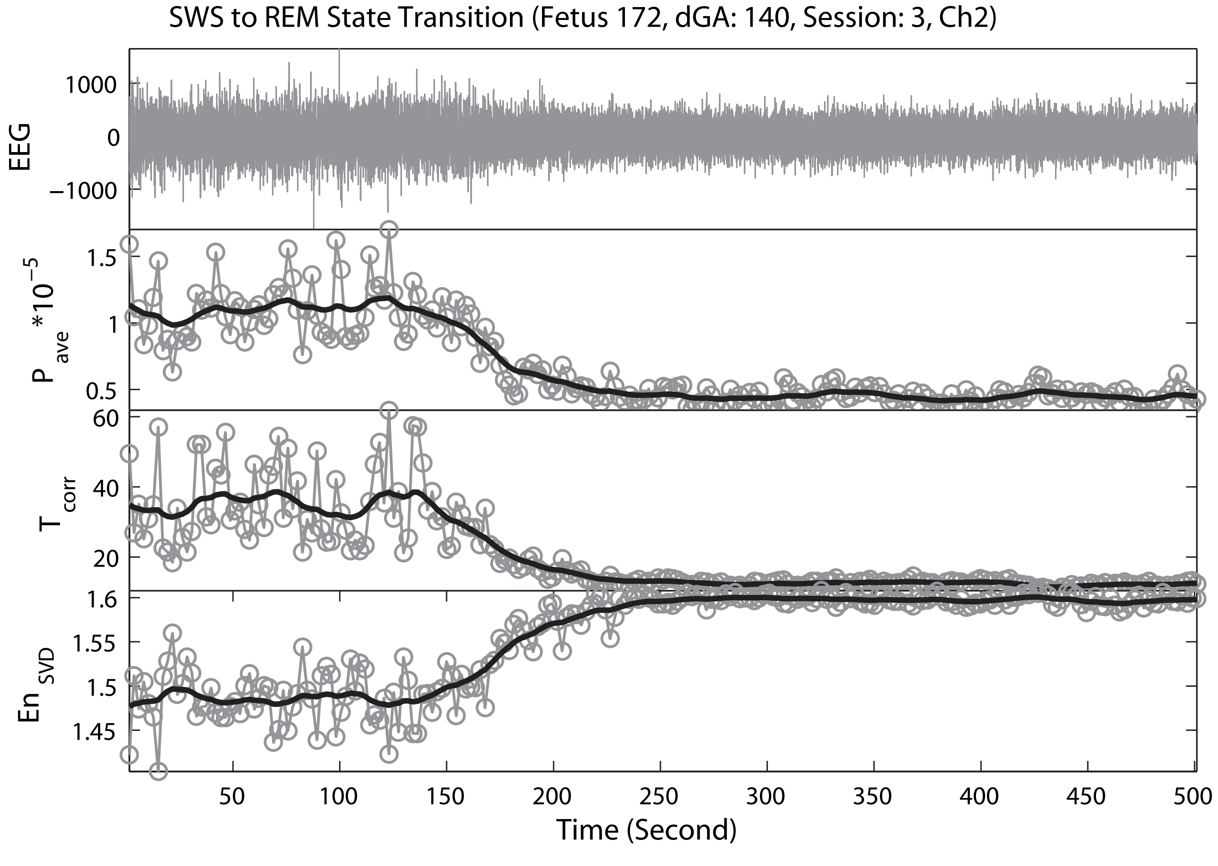
SWS to REM State Transition (Fetus 172, dGA: 140, Session: 3, Ch2)
EEG
1000
0
−1000
$P_{ave}*10^{-5}$
1.5
1
0.5
T_{corr}
60
40
20
En_{SVD}
1.6
1.55
1.5
1.45
50
100
150
200
250
300
350
400
450
500
Time (Second)

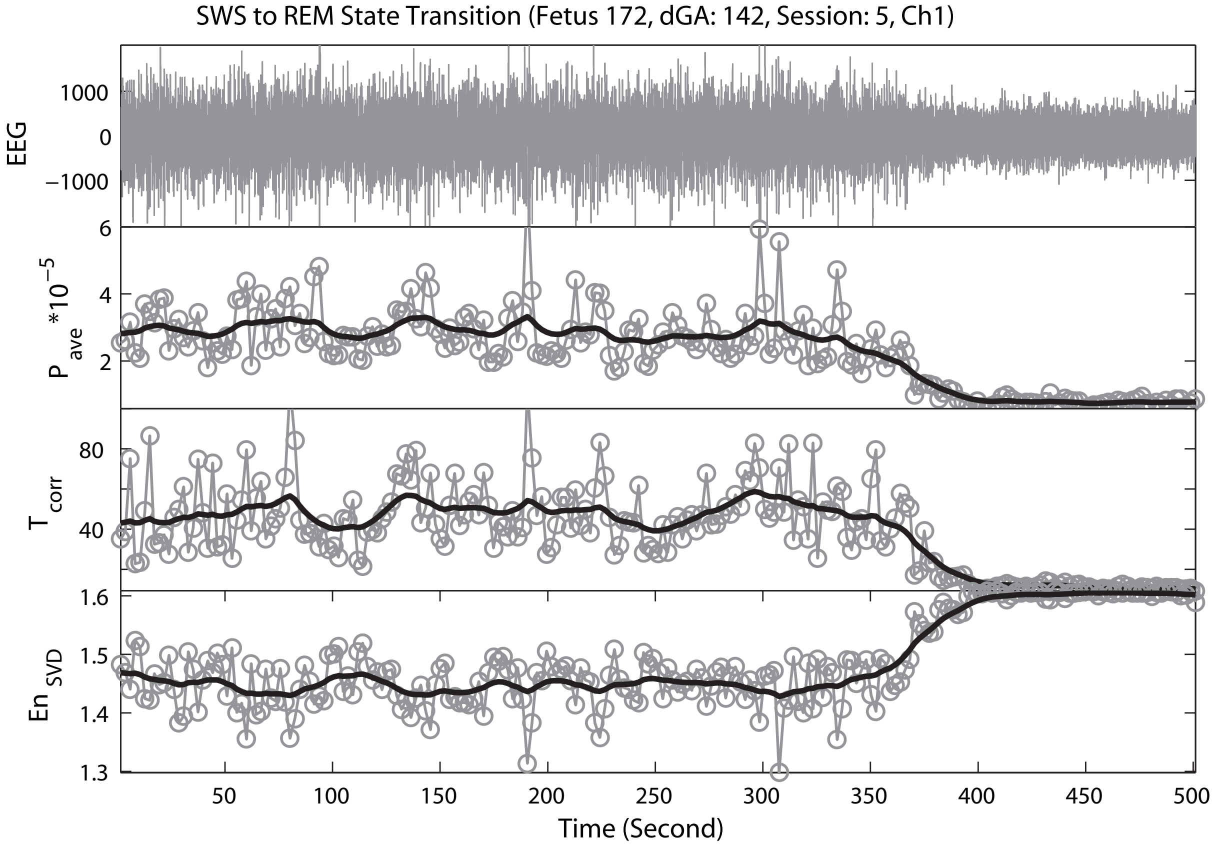
SWS to REM State Transition (Fetus 172, dGA: 142, Session: 5, Ch1)

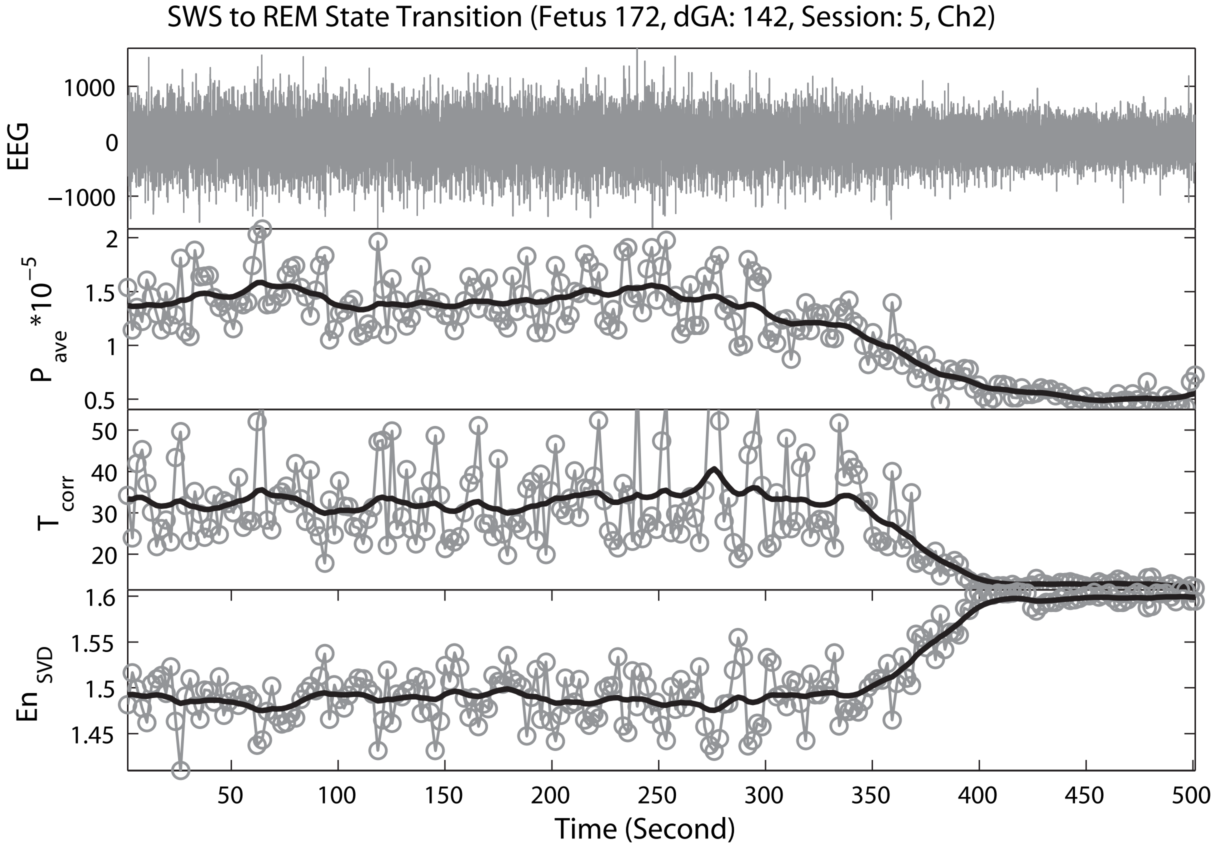
SWS to REM State Transition (Fetus 172, dGA: 142, Session: 5, Ch2)

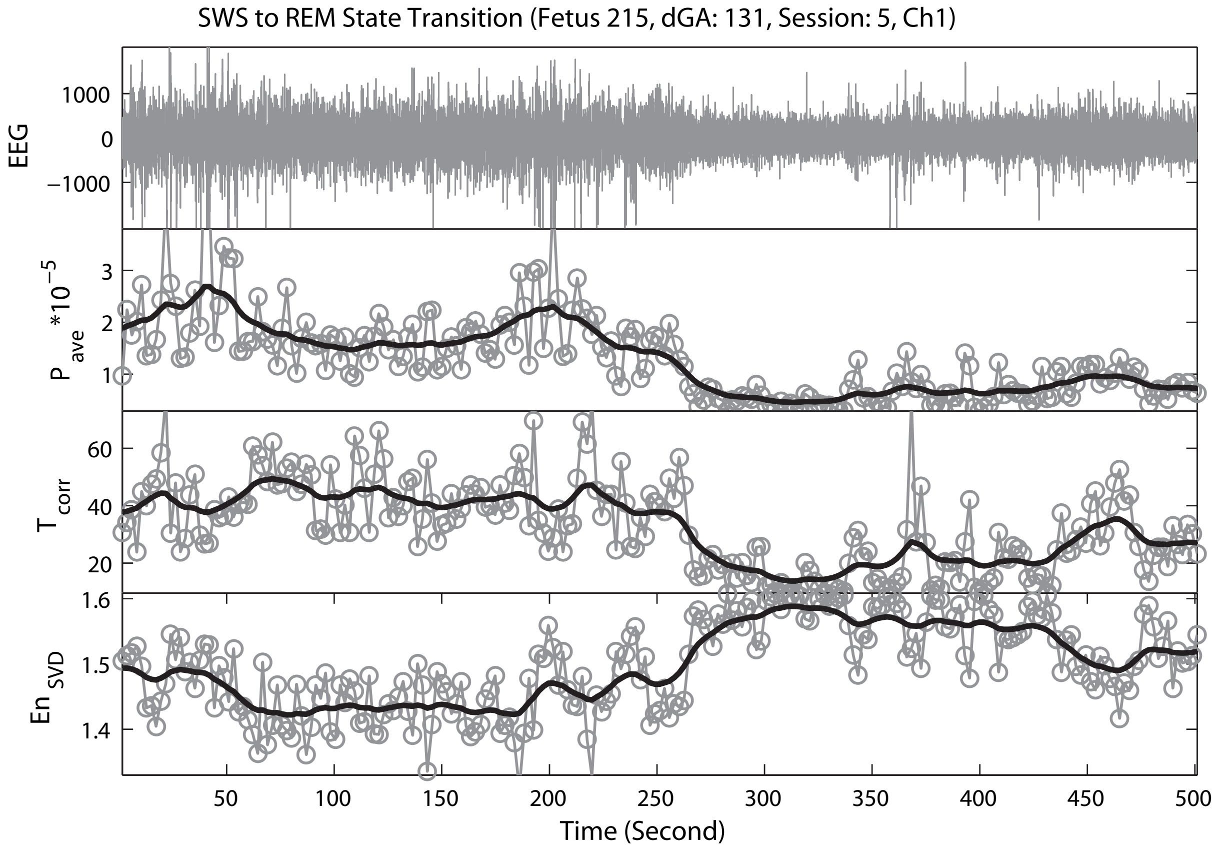
SWS to REM State Transition (Fetus 215, dGA: 131, Session: 5, Ch1)

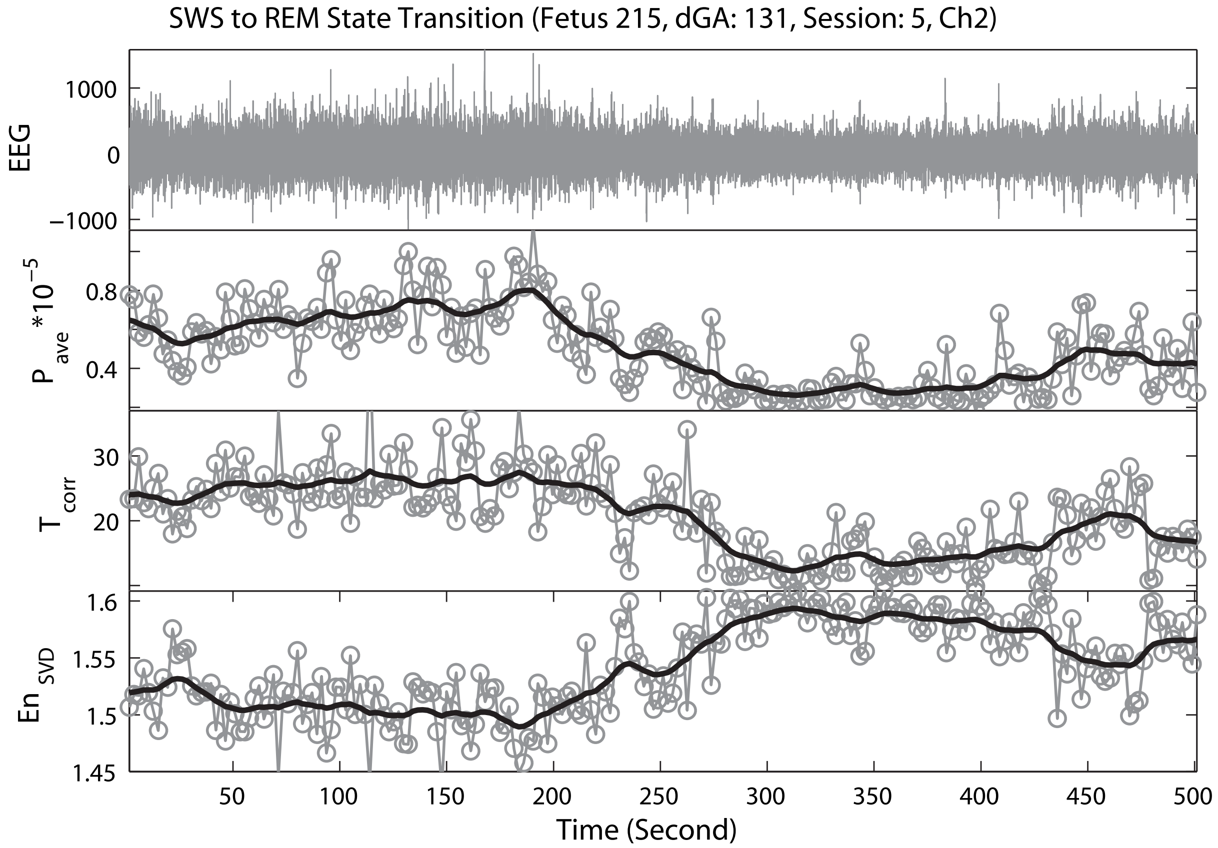
SWS to REM State Transition (Fetus 215, dGA: 131, Session: 5, Ch2)

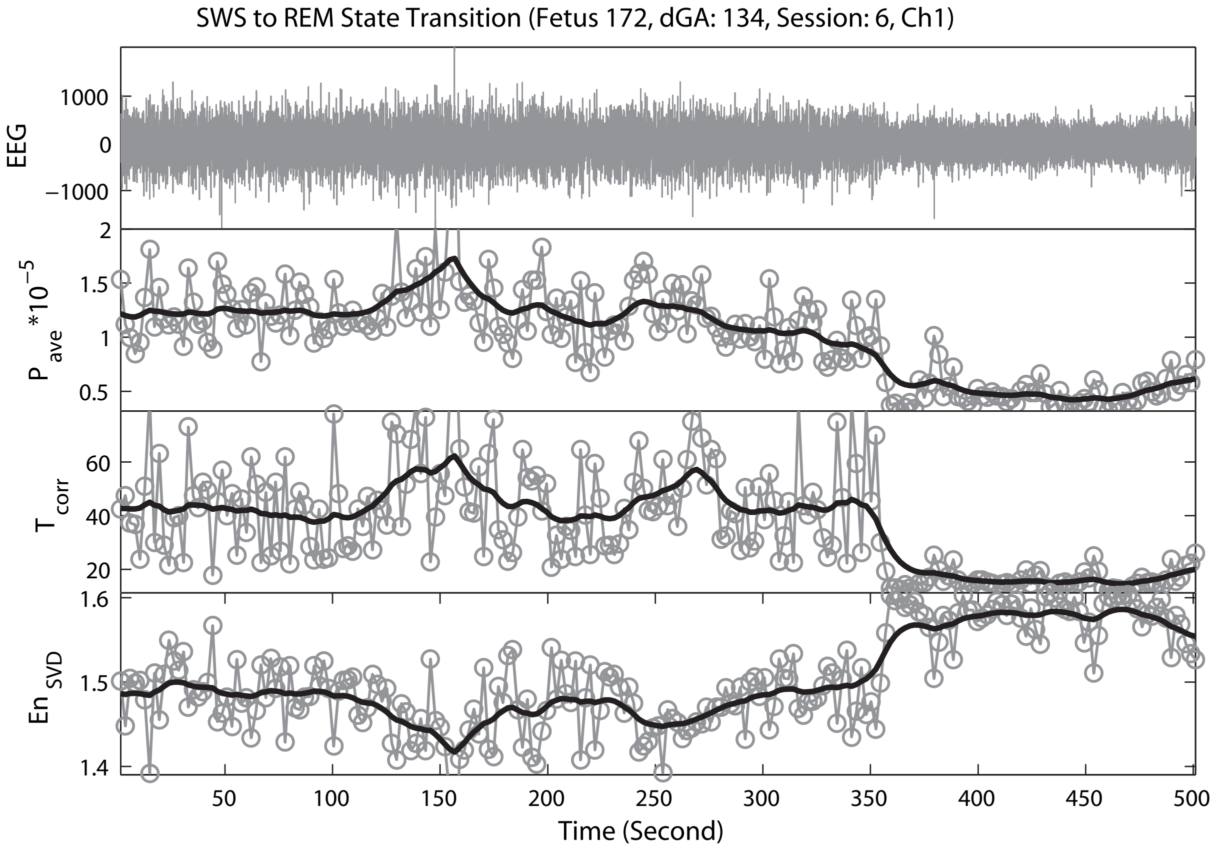
SWS to REM State Transition (Fetus 172, dGA: 134, Session: 6, Ch1)

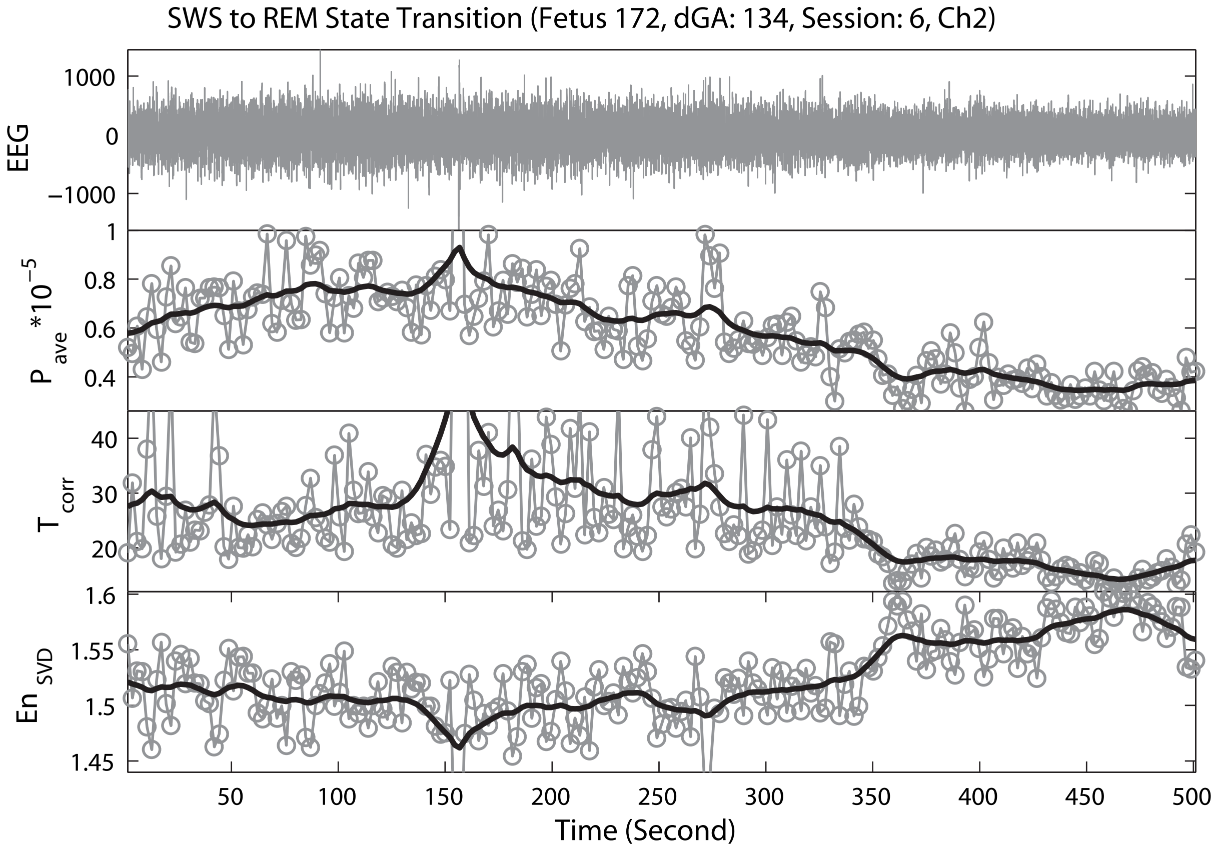
SWS to REM State Transition (Fetus 172, dGA: 134, Session: 6, Ch2)

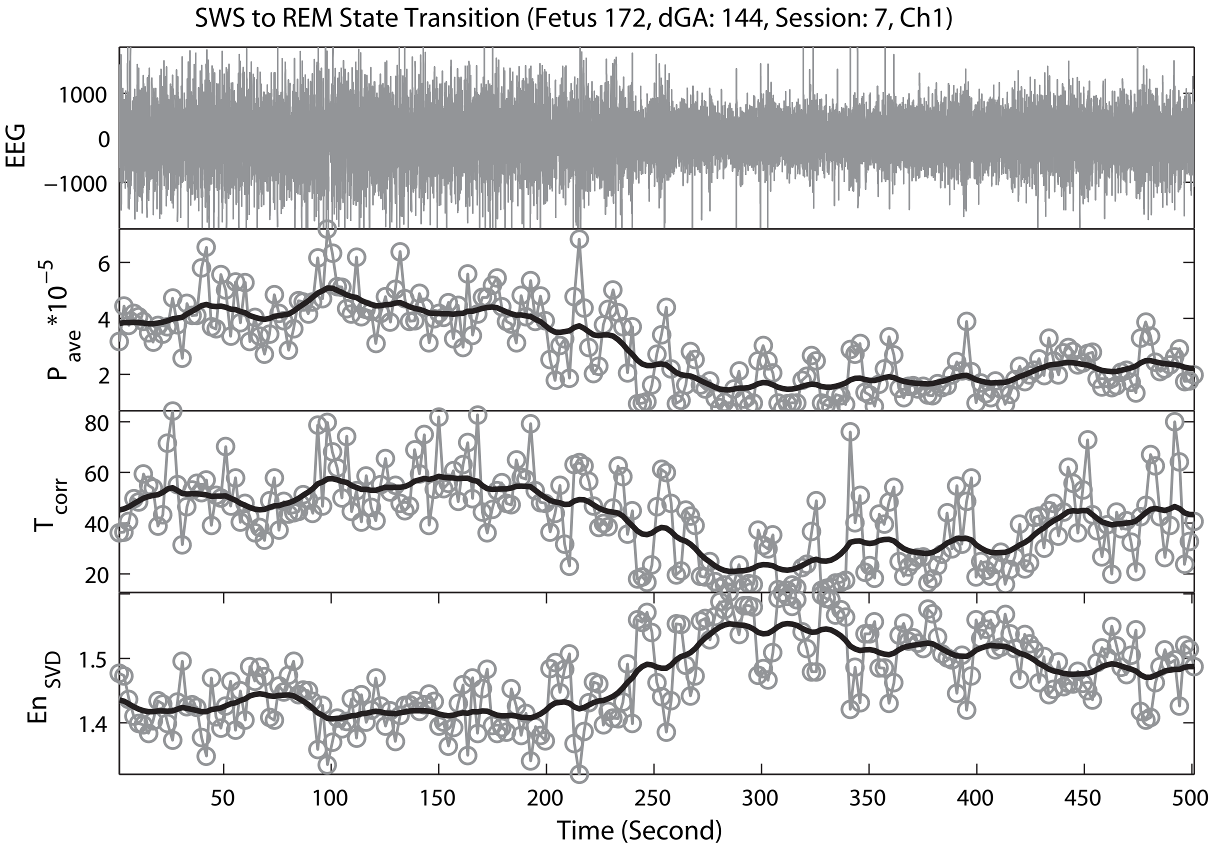
SWS to REM State Transition (Fetus 172, dGA: 144, Session: 7, Ch1)

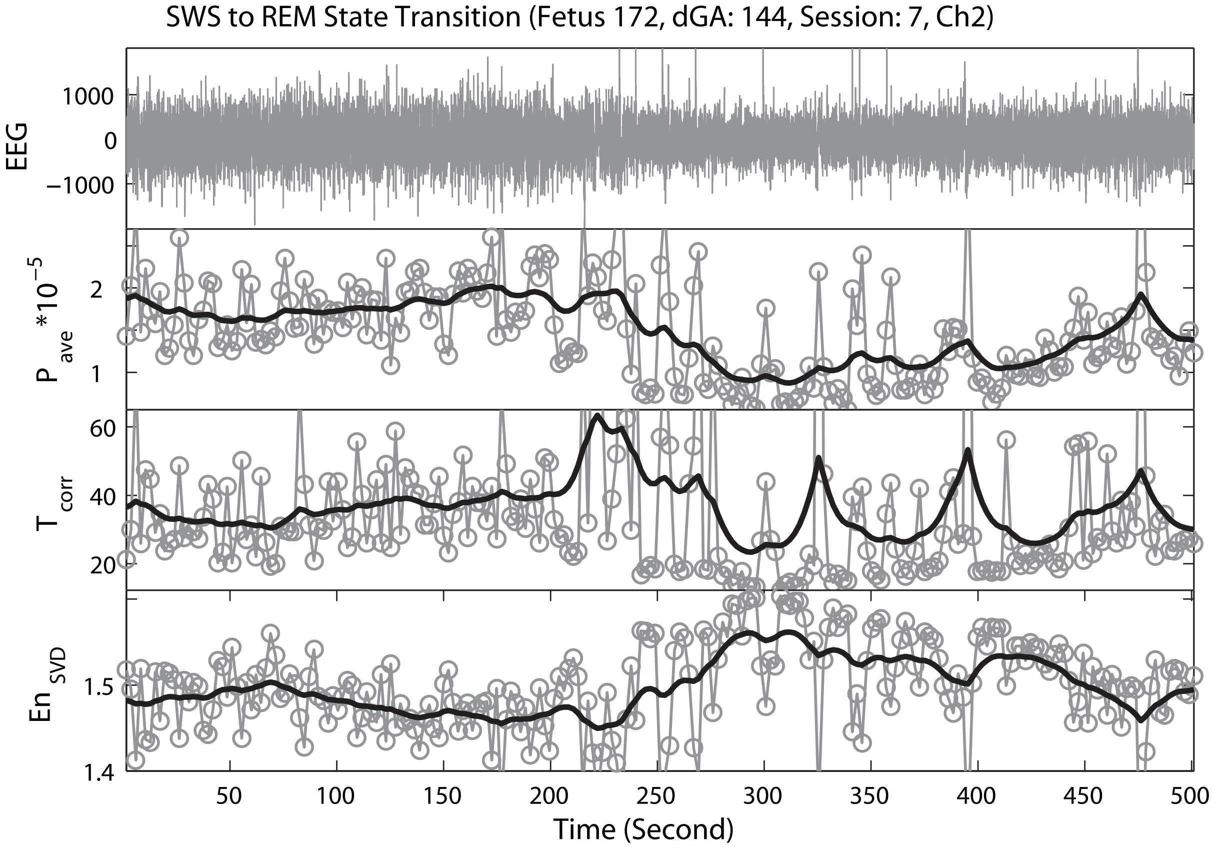
SWS to REM State Transition (Fetus 172, dGA: 144, Session: 7, Ch2)

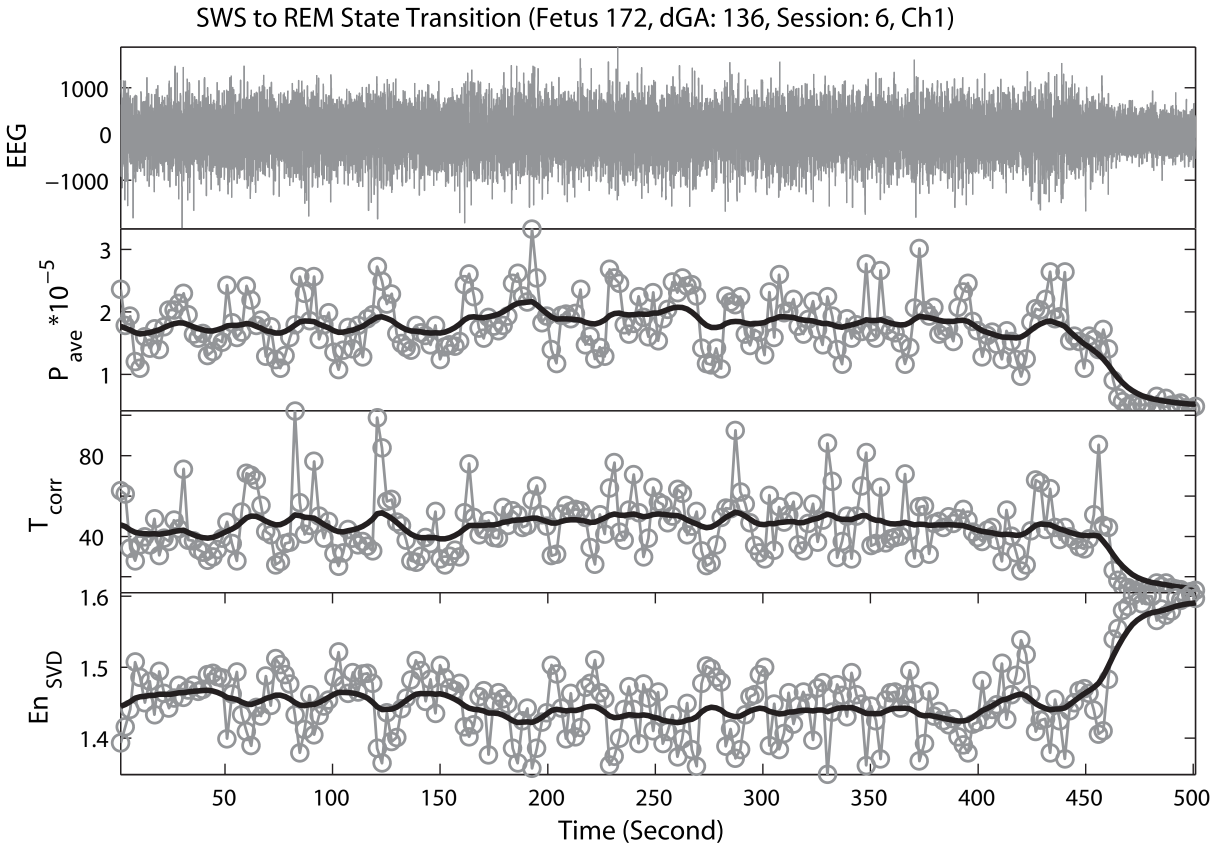

SWS to REM State Transition (Fetus 172, dGA: 136, Session: 6, Ch1)

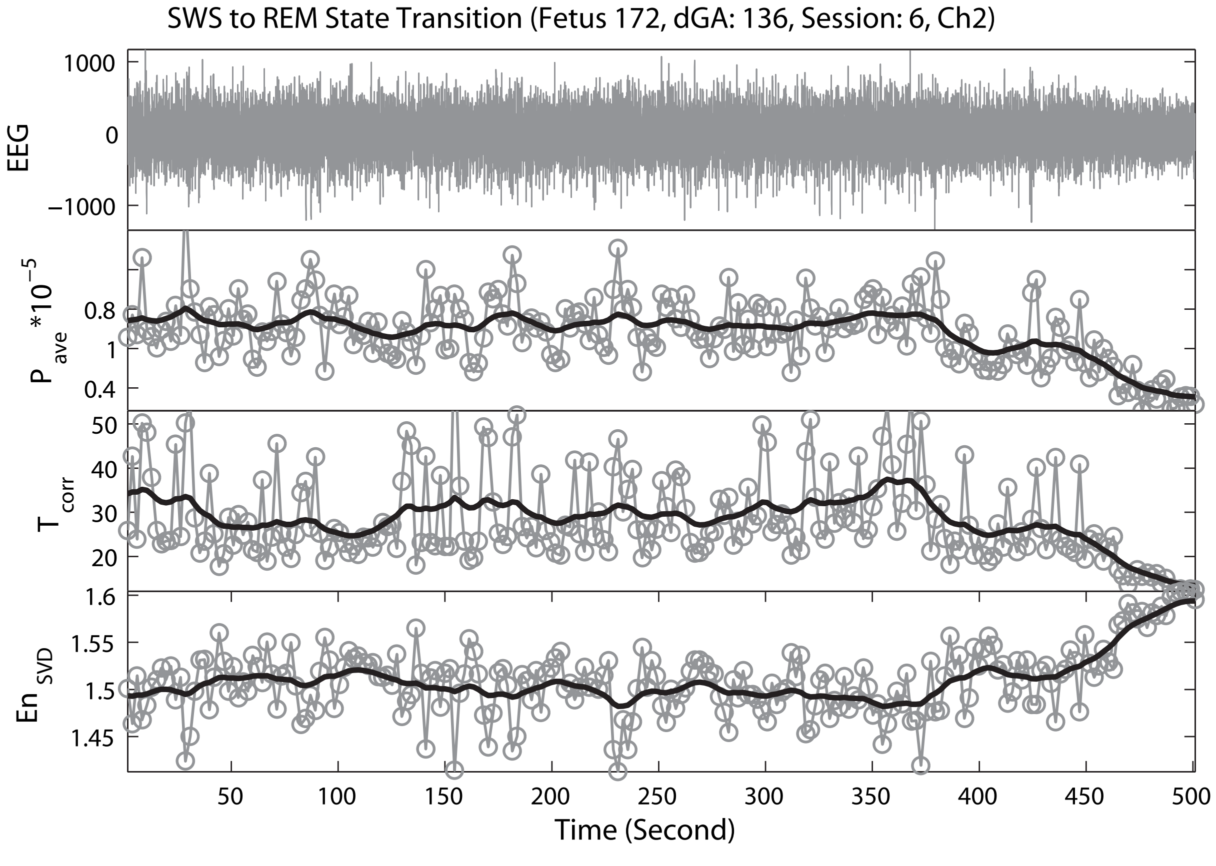

SWS to REM State Transition (Fetus 172, dGA: 136, Session: 6, Ch2)

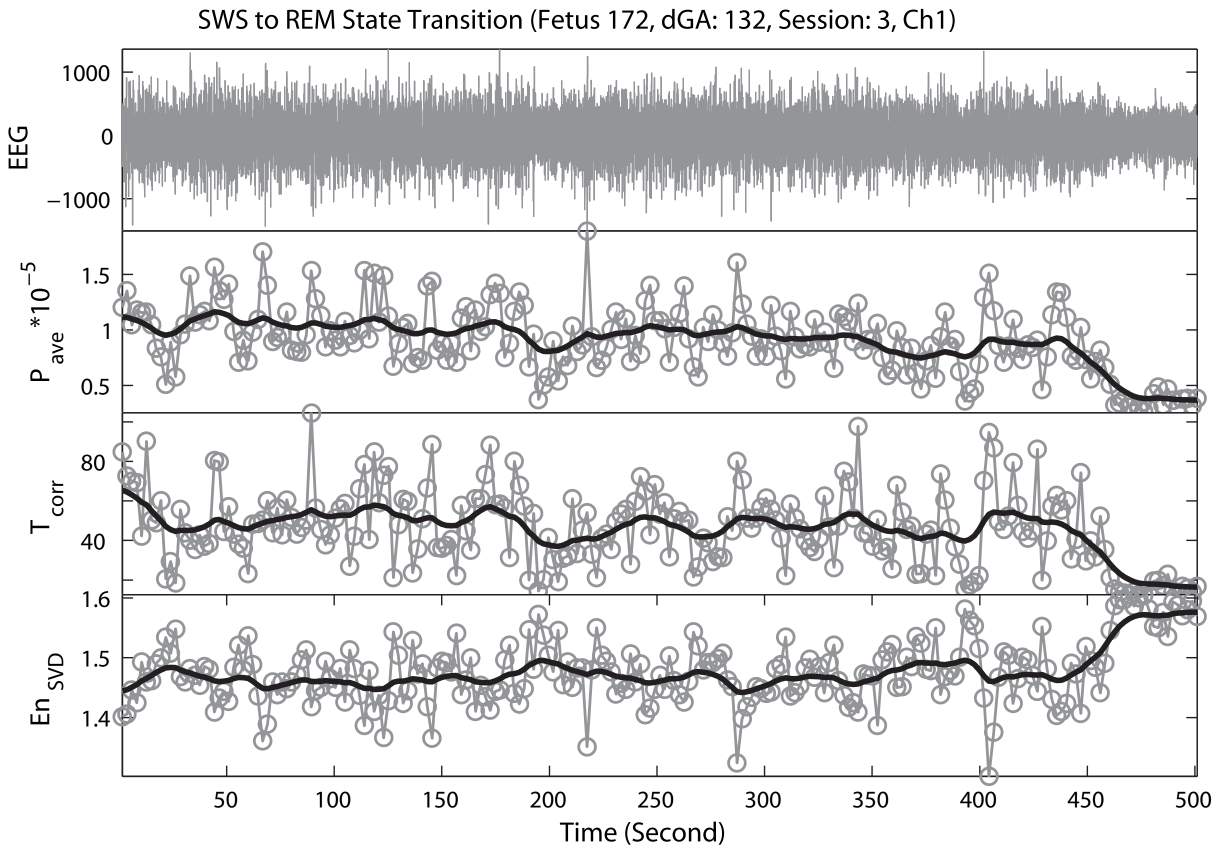
SWS to REM State Transition (Fetus 172, dGA: 132, Session: 3, Ch1)
EEG
1000
0
−1000
P_ave *10^−5
1.5
1
0.5
T_corr
80
40
1.6
En_SVD
1.5
1.4
50
100
150
200
250
300
350
400
450
500
Time (Second)

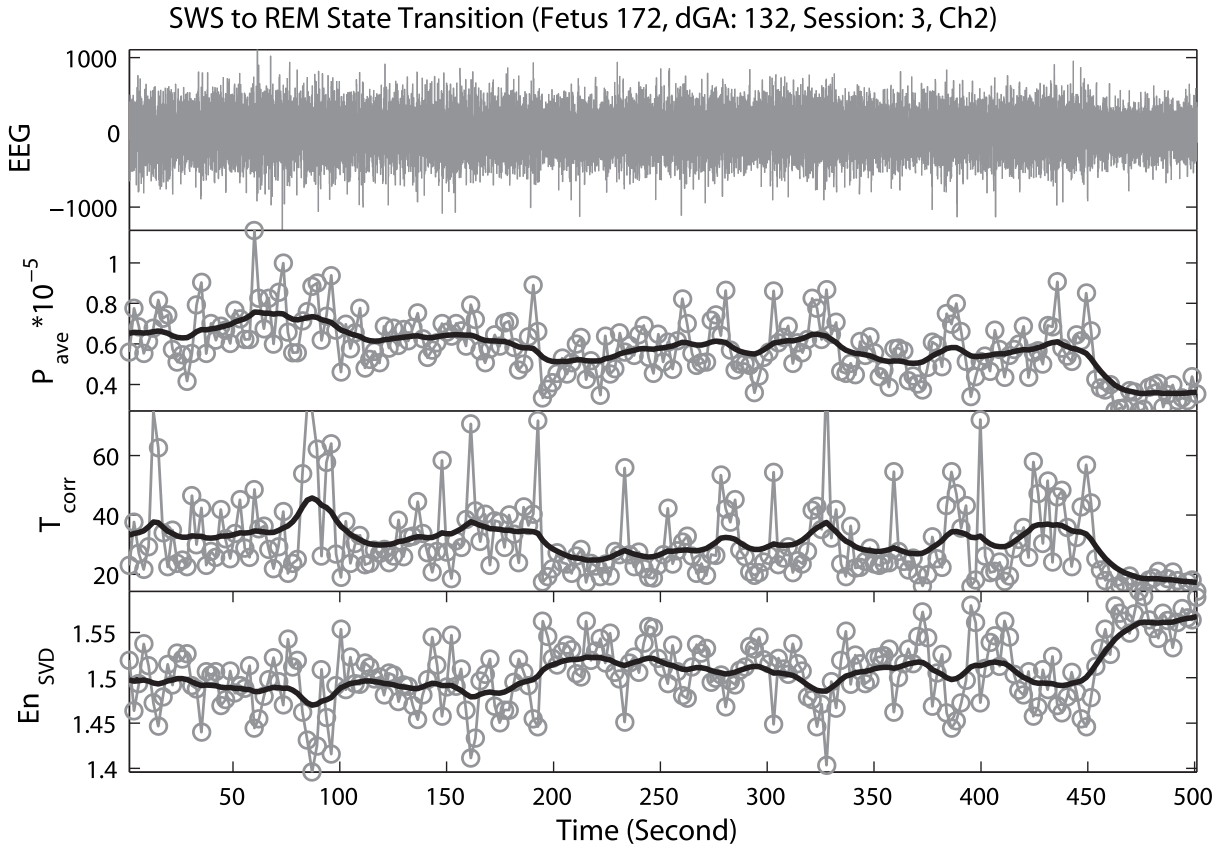
SWS to REM State Transition (Fetus 172, dGA: 132, Session: 3, Ch2)
EEG
1000
0
−1000
P_ave *10^−5
1
0.8
0.6
0.4
T_corr
60
40
20
En_SVD
1.55
1.5
1.45
1.4
50
100
150
200
250
300
350
400
450
500
Time (Second)

SWS to REM State Transition (Fetus 172, dGA: 142, Session: 1, Ch1)

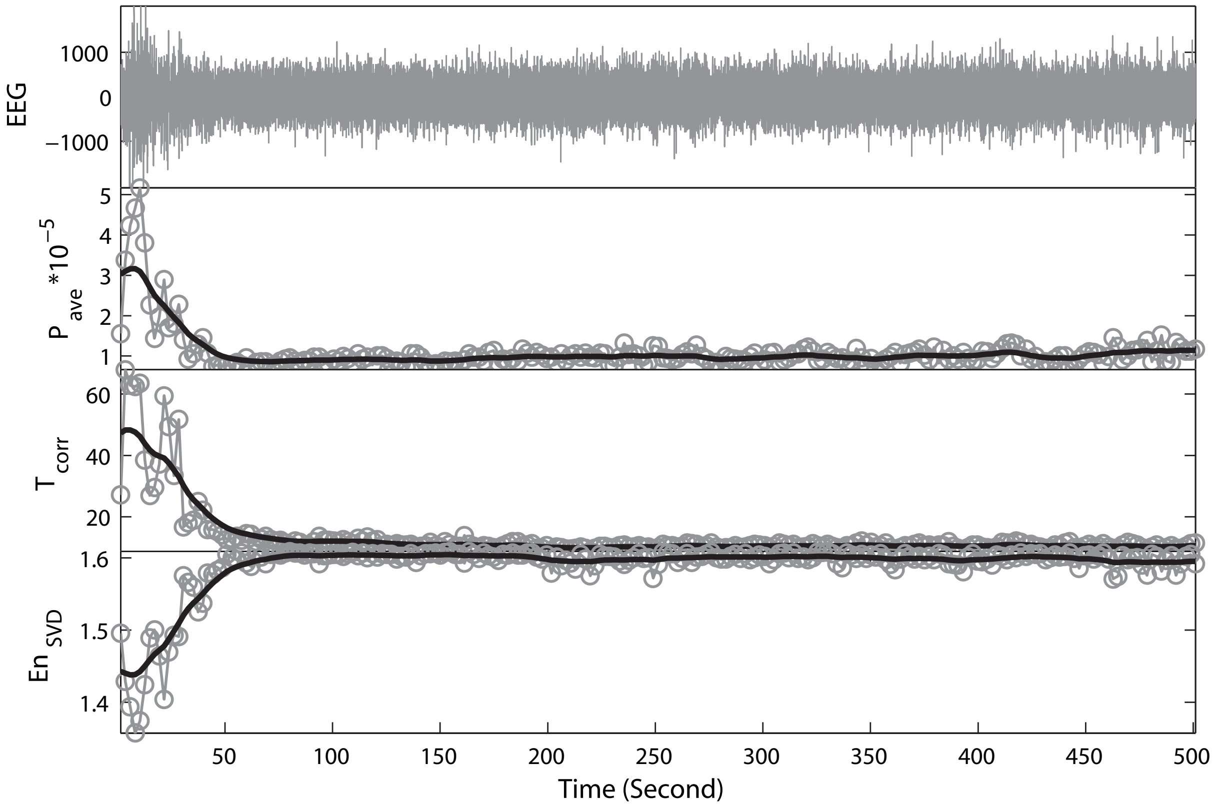

SWS to REM State Transition (Fetus 172, dGA: 142, Session: 1, Ch2)

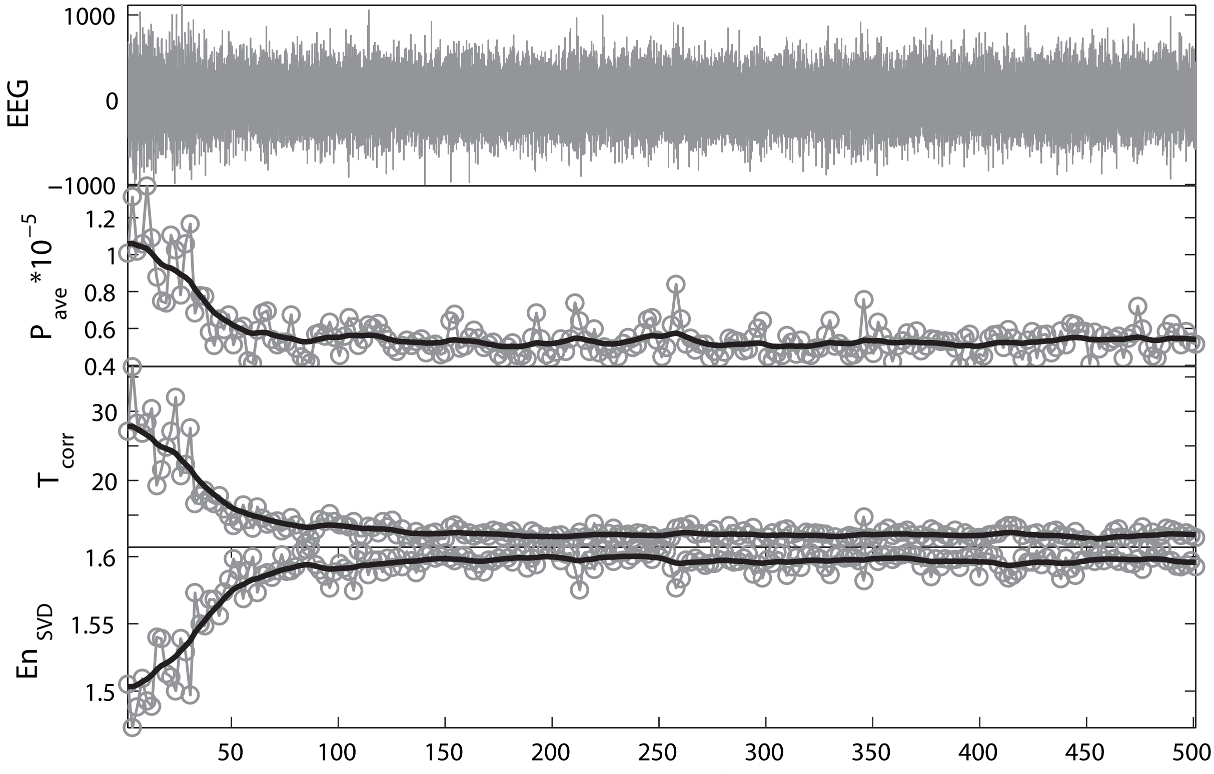

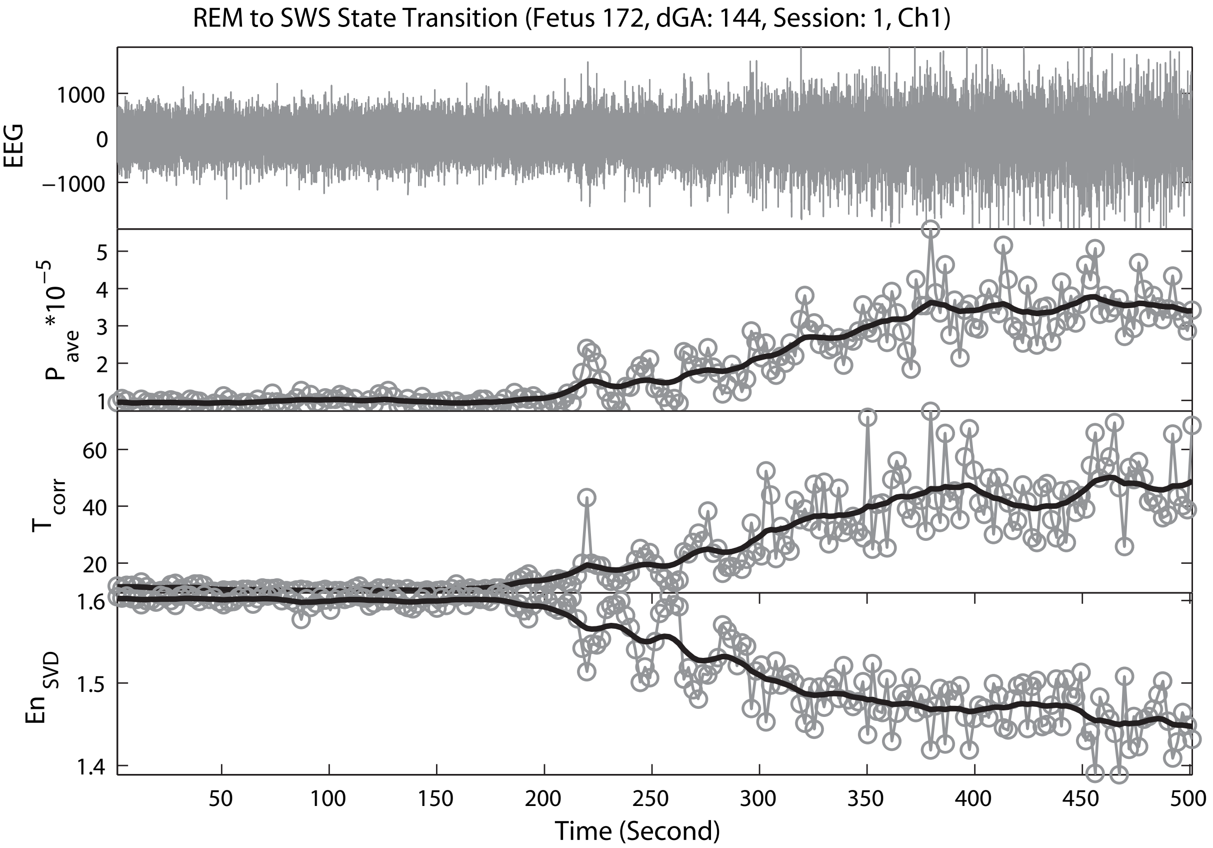
REM to SWS State Transition (Fetus 172, dGA: 144, Session: 1, Ch1)
EEG
1000
0
−1000
P_ave *10^−5
5
4
3
2
1
T_corr
60
40
20
En_SVD
1.6
1.5
1.4
50
100
150
200
250
300
350
400
450
500
Time (Second)

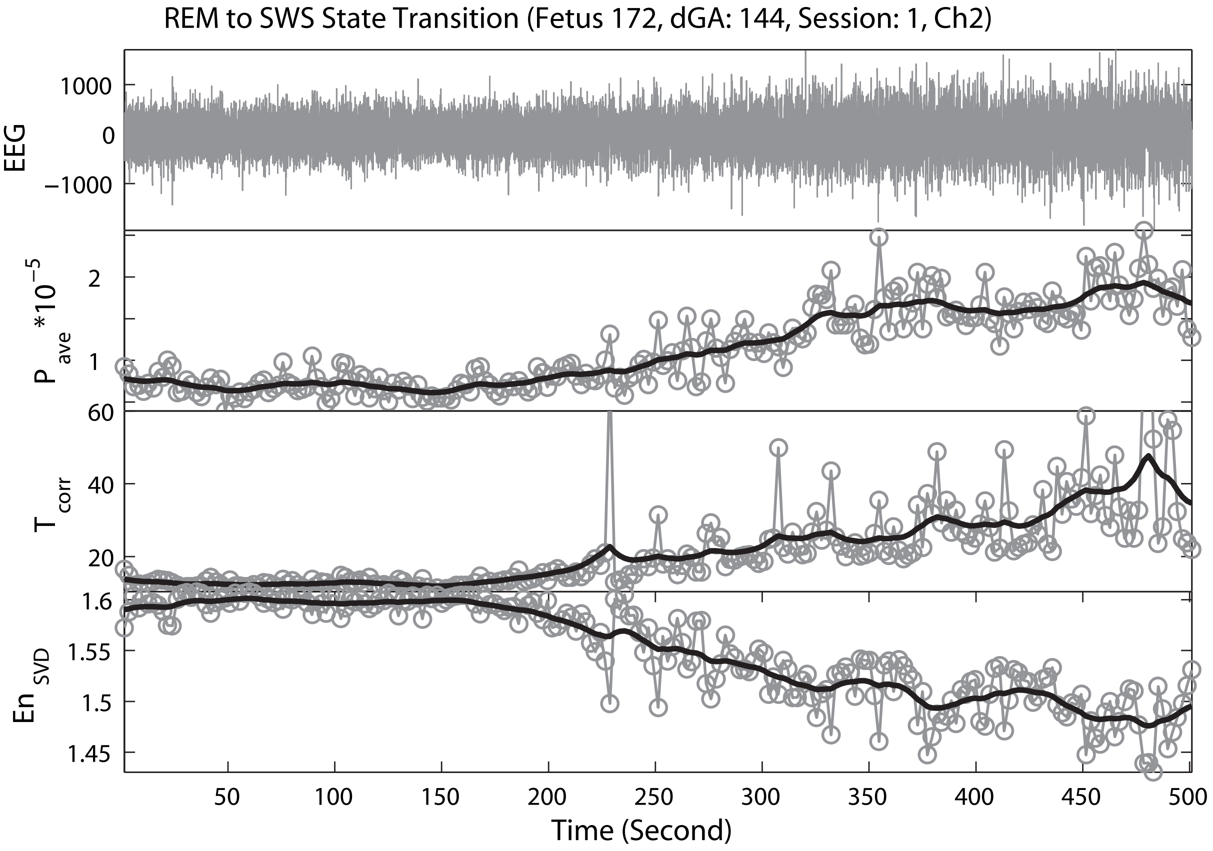
REM to SWS State Transition (Fetus 172, dGA: 144, Session: 1, Ch2)
EEG
1000
0
−1000
P_ave *10^−5
2
1
T_corr
60
40
20
En_SVD
1.6
1.55
1.5
1.45
50
100
150
200
250
300
350
400
450
500
Time (Second)

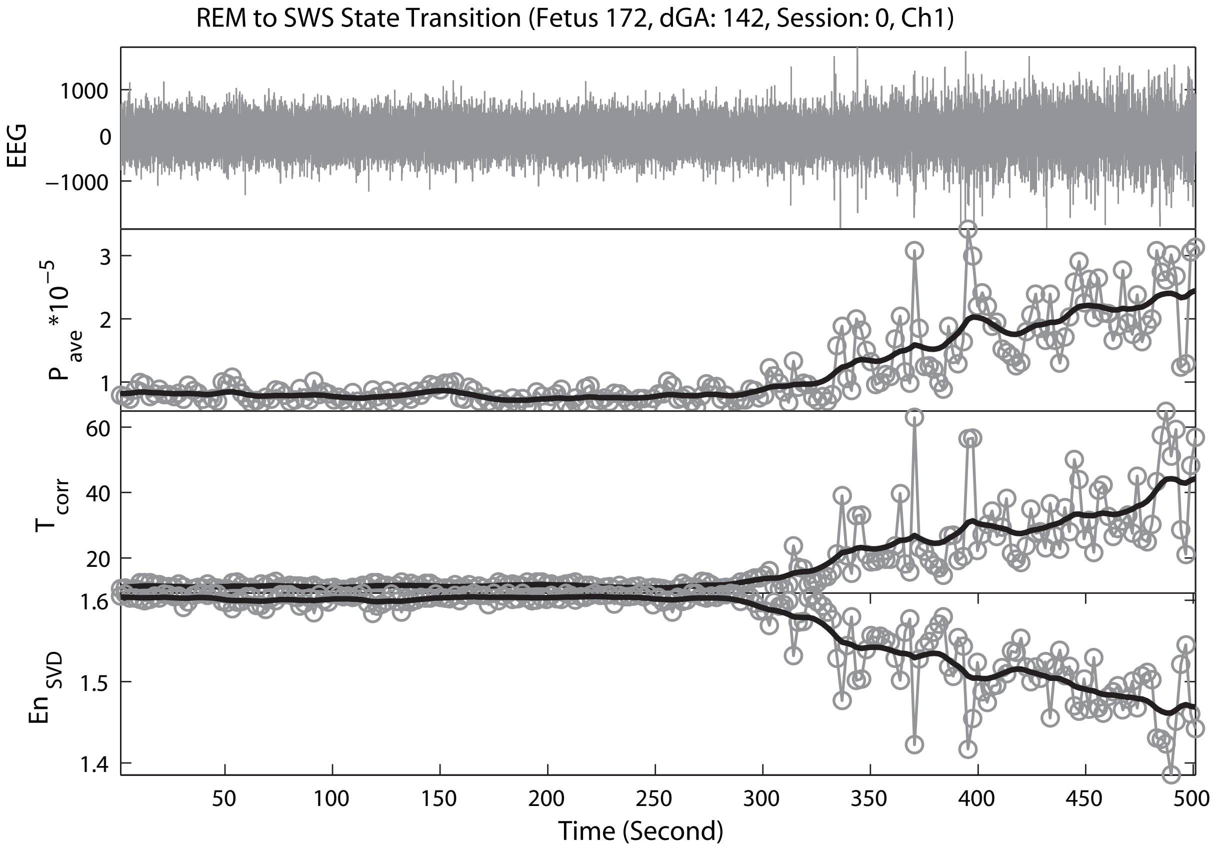
REM to SWS State Transition (Fetus 172, dGA: 142, Session: 0, Ch1)
EEG
1000
0
−1000
P_ave*10^−5
3
2
1
T_corr
60
40
20
En_SVD
1.6
1.5
1.4
50
100
150
200
250
300
350
400
450
500
Time (Second)

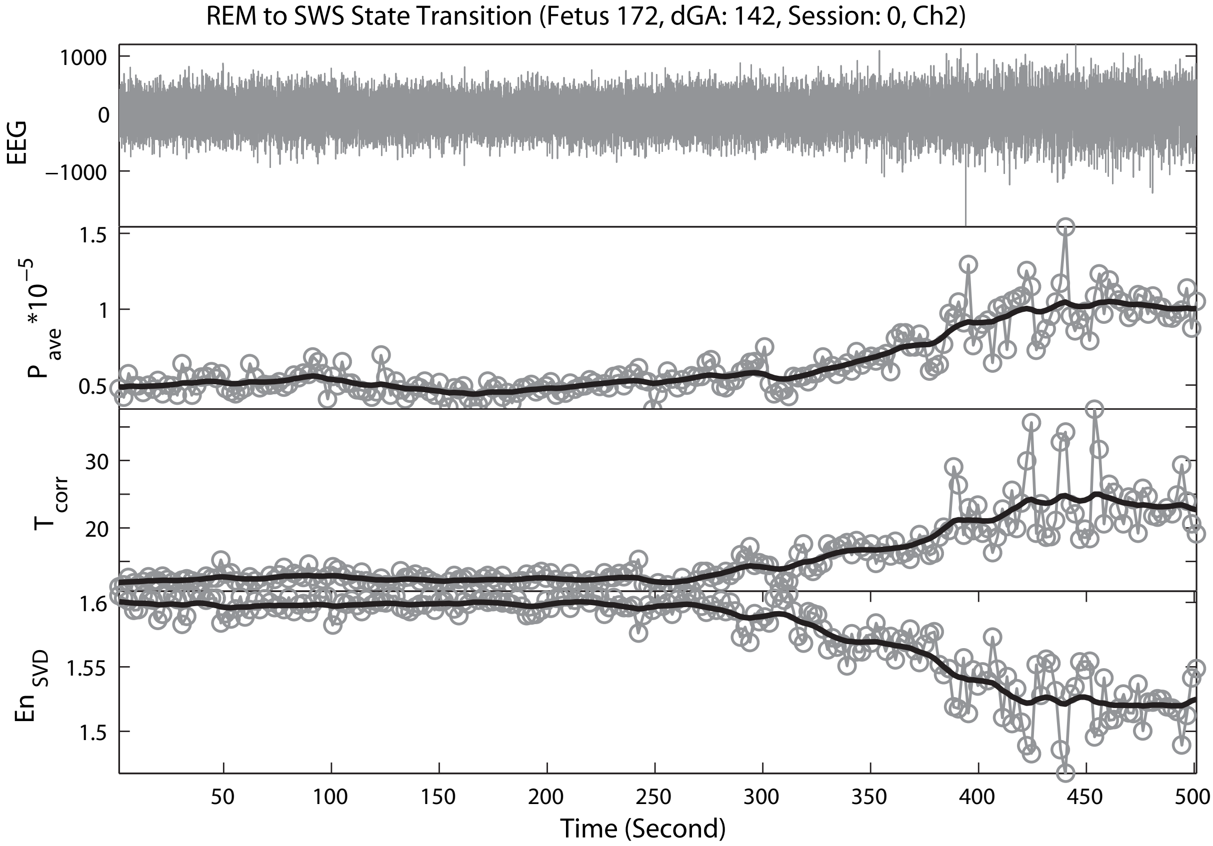
REM to SWS State Transition (Fetus 172, dGA: 142, Session: 0, Ch2)
EEG
1000
0
−1000
P_ave*10^−5
1.5
1
0.5
T_corr
30
20
En_SVD
1.6
1.55
1.5
50
100
150
200
250
300
350
400
450
500
Time (Second)

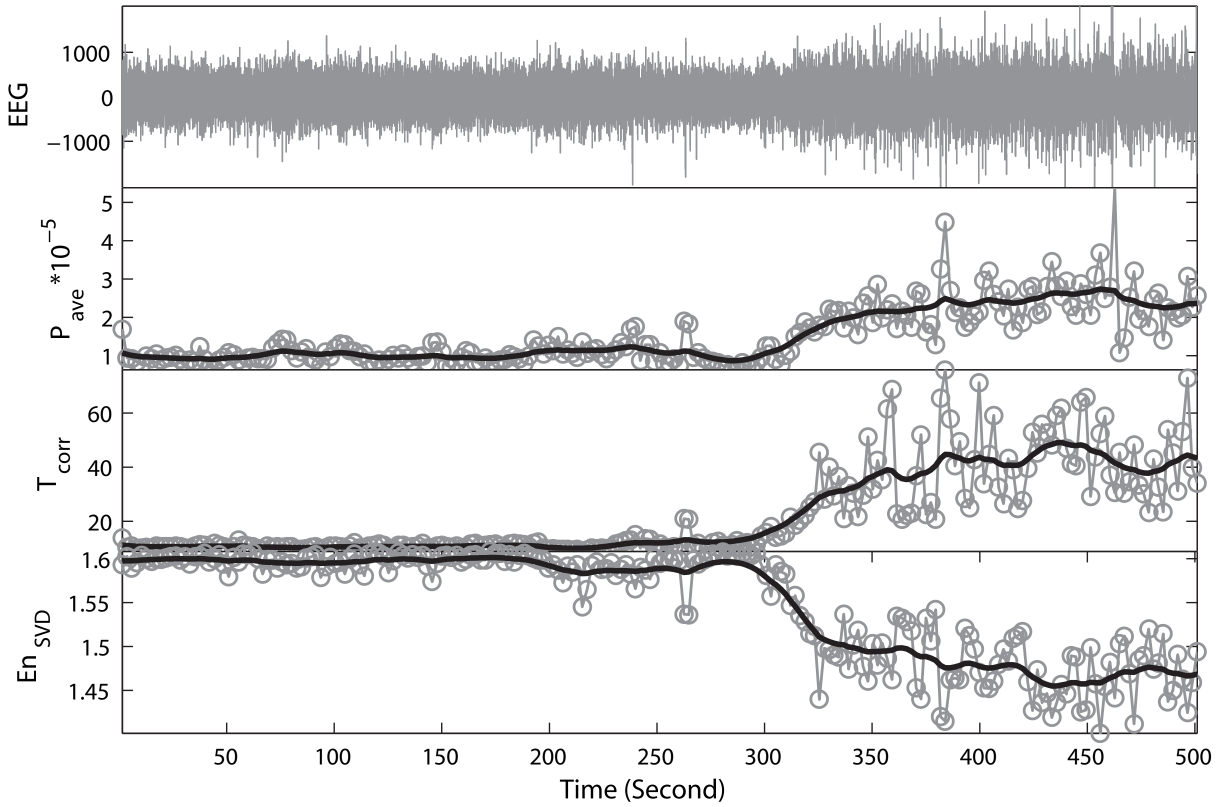

REM to SWS State Transition (Fetus 172, dGA: 140, Session: 6, Ch1)

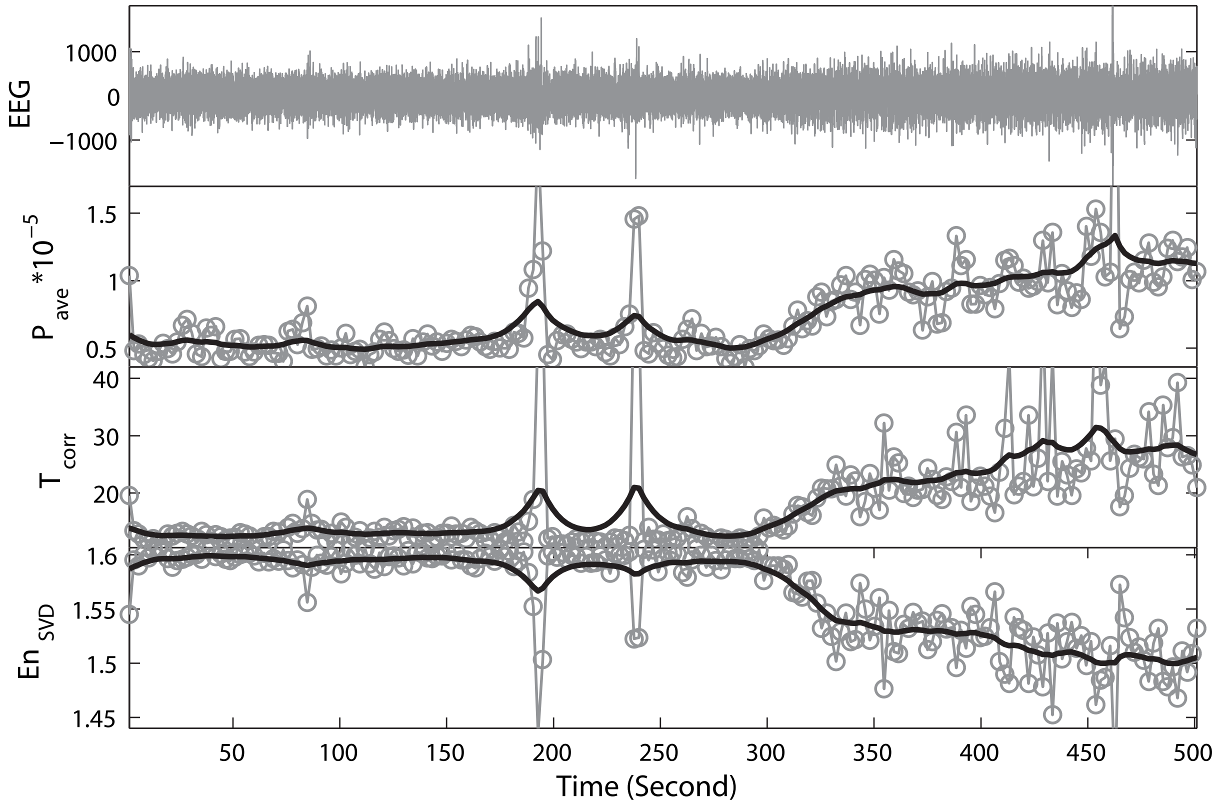

REM to SWS State Transition (Fetus 172, dGA: 140, Session: 6, Ch2)

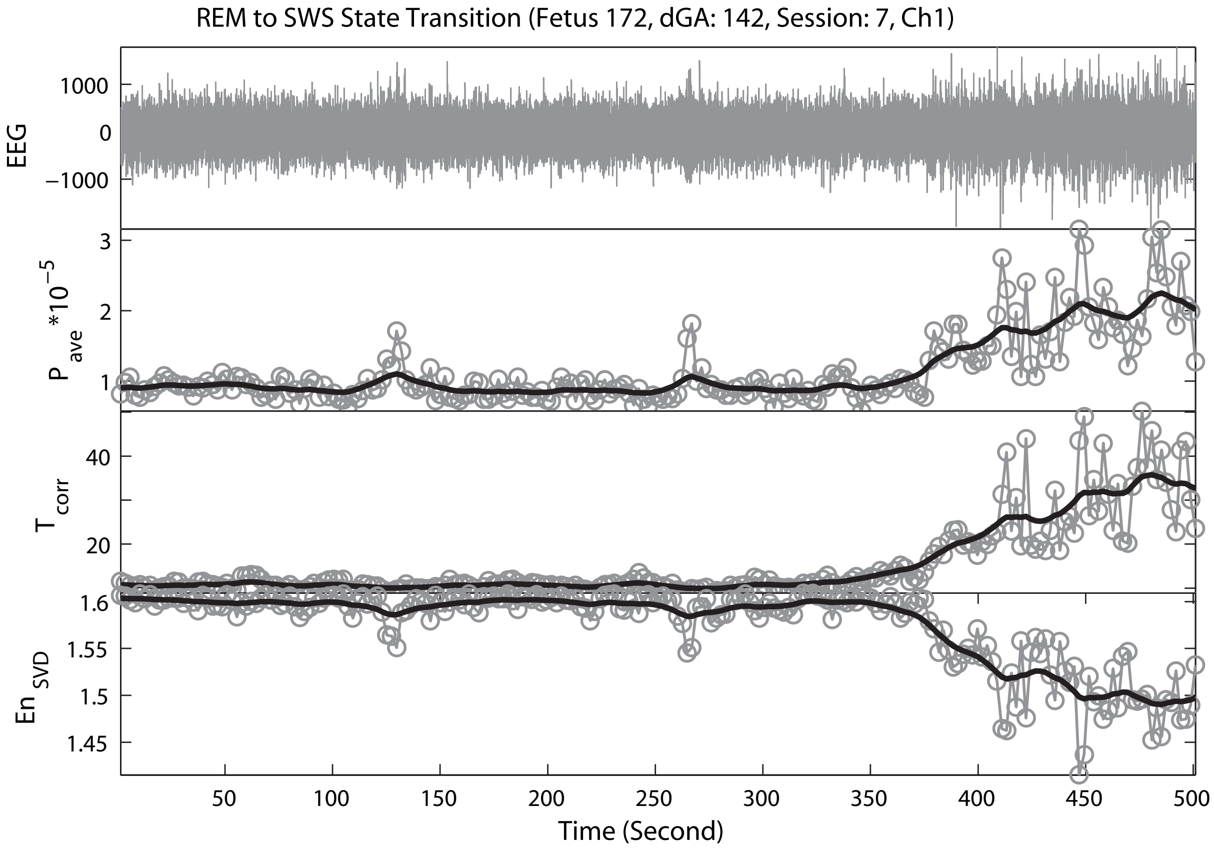
REM to SWS State Transition (Fetus 172, dGA: 142, Session: 7, Ch1)

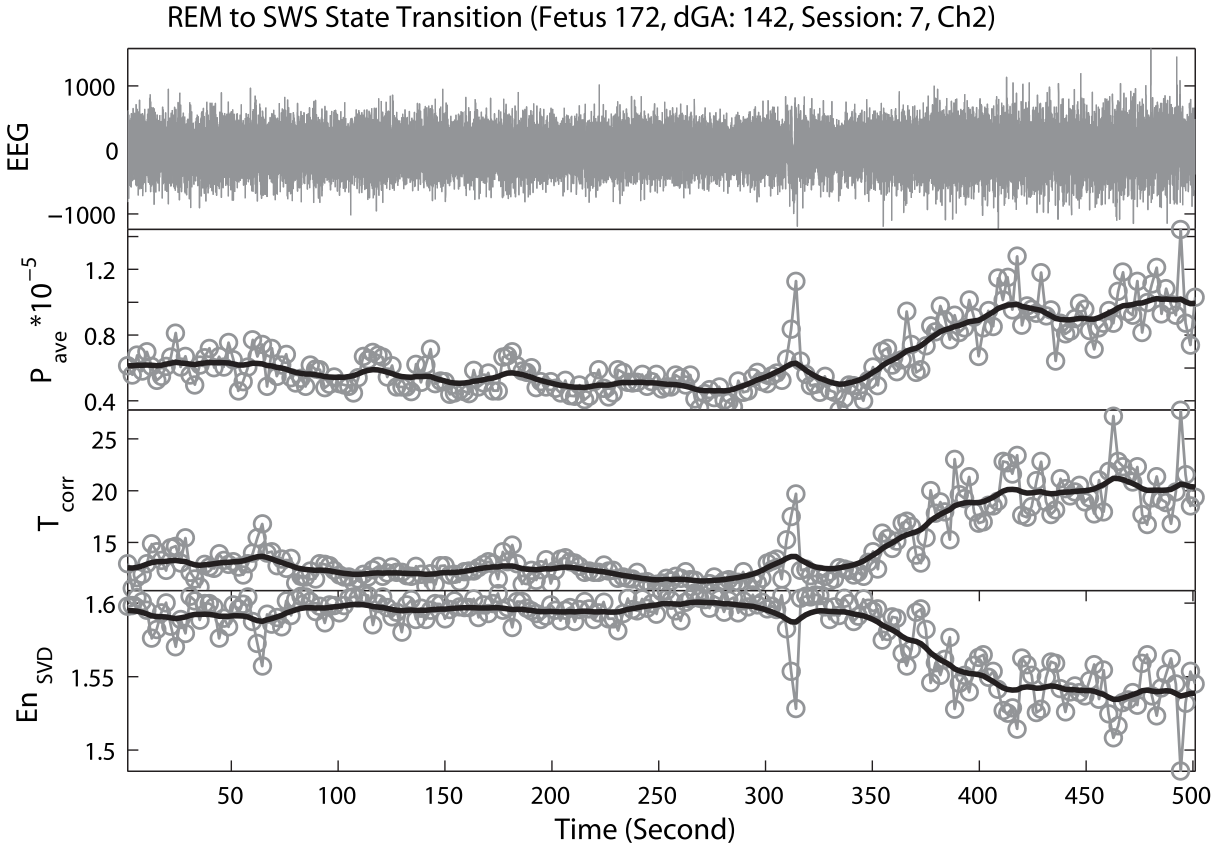
REM to SWS State Transition (Fetus 172, dGA: 142, Session: 7, Ch2)

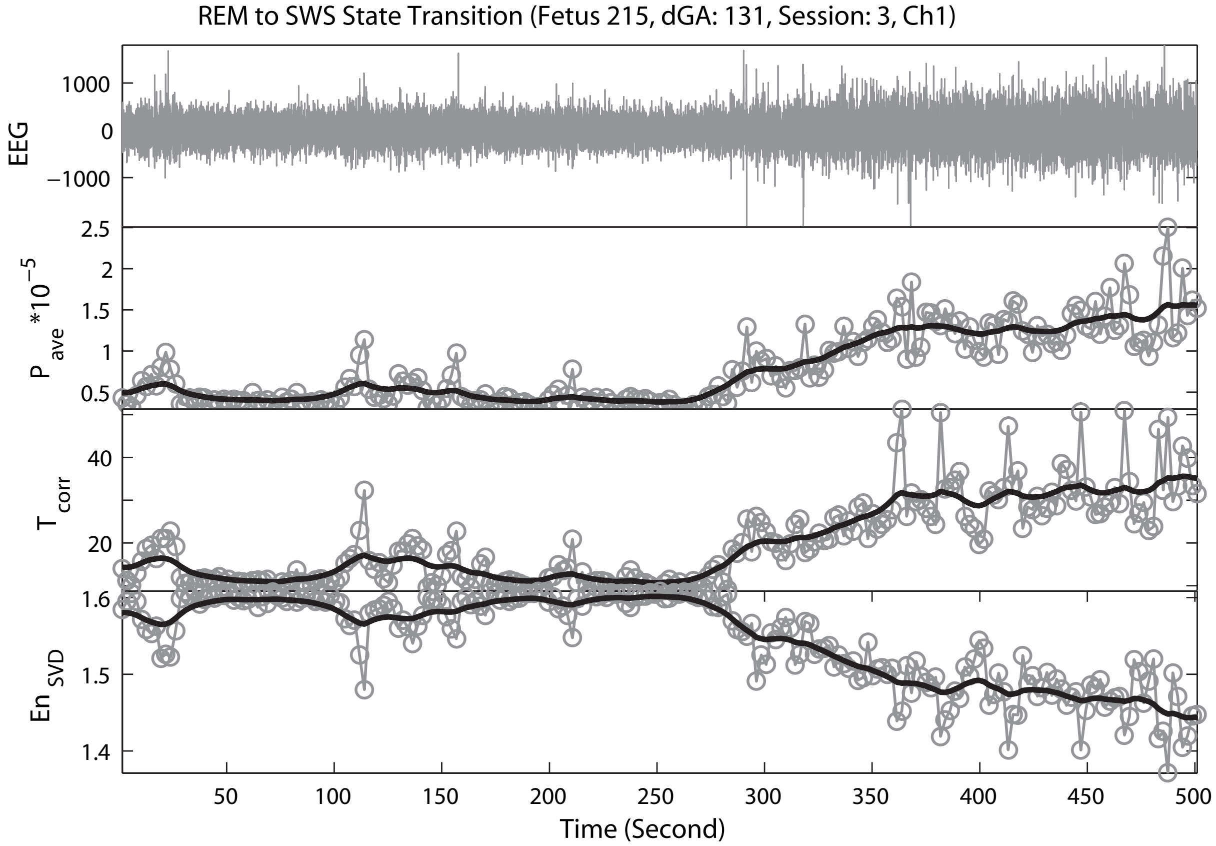
REM to SWS State Transition (Fetus 215, dGA: 131, Session: 3, Ch1)
EEG
1000
0
−1000
$P_{ave}*10^{-5}$
2.5
2
1.5
1
0.5
T_{corr}
40
20
En_{SVD}
1.6
1.5
1.4
50
100
150
200
250
300
350
400
450
500
Time (Second)

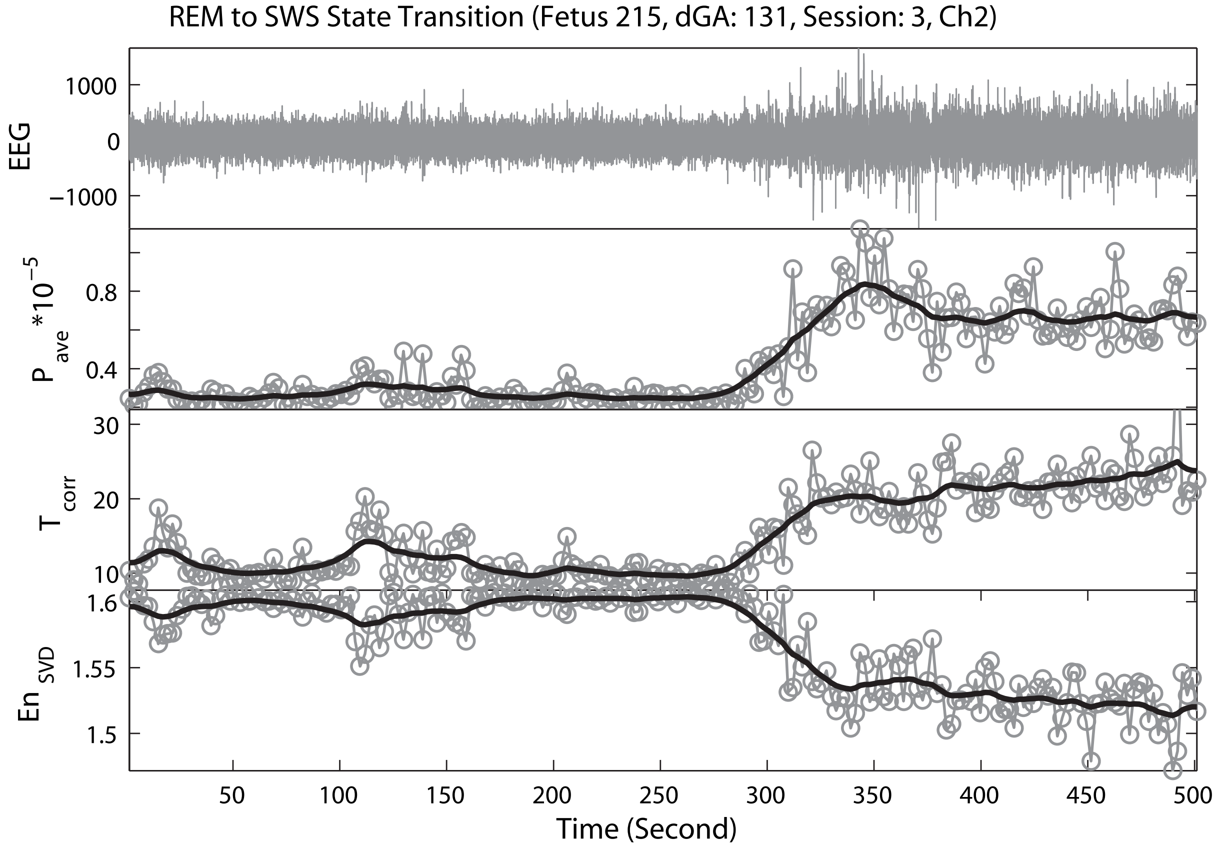
REM to SWS State Transition (Fetus 215, dGA: 131, Session: 3, Ch2)
EEG
1000
0
−1000
$P_{ave}*10^{-5}$
0.8
0.4
T_{corr}
30
20
10
En_{SVD}
1.6
1.55
1.5
50
100
150
200
250
300
350
400
450
500
Time (Second)

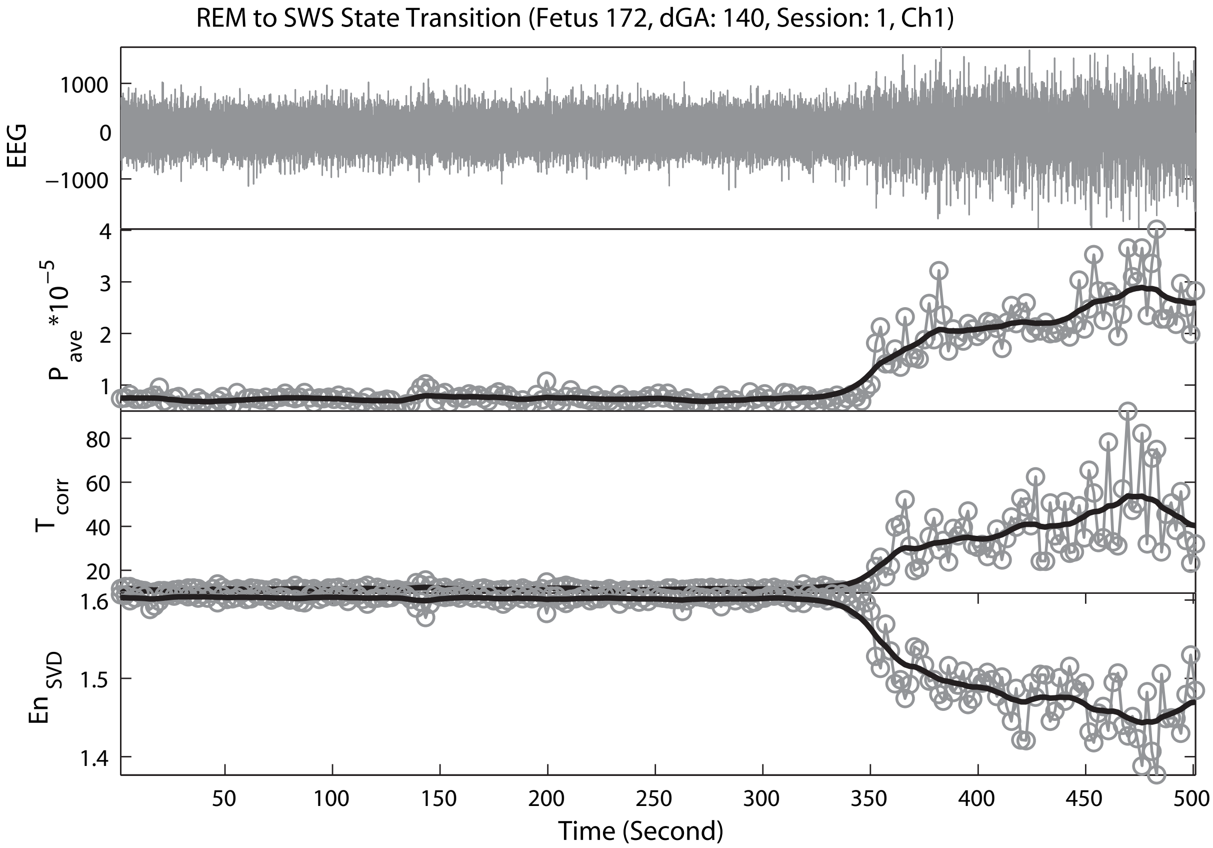
REM to SWS State Transition (Fetus 172, dGA: 140, Session: 1, Ch1)
EEG
1000
0
−1000
$P_{ave}*10^{-5}$
4
3
2
1
T_{corr}
80
60
40
20
En_{SVD}
1.6
1.5
1.4
50
100
150
200
250
300
350
400
450
500
Time (Second)

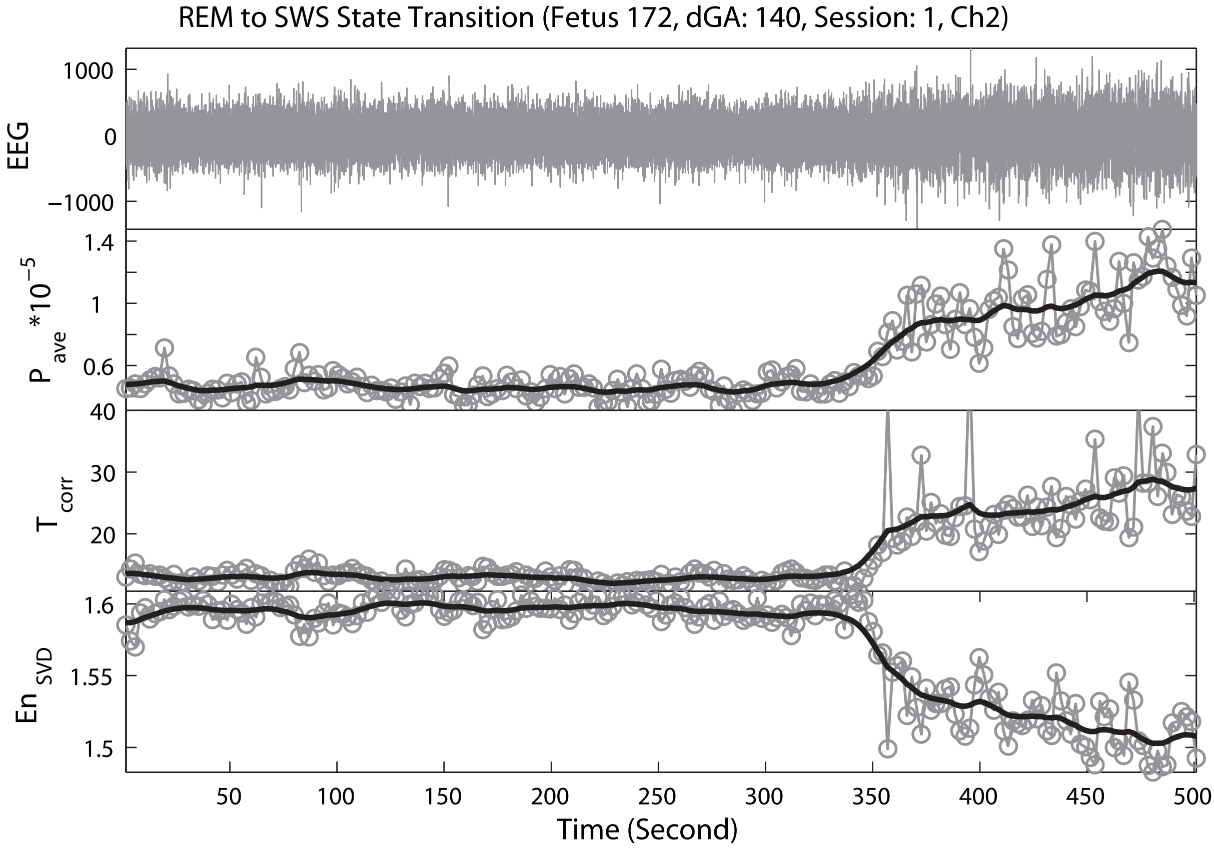
REM to SWS State Transition (Fetus 172, dGA: 140, Session: 1, Ch2)
EEG
1000
0
−1000
$P_{ave}*10^{-5}$
1.4
1
0.6
T_{corr}
40
30
20
En_{SVD}
1.6
1.55
1.5
50
100
150
200
250
300
350
400
450
500
Time (Second)

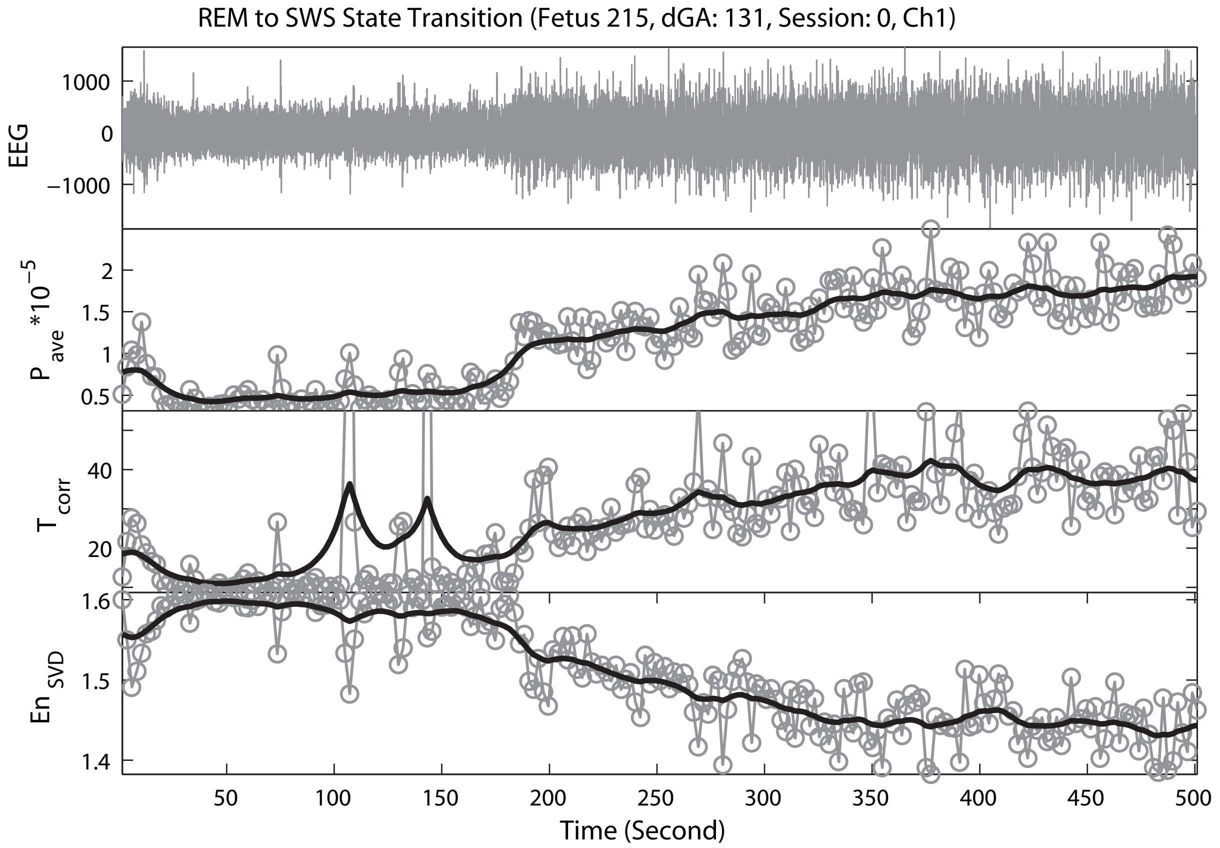
REM to SWS State Transition (Fetus 215, dGA: 131, Session: 0, Ch1)

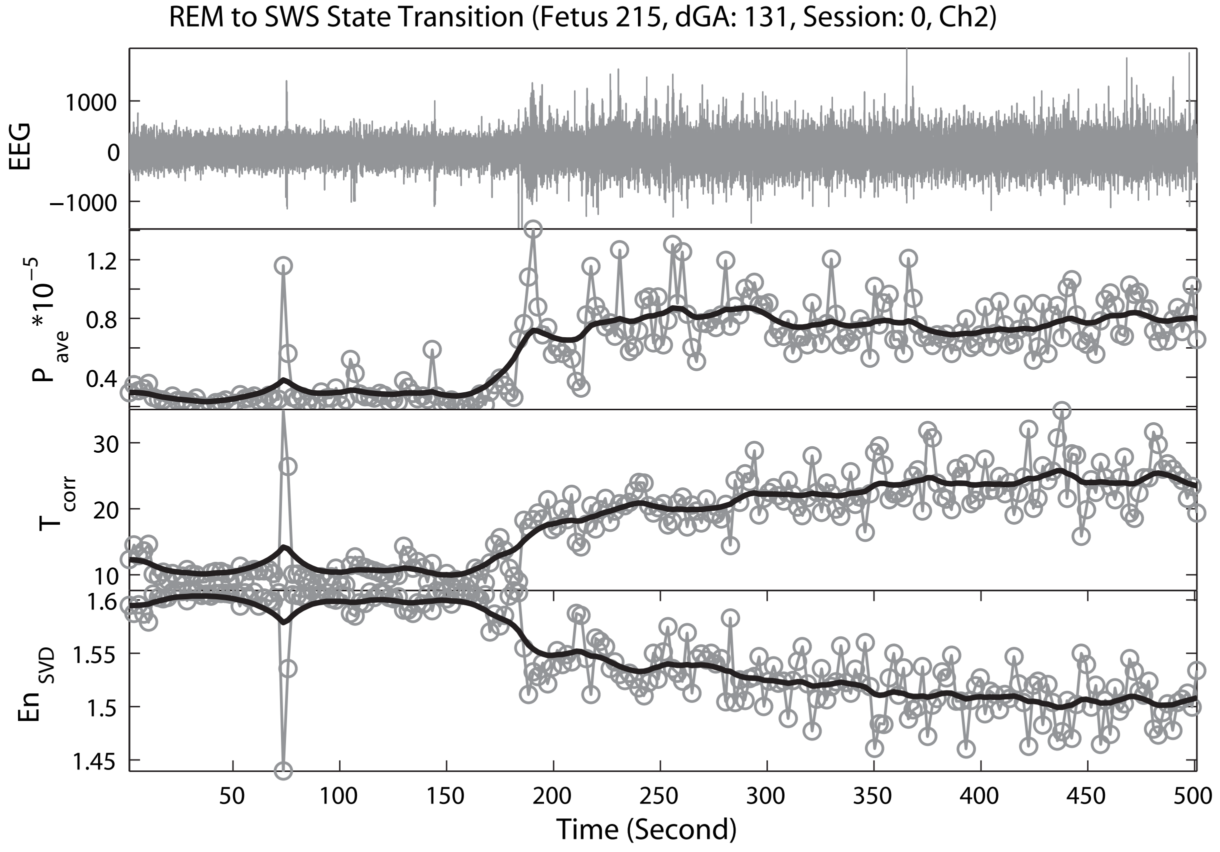
REM to SWS State Transition (Fetus 215, dGA: 131, Session: 0, Ch2)

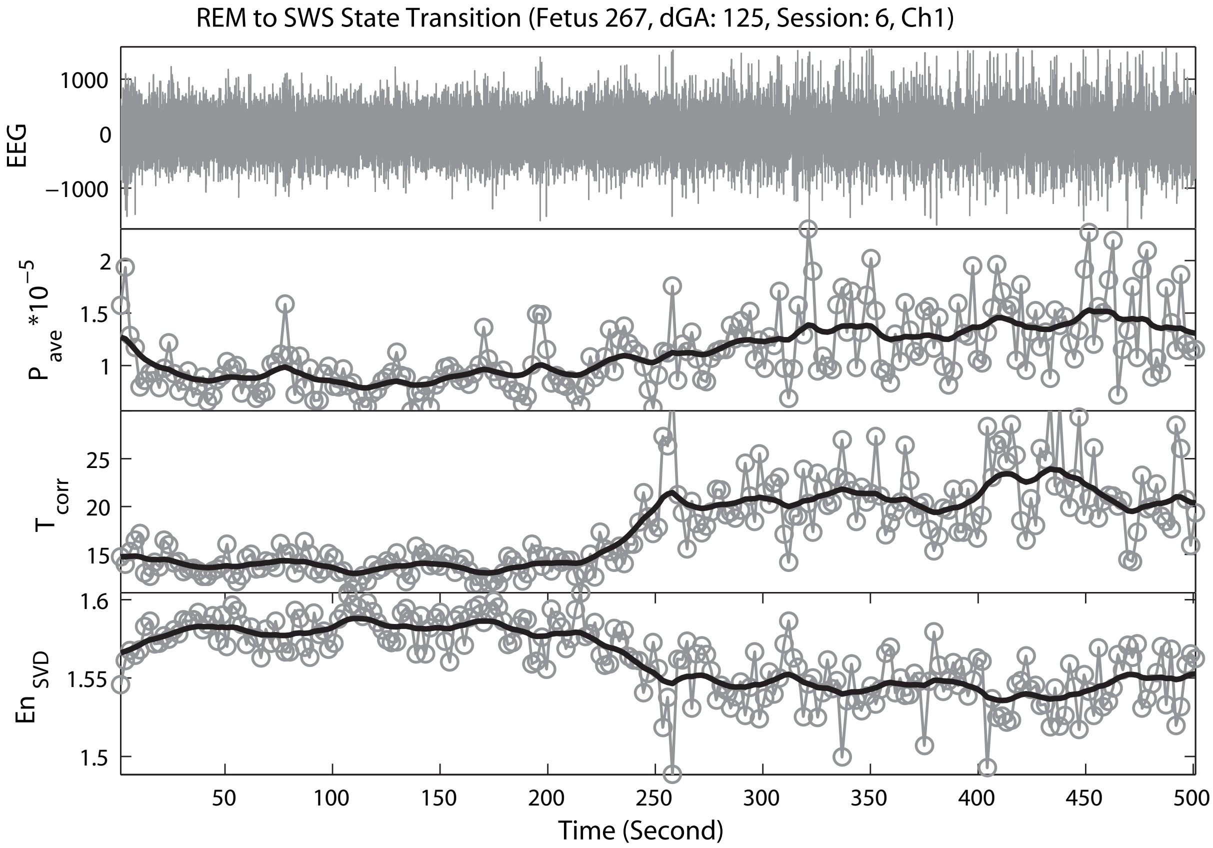
REM to SWS State Transition (Fetus 267, dGA: 125, Session: 6, Ch1)
EEG
1000
0
−1000
P_ave *10^−5
2
1.5
1
T_corr
25
20
15
En_SVD
1.6
1.55
1.5
50
100
150
200
250
300
350
400
450
500
Time (Second)

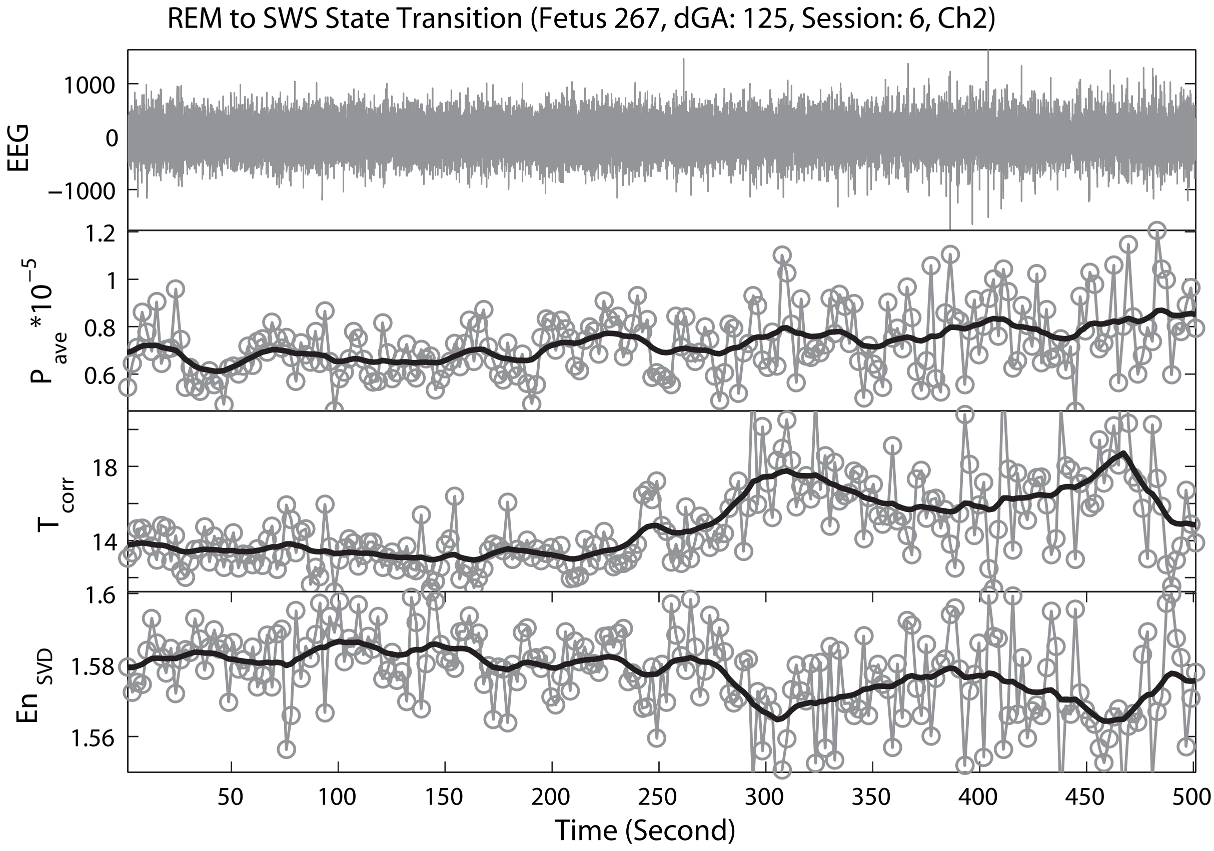
REM to SWS State Transition (Fetus 267, dGA: 125, Session: 6, Ch2)
EEG
1000
0
−1000
P_ave *10^−5
1.2
1
0.8
0.6
T_corr
18
14
En_SVD
1.6
1.58
1.56
50
100
150
200
250
300
350
400
450
500
Time (Second)

Bibliography

[1] Abarbanel, H.D.I., Brown, R., Kadtke, J.B.: Prediction and system identification in chaotic nonlinear systems: Time series with broadband spectra. Physics Letters A **138**, 401–408 (1989)

[2] Akay, M., Akay, Y.M., Cheng, P., Szeto, H.H.: Time-frequency analysis of the electrocortical activity during maturation using wavelet transform. Biological Cybernetics **71**, 169–176 (1994)

[3] Akay, M., Szeto, H.H., Cheng, P.: Time-frequency analysis of the electrocortical activity during maturation using wavelet transform. In: Second International Hans-Berger Conference, Germany (1993)

[4] Albano, A.M., Muench, J., Schwartz, C., Mees, A.I., Rapp, P.E.: Singular-valule decomposition and the Grassberger-Procaccia algorithm. Physical Review A **38**, 3017–3026 (1988)

[5] Amari, S.: Dynamics of pattern formation in laternal-inhibition type neural fields. Biological Cybernetics **27**, 77–87 (1977)

[6] Amit, D.J.: Modelling of Attractor Neural Networks. Cambridge University Press, cambridge, England (1989)

[7] Anders, T.R., Emde, R., Parmeleeé, A.H.: A Manual of Standardized Terminology, Techniques and Criteria for Scoring of States of Sleep and Wakefulness in Newborn Infants. Los Angeles, California: UCLA Brain Information Service, NINDS Neurological Information Network (1971)

[8] Arduini, D., Rizzo, G., Giorlandino, C., Valensise, H., DellÁcqua, S., Romanini, C.: The development of fetal behavioural states: a longitudinal study. Prenatal Diagnosis **6**, 117–124 (1986)

[9] Arumugam, H., Liu, X., Colombo, P.J., Corriveau, R.A., Belousov, A.B.: NMDA receptors regulate developmental gap junction uncoupling via CREB signaling. Nature Neuroscience **8**, 1720–1726 (2005)

[10] Barcroft, J., Barron, D.H.: Movement in the mammalian foetus. Ergebnisse der Physiologie **42**, 107–152 (1939)

[11] Ben-Ari, Y.: Developing networks play a similar melody. Trends in Neurosciences **24**, 353–360 (2001)

[12] Ben-Ari, Y.: Excitatory actions of GABA during development: the nature of the nurture. Nature Reviews Neuroscience **3**, 728–739 (2002)

[13] Bennett, M.V., Zukin, R.S.: Electrical coupling and neuronal synchronization in the mammalian brain. Neuron **41**, 495–511 (2004)

[14] Bernhard, C.G., Kaiser, I.H., Kolmodin, G.M.: On the development of cortical activity in fetal sheep. Acta Physiologica Scandinavica **47**, 333–349 (1959)

[15] Bernhard, C.G., Kaiser, I.H., Meyerson, B.A.: On the prenatal development of function and structure in the somesthetic cortex of the sheep. In: C.G. Bernhard, J.P. Schadé (eds.), Progress in Brain Research, vol. 26, Elsevier, Amsterdam (1967)

[16] Bernhard, C.G., Meyerson, B.A.: Early ontogenesis of electrocortical activity. With special reference to experimental studies on the fetal sheep. In: P. Kellaway, I. Petersén (eds.), Clinical Electroencephalography of Children, vol. 26, Grune and Stratton, New York (1968)

[17] Beurle, R.L.: Properties of a mass of cells capable of regenerating pulses. Philosophical Transactions of the Royal Society of London. Series B, Biological Sciences **240**, 55–94 (1956)

[18] Braitenberg, V., Schüz, A.: Anatomy of the Cortex: Statistics and Geometry. Springer-Verlag, Berlin, New York (1991)

[19] Brazier, M.A.B.: A history of the Electrical Activity of the Brain, the First Half-century. Pitman Medical Publishing, 39 Parker Street, London W. C. 2 (1961)

[20] Broomhead, D.S., King, G.P.: Extracting qualitative dynamics from experimental data. Physica D **20**, 217–236 (1986)

[21] Clancy, B., Darlington, R.B., Finlay, B.L.: Translating developmental time across mammalian species. Neuroscience **105**, 7–17 (2001)

[22] Clewlow, F., Dawes, G.S., Johnston, B.M., Walker, D.W.: Changes in breathing, electrocortical and muscle activity in unanaesthetized fetal lambs with age. Journal of Physiology **341**, 463–476 (1983)

[23] Craven, P., Wahba, G.: Smoothing noisy data with spline functions. Numerische Mathematik **31**, 377–403 (1979)

[24] da Silva, F.H.L.: Analysis of EEG non-stationarities. Electroencephalography Clinical Neurophysiology Supplement **34**, 163–179 (1978)

[25] da Silva, F.H.L., Hoeks, A., Smits, H., Zetterberg, L.H.: Model of brain rhythmic activity. Kybernetik **15**, 27–37 (1974)

[26] da Silva, F.H.L., van Rotterdam, Barts, P., van Heusden, E., Burr, W.: Models of neuronal populations: the basic mechanisms of rhythmicity. Progress in Brain Research **45**, 281–308 (1976)

[27] Dawes, G.S.: The 1987 James A. F. Stevenson Memorial Lecture. The development of fetal behavioural patterns. Canadian Journal of Physiology and Pharmacology **66**, 541–548 (1988)

[28] Dawes, G.S., Fox, H.E., Leduc, B.M., Liggins, G.C., Richards, R.T.: Respiratory movements and rapid eye movement sleep in the fetal lamb. Journal of Physiology **220**, 119–143 (1972)

[29] Dawes, G.S., Gardner, W.N., Johnston, B.M., Walker, D.W.: Breathing in fetal lambs: the effects of brain stem section. The Journal of Physiology **335**, 535–553 (1983)

[30] Dawes, G.S., Gardner, W.N., Johnston, B.M., Walker, D.: Activity of intercostals muscles in relation to breathing movements, electrical activity and gestational age in fetal lambs. The Journal of Physiology **307**, 47P–48P (1980)

[31] Dietsch, G.: Fourier analyse von elektroenzephalogrammen des menschen. Pflgers Arch Ges Physiol **230**, 106–112 (1932)

[32] Dominguez-Perrot, C., Feltz, P., Poulter, M.O.: Recombinant GABAA receptor desensitization: the role of the gamma 2 subunit and its physiological significance. The Journal of Physiology **497**, 145–159 (1996)

[33] Eilers, P.H.C.: Smoothing and interpolation with finite differences. In: P.S. Heckbertén (ed.), Graphic Gems, vol. IV, Academic Press (1994)

[34] Frank, G.W., Lookman, T., Nerengerg, M.A.H., Essex, C., Lemieux, J., Blume, W.: Chaotic time series analyses of epileptic seizures. Physica D **46**, 427–438 (1990)

[35] Fraser, A.M., Swinney, H.L.: Independent coordinates for strange attractors from mutual information. Physical Review A **33**, 1134–1140 (1986)

[36] Freeman, W.J.: A linear distributed feedback model for prepyriform cortex. Experimental Neurology **10**, 525–547 (1964)

[37] Freeman, W.J.: Mass Action in the Nervous System. Academic Press, New York (1975)

[38] Freeman, W.J.: Nonlinear dynamics of paleocortex manifested in the olfactory EEG. Biological Cybernetics **35**, 21–37 (1979)

[39] Freeman, W.J.: Predictions on neocortical dynamics derived from studies on paleocortex. In: Induced Rhythms of the Brain, Birkhaeuser, Boston (1991)

[40] Freeman, W.J., Holmes, M., West, G.A., Vanhatalo, S.: Fine spatiotemporal structure of phase in human intracranial EEG. Clinical Neurophysiology **117**, 1228–1243 (2006)

[41] Garaschuk, O., Linn, J., Eilers, J., Konnerth, A.: Large-scale oscillatory calcium waves in the immature cortex. Nature Neuroscience **3**, 452–459 (2000)

[42] Gillies, I.P.: Experimental evidence for cortical phase transitions in natural sleep. Master's thesis, University of Waikato, Hamilton, New Zealand (2006)

[43] Gluckman, P.D., Parsons, Y.: Stereotaxic method and atlas for the ovine fetal forebrain. Journal of Developmental Physiology **5**, 101–128 (1983)

[44] Gluckman, P.D., Parsons, Y.: Stereotaxic neurosurgery on the ovine fetus. In: P. Nathanlielszé (ed.), Animal Models in Fetal Medicine, vol. 3, Perinatology Press, New York (1984)

[45] Golub, G.H., van Loan, D.F.: Matrix Computations. Johns Hopkins University Press, Baltimore (1983)

[46] Grabauskas, G., Bradley, R.M.: Postnatal development of inhibitory synaptic transmission in the rostral nucleus of the solitary tract. Journal of Neurophysiology **85**, 2203–2212 (2001)

[47] Hastie, T., Tibshirani, R.: Generalized Additive Models. Chapman and Hall, London (1990)

[48] Hausser, W., Roth, A.: Dendritic and somatic glutamate receptor channels in rat cerebellar Purkinje cells. The Journal of Physiology **501**, 77–95 (1997)

[49] Hill, S., Tononi, G.: Modeling sleep and wakefulness in the thalamocortical system. Journal of Neurophysiology **93**, 1671–1698 (2005)

[50] Hodgkin, A.L., Huxley, A.F.: A quantitative description of membrane current and its application to conduction and excitation in nerve. The Journal of Physiology **117**, 500–544 (1952)

[51] Hodgkin, A.L., Rushton, W.A.H.: The electrical constants of a crustacean nerve fibre. Proceedings of the Royal Society of London. Series B, Biological Sciences **133**, 444–479 (1946)

[52] Huttenlocher, P.R., de Courten, C., Garey, L.J., van der Loos, H.: Synaptogenesis in human visual cortex — evidence for synapse elimination during normal development. Neuroscience Letters **33**, 247–252 (1982)

[53] Ioffe, S., Jansen, A., Russell, B., Chernick, V.: Sleep, wakefulness and monosynaptic reflexes in fetal and newborn lambs. Pfgers Archiv fr die gesamte Physiologie des Menschen und der Tiere (Pflugers Archives European Journal of Physiology) **388**, 149–157 (1980)

[54] Jenkins, G.M.: General considerations in the analysis of spectra. Technometric **3**, 142–149 (1961)

[55] Jirsa, V.K., Haken, H.: Field theory of electromagnetic brain activity. Physical Review Letters **77**, 960–963 (1996)

[56] Jirsa, V.K., Haken, H.: A derivation of a macroscopic field theory of the brain from the quasi-microscopic neural dynamics. Physica D **99**, 503–526 (1997)

[57] Jost, R.G., Quilligan, E.J., Yeh, S.H., Anderson, G.C.: Intrauterine electroencephalogram of the sheep fetus. American Journal of Obstetrics and Gynecology **114**, 535–539 (1972)

[58] Kaila, K.: Ionic basis of $\mathrm{GABA_A}$ receptor channel function in the nervous system. Progress in neurobiology **42**, 489–537 (1994)

[59] Khazipov, R., Khalilov, I., Tyzio, R., Morozova, E., Ben-Ari, Y., Holmes, G.L.: Developmental changes in GABAergic actions and seizure susceptibility in the rat hippocampus. European Journal of Neuroscience **19**, 590–600 (2004)

[60] Kim, H.S., Eykholt, R., Salas, J.D.: Nonlinear dynamics, delay times, and embedding windows. Physica D **127**, 48–60 (1999)

[61] Larkum, M.E., Zhu, J.J., Sakmann, B.: Dendritic mechanisms underlying the coupling of the dendritic with the axonal action potential initiation zone of adult rat layer 5 pyramidal neurons. The Journal of Physiology (London) **533**, 447–466 (2001)

[62] Lester, R.A., Jahr, C.E.: NMDA channel behavior depends on agonist affinity. Journal of Neurosceince **12**, 635–643 (1992)

[63] Liley, D.T.J., Cadusch, P.J., Wright, J.J.: A continuum theory of electro-cortical activity. Neurocomputing **1999**, 795–800 (1999)

[64] Liley, D.T.J., Wright, J.J.: Intracortical connectivity of pyramidal and stellate cells. Network: Computation in Neural Systems **26**, 175–189 (1994)

[65] London, M., Häusser, M.: Dendritic computation. Annual Review Neuroscience **28**, 503–532 (2005)

[66] Loomis, A.L., Harvey, E.N., Hobart, G.: Potential rhythms of the cerebral cortex during sleep. Science **81**, 597–598 (1935)

[67] Loomis, A.L., Harvey, F.N., Hobart, G.: Further observation on the potential rhythms of the cerebral cortex during sleep. Science **82**, 198–200 (1935)

[68] Lumber, F.D., Edelman, G.M., Tononi, G.: Neural dynamics in a model of the thalamocortical system. I. Layers, loops and the emergence of fast synchronous rhythms. Cerebral Cortex **7**, 207–227 (1997)

[69] Lumber, F.D., Edelman, G.M., Tononi, G.: Neural dynamics in a model of the thalamocortical system. II. The role of neural synchrony tested through perturbations of spiking timing. Cerebral Cortex **7**, 228–236 (1997)

[70] Mann, L.I., Duchin, S., Weiss, R.: Fetal EEG sleep stages and physiologic variability. American Journal of Obstetrics and Gynecology **119**, 533–538 (1972)

[71] Markus, E.J., Petit, T.L.: Neocortical synapstogenesis, aging, and behavior: lifespan development in the motor-sensory system of the rat. Experimental Neurology **1987**, 262–278 (1987)

[72] Marsaglia, G., Zaman, A.: Towards a Universal Random Number Generator. Florida State University Report: FSU-SCRI-87-50 (1987)

[73] McEwen, J.A., Anderson, G.B.: Modeling the stationary and gaussianity of spontaneous electroencephalographic activity. IEEE Transactions on Biomedical Engineering **22**, 361–369 (1975)

[74] Meyerson, B.A.: Ontogeny of interhemispheric functions: An electrophysiological study in pre- and postnatal sheep. Acta Physiologica Scandinavica Supplementum **312**, 1–111 (1968)

[75] Nunez, P.L.: The brain wave equation: A model for the EEG. Mathematical Biosciences **21**, 279–297 (1974)

[76] Nunez, P.L.: Wave-like properties of the alpha rhythm. IEEE Transactions on Biomedical Engineering **21**, 473–482 (1974)

[77] Nunez, P.L.: Neocortical Dynamics and Human EEG Rhythms. Oxford University Press, New York, Oxford (1995)

[78] Okai, T., Kozuma, S., Shinozuka, N., Kuwabara, Y., Mizuno, M.: A study on the development of sleep-wakefulness cycle in the human fetus. Early Human Development **29**, 391–396 (1992)

[79] O'Kusky, J.R.: Postnatal changes in the numerical density and total number of asymmetric and symmetric synapses in the hypoglossal nucleus of the rat. Developmental Brain Research **108**, 179–191 (1998)

[80] Rall, W.: Theory and physiological properties of dendrites. Annals of the New York Academy of Sciences **96**, 1071–1092 (1962)

[81] Rechtschaffen, A., Kales, A.: A Manual of Standardized Terminology, Techniques and Scoring System for Sleep Stages of Human Subjects. National Institute of Health Publication No. 204, Washington, DC: US Government Printing Office (1968)

[82] Rennie, C.J., Wright, J.J., Robinson, P.A.: Mechanisms of cortical electrical activity and the emergence of gamma rhythm. Journal of Theoretical Biology **205**, 17–35 (2000)

[83] Rheims, S., Minlebaev, M., Ivanov, A., Represa, A., Khazipov, R., Holmes, G.L., Ben-Ari, Y., Zilberter, Y.: Excitatory GABA in rodent developing neocortex in vitro. Journal of Neurophysiology **100**, 609–619 (2008)

[84] Rivera, C., Voipio, J., Kaila, K.: Two developmental switches in GABAergic signalling: the K^+-Cl^- cotransporter KCC2 and carbonic anhydrase CAVII. The Journal of Physiology **562**, 27–36 (2005)

[85] Roberts, S.J., Penny, W., Rezek, I.: Temporal and spatial complexity measures for electroencephalogram based brain-computer interfacing. Medical and Biological Engineering and Computing **37**, 93–98 (1999)

[86] Robinson, P.A., Rennie, C.J., Wright, J.J.: Propagation and stability of waves of electrical activity in the cerebral cortex. Physical Review E **56**, 826–840 (1997)

[87] Robinson, P.A., Rennie, C.J., Wright, J.J., Bourke, P.D.: Steady states and global dynamics of electrical activity in the cerebral cortex. Physical Review E **56**, 826–840 (1998)

[88] Ruckebusch, Y.: Activité electro-corticale chez le foetus de la brebis (Ovis aries) et de la vache (Bos tauris). Revue dé Médecine Vétérinaire **122**, 483–510 (1971)

[89] Ruckebusch, Y.: Development of sleep and wakefulness in the foetal lamb. Electroencephalography and Clinical Neurophysiology **32**, 119–128 (1972)

[90] Ruckebusch, Y., Gaujoux, M., Eghbali, B.: Sleep cycles and kinesis in the fetal lamb. Electroencephalography and Clinical Neurophysiology **42**, 226–237 (1977)

[91] Schmidt, K., Kott, M., Müller, T., Schubert, H., Schwab, M.: Developmental changes in the complexity of the electrocortical activity in foetal sheep. The Journal of Physiology (Paris) **94**, 435–443 (2000)

[92] Schmidt, K.M., Schwab, M., Kott, M., Szeto, H.H.: Nonlinear investigation of developmental changes of the ECoG activity in fetal sheep. In: Proceedings of the 20th Annual International Conference of the IEEE Engineering in Medicine and Biology Society, 20, pp. 2034–2037 (1998)

[93] Scholl, D.A.: The Organization of the Cerebral Cortex. Wiley, Washington (1956)

[94] Schwab, K., Groh, T., Schmidt, M., Witte, H.: Nonlinear analysis and modelling of cortical activation and deactivation patterns in the immature fetal electrocorticogram. Chaos **19**, 015111–015118 (2009)

[95] Schwab, M., Schmidt, K., Witte, H., Abrams, R.M.: Inverstigation of nonlinear ECoG changes during spontaneous sleep state changes and cortical arousal in fetal sheep. Cerebral Cortex **10**, 142–148 (2000)

[96] Selton, D., Andre, M., Hascoet, J.M.: Normal EEG in very premature infants: reference criteria. Clinical Neurophysiology **111**, 2116–2124 (2000)

[97] Sergejew, A.A.: Signal modeling of ECoG maturation in the fetal lamb: tests of a brain model. Ph.D. thesis, University of Auckland (1997)

[98] Shinozuka, N., Nathanielsz, P.W.: Nathanielsz. Electrocortical activity in fetal sheep in the last seven days of gestation. The Journal of Physiology **513**, 273–281 (1998)

[99] Steyn-Ross, D.A., Steyn-Ross, M.L., Sleigh, J.W., Wilson, M.T., Gillies, I.P., Wright, J.J.: The sleep cycle modelled as a cortical phase transition. Journal of Biological Physics **31**, 547–569 (2005)

[100] Steyn-Ross, D.A., Steyn-Ross, M.L., Wilcocks, L.C., Sleigh, J.W.: Toward a theory of the general anesthetic-induced phase transition of the cerebral cortex: II. Stochastic numerical simulations, spectral entropy, and correlations. Physical Review E **64**, 011918 (2001)

[101] Steyn-Ross, M.L., Steyn-Ross, D.A., Sleigh, J.W., Liley, D.T.J.: Theoretical electroencephalogram stationary spectrum for a white-noise-driven cortex: Evidence for a general anesthetic-induced phase transition. Physical Review E **60**, 7299–7311 (1999)

[102] Steyn-Ross, M.L., Steyn-Ross, D.A., Sleigh, J.W., Wilcocks, L.C.: Toward a theory of the general anesthetic-induced phase transition of the cerebral cortex: I. A statistical mechanics analogy. Physical Review E **64**, 011917 (2001)

[103] Steyn-Ross, M.L., Steyn-Ross, D.A., Wilson, M.T., Sleigh, J.W.: Gap junctions mediate large-scale turing structures in a mean-field cortex driven by subcortical noise. Physical Review E **76**, 011916 (2007)

[104] Steyn-Ross, M.L., Steyn-Ross, D.A., Wilson, M.T., Sleigh, J.W.: Modelling brain activation patterns for the default and cognitive states. Neuroimage **45**, 298–311 (2009)

[105] Stuart, G.J., Sakmann, B.: Active propagation of somatic action potentials into neocortical cell pyramidal dendrites. Nature **367**, 69–72 (1994)

[106] Swartz, B.E.: Timeline of the history of EEG and associated fields. Electroencephalography and Clinical Neurophysiology **106**, 173–176 (1998)

[107] Szeto, H.H.: Spectral edge frequency as a simple quantitative measure of the maturation of electrocortical activity. Pediatric Research **27**, 289–292 (1990)

[108] Szeto, H.H., Hinman, D.J.: Prenatal development of sleep-wake patterns in sheep. Sleep **8**, 347–355 (1985)

[109] Szeto, H.H., Vo, T.D.H., Dwyer, G., Dogramajian, M.E., Cox, M.J., Senger, G.: Prenatal development of sleep-wake patterns in sheep. American Journal of Obstetrics and Gynecology **153**, 462–266 (1985)

[110] Takens, F.: Detecting strange attractors in turbulence. In: Dynamical Systems and Turbulence, vol. 898 of Lecture Notes in Mathematics, pp. 366–381, Springer Berlin / Heidelberg (1981)

[111] Thomson, A.M.: Activity dependent properties of synaptic transmission at two classes of connections made by rat neocortical pyramidal neurons in vitro. The Journal of Physiology **502**, 131–147 (1997)

[112] Thomson, A.M., West, D.C., Hahn, J., Deuchars, J.: Single axon IPSP's elicited in pyramidal cells by three classes of interneurones in slices of rat neocortex. The Journal of Physiology **496**, 81–102 (1996)

[113] van Rotterdam, A., da Silva, F.H.L., J. van den Ende, M.A.V., Hermans, A.J.: A model of the spatial-temporal characteristics of the alpha rhythm. Bulletin of Mathematical Biology **58**, 3557–3571 (1982)

[114] Wahba, G., Wold, S.: A completely automatic french curve: Fitting spline functions by cross-validation. Communications in statistics **4**, 1–17 (1975)

[115] Whittaker, E.T.: On a new method of graduation. Proceedings of the Edinburgh Mathematical Society **41**, 63–75 (1923)

[116] Wiener, N.: Extrapolation, Interpolation, and Smoothing of Stationary Time Series. National Institute of Health Publication No. 204, Washington, DC: US Government Printing Office (1968)

[117] Williams, C.E., Gluckman, P.D.: Real-time spectral intensity analysis of the EEG on a microcomputer. Journal of Neuroscientific Methods **32**, 9–13 (1990)

[118] Williams, C.E., Gunn, A.J., Synek, B., Gluckman, P.D.: Delayed seizures occurring with hypoxic-ischemic encephalopathy in the fetal sheep. Pediatric Research **27**, 561–565 (1990)

[119] Wilson, H.R., Cowan, J.D.: Excitatory and inhibitory interactions in localized populations of model neurons. Biophysical Journal **12**, 1–24 (1972)

[120] Wilson, H.R., Cowan, J.D.: A mathematical theory of the functional dynamics of cortical and thalamic nervous tissue. Kybernetik **13**, 55–80 (1973)

[121] Wilson, M., Bower, J.M.: Cortical oscillations and temporal interactions in a computer simulation of piriform cortex. Journal of Neurophysiology **67**, 981–995 (1992)

[122] Wilson, M.T., Steyn-Ross, D.A., Sleigh, J.W., Steyn-Ross, M.L., Wilcocks, L.C., Gillies, I.P.: The K-complex and slow oscillation in terms of a mean-field cortical model. Journal of Computational Neuroscience **27**, 243–257 (2006)

[123] Wilson, M.T., Steyn-Ross, M.L., Steyn-Ross, D.A., Sleigh, J.W.: Predictions and simulations of cortical dynamics during natural sleep using a continuum approach. Physical Review E **72**, 051910 (2005)

[124] Wright, J.J.: EEG simulation: Variation of spectral envelope, pulse synchrony and ≈ 40 Hz oscillation. Biological Cybernetics **76**, 181–194 (1997)

[125] Wright, J.J.: Simulation of EEG: Dynamic changes in synaptic efficacy, cerebral rhythms, and dissipative and generative activity in cortex. Biological Cybernetics **81**, 131–147 (1999)

[126] Wright, J.J.: Cortical phase transitions: Properties demonstrated in continuum simulations at mesoscopic and macroscopic scales. New Mathematics and Natural Computation. Special Issue in honour of W. J. Freeman **in press** (2009)

[127] Wright, J.J.: Generation and control of cortical gamma: Findings from simulation at two scales. Neural Networks **22**, 373–384 (2009)

[128] Wright, J.J., Liley, D.T.J.: Dynamics of the brain at global and microscopic scales: Neural networks and the EEG. Behavioral and Brain Sciences **19**, 285–320 (1996)